

**EVIDENCE OF REOPENED MICROFRACTURES IN PRODUCTION DATA
OF HYDRAULICALLY FRACTURED SHALE GAS WELLS**

A Thesis

by

SIPPAKORN APIWATHANASORN

Submitted to the Office of Graduate Studies of
Texas A&M University
in partial fulfillment of the requirements for the degree of

MASTER OF SCIENCE

August 2012

Major Subject: Petroleum Engineering

Evidence of Reopened Microfractures in Production Data of Hydraulically Fractured
Shale Gas Wells

Copyright 2012 Sippakorn Apiwathanasorn

**EVIDENCE OF REOPENED MICROFRACTURES IN PRODUCTION DATA
OF HYDRAULICALLY FRACTURED SHALE GAS WELLS**

A Thesis

by

SIPPAKORN APIWATHANASORN

Submitted to the Office of Graduate Studies of
Texas A&M University
in partial fulfillment of the requirements for the degree of

MASTER OF SCIENCE

Approved by:

Chair of Committee,	Christine Ehlig-Economides
Committee Members,	David S. Schechter
	Maria A. Barrufet
Head of Department,	A. Daniel Hill

August 2012

Major Subject: Petroleum Engineering

ABSTRACT

Evidence of Reopened Microfractures in Production Data of Hydraulically Fractured
Shale Gas Wells⁰(August 2012)

Sippakorn Apiwathanasorn, B.Eng., Chulalongkorn University

Chair of Advisory Committee: Dr.'Christine Ehlig-Economides

Frequently a discrepancy is found between the stimulated shale volume (SSV) estimated from production data and the SSV expected from injected water and proppant volume. One possible explanation is the presence of a fracture network, often termed fracture complexity, that may have been opened or reopened during the hydraulic fracturing operation.

The main objective of this work is to investigate the role of fracture complexity in resolving the apparent SSV discrepancy and to illustrate whether the presence of reopened natural fracture network can be observed in pressure and production data of shale gas wells producing from two shale formations with different well and reservoir properties.

Homogeneous, dual porosity and triple porosity models are investigated. Sensitivity runs based on typical parameters of the Barnett and the Horn River shale are performed. Then the field data from the two shales are matched.

Homogeneous models for the two shale formations indicate effective infinite conductivity fractures in the Barnett well and only moderate conductivity fractures in the

Horn River shale. Dual porosity models can support effectively infinite conductivity fractures in both shale formations.

Dual porosity models indicate that the behavior of the Barnett and Horn River shale formations are different. Even though both shales exhibit apparent bilinear flow behavior the flow behaviors during this trend are different. Evidence of this difference comes from comparing the storativity ratio observed in each case to the storativity ratio estimated from injected fluid volumes during hydraulic fracturing. In the Barnett shale case similar storativity ratios suggest fracture complexity can account for the dual porosity behavior. In the Horn River case, the model based storativity ratio is too large to represent only fluids from hydraulic fracturing and suggests presence of existing shale formation microfractures.

To my family

ACKNOWLEDGEMENTS

I would like to thank my committee chair, Dr. Christine Ehlig-Economides for her dedication and support throughout the course of this research. Also thanks to my committee members, Dr. David S. Schechter, and Dr. Maria A. Barrufet.

I would like to thank also Dr. Robert A. Wattenbarger for his helpful guidance.

Thanks also to Apache Canada, Ltd., and EOG Resources, Inc. for providing the data for this research.

Also thanks to PTT Exploration and Production PLC for funding and supports.

Thanks also to all friends, colleagues, and the department faculty and staff for making my time at Texas A&M University an invaluable experience.

Finally, thanks to my mother, father, and family for their encouragement and to my girlfriend for her patience, love, and great support.

NOMENCLATURE

A_{cw}	=	Cross sectional area to the flow, ft ²
A_{fb}	=	Fracture area per unit of bulk volume, 1/ft
A_{fD}	=	Dimensionless fracture area
A_{fma}	=	Fracture area per unit of matrix volume, 1/ft
b	=	Fracture width, ft
c_f	=	Initial rock compressibility, 1/psi
c_g	=	Initial gas compressibility, 1/psi
c_t	=	Initial total compressibility, 1/psi
c_w	=	Initial water compressibility, 1/psi
C_{fD}	=	Dimensionless hydraulic fracture conductivity
h	=	Formation thickness, ft
h_{ma}	=	Matrix volume element length or fracture network spacing, ft
k	=	Formation permeability, md
k_F	=	Hydraulic fracture permeability, md
k_{fb}	=	Bulk fracture permeability, md
k_{ma}	=	Matrix permeability, md
L_w	=	Horizontal well length, ft
$m(p)$	=	Real gas pseudopressure, psi ² /cp
n_F	=	Number of hydraulic fractures
p_i	=	Initial pressure at formation depth, psi

$p_{i,s}$	=	Initial pressure converted to surface, psi
p_{WD}	=	Dimensionless bottomhole flowing pressure
p_{wf}	=	Bottomhole flowing pressure, psi
Q	=	Cumulative production, scf
Q	=	Gas production rate, Mscf/d
q_D	=	Dimensionless production rate
r_w	=	wellbore radius
s_g	=	Gas saturation, fraction
s_w	=	Water saturation, fraction
T	=	Time, hr
T	=	Formation temperature, °F
t_{DxF}	=	Dimensionless time respect to fracture half-length
t_e	=	Material balance time, day
$t_{e,elf}$	=	End of linear flow material balance time, day
t_{elf}	=	End of linear flow actual time, day
V	=	Volume, ft ³
x	=	distance, ft
x_e	=	Total length of stimulated shale volume, ft
x_F	=	Hydraulic fracture half-length, ft
x_s	=	Hydraulic fractures spacing, ft
z_w	=	Vertical distance to lower boundary, ft

Greek variables

ϕ	=	Porosity, fraction
γ_γ	=	Gas specific gravity, fraction
λ	=	Interporosity flow coefficient
μ	=	Gas viscosity, cp
η_{maD}	=	Dimensionless matrix hydraulic diffusivity
ω	=	Storativity ratio
ω_{inj}	=	Injection volume derived storativity ratio

Subscripts

D	=	Dimensionless
e	=	Material balance time
elf	=	End of linear flow
f	=	Fracture network or microfractures
F	=	Hydraulic fractures
fb	=	Bulk fractures
ma	=	Matrix
p	=	Constant pressure
r	=	Constant rate

TABLE OF CONTENTS

	Page
ABSTRACT	iii
DEDICATION	v
ACKNOWLEDGEMENTS	vi
NOMENCLATURE	vii
TABLE OF CONTENTS	x
LIST OF FIGURES	xiii
LIST OF TABLES	xix
CHAPTER I INTRODUCTION	1
1.1 Problem descriptions	1
1.2 Objectives	3
1.3 Methodology	3
1.4 Organization of this thesis	4
CHAPTER II LITERATURE REVIEW	7
2.1 Shale gas production using MTFHW technique	7
2.2 Rate normalized pressure (RNP) and RNP derivatives	8
2.3 Single porosity (homogeneous) model	9
2.4 Complexity in shale formation	11
2.5 Dual porosity model	13
2.6 Triple porosity model	19
2.7 Available models in commercial software (Ecrin)	24
2.8 Chapter summary	26
CHAPTER III MODEL SENSITIVITY STUDIES BASED ON THE BARNETT SHALE	27
3.1 Practical time windows	28
3.2 Barnett shale formation characterization	31
3.2.1 Field background	31
3.2.2 Data overview	34

3.3 Sensitivity studies using the single porosity (homogeneous) model.....	39
3.3.1 Permeability.....	39
3.3.2 Hydraulic fracture spacing (x_s).....	44
3.3.3 Hydraulic fracture half-length (x_F).....	46
3.3.4 Dimensionless Fracture conductivity (C_{fD}).....	48
3.4 Sensitivity studies using the dual porosity model	50
3.4.1 Interporosity coefficient (λ)	50
3.4.2 Storativity ratio (ω)	53
3.5 Model matches with Barnett well field data.....	58
3.5.1 Data diagnosis	58
3.5.2 Model inputs.....	60
3.5.3 Homogeneous model matching.....	62
3.5.4 Dual porosity model matching.....	66
3.6 Discussion	75
3.7 Chapter summary	80
 CHAPTER IV MODEL SENSITIVITY STUDIES BASED ON THE HORN RIVER SHALE.....	 81
4.1 Horn River shale formation characterization	81
4.1.1 Field background.....	81
4.1.2 Data overview.....	84
4.2 Sensitivity studies using the single porosity (homogeneous) model.....	88
4.2.1 Permeability.....	88
4.2.2 Dimensionless Hydraulic Fracture conductivity (C_{fD}).....	92
4.2.3 Hydraulic fracture half-length (x_F).....	93
4.2.4 Hydraulic fracture spacing (x_s).....	94
4.3 Sensitivity studies using the dual porosity model	96
4.3.1 Interporosity flow coefficient (λ)	97
4.3.2 Storativity ratio (ω)	98
4.4 Model matches with Horn River well field data	101
4.4.1 Data diagnosis	101
4.4.2 Model inputs.....	104
4.4.3 Homogeneous model matching.....	106
4.4.4 Dual porosity model matching.....	110
4.5 Discussion	124
4.6 Chapter summary	126
 CHAPTER V CONCLUSIONS AND RECOMMENDATIONS	 128
REFERENCES	132
APPENDIX A SINGLE POROSITY (HOMOGENEOUS) MODEL BEHAVIOR	139

A.1. Formation Pseudolinear flow	139
A.2 Hydraulic Fractures - Matrix Bilinear flow	141
APPENDIX B DUAL POROSITY MODEL BEHAVIOR	145
B.1 Fracture Network to Hydraulic Fracture Bilinear Flow (FN-HF)	149
B.2 Matrix to Fracture Network to Hydraulic Fractures Trilinear Flow (M-FN-HF)	152
B.3 Total System to Hydraulic Fractures Bilinear Flow (TS-HF)	154
B.4 Fracture Network Linear Flow (FN)	155
B.5 Matrix to fracture Network Bilinear Flow (M-FN)	156
B.6 Total System Linear Flow (TS)	157
APPENDIX C TRIPLE POROSITY MODEL BEHAVIOR	160
C.1 Main flow regimes	161
C.2 Flow regime combinations	163
APPENDIX D DIAGNOSIS USING RNP AND ITS DERIVATIVE	173
D.1 Bilinear flow	173
D.2 Linear flow	176
D.3 Distance of investigation	179
D.4 Observations	180
APPENDIX E BARNETT WELL SPECIALIZED PLOTS	182
APPENDIX F HORN RIVER SHALE SPECIALIZED PLOTS	206
VITA	221

LIST OF FIGURES

	Page
Figure 2.1: A multi-transverse hydraulically fractured horizontal well.....	8
Figure 2.2: Potential flow regimes during MTFHW production	10
Figure 2.3: Fractures growth and complexity scenarios.....	12
Figure 2.4: General flow regimes for dual porosity system comparing pseudosteady state and transient flow conditions	15
Figure 2.5: Map view showing vertically fractured well in double porosity reservoir	16
Figure 2.6: Pressure and pressure derivative plots for case with infinite conductivity hydraulic fracture (regime 7, 8, 9)	17
Figure 2.7: Pressure and pressure derivative plots for case with finite conductivity hydraulic fracture (regime 1, 2, 3)	17
Figure 2.8: Cross-sectional view of horizontal slab matrix blocks	19
Figure 2.9: Top view representing multi-traverse fractured horizontal well in triple porosity system (Modified from Al-Ahmadi et al., 2010).....	21
Figure 2.10: Five flow regions for the triple porosity model (Al-Ahmadi et al. 2010) ...	22
Figure 2.11: Transient slab and sphere model comparison on log-log pressure and pressure derivative plots	26
Figure 3.1: MTFHW dimension for Figure 3.2.....	29
Figure 3.2: Practical time windows example	29
Figure 3.3: Barnett shale stratigraphy and location (extracted from Montgomery et al., 2005)	32
Figure 3.4: Base case MTFHW dimension and SRV boundary for Barnett shale.....	33
Figure 3.5: Pressure and production history of the well from the Horn River Basin shale	35
Figure 3.6: Log-log diagnostic plots example for a BU test of the Barnett shale well.....	36

Figure 3.7: Log-log diagnostic plots example for the long term production data of the Barnett shale well.....	37
Figure 3.8: Log-log diagnostic plots example for the long term production data of the Barnett shale well after removing artificial points.....	38
Figure 3.9: Permeability and fracture spacing versus material balance time	41
Figure 3.10: Log-log diagnostic plot based on base case parameters of Barnett shale	42
Figure 3.11: Barnett shale permeability sensitivity results	43
Figure 3.12: Barnett shale hydraulic fracture spacing sensitivity results.....	45
Figure 3.13: Barnett shale hydraulic fracture half-length sensitivity results	47
Figure 3.14: Barnett shale hydraulic fracture conductivity sensitivity results	48
Figure 3.15: Barnett shale interporosity flow coefficient (λ) sensitivity results.....	51
Figure 3.16: Typical ω value for the Barnett shale based on injection volume	54
Figure 3.17: Barnett shale storativity ratio (ω) sensitivity results.....	56
Figure 3.18: Barnett shale storativity ratio (ω) sensitivity results with lower fracture network permeability	56
Figure 3.19: Barnett shale storativity ratio (ω) sensitivity results with lower fracture network permeability and higher λ	58
Figure 3.20: Pressure and production history plots of representative well for the Barnett shale	59
Figure 3.21: RNP and RNP' plots of the representative well for Barnett shale.....	60
Figure 3.22: Well geometry and boundary dimension for Barnett well.....	61
Figure 3.23: Log-log RNP and RNP' plots showing field data and homogeneous model matching comparison ($k=6.5$ nd, $skin=0.00013$)	62
Figure 3.24: Production and cumulative production plots showing field data and homogeneous model matching comparison ($k=6.5$ nd, $skin=0.00013$).....	63

Figure 3.25: Casing pressure plots showing field data and homogeneous model matching comparison ($k=6.5$ nd, $skin=0.00013$)	63
Figure 3.26: Log-log RNP and RNP' plots showing field data and homogeneous model matching comparison ($k=6.5$ nd, $F_C=0.8$ md-ft, $skin=0$)	64
Figure 3.27: Production and cumulative production plots showing field data and homogeneous model matching comparison ($k=6.5$ nd, $F_C=0.8$ md-ft, $skin=0$)	65
Figure 3.28: Casing pressure plots showing field data and homogeneous model matching comparison ($k=6.5$ nd, $F_C=0.8$ md-ft, $skin=0$)	65
Figure 3.29: Log-log RNP and RNP' plots showing FN-HF and FN flow regime sequence matching ($k=8.6$ nd, $FC=0.80$ md-ft, $\omega=0.80$, $\lambda=1.0E-12$)	67
Figure 3.30: Gas rate and cumulative gas plots showing FN-HF and FN flow regime sequence matching ($k=8.6$ nd, $FC=0.80$ md-ft, $\omega=0.80$, $\lambda=1.0E-12$)	68
Figure 3.31: Casing pressure plots showing FN-HF and FN flow regime sequence matching ($k=8.6$ nd, $FC=0.80$ md-ft, $\omega=0.80$, $\lambda=1.0E-12$)	68
Figure 3.32: Log-log RNP and RNP' plots showing TS-HF and TS flow regime sequence matching ($k=6.5$ nd, $FC=0.80$ md-ft, $\omega=0.01$, $\lambda=1.0$)	70
Figure 3.33: Gas rate and cumulative gas plots showing TS-HF and TS flow regime sequence matching ($k=6.5$ nd, $FC=0.80$ md-ft, $\omega=0.01$, $\lambda=1.0$)	71
Figure 3.34: Casing pressure plots showing TS-HF and TS flow regime sequence matching ($k=6.5$ nd, $FC=0.80$ md-ft, $\omega=0.01$, $\lambda=1.0$)	71
Figure 3.35: Log-log RNP and RNP' plots showing M-FN and TS flow regime sequence matching ($k=5.5$ nd, $F_C=IFC$, $\omega=0.01$, $\lambda=0.008$)	72
Figure 3.36: Gas rate and cumulative gas plots showing M-FN and TS flow regime sequence matching ($k=5.5$ nd, $F_C=IFC$, $\omega=0.01$, $\lambda=0.008$)	73
Figure 3.37: Casing pressure plots showing M-FN and TS flow regime sequence matching ($k=5.5$ nd, $F_C=IFC$, $\omega=0.01$, $\lambda=0.008$)	73
Figure 3.38: Log-log RNP and RNP' plots showing different flow regime matching comparison	75

Figure 4.1: Horn River Basin stratigraphy and location (National Energy Board, 2009)	82
Figure 4.2: Base case MTFHW dimension and SRV boundary for Horn River shale	83
Figure 4.3: Pressure and production history of the well from Horn River shale	85
Figure 4.4: Log-log diagnostic plots example for a BU test of the Horn River well	86
Figure 4.5: Log-log diagnostic plots example for the long term production data of the Horn River shale well	87
Figure 4.6: Permeability and fracture spacing versus material balance time for the Horn River shale	89
Figure 4.7: Log-log diagnostic plot based on base case parameters of Horn River	90
Figure 4.8: Horn River shale permeability sensitivity results	91
Figure 4.9: Horn River shale hydraulic fracture conductivity sensitivity results	92
Figure 4.10: Log-log diagnostic plot based on base case parameters of Horn River shale with finite C_{FD}	93
Figure 4.11: Horn River shale hydraulic fracture half-length sensitivity results	94
Figure 4.12: Horn River shale hydraulic fracture spacing sensitivity results	95
Figure 4.13: Dual porosity transient slab versus sphere model comparison	97
Figure 4.14: Horn River shale interporosity flow coefficient (λ) sensitivity results	98
Figure 4.15: Typical ω value for Horn River shale based on injection volume	99
Figure 4.16: Horn River shale storativity ratio (ω) sensitivity results	100
Figure 4.17: Pressure and production history of the Horn River well	102
Figure 4.18: Long term production RNP and RNP derivative log-log plots for a Horn River shale well	103
Figure 4.19: Pressure and pressure derivative for the two build-up periods for Horn River well	104

Figure 4.20: Well geometry and boundary dimension for Horn River well	106
Figure 4.21: Log-log RNP and RNP' plots showing field data and homogeneous model matching comparison ($k = 19$ nd, $F_C = 0.30$ md-ft)	107
Figure 4.22: Production and cumulative production plots showing field data and homogeneous model matching comparison ($k=19$ nd, $F_C=0.30$ md-ft).....	107
Figure 4.23: Casing pressure plots showing field data and homogeneous model matching comparison ($k = 19$ nd, $F_C = 0.30$ md-ft)	108
Figure 4.24: Pressure and pressure derivative showing field data and homogeneous model matching comparison for the 1 st buildup ($k = 19$ nd, $F_C = 0.30$ md-ft)	109
Figure 4.25: Pressure and pressure derivative showing field data and homogeneous model matching comparison for the 2 nd buildup ($k = 16$ nd, $F_C = 1.30$ md-ft)	109
Figure 4.26: Log-log RNP and RNP' plots showing FN-HF flow regime matching ($k = 36$ nd, $F_C = 0.30$ md-ft, $\omega = 0.50$, $\lambda=1.0E-8$)	111
Figure 4.27: Gas rate and cumulative gas plots showing FN-HF flow regime matching ($k=36$ nd, $F_C=0.30$ md-ft, $\omega=0.50$, $\lambda=1.0E-8$)	111
Figure 4.28: Casing pressure plots showing FN-HF flow regime matching ($k=36$ nd, $F_C = 0.30$ md-ft, $\omega = 0.50$, $\lambda = 1.0E-8$)	112
Figure 4.29: Pressure and pressure derivative FN-HF flow regime matching for the 1 st buildup ($k=36$ nd, $F_C=0.30$ md-ft, $\omega=0.50$, $\lambda=1.0E-8$)	114
Figure 4.30: Pressure and pressure derivative FN-HF flow regime matching for the 2 nd buildup ($k=30$ nd, $F_C=0.52$ md-ft, $\omega=0.50$, $\lambda=1.0E-8$)	114
Figure 4.31: Log-log RNP and RNP' plots showing TS-HF flow regime matching ($k = 19$ nd, $F_C = 0.30$ md-ft, $\omega = 0.001$, $\lambda = 10$)	115
Figure 4.32: Gas rate and cumulative gas plots showing TS-HF flow regime matching ($k = 19$ nd, $F_C = 0.30$ md-ft, $\omega = 0.001$, $\lambda = 10$)	116
Figure 4.33: Casing pressure plots showing TS-HF flow regime matching comparison ($k = 19$ nd, $F_C = 0.30$ md-ft, $\omega = 0.001$, $\lambda = 10$).....	116

Figure 4.34: Pressure and pressure derivative showing TS-HF flow regime matching for the 1 st buildup ($k=19$ nd, $F_C=0.30$ md-ft, $\omega=0.001$, $\lambda=10$)...	118
Figure 4.35: Pressure and pressure derivative showing TS-HF flow regime matching for the 2 nd buildup ($k=15.8$ nd, $F_C=0.57$ md-ft, $\omega=0.001$, $\lambda=10$).....	118
Figure 4.36: Log-log RNP and RNP' plots showing M-FN flow regime matching ($k=16$ nd, $F_C=IFC$, $\omega=0.05$, $\lambda=6E-4$).....	120
Figure 4.37: Gas rate and cumulative gas plots M-FN flow regime matching ($k=16$ nd, $F_C=IFC$, $\omega=0.05$, $\lambda=6E-4$)	120
Figure 4.38: Casing pressure plots showing M-FN flow regime matching ($k=16$ nd, $F_C=IFC$, $\omega=0.05$, $\lambda=6E-4$)	121
Figure 4.39: Pressure and pressure derivative showing M-FN flow regime matching for the 1 st buildup ($k=16$ nd, $F_C=IFC$, $\omega=0.05$, $\lambda=6E-4$)	123
Figure 4.40: Pressure and pressure derivative showing M-FN flow regime matching for the 2 nd buildup ($k=13.8$ nd, $F_C=IFC$, $\omega=0.1$, $\lambda=0.01$)	123
Figure 4.41: Log-log RNP and RNP' plots showing different flow regime matching comparison.....	125

LIST OF TABLES

	Page
Table 2.1: Fractured well in dual porosity formation flow regime combinations.....	16
Table 2.2: Flow solutions for dual porosity models.....	18
Table 3.1: Estimate range of sensitivity parameters for the Barnett shale study	34
Table 3.2: Barnett shale model input parameters	61
Table 3.3: Barnett shale dual porosity model matching results summary.....	75
Table 4.1: Estimate range of sensitivity parameters for the Horn River shale study	84
Table 4.2: Horn River model input parameters.....	105
Table 4.3: Horn River shale dual porosity model matching results summary	124

CHAPTER I

INTRODUCTION

Gas production from shale formation has been developed extensively during the last decades followed the success of multi-traverse fractured horizontal well completion. However, knowledge of pressure and production behavior in this type of shale gas wells is still not fully understood. The problem is due mainly to the complex nature of flow in the shale formation once the well completion is in place, as well as an ambiguity in modeling the flow behavior.

1.1 Problem descriptions

It has been observed for some time that there exists a discrepancy between fractured half-length calculated from production data analysis (PDA) or pressure transient analysis (PTA) and those obtained from other methods such as microseismic or fracture treatment calculation. To be more specific, it is frequently found that the numbers obtained from PDA and from PTA are always smaller than what being seen from other methods.

One possible explanation for this discrepancy is the presence of reopened natural fracture networks that may have been reactivated during the hydraulic fracturing operation. The role of reopened natural fractures, or microfracture networks, is that they

may require less pressure to be activated than to fracture new shale formation. As a result, fracturing fluids may be more likely to reopen these natural fractures network than to propagate the hydraulic fractures. This obviously can shorten the propped fracture half-length to less than that expected if the reopened natural fractures do not exist.

The question is whether we can see conclusive evidence of these reopened natural fracture networks in well production and pressure data. Even though theoretical models indicate multiple series of flow regimes exhibiting linear, bilinear, and even trilinear flow, characterizing the various flow regimes in field data is challenging because typically only one or two of the flow regimes are likely to appear in any one transient data set. As a result, a unique characterization of the flow behavior is unlikely since all the solutions involve lots of unknowns including hydraulic fracture half-length and conductivity, permeability, spacing, width, and extent of the natural fracture network, which cannot be calculated uniquely unless complete series of flow regimes are seen.

Numbers of methods have been studied so far in an attempt to eliminate or limit the unknown to minimum so that the unique solution can be achieved, but still there are lots of possible answers to the question, and even a simple model still gives ambiguous results as different sets of parameters can match the behaviors observed in data equally well.

Therefore, it is important to have more understanding about the flow behavior of the shale gas wells by investigating various possible flow models that can represent

production and pressure characteristic including simple homogeneous model, dual porosity model, and triple porosity model so that the properties consistent with each model can be quantified.

1.2 Objectives

The main objective of this work is to investigate the role of fracture complexity in resolving the apparent discrepancy between the SRV calculated from production data and the SRV expected from injected water and proppant volume and to illustrate how likely or unlikely the presence of reopened natural fracture network can be observed from the actual pressure and production data of shale gas wells producing from various shale formation with different well and reservoir properties.

1.3 Methodology

The flow models representing flow behavior of multi-traverse fractured shale gas wells include 1) the hydraulically fractured horizontal well in a homogeneous single porosity reservoir, 2) the hydraulically fractured horizontal well in a dual porosity reservoir consisting of a reopened fracture network and shale matrix, and 3) a triple porosity model which treats the hydraulic fractures, reopened natural fractures, and the shale matrix as three different continuum media.

All possible flow regime combinations that may be seen in the pressure and production data are shown. Then sensitivity studies with typical shale properties and

well completions from the actual shale gas fields are generated to show combinations of the flow regimes that can happen in reality.

Actual field data from various shale formations including the Barnett shale and the Horn River shale are analyzed based on all possible models and combinations. The results are then compared to filter out the model and combinations that is not likely to occur or gives impractical results.

Finally, the conclusions are addressed whether or not the model represented by a reopened microfracture network, or “complexity”, as this has been called by some authors, can characterize the behavior of hydraulically fractured shale gas wells in each shale formation.

1.4 Organization of this thesis

Five chapters are included in this thesis. The details of each chapter are as follows:

Chapter I: Introduction - this chapter gives information about problem description, general idea to the problem, objectives, methodology, and organization of the thesis.

Chapter II: Literature survey - this chapter provides a brief review of available flow models that may be used to characterize flow behavior of shale gas wells including homogeneous single porosity, dual porosity, and triple porosity. The model available in the commercial software will also be reviewed. The concept of complexity in shale formation is also included.

Chapter III: Model sensitivity based on the Barnett Shale - this chapter investigates the Barnett shale by running sensitivity on the important parameters using single porosity and dual porosity models. The expected flow regimes will be shown based on base case parameters. Then the matching results of the Barnett well case example will be revealed. The conclusion will be made how the reopened fracture network is likely or unlikely to model the flow behavior of the Barnett shale.

Chapter IV: Model sensitivity based on the Horn River Shale - this chapter uses the same procedures as shown in Chapter III to investigate the Horn River shale. The sensitivity run on the important parameters using single porosity and dual porosity models will be shown. The expected flow regimes will be shown based on base case parameters. Then the matching results of the Horn River well case example will be shown. The conclusion will be made how the reopened fracture network is likely or unlikely to model the flow behavior of the Horn River shale.

Chapter V: Conclusions and recommendations - this chapter concludes all the findings and ideas developed throughout the thesis. The similarities and differences of two shales will be concluded, and the role of reopened fracture network on each of the shale will be summarized. Observation and recommendation of how this work can be improved are also included.

Appendices: appendices A-C are provided to give more insight about each of the flow models, i.e. the single porosity, dual porosity, and triple porosity. For the triple porosity model, additional flow regimes combinations will be introduced. Appendix D gives information about material balance time application for linear and bilinear flow

regime. Appendix E and F provide a set of specialized plots for the Barnett and the Horn River shale, respectively.

CHAPTER II

LITERATURE REVIEW

This chapter provides information from the literature about shale gas production behavior in multiple transverse fractured horizontal wells (MTFHW), descriptions of complexity in shale formations, and the analytical flow models that can be used to investigate the evidence of shale formation complexity in production data. These flow models include the homogeneous (single porosity) model, dual porosity model, and triple porosity model.

2.1 Shale gas production using MTFHW technique

Shale gas formations typically have very low permeability compared with conventional reservoirs, with permeability values ranging from 10 to 100 nd (Cipolla et al. 2009). Therefore, economic production from a shale formation depends intensely on technologies that can enhance productivity of the shale. Hydraulic fracturing and horizontal drilling are considered the two key technologies that have triggered the economic development of shale gas (Meyer et al. 2010). The multiple transverse fractured horizontal wells (MTFHW) completion technology which combines the hydraulic fracturing and horizontal well drilling techniques has been used extensively. Figure 2.1 illustrates the 2-D schematic model for the MTFHW which will be used throughout this work. The model consists of a transversely fractured horizontal well located inside a shale formation with a rectangular boundary. Note that the boundary

here is not a real physical boundary but rather is defined by the interference boundary between adjacent wells. When productive hydraulic fracture half-lengths fully penetrate half the distance between adjacent horizontal wells, the interference boundaries correspond to the stimulated reservoir volume (SRV). Because production beyond the SRV boundary is not expected due to the low shale permeability, Song, et al. (2011) defined the extent of the SRV by the productive extent of created hydraulic fractures, which may or may not correspond to the drainage area defined by the horizontal well spacing. Figure 2.1 illustrates nomenclature to be used in this thesis for the horizontal well length, L_w , the productive half-length, x_f , of the hydraulic fractures and the spacing, x_s , between them.

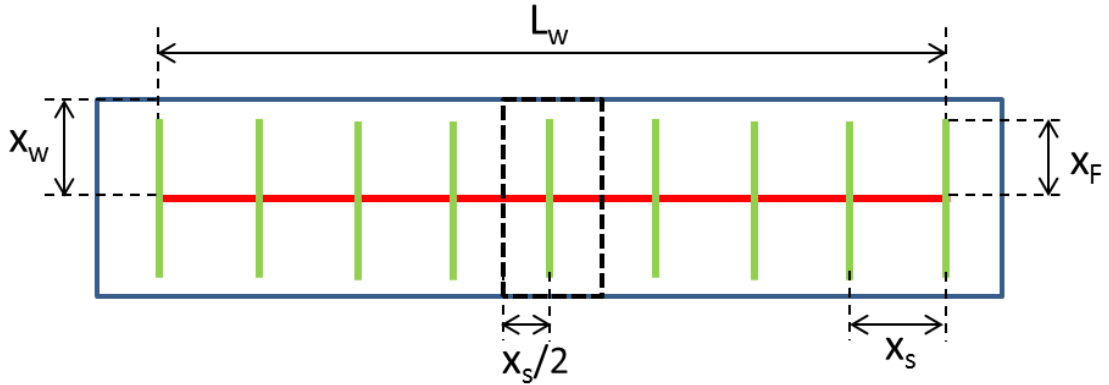


Figure 2.1: A multi-transverse hydraulically fractured horizontal well

2.2 Rate normalized pressure (RNP) and RNP derivatives

Many models for constant rate pressure drawdown and constant pressure rate decline have been developed. However, the actual long-term production behavior exhibits neither constant pressure nor constant rate, but rather shows variation in both

rate and pressure. The use of material balance time (t_e) and pressure normalized rate (PNR) defined as instantaneous productivity index allow the long-term production data to be seen as a single virtual rate decline at constant pressure (Palacio and Blasingame, 1993). Alternatively, the rate normalized pressure (RNP) defined as reciprocal of the instantaneous productivity index allows the long-term production data to be seen as a virtual pressure drawdown at constant rate, also when graphed versus the material balance time. Note that the constant rate condition is more favorable for flow regime investigation because it shows characteristic slopes when viewed as the derivative of the pressure change with respect to the natural log of time (Ehlig-Economides et al. 2009). Therefore, RNP and RNP derivative (RNP') will be used in this work to investigate the flow regimes. Eq. 2.1 and Eq. 2.2 show the definitions for RNP and RNP' when pseudopressure function, $m(p)$, is used.

$$RNP = \frac{m(p_i) - m(p_{wf})}{q} \quad \dots(2.1)$$

$$RNP' = \frac{dRNP}{d\ln t_e} = \frac{d[m(p_i) - m(p_{wf})]/q}{d\ln t_e} \quad \dots(2.2)$$

2.3 Single porosity (homogeneous) model

The single porosity model represents flow behaviors of MTFHW producing from homogeneous or single porosity reservoir without any opened, reopened, or natural fractures. Song and Ehlig-Economides (2011) presented a sequence of flow regimes for the MTFHW production on log-log rate normalized pressure (RNP) and its derivative (RNP') versus material balance time (t_e). Five flow regimes are shown in Figure 2.2

including pseudolinear flow (PL) normal to hydraulic fractures, pseudo pseudosteady state flow (PPSS) indicating interference boundary between two fractures, compound linear flow with production from beyond fracture tips, pseudoradial flow, and drainage boundary behavior induced by the well spacing. They also show the field examples from Fayetteville, Haynesville, and New Albany shale with the Haynesville shale example show only PPSS and the New Albany shale example show only PL while the Fayetteville shale example shows both PL and PPSS flow regimes.

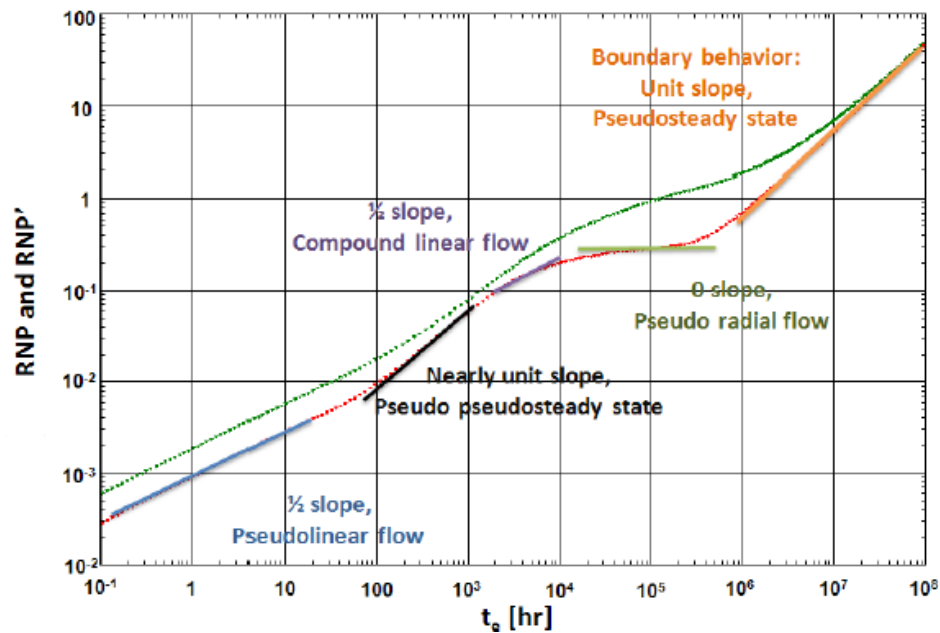


Figure 2.2: Potential flow regimes during MTFHW production

Song et al. (2011) provided an equation to calculate the parameters when PL regime is observed. Eq. 2.3 and Eq. 2.4 can be used for gas when pseudopressure function, $m(p)$, is used.

$$RNP = \frac{40.93T}{n_F h x_F \sqrt{k} \sqrt{(\phi \mu c_t)_i}} \sqrt{t} \quad \dots(2.3)$$

$$RNP' = \frac{1}{2} \left[\frac{40.93T}{n_F h x_F \sqrt{k} \sqrt{(\phi \mu c_t)_i}} \sqrt{t} \right] \quad \dots(2.4)$$

Eq. 2.3 and 2.4 also indicate that MTFHW will exhibit a 1/2 slope straight line for both RNP and RNP' on log-log plots versus material balance time during the formation pseudolinear flow regime. Also, it emphasizes that the RNP and RNP' will be separated by a factor of two (2) when fracture skin is negligible. A detailed derivation of these equations and observations on the single porosity model can be found in Appendix A.

2.4 Complexity in shale formation

The existence of natural fractures is usually anticipated in shale formation. It is considered as a critical factor that controls productivity of shale gas wells by some authors (Kucuk and Sawyer, 1980; Gaskari and Mohaghegh, 2006), but is also countered by others (Montgomery 2005; Bowker 2007). Gale et al. (2007) indicated that the fractures that exist in the Barnett shale are mostly sealed with calcite cement and there is no evidence of widespread open natural microfractures. Bowker (2007) indicated that if there are abundances of open natural fractures in the Barnett, there would be much less gas accumulation because the gas would have migrated out of the shale.

In many shales, opening-mode natural fractures can block hydraulic fractures from propagation (Warpinski and Teufel, 1987) and thus hinder the efficiency of hydraulic fracturing treatment. However, this may not cause a problem for the Barnett

shale (Warpinski et. al, 2005). Warpinski et al. (2005) indicated that the hydraulic fracture treatments can affect the stability of planes of weakness such as natural fractures and induce them to slip and thereby become conductive. Gale et al. (2007) also showed evidence that natural fractures in the Barnett shale have low tensile strength at the contact between the calcite cement and the shale wall, thereby allowing them to reopen when encountering fracturing fluids.

Cipolla et al. (2008) also showed that complexity in hydraulic fracture growth is frequently associated with the pre-existing natural fractures, fissures, or cleats. They also postulate four categories of hydraulic fracture growth, namely, planar-coupled growth, planar-decoupled growth or fissure opening, complex growth (communicating or non-communicating), and network growth, as shown in Figure 2.3.

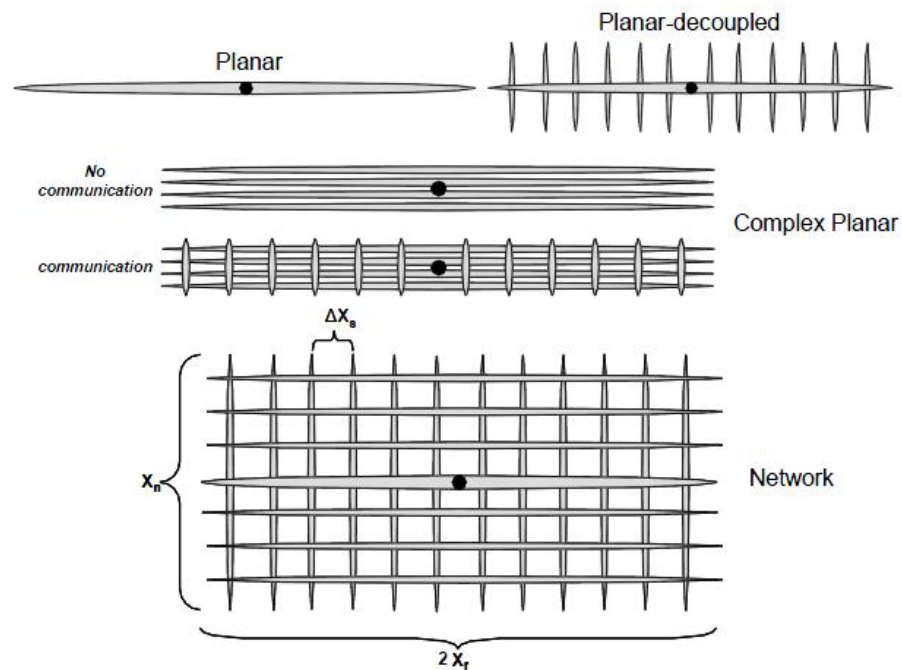


Figure 2.3: Fractures growth and complexity scenarios

The microseismic fracture mapping in Barnett shale also indicates the fractures growth in two directions, i.e. NE to SW - present day maximum stress direction, and NW-SE - global natural fractures direction (Gale et al., 2007).

Fisher et al. (2004) showed microseismic evidence of propagation suggesting that reactivation of the natural fracture network can improve the efficiency of fracturing stimulation.

Cipolla et al. (2009) investigated the sensitivity to whether proppant is present in the reopened fracture network on the productivity of the fractured wells. They indicated that, for an unconventional or low permeability formation (100 nd), if the un-propped fracture network conductivity is high enough (5 md-ft), it can improve productivity even with no proppant fill.

In this study, we define “complexity” as unpropped fractures that may be induced by the hydraulic fracturing treatment while an existing network of fracture that are naturally open to flow will be referred as a natural microfracture network.

To investigate the behavior of unpropped fractures in the production data of MTFHW, two models, namely, dual porosity and triple porosity models will be used in this study.

2.5 Dual porosity model

The conventional dual porosity system consists of a fracture network with low storativity but high conductivity, and matrix rock with high storativity but very low permeability. The fracture network provides the flow path to the wellbore, while the

matrix is the source of most of the produced fluid. The dual porosity model has been studied extensively since the classic model of Warren and Root (1963) which provided a solution for idealized sugar-cube dual porosity system with psuedosteady state flow describing flow from matrix to fractures. It was shown that the semi-log plots of pressure versus time will reveal two parallel straight lines correlated by two factors, i.e., storativity ratio (ω) and inter-porosity flow coefficient (λ), which were defined by:

$$\omega = \frac{(\phi V c_t)_f}{(\phi V c_t)_f + (\phi V c_t)_{ma}} = \frac{(\phi V c_t)_f}{(\phi V c_t)_t} \quad \dots(2.5)$$

$$\lambda = 4n(n+2) \frac{r_w^2}{h_{ma}^2} \frac{k_{ma}}{k_f} \quad \dots(2.6)$$

Where n is the number of normal set of fractures (1 for slab, 2 for matchstick, and 3 for spherical or sugar cube)

Kazemi et al. (1969) later studied the unsteady state or transient flow condition for flow from the matrix to fractures and showed behavior distinct from that described by Warren and Root (1963).

Serra (1983) provided an equation for the transient flow period that enabled calculation of matrix permeability.

Figure 2.4 compares the results from Warren and Root (1963) and Kazemi (1969) (after Kazemi, 1969). The inserts in Figure 2.4 indicate the general flow regimes for the dual porosity system including fracture dominated flow, transition flow, and total system dominated flow regimes.

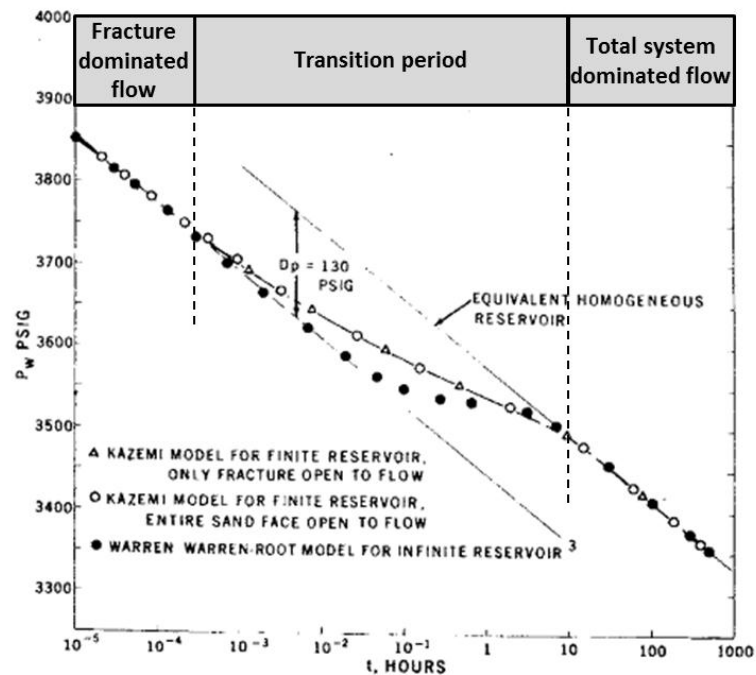


Figure 2.4: General flow regimes for dual porosity system comparing pseudosteady state and transient flow conditions

When the well in dual porosity reservoir is hydraulically fractured, the behavior of hydraulic fracture also needs to be considered. Cinco-Ley & Meng (1988) presented a semi-analytical model that characterizes behavior of a vertical well with a single vertical finite conductivity hydraulic fracture in a dual porosity reservoir (Figure 2.5).

In this case, the behaviors of the well will be a combination of the behaviors of a fractured well in homogeneous reservoir, and an un-fractured well in dual porosity reservoir. The flow regime combinations are summarized in Table 2.1

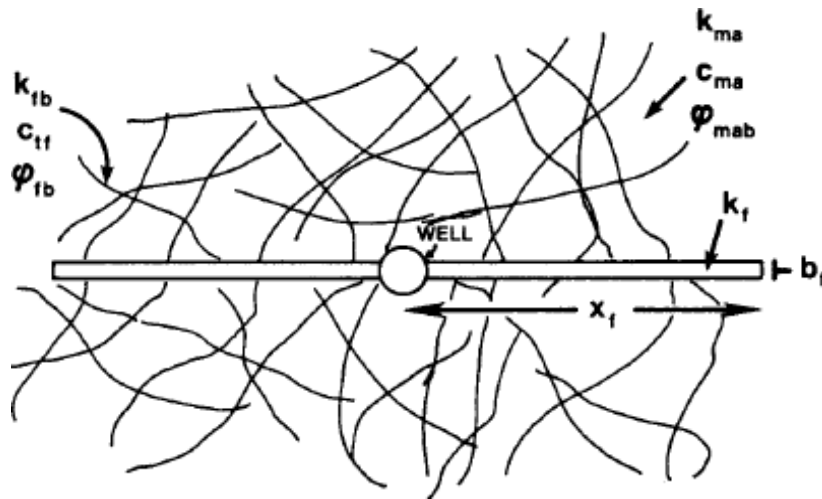


Figure 2.5: Map view showing vertically fractured well in double porosity reservoir (Cinco-Ley and Meng, 1988)

Table 2.1: Fractured well in dual porosity formation flow regime combinations

Flow Regime	Abbrev.	Visible Slope	Flow Behavior			*
			Hydraulic Fracture Behavior	Formation Dual Porosity Behavior	Flow Character	
Fracture Network Linear	FN	1/2	Infinite Conductivity	Fracture dominated linear flow	linear flow	7
Matrix to Fracture Network Bilinear	M-FN	1/4	Infinite Conductivity	Transition flow	bilinear flow	8
Total System Linear	TS	1/2	Infinite Conductivity	Total system dominated linear flow	linear flow	9
Fracture Network to Hydraulic Fracture Bilinear	FN-HF	1/4	Finite Conductivity	Fracture dominated linear flow	bilinear flow	1
Matrix to Fracture Network and Hydraulic Fractures Trilinear	M-FN-HF	1/8	Finite Conductivity	Transition flow	trilinear flow	2
Total System to Hydraulic Fractures Bilinear	TS-HF	1/4	Finite Conductivity	Total system dominated linear flow	bilinear flow	3

**flow regime as shown in Table 2 in Cinco-Ley & Meng (1988)*

Log-log pressure and pressure derivative behavior for all flow regimes in Table 2.1 are shown in Figure 2.6 (flow regime 7, 8, 9) and 2.7 (flow regime 1, 2, 3) (modified

from Cinco-Ley and Meng, 1988). Note that different lines indicate different values of ω ranging from 0.0001 to 1 for Figure 2.5 and from 0.001 to 1 for Figure 2.6.

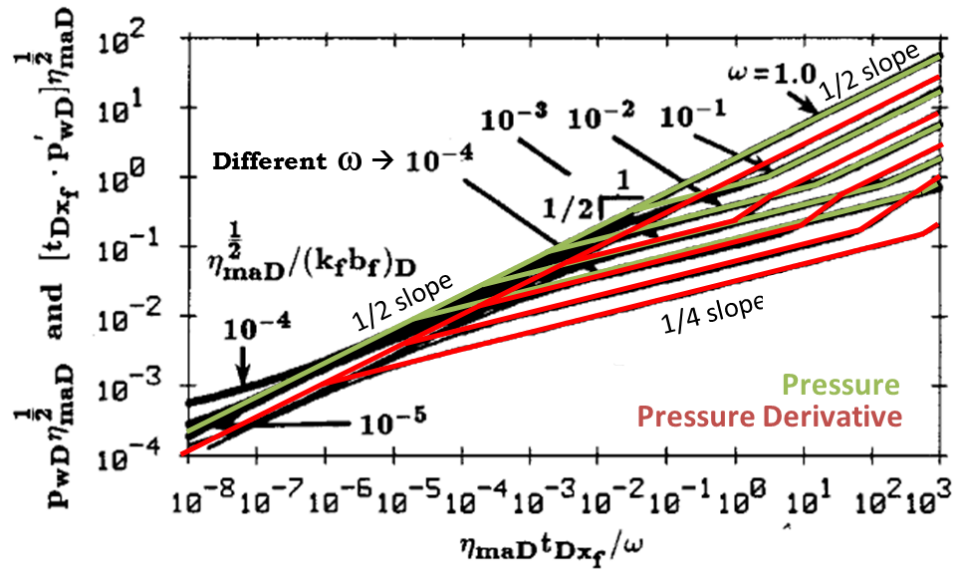


Figure 2.6: Pressure and pressure derivative plots for case with infinite conductivity hydraulic fracture (regime 7, 8, 9)

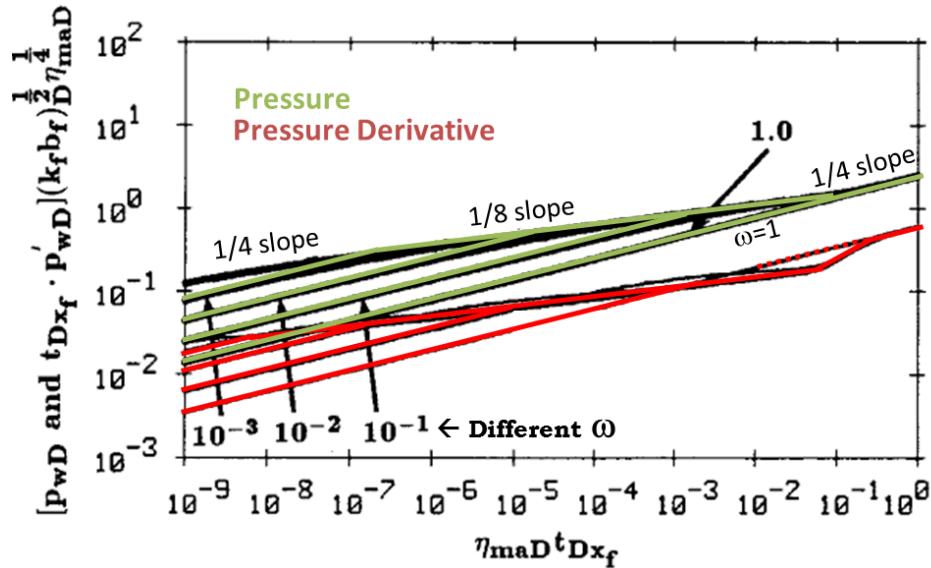


Figure 2.7: Pressure and pressure derivative plots for case with finite conductivity hydraulic fracture (regime 1, 2, 3)

Flow equations for all flow regimes in Table 2.1 are summarized in Table 2.2.

The derivation and information of these solutions can be found in Appendix B.

Table 2.2: Flow solutions for dual porosity models

Flow Regime	Dimensional Solutions
FN	$\Delta m(p) = \frac{40.93qT}{n_F h x_F \sqrt{k_{fb}} \sqrt{\phi \mu c_t}} \sqrt{\frac{t}{\omega}} + \frac{1491.2qT}{n_F h} \frac{x_F}{k_F b_F}$
M-FN	$\Delta m(p) = \frac{314.47qT}{n_F h x_F \sqrt{A_{fb} k_{fb}} k_{ma}^{1/4} (\phi \mu c_t)^{1/4}} \sqrt[4]{t} + \frac{1491.2qT}{n_F h} \frac{x_F}{k_F b_F}$
TS	$\Delta m(p) = \frac{40.93qT}{n_F h x_F \sqrt{k_{fb}} (\phi \mu c_t)^{1/2}} \sqrt{t} + \frac{1491.2qT}{n_F h} \frac{x_F}{k_F b_F}$
FN-HF	$\Delta m(p) = \frac{444.75qT}{n_F h \sqrt{k_F b_F} (\phi \mu c_t)^{1/4} k_{fb}^{1/4}} \sqrt[4]{\frac{t}{\omega}}$
M-FN-HF	$\Delta m(p) = \frac{1199.1qT}{n_F h \sqrt{k_F b_F} k_{fb}^{1/4} (\phi \mu c_t)^{1/8} A_{fb}^{1/4} k_{ma}^{1/8}} \sqrt[8]{t}$
TS-HF	$\Delta m(p) = \frac{444.75qT}{n_F h \sqrt{k_F b_F} (\phi \mu c_t)^{1/4} k_{fb}^{1/4}} \sqrt[4]{t}$

It must be noted here that Cinco-Ley and Meng (1988) considered a single fractured vertical well which is not the same as the current shale gas well completion design, i.e. MTFHW. Moreover, the fracture network “slab” model was defined as horizontal fracture planes interbedded with matrix layers or layer-cake model (**Figure 2.8**) which is not likely for shale formation unless shale gas exists at very shallow depth. Thus, modifications are required to convert those solutions into applicable forms for MTFHW. Also note that the constant rate solution are shown here since they are more

favorable for flow regime investigation as mentioned earlier and it can be used to represent also the variable rate flow behavior by applying proper superposition time function to the constant rate solutions.

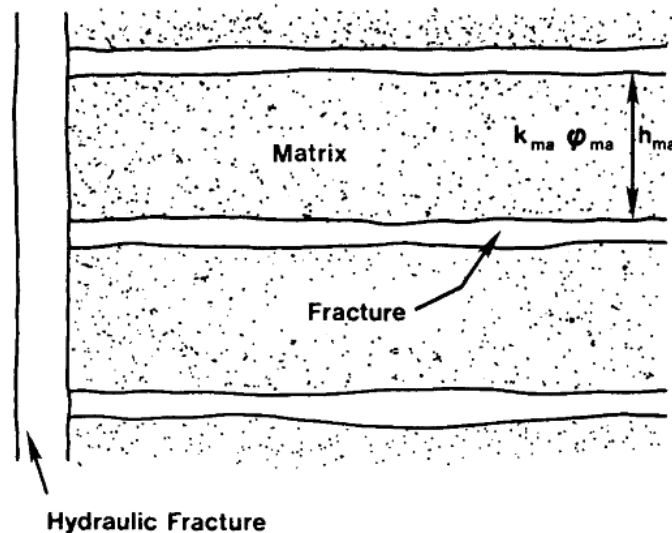


Figure 2.8: Cross-sectional view of horizontal slab matrix blocks

2.6 Triple porosity model

Noting reported evidence that calcified fractures in Barnett shale were oriented in the direction normal to present day minimum stress and therefore parallel to the direction of a horizontal well drilled in the direction to create transverse hydraulic fractures according to the modern minimum stress direction, Al-Ahmadi et al. (2010) developed a triple porosity solution for flow to fractured wells in a fractured reservoir. The three porosities in this model are referred to as three different media, i.e. macrofractures for hydraulic fractures, microfractures for a natural fracture network, and matrix. The matrix with ultra-low permeability has the highest storativity while the other two fracture media

have high permeability but small storativity. The model ensures that flow occurs in sequence, i.e. fluid in the matrix flows to the fracture network through which fluid flows to the macrofractures. Moreover, it is assumed that no flow occurs directly between the matrix and macrofractures nor between the matrix and the wellbore, nor between microfractures and the wellbore which means that the fluids only enter the wellbore through macrofractures. These assumptions are valid when permeability difference between shale matrix and microfractures are large which is very likely in shale gas.

Figure 2.9 presents triple porosity model setting. Note that for Barnett shale, microfractures represent reopened fractures perhaps of the sort discussed by Warpinski et al. (2005) and Gale et al. (2007). The strict fracture geometry imposed by this model may not apply as readily to other shales. The letter L in Figure 2.9 represents fracture spacing while the subscripts F and f denote macrofractures and microfractures, respectively. The x_e is used for the total length of stimulated shale volume.

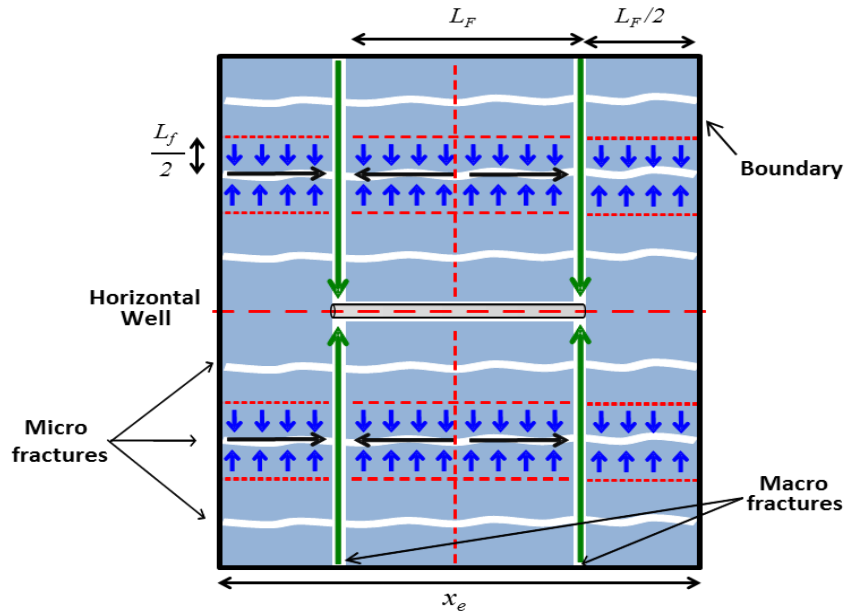


Figure 2.9: Top view representing multi-traverse fractured horizontal well in triple porosity system (Modified from Al-Ahmadi et al., 2010)

Al-Ahmadi et al. (2010) proposed four sub-models based on the interporosity flow condition between the two media, i.e., transient or pseudosteady state flow. However, because of its ultra-low permeability flow in all three of the media is more likely to be transient, and thus only the fully transient model will be considered in this work.

Five flow regions are illustrated in Al-Ahmadi et al. (2010) as shown in Figure 2.10. Note that Figure 2.10 was generated using extremely high macrofracture permeability in the range of millions darcies with ultra-low porosity in the range of 10^{-6} . As well, this illustration shows 22 logarithmic time cycles. Noting that the number of logarithmic cycles representing time from one second to 100 years is 9, we do not expect to see the complete flow region sequence in field data.

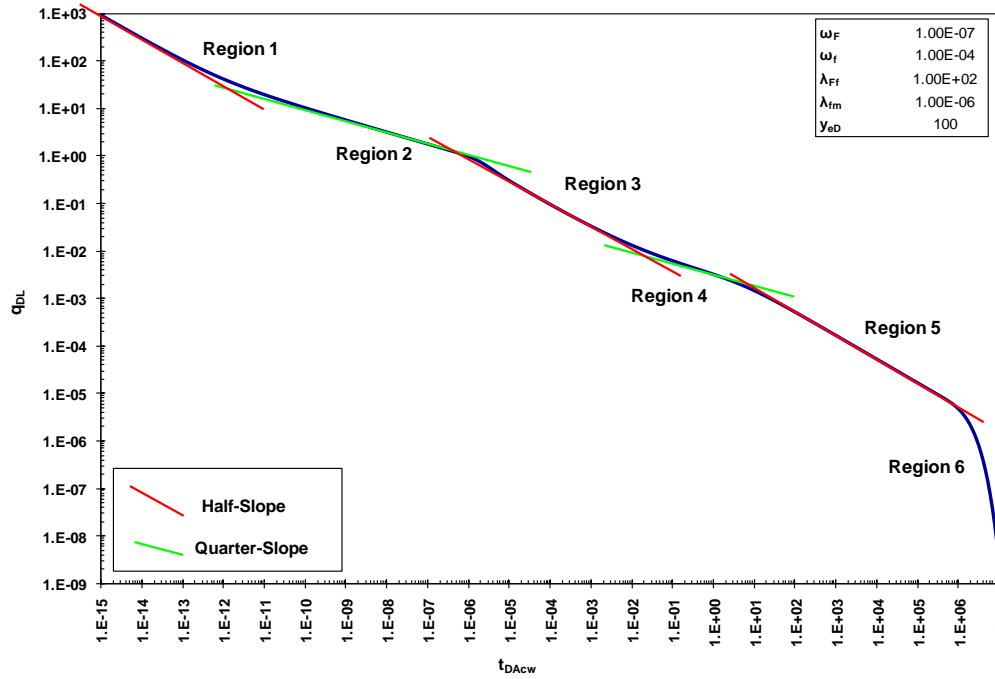


Figure 2.10: Five flow regions for the triple porosity model (Al-Ahmadi et al. 2010)

Samandarli et al. (2011) added more details to the Al-Ahmadi et al. (2010) and defined eleven flow regimes and showed the asymptotic equations that represent each of them. However, the explanations for the flow regimes are still ambiguous and this work still did not cover all possible flow regime combinations. Appendix C provides a more comprehensive list of the possible flow regime sequences for the triple porosity model.

The main difference between the triple porosity model and the dual porosity model shown earlier is the definition of inter-porosity flow coefficient (λ). Two λ values are defined in the triple porosity model to represent inter-porosity between macrofractures and microfractures, and between microfractures and matrix as shown in Eq.2.7 and 2.8 for the transient slab model.

$$\lambda_{AC,Ff} = \frac{12}{L_F^2} \frac{k_f}{k_F} A_{cw} \quad \dots(2.7)$$

$$\lambda_{AC,fm} = \frac{12}{L_f^2} \frac{k_m}{k_F} A_{cw} \quad \dots(2.8)$$

Note that the traditional λ as defined in Eq. 2.6 may be seen as analogous to Eq.2.8 and the dual porosity model can be seen as analogous to the triple porosity model. Where the two models are fundamentally different is in the second λ value provided in Eq. 2.7 that interacts with the set of hydraulic fractures with the well with transient slab dual porosity behavior in which the medium between the hydraulic fractures is itself another dual porosity medium also behaving as dual porosity slabs. In case the medium between the hydraulic fractures is homogeneous, the triple porosity model will reproduce the homogeneous model described in section 2.3.

Because the definitions for λ are different in the two models, very different values for λ will result in matches with data. In the triple porosity model hydraulic fracture permeability is always used in calculating λ even in Eq.2.8 which is considering the matrix system flowing into the microfracture network. Also, the triple porosity model defined λ differently by using well parameters, A_{cw} , defined as horizontal well surface area ($2 \cdot h \cdot x_e$ where h is thickness and x_e is the SRV length) instead of the wellbore radius used in the double porosity model. We note that the storativity ratio (ω) was defined similarly in both models.

2.7 Available models in commercial software (Ecrin)

In this work, commercial software, i.e. Ecrin version 4.20.02 by Kappa engineering is used to investigate homogeneous and dual porosity models. Song and Ehlig-Enonomides (2011) described behavior of MTFHW in a single porosity homogeneous model using the available module in the Ecrin.

Both analytical and numerical models are available. The analytical model allows faster model generation with reasonable accuracy, while numerical model allows better accuracy but requires longer runtime. The numerical model is required when allowing for shale diffusivity flow or gas desorption. However, the numerical model does not allow the transient flow condition in dual porosity reservoir which is more likely the flow condition for shale gas production. Therefore, this study will only focus on the analytical model, and gas desorption will not be considered.

The options available in the software include well geometry, i.e. vertical well with or without vertical fracture, or horizontal well unfractured or with 2 or more transverse hydraulic fractures all with equal half-lengths and conductivities, and also reservoir descriptions including homogeneous and dual porosity. The reservoir boundary choices include infinite acting (no boundary) and a rectangular closed boundary. While many other options are available, they are not relevant to this work.

The fractured horizontal well option is a built-in module which allows user to create MTFHW by entering horizontal section length, number of fractures, fracture half-length, as well as fracture angle.

When working with the dual porosity reservoir model, there are also options for transient or pseudo steadystate flow conditions. Slab and sphere models are also available for the transient flow condition. The slab model consists of layers of matrix interbedded with layers of high permeability media, e.g., fractures. The sphere model may be seen as equivalent to the sugar-cube model of Warren and Root (1963).

The difference of flow behavior of the slab and sphere models is observed only during the transition period as shown in Figure 2.11 for the radial flow case. Note that in this study, both slab and sphere models are used to represent different scenarios.

The Ecrin model provides a continuous model from as early as a fraction of a second to thousands of years in time, and most model inputs are dimensioned to actual field values.

The triple porosity model that can be used to represent the system with macrofractures, microfractures, and matrix as shown in Al-Ahmadi et al. (2010) is not available in Ecrin. External triple porosity models designed for carbonate reservoirs with vugular porosity are provided, but these do not provide the specific geometry of the Al-Ahmadi triple porosity model.

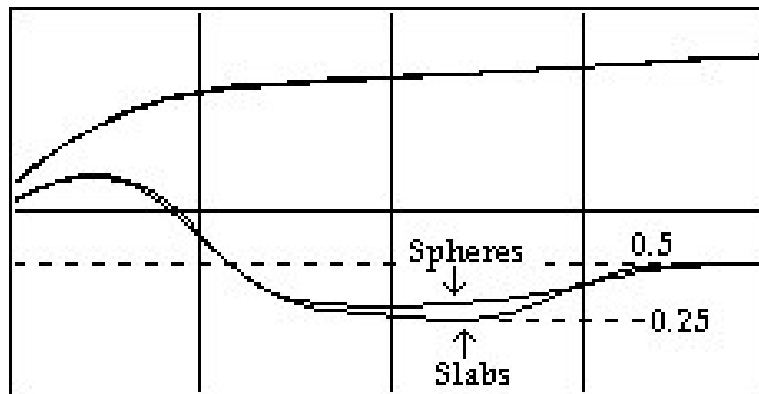


Figure 2.11: Transient slab and sphere model comparison on log-log pressure and pressure derivative plots

2.8 Chapter summary

This chapter has provided information about shale gas production with a MTFHW completion, general background about shale heterogeneity including pre-existing natural microfractures and reopened fractures that some call complexity. Three models were reviewed including a single porosity homogeneous model, a dual porosity model, and a triple porosity model. The commercial Ecrin software by Kappa Engineering was also introduced to show the available options can be used for modeling single and dual porosity flow to the MTFHW.

Chapter III will apply these theories and models to see whether presence of a reopened fracture network is evident in Barnett shale production data.

CHAPTER III

MODEL SENSITIVITY STUDIES BASED ON THE BARNETT SHALE

Chapter II briefly described three models for flow to a multiple transverse fracture horizontal well (MTFHW): a single porosity (homogeneous reservoir) model, a dual porosity model with transient interporosity flow, and a triple porosity model that includes the hydraulic fractures as one of three flow media. This chapter will show sensitivity behavior of the single porosity and dual porosity models using parameters typical for the Barnett shale.

The chapter will begin with insight about practical time ranges for two types of transient data: buildup data acquired when the well is shut in, and long-term pressure and rate production data acquired while the well is flowing. The practical time windows for each type of data will be defined.

Then background information about the Barnett shale will be provided, and baseline parameters for the Barnett shale will be specified based on information found in the literature and an available data set.

Sensitivity runs will be used to show which flow regimes may appear in the windows of time represented by a buildup test or by long term production data depending on the shale effective permeability, the fluid compressibility, the length of the well and the spacing and extent or half length of the created hydraulic fractures for a homogeneous formation and on additional parameters for dual porosity flow behavior. A

section is provided for sensitivity runs using each of the three models. Each section will describe the model in terms of the expected flow regimes for flow to the MTFHW.

A final section shows matches for buildup and long term production data for a Barnett shale well using various possible models and considers which of the models are more reasonable representations of the likely reality.

3.1 Practical time windows

It is important to note that the succession of flow regimes seen in any of the three models can require a time range from a fraction of a second to 1000 years or more which implies that at least 10 log cycles may be required to capture the complete flow regimes.

A pressure buildup test may provide data ranging in time from 1 second to as much as a month (up to 6 log cycles) while long term production data is typically recorded once per day for the life of the well which could be at least 30 years (~ 4 log cycles). Therefore, the combination of both could provide information about 9 log cycles given that the period between 1 day and one month overlaps between the two types of transient data. Note that in this study, a buildup test is meant to imply high data sampling rate, e.g. every second or less, because the buildup data with sampling rate less than one day does not provide much information over what production data acquired on a daily basis would provide. Flow regimes related to hydraulic fractures may appear in less than 24 hours and are frequently absent in the long term daily production data.

Figure 3.1 shows the MTFHW geometry used to simulate the flow behavior shown in Figure 3.2 for transient dual porosity reservoir flow. Figure 3.2 shows the practical time windows in buildup test and long term production data for this case.

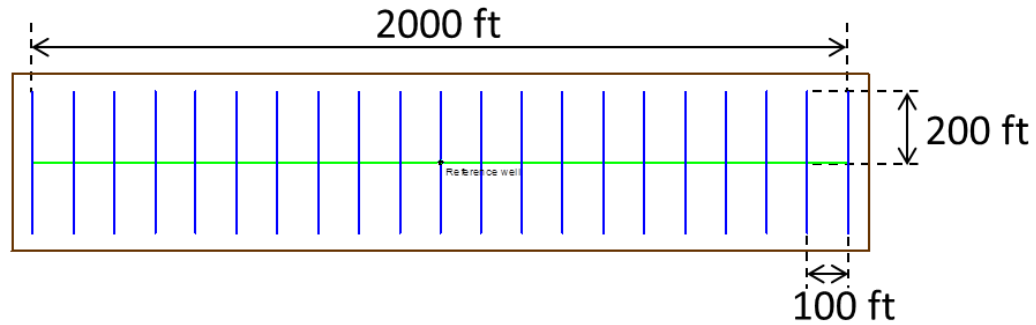


Figure 3.1: MTFHW dimension for Figure 3.2

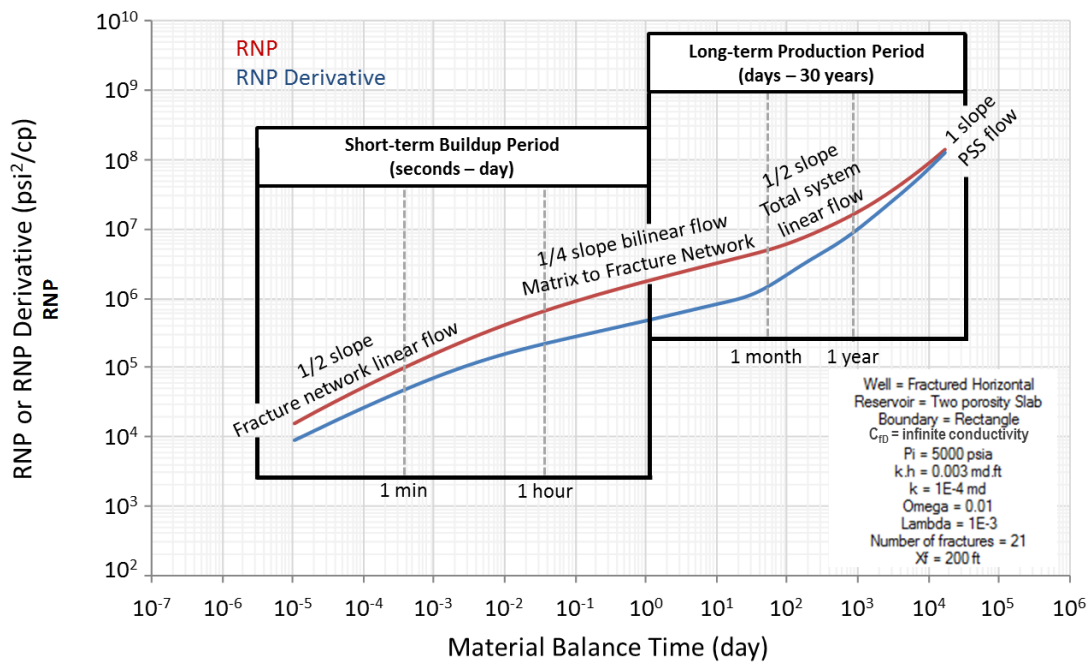


Figure 3.2: Practical time windows example

Two practical time windows are shown in Figure 3.2 - short term buildup test period lasting from 1 second to 1 day (5 log cycles) and the long term production period lasting from 1 day to 30 years (4 log cycles), giving the total practical time windows of 9 log cycles. In this example, both half slope fracture network linear flow (FN) and quarter slope matrix to fracture network bilinear flow (M-FN) can be observed in the buildup window. The long term production window also captures part of the quarter slope M-FN flow regime, part of the half slope total system linear flow regime (TS), and a unit slope trend indicating PSS flow regime. Note that Figure 3.2 also shows that a quarter slope can occur even with effectively infinite conductivity hydraulic fractures. The results indicate that the FN flow regime may not be seen in the long term production data, and even with buildup test with high data sampling rate, the FN flow regime ended within couple minutes and might not be observed practically. The PSS flow regime in this example can be seen after about 6 months of production. (See Appendix B for more information about flow regime descriptions.)

Note that this example is shown here in an attempt to describe the use of practical time window only and the results shown in this section are only based on one random set of parameters. The practical flow regimes we can expect to see in the practical time windows for Barnett shale will be investigated in the following sections.

3.2 Barnett shale formation characterization

In this section, the background information of the Barnett shale will be reviewed including shale properties and typical well completion. Then the raw data will be used to investigate the overall behavior of the wells producing from the Barnett shale.

3.2.1 Field background

The Barnett Shale in a middle-late Mississippian age has been considered as source rock for hydrocarbons in the north-central Texas. Figure 3.3 shows the production area and stratigraphy of the Barnett shale.

The shale was not a target for development after repeated tries found that the production from low-permeability shale was not economical. Macroscopic natural fractures are observed in conventional cores taken from the Barnett. These natural fractures are commonly sealed, but evidence of reopened fracture network or complexity is encountered in the direction related to the fault trends and perpendicular to the propagation of transverse hydraulic fractures. The opening-mode natural fractures, if they exist, could generally have the apertures of less than 0.01 ft, but could also be as high as 0.1 ft (Gale et al., 2007).

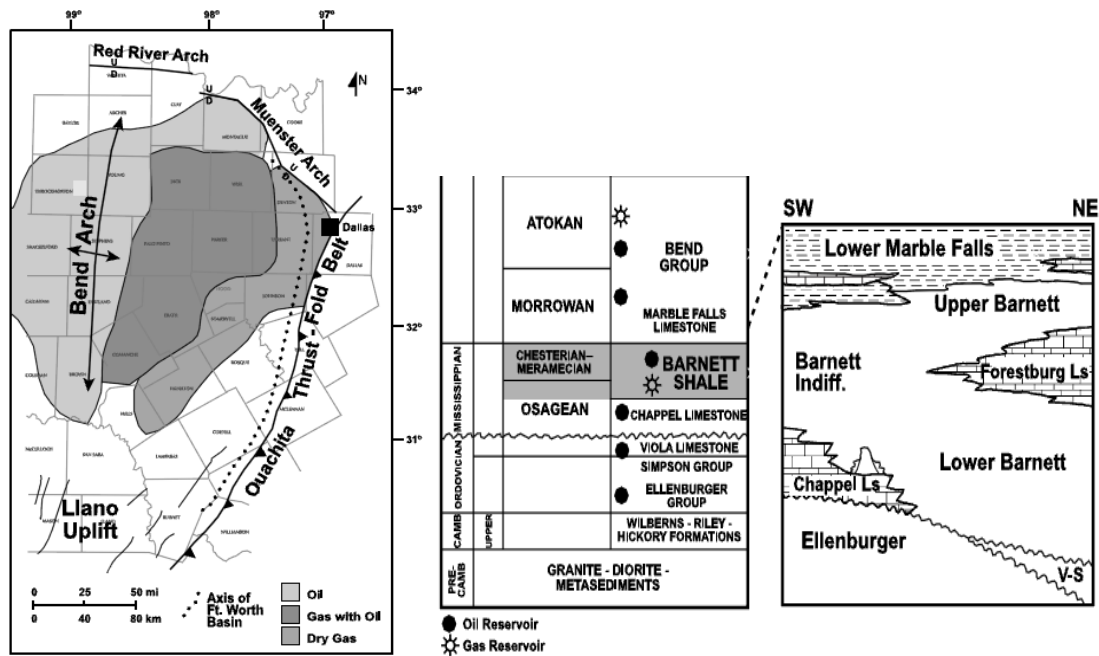


Figure 3.3: Barnett shale stratigraphy and location (extracted from Montgomery et al., 2005)

The Barnett shale has moderate temperature and is slightly over pressured with an average temperature of 150°F and initial pressure of around 3500-4400 psi giving a 0.52 psi/ft formation pressure gradient. Average porosity in the formation of interest is 0.03. Shale matrix permeability is commonly reported to range from 10-100 nd (Kale et al., 2010; Cipolla et al., 2009; Nieto et al., 2009), but with exceptional higher values ranging from 0.01md to 0.001 md (Montgomery et al., 2005) in some areas. The Fracture network conductivity range of 0.5 to 5.0 md-ft is assumed to represent low and high case of reopened fracture network (Mayerhofer et al., 2006; Cipolla et al., 2008).

Data from 60 wells drilled in the Barnett shale indicated the wells have approximate TD at around 10,300 ft.MD (7,150 ft.TVD) and were cased with 5.5"

casing. Average well spacing to adjacent wells is found to be approximately 500 ft. The wells were hydraulically fractured with 3 to 15 stages (averaging 6 stages) with a total of 8 to 75 (average 40) perforation clusters along the 2,800 ft average horizontal section length. The average fracture spacing can be calculated to range from 50 to 500 ft with average value at 80 ft. Hydraulic fracture conductivity is reported to range from less than 1 md-ft in the event of crushed proppant to as high as thousands of md-ft.

Figure 3.4 summarizes the base case well dimension and SRV boundary setting. Average horizontal section (L_w) is 2800 ft with average number of hydraulic fractures of 41 giving the base case fractures spacing (x_s) of 80 ft. The SRV length is calculated by adding L_w with $0.5x_s$. Fracture half-length is 250 ft or half of well spacing which can be considered as maximum half-length if no fracture interference can be observed between the adjacent wells. The SRV half-width is estimated by adding fracture half-length with $0.5x_s$ estimated distance the pressure might penetrates beyond fracture tip. However, if the fractures are touching (tips-to-tips), the SRV half-width will be equal to the fracture half-length, and there will be no production from outside the SRV.

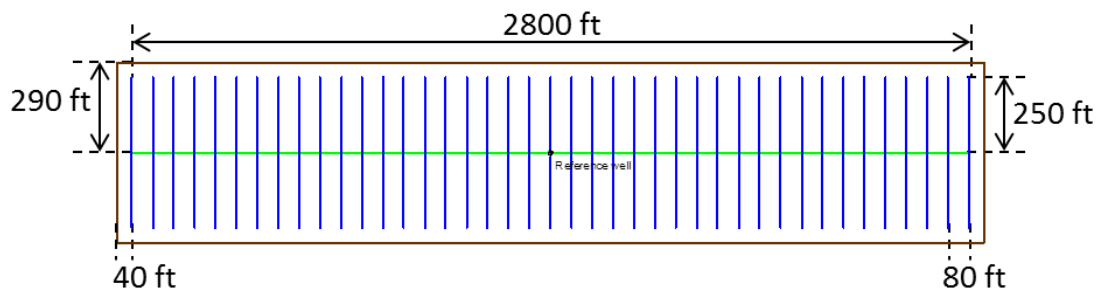


Figure 3.4: Base case MTFHW dimension and SRV boundary for Barnett shale

The general range of shale properties and well completion information from literature and available raw data are summarized in Table 3.1. The exact range will be investigated further in the following sections.

Table 3.1: Estimate range of sensitivity parameters for the Barnett shale study

Properties	Value	Unit
Shale matrix permeability (k_{ma})	0.000001-0.1 (1-100000)	md (nd)
Hydraulic fracture conductivity (C_{FD})	1 - 10000	md-ft
Hydraulic fracture half-length (x_F)	50 - 250 - 500 (well spacing)	ft
Hydraulic fracture spacing (x_s)	50 - 80 - 500	ft

3.2.2 Data overview

Available pressure and production data from the Barnett shale covers a period of about 5.5 years. The gauge data include surface casing and tubing pressure, surface production rate (gas and water), and production hour. These pressure and production data are collected on daily basis. Casing pressure is used to represent flowing bottomhole pressure by adding gas column static pressure to the measured surface casing pressure. The example of production and pressure history plots of the MTFHW producing from the Barnett shale are shown in Figure 3.5.

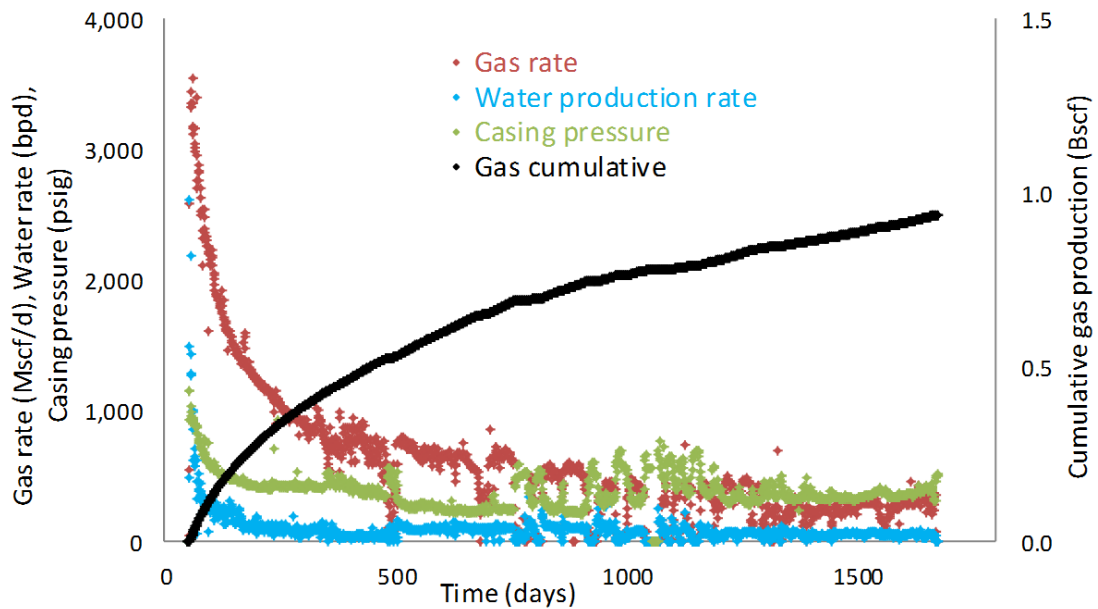


Figure 3.5: Pressure and production history of the well from the Barnett shale

In general, there are several shut-in periods can be recognized, however there is no proper pressure measurement during the shut-in period. Figure 3.6 shows log-log pressure and pressure derivative plots example of buildup (BU) data from one of the wells. It is found that there is no obvious slope trend can be observed on the buildup test. Even though a $1/8$ slope trend is possible, it is not very convincing. Therefore, no buildup test is available for the Barnett shale from this well. The problem is that the buildup data are acquired at the same daily rate as are production data. To provide more interpretable results, the buildup data acquisition rate should be higher.

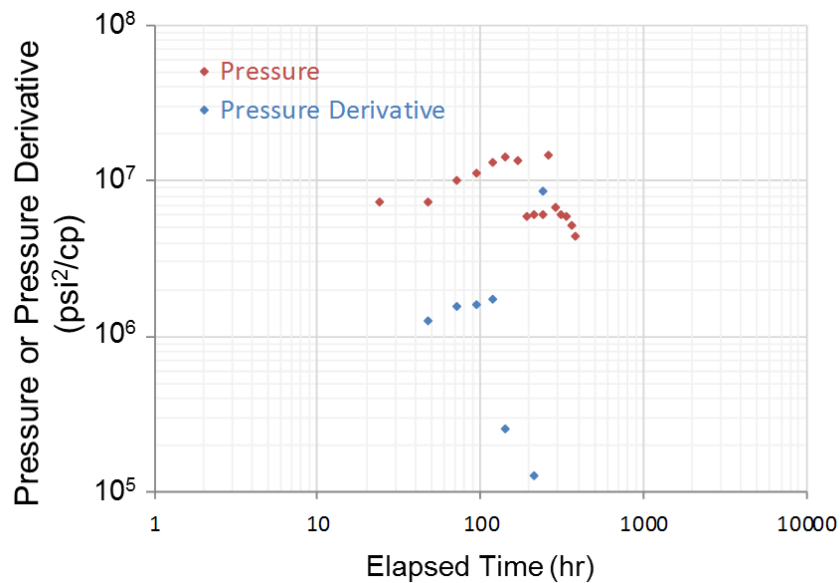


Figure 3.6: Log-log diagnostic plots example for a BU test of the Barnett shale well

Figure 3.7 shows log-log RNP and RNP derivative (RNP') plots from the same well. The RNP trend seems smooth while RNP' plots are quite scattered but still with identifiable trends. Sometimes RNP' plots are too scattered to observe clear trends, as will be seen in Chapter IV showing data from a Horn River shale gas well.

The RNP plot indicates that long term production data shows 1/4 slope followed by 1/2 slope and then unit slope trends. However, the RNP derivative during the 1/4 slope trend does not separate from the RNP trend by a factor of 4 and seems instead to have the same 1/2 slope trend seen later. This indicates that the 1/4 slope trend seen on the RNP plot might not represent the actual bilinear flow regime.

One of the possible causes of the bending from linear flow trend at early stage was explained by Bello and Wattenbarger (2009) as early-time skin effect. However, in

reality skin is a constant pressure drop value (unless there is time dependent skin), and the reason it appears evident in early time is because its magnitude eventually becomes negligible compared to increasing RNP values. Since the dominant flow geometry for the well is flow to hydraulic fractures, the likely source of skin is fracture skin that could represent a small pressure drop in the connection between fractures in the wellbore causing a choke skin, or it could represent fracture face skin related to leak-off of fracture fluids into a fracture network or shale matrix near the fracture face.

When it is not too scattered, by far the best indicator of flow behavior is RNP', not RNP. In this case the bending up of RNP opposite early 1/2 slope in the derivative should be modeled as skin.

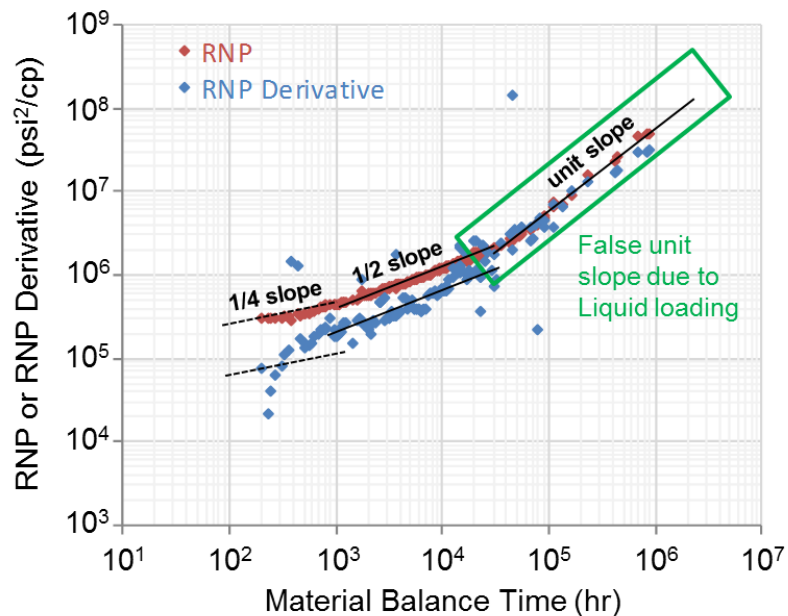


Figure 3.7: Log-log diagnostic plots example for the long term production data of the Barnett shale well

Apart from the false bilinear quarter slope, the unit slope trend in this example is also misleading and does not conclusively represent a PPSS or PSS boundary flow regime. Rather, it is an artifact resulted from liquid loading in the wellbore when gas velocity is too low to carry liquid to surface. The method for identifying liquid loading behavior based on a critical rate is explained in Turner et al. (1969)

Figure 3.8 shows the log-log RNP and RNP derivative after all artificial points had been removed. Now only 1/2 slope trend with possible early-time skin effect can be observed in the RNP, while the RNP' shows deviation from 1/2 to unit slope at about 8,000 hr or slightly before 1 year. This information will be used to define range of permeability for the sensitivity study in the next sections.

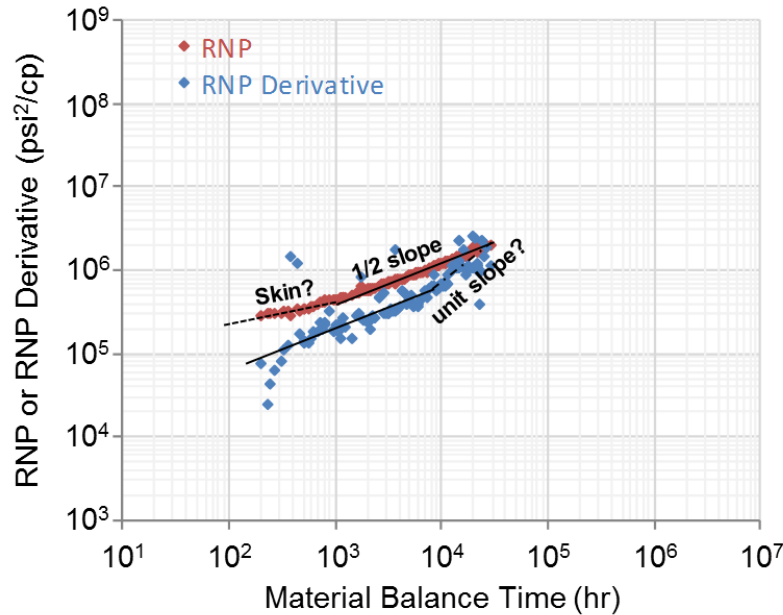


Figure 3.8: Log-log diagnostic plots example for the long term production data of the Barnett shale well after removing artificial points

3.3 Sensitivity studies using the single porosity (homogeneous) model

First, the depth of investigation equation will be used to calculate the expected range of permeability for the Barnett shale based on the known typical range of fracture spacing (x_s) seen in the field data. Then, the effect of x_s and hydraulic fracture half-length (x_F) will be investigated using the base case permeability established earlier. Sensitivity runs will be shown on both x_s and x_F . Finally, the effect of hydraulic fracture conductivity (C_{fD}) will be investigated. Note that the only possibility for bilinear flow to occur in the homogeneous model is when hydraulic fracture conductivity is not effectively infinite, which Cinco-Ley et al., 1978 defined as when $C_{fD} < 300$. The sensitivity run will reveal more specific values of C_{fD} for the Barnett shale required to allow bilinear flow to be seen in each of the practical time windows.

3.3.1 Permeability

Permeability, fracture spacing, and time to see the effect of PPSS boundary can be correlated using the distance of investigation equation for linear flow as following.

$$x = 0.1125 \sqrt{\frac{kt_{e,elf}}{(\phi\mu c_t)_i}} \quad \dots(3.1)$$

Where $t_{e,elf}$ is material balance time in days at the end of 1/2 slope linear flow as seen on log-log RNP and RNP' versus material balance time plots. Note that Eq.3.1 has been adjusted to account for the superposition time function difference when using material balance time function while the response has not reached pseudosteady state as yet. (See Appendix D for more information about material balance time function)

Because PPSS behavior results from the imaginary interference boundary occurring at the middle of hydraulic fracture spacing as a result of production interference between the two adjacent hydraulic fractures, once this boundary is sensed, the RNP' will deviate from the straight line linear or bilinear flow toward an almost unit slope straight line of PPSS flow regime (Song and Ehlig-Economides, 2011). If productive hydraulic fractures half-lengths are equal to $1/2$ the horizontal well spacing, an upward departure to unit slope representing pss is expected.

Now, the expected range of permeability for the Barnett shale can be estimated based on the actual range of hydraulic fracture spacing (x_s) and the actual $t_{e,elf}$ observed from the log-log RNP and RNP' plots of the Barnett shale well data. The data shows that the $t_{e,elf}$ can range from 1 year to 3 years, but the value of 1 year will be used as base case. The set of specialized plots including linear plots, bilinear plots, log-log plots, Cartesian plots, WGR plots, and water production plots for selected wells can be found in Appendix E.

Figure 3.9 relates permeability with hydraulic fracture spacing and the material balance time required to see the end of linear flow.

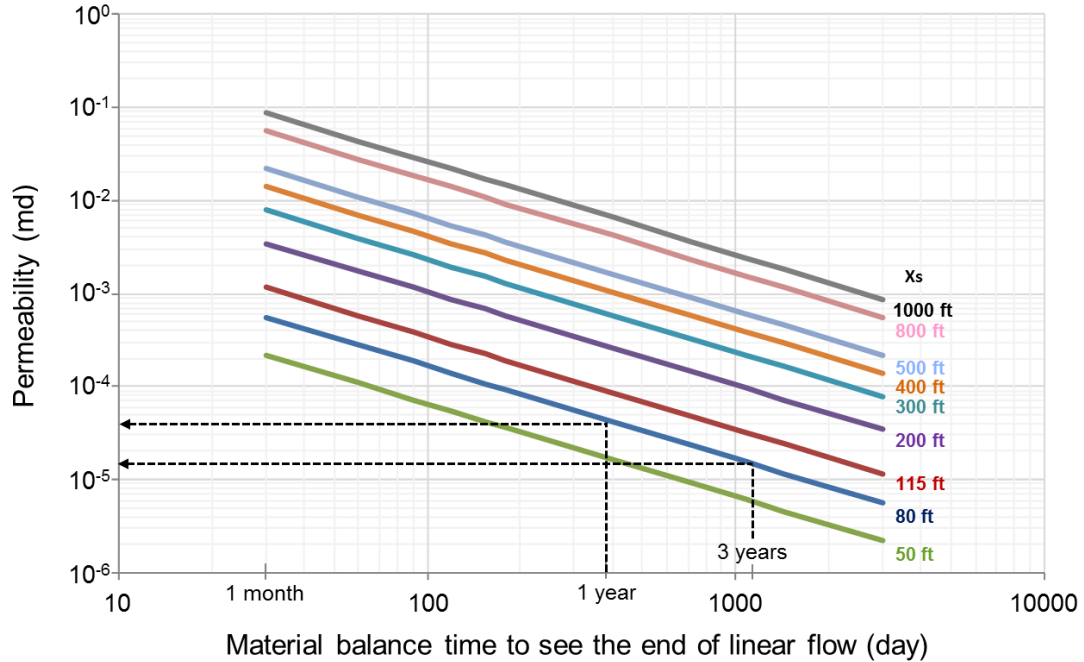


Figure 3.9: Permeability and fracture spacing versus material balance time

Considering Figure 3.9 with base case x_s of 80 ft and actual $t_{e,elf}$ ranging from 1 to 3 years, the expected range of permeability can be estimated to be ranging from 35 nd to 15 nd, respectively. Therefore, base case permeability will be defined to be 35 nd. Note that these plots are generated based on the average properties of the Barnett shale, and the results are sensitive to pressure related properties, i.e., gas viscosity and total compressibilities so that they will vary among the shales.

Figure 3.10 shows the log-log RNP and RNP' diagnostic plots based on the base case parameters, i.e., $k = 35$ nd, $x_F = 250$ ft, and $x_s = 80$ ft indicating flow regimes expected to see within each of the practical time windows; short term buildup test and long term production period.

35,000 nd (0.035 md) based on the base case x_F of 250 ft, i.e. half-way of the average well spacing.

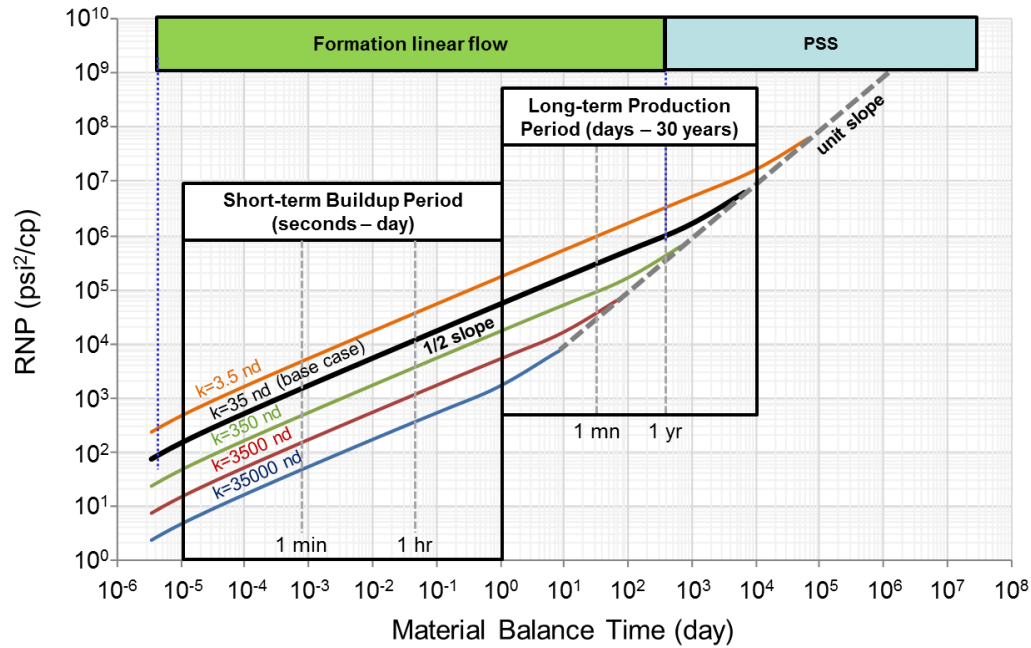


Figure 3.11: Barnett shale permeability sensitivity results

The results indicate that the short-term buildup period will only see half slope formation linear flow while the long-term production data will see first a half slope trend before seeing the effect of PPSS boundary. The time to see PPSS boundary is varied though. It is found that it may take more than 30 years before the PPSS boundary could be sensed when formation permeability is less than 3.5 nd with the x_s of 80 ft and only linear flow is expected to see for the entire well life. On the other hand, when permeability is as high as 350 nd, it is expected that evidence of PPSS boundary should be observed within only 2 month with the same x_s . Note that the flow regime labels

showing in Figure 3.11 are marked for the base case scenario only because the starts and ends of PPSS, pseudo radial, and PSS flow regimes vary according the value of permeability used.

Formation permeability also affects level of RNP and RNP'. The value of RNP and RNP' are inversely proportional to the square root of permeability during linear flow regime (see Eq.2.3 and 2.4). As a result, when permeability is changed by 10 times, RNP and RNP' will shift by square root of 10 times or half log cycle. The effect of increased permeability can also be seen as a delay in the pressure response. For example, when permeability is increased by 10 times, the time to achieve the same RNP and RNP' level will be shifted also by 10 times or 1 log cycle. This is because when permeability is increased, pressure drop will decrease, and thus it will require more time before the same pressure drop would be achieved under constant flow rate production (or in this case the virtual constant flow rate behavior provided by the RNP).

3.3.2 Hydraulic fracture spacing (x_s)

The role of x_s on the RNP and RNP' behavior is that it affects the time required before the pressure perturbation will reach the virtual closed boundary between adjacent fractures that induces pseudo pseudosteady state (PPSS) flow behavior causing the upward deviation from a half slope or quarter slope trend to approximately unit slope behavior. The average input value of x_s can be calculated using the length of the horizontal well section (distance between the first and the last perforation cluster)

divided by one less than the total number of clusters. Figure 3.12 shows the sensitivity to hydraulic fracture spacing (or number of hydraulic fractures, n_F).

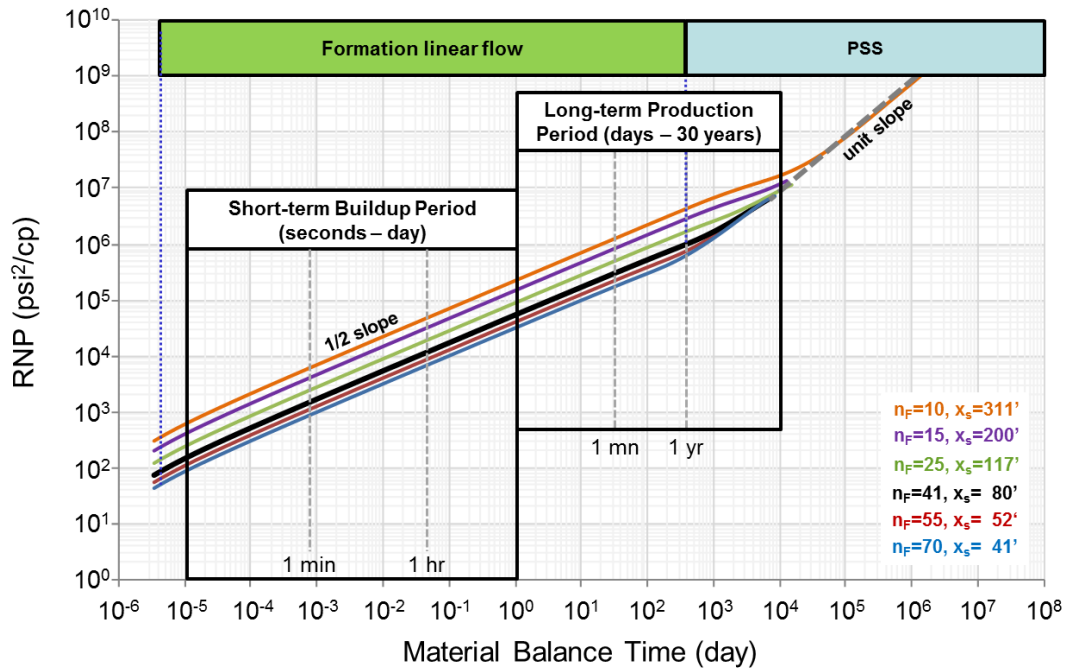


Figure 3.12: Barnett shale hydraulic fracture spacing sensitivity results

Figure 3.12 shows that same characteristic as the permeability sensitivity, i.e., only 1/2 slope fracture linear flow will be seen in the BU timeframe, while both 1/2 slope and almost unit slope PPSS flow regime will be seen during the long term production period. This is because x_s and n_F do not affect the slope of the RNP and RNP', but they only affect the level of the RNP and RNP'. That is, the number of hydraulic fracture is inversely proportional to the level of RNP (and RNP'). For example, when n_F is increased from 10 to 70, i.e., 7 times, RNP in this plot inversely decreased also by 7 times. This is true only for n_F , but not exactly for x_s .

The results also indicate that x_s and n_F have effect on $t_{e,elf}$, i.e., the shorter the hydraulic fracture spacing, the faster the PPSS will be observed. Although, the SRV volumes for all cases are the same since the well length and fracture half-length are kept constant, if the time required to see PPSS boundary is too long, it implies that the well will not produce the whole SRV and the hydraulic fracture spacing should be reduced. For example, when $x_s = 311$ ft, it will take about 12 years before PPSS can be seen. Therefore, placing more hydraulic fractures can help to accelerate the production and improve SRV recovery factor.

3.3.3 Hydraulic fracture half-length (x_F)

Hydraulic fracture half-length (x_F) is an unknown which must be estimated from a model match with data. The role of x_F is that it defines a width of SRV, i.e., the longer the x_F is the bigger the SRV will be. Fracture half-length cannot be determined uniquely when only linear flow can be seen without any upward deviation from the half slope trend. However, the minimum value for x_f is determined by estimating what permeability would correspond to departure toward ppss at the end of the known data, and a maximum value for x_f is given by half of the well spacing.

For the Barnett shale data used in this work, the average well spacing is approximately 500 ft. Thus, the base case fracture half-length of 250 ft is used with a range varied from 50 ft to 250 ft and 35 nd base case permeability.

The results shown in Figure 3.13 indicate that x_F only alter the level of RNP, but does not affect the time to see boundary. However, the \sim unit slope seen in the PPSS

behavior sets the SRV and therefore the productive fracture length. With that, the permeability can also be estimated from the earlier linear flow behavior.

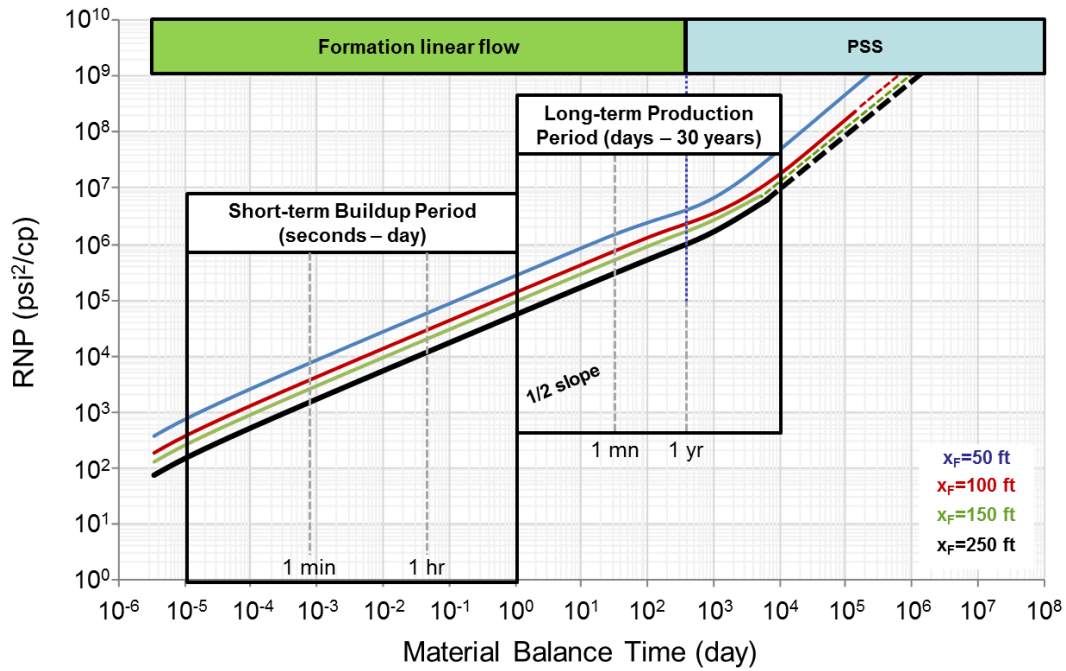


Figure 3.13: Barnett shale hydraulic fracture half-length sensitivity results

Note that x_F and RNP are inversely proportional, i.e. the highest RNP is achieved with the shortest fracture half-length. This implies that flow rate is direct proportional to the fracture extension because higher RNP level indicates lower flow rate given that pressure difference is constant. On the other hand, if the flow rate is constant, then it implies that shorter x_F requires higher pressure difference to achieve the same flow rate.

3.3.4 Dimensionless Fracture conductivity (C_{fD})

Hydraulic fracture conductivity [$k_F.b_F$] is the only factor that can generate quarter slope trend in the homogeneous model. In this analysis, C_{fD} defined as $k_F.b_F/k_X$ was varied from 1 to effectively infinite conductivity (IFC). The results are shown in Figure 3.14.

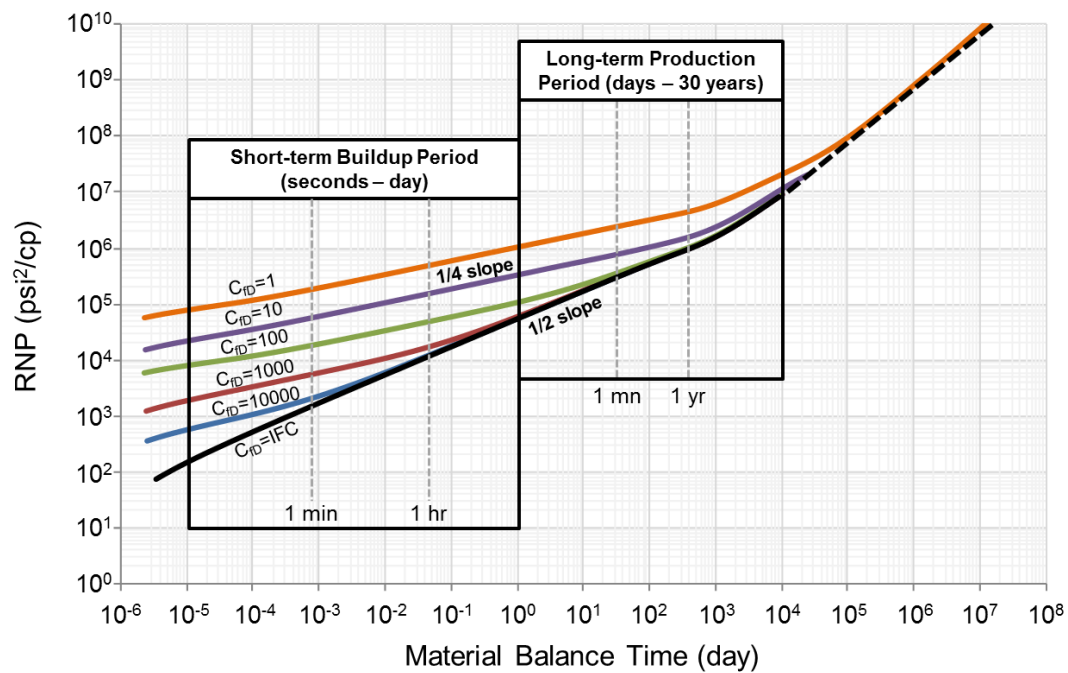


Figure 3.14: Barnett shale hydraulic fracture conductivity sensitivity results

The results indicate that a short-term buildup test can capture a quarter slope of the formation to hydraulic fracture bilinear flow behaviors for all C_{fD} value except the case with infinite conductivity. However, when C_{fD} is higher than 10000, the quarter slope trends may not be seen in practice because early time BU data is likely to be masked by wellbore storage. A quarter slope trends may be observed in the long-term

production data only for C_{fD} less than or equal to 100, but may be more obvious when it is lower than 100, e.g., 10. Note that C_{fD} of 10 gives a hydraulic fracture conductivity of 0.09 md-ft which can be converted to hydraulic fracture permeability (k_F) of 9-90 md based on hydraulic fracture width of 0.01-0.001 ft, respectively. Actually, when C_{fD} is lower than 10, for example when $C_{fD} = 1$ ($k_F = 0.9 - 9$ md), it is found that no $1/2$ slope trend could be observed throughout the entire well life. The results only show a $1/4$ slope trend followed directly by PPSS boundary dominated and pseudo radial flow regime. On the other hand, when C_{fD} is as high as 500 ($k_F = 0.4 - 4$ darcies), a $1/4$ slope trend will be seen on the buildup data, but only $1/2$ slope trend will be seen on the long term production data. Thus, having high data sampling frequency in the buildup data is important to confirm hydraulic fracture conductivity. The propped hydraulic fracture permeability is generally claimed to be in darcy permeability range, but we often see $1/4$ slope during the first weeks or even several months of the field data. This is consistent with two possibilities: finite conductivity hydraulic fractures draining effectively homogeneous single porosity shale, or effectively infinite conductivity hydraulic fractures draining a dual porosity formation with bilinear flow between a fracture network and the shale matrix. The dual porosity model possibility is investigated in the next section.

3.4 Sensitivity studies using the dual porosity model

In this section, two parameters related to fracture network, namely interporosity coefficient (λ) and storativity ratio (ω) will be investigated to see at which condition should the real field data show 1/2 slope or 1/4 slope.

There are two options available in transient dual porosity model, i.e. slab or sphere. In this case, the system is more suitable with the dual porosity transient slab model because the reopened fracture network may consist of parallel planes with narrow apertures. Therefore, the dual porosity transient slab model will be used to investigate the Barnett shale.

3.4.1 Interporosity coefficient (λ)

The interporosity coefficient defines the level of 1/4 slope transition period as well as the end of 1/4 trend which is approximately the beginning of the total system dominated linear flow period. Recalling Eq. 2.6, the smaller the value of λ , the lower the matrix permeability compared to the fracture permeability and/or the larger the spacing between the fracture planes, the later the matrix will start flowing into fracture network and thus the later the beginning of the bilinear transition flow behavior.

Figure 3.15 shows the sensitivity analysis results on the value of λ using base case parameters defined earlier with effectively infinite conductivity hydraulic fractures and for ω of 0.1.

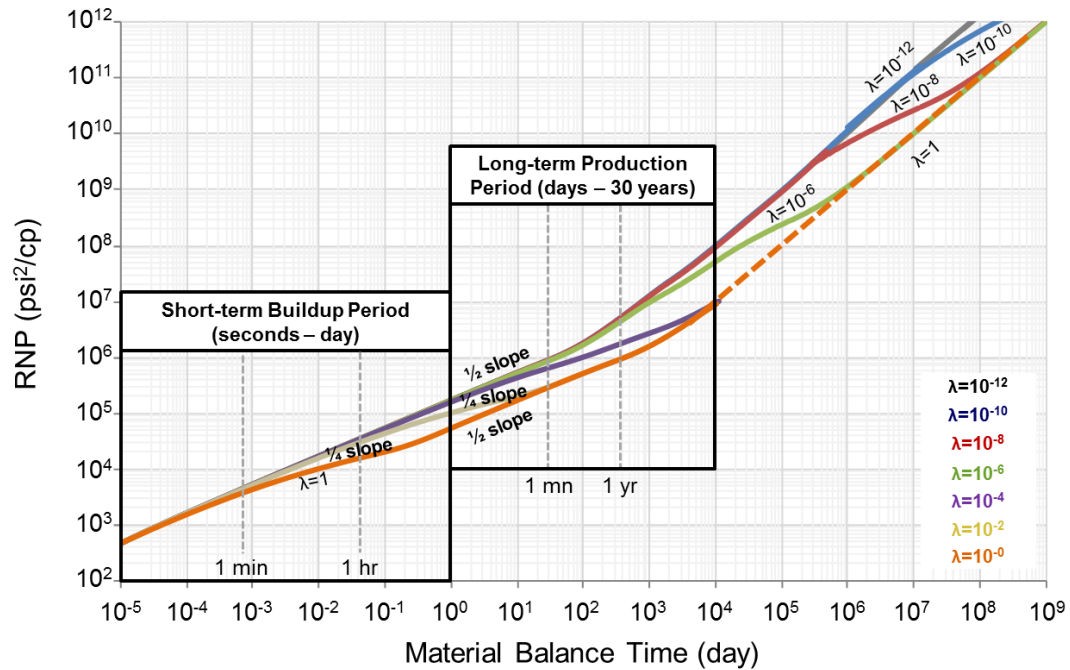


Figure 3.15: Barnett shale interporosity flow coefficient (λ) sensitivity results

From this result, it is found that when only 1/2 slope is seen on the long-term production data, there are two possibilities, i.e., fracture linear flow and total system linear flow. These two flow regimes occur in totally different conditions.

When the 1/2 slope belongs to the fracture network linear flow regime, the value of λ required will be very small, i.e., less than 10^{-6} . However, in this case at the time of PPSS the volume that is being produced will only come from the fracture network storativity which is obviously smaller than the SRV volume by the factor of ω . As a result, a boundary dominated flow regime where the data deviate from 1/2 slope trend will occur faster also by the factor of ω . In Figure 3.15, ω of 0.1 is used and the end of fracture linear flow is expected at around 1 month. The fact that we don't see boundary

related flow so early in the observed data therefore indicates that fracture network dominated flow is not likely to explain the $1/2$ slope observed on the field data. Note that the only possibility that could allow the fracture dominated flow to represent the $1/2$ slope trend being seen on long term production is when ω is very high, i.e., 0.5 or more which is very unlikely because if the fracture network in the dual porosity system was created during hydraulic fracturing, its volume is limited to the volume of fluid that leaked off.

When the $1/2$ slope belongs to the total system linear flow regime, the results indicate that λ should be larger than 0.01 if only half slope is observed on the long-term production data, otherwise a quarter slope line should be expected. The fact that λ must be relatively high implies either that the difference between fracture network and matrix permeabilities is small or that the distance between reopened fractures is small. For comparable permeability values, Eq. 2.6 suggests that the spacing between reopened fractures should be about 10 ft. Smaller ratio between shale matrix and fracture network permeability implies smaller spacing among reopened fractures. The exact value of matrix permeability cannot be found from the $1/2$ slope trend without an estimate for the average spacing between reopened fractures. Note that the finding that formation permeability should be less than 35 md obtained from the homogeneous model sensitivity can also apply here for the fracture network permeability because the total system permeability in the dual porosity model is dominated by the fracture network permeability value.

Again, Figure 3.15 show that a short-term buildup data with high data sampling frequency, e.g. 1 second per sample, can be very helpful to confirm the presence of fracture network in case that 1/4 slope trend is not observed on the daily production data.

3.4.2 Storativity ratio (ω)

The storativity ratio defines the duration of the 1/4 slope transition period. The smaller the ω is, the higher the difference between fracture volume and matrix volume, and thus the longer the transition period will last given that the same λ is used. The ω is defined as the ratio between fracture storativity to the total system storativity and can be shown as:

$$\omega = \frac{(\phi V c_t)_f}{(\phi V c_t)_f + (\phi V c_t)_{ma}} = \frac{(\phi V c_t)_f}{(\phi V c_t)_t} \quad \dots(3.1)$$

Based on the claims in the literature of the Barnett shale as mentioned in Chapter II, reopened natural fractures will likely dominate the dual porosity behavior even if natural microfractures exist. Therefore, the fracture flow behaviors observed in the field data likely represents the reopened fracture network or complexity. In this case, the fracture volume that contributes to the value of storativity ratio will be mainly from the reopened fracture network, and the ω could be related to the volume of injection fluid injected during fracturing treatment. Note that this volume is relatively small compared to the total shale bulk volume per created fracture, and thus the ω in this case is expected to be small.

The typical value of injection-volume derived storativity ratio (ω_{inj}) for the reopened fracture network of the representing Barnett shale may be estimated using the fracture injection volume by assuming that 100% of fracturing fluid injected to create hydraulic fracture will become reopened fracture network volume. This assumption will give a maximum value ω that should belong only to the reopened fracture network. The results of this estimation are plotted in Figure 3.16. Note that the volume of hydraulic fractures may be ignored here since it is very small comparing with the injected volume. For example, the hydraulic fractures with 500 ft half-length and 300 ft height will occupy only 55 ft³ assuming that the fracture has width of 0.001 ft while the typical injection volume per cluster for this Barnett shale is found to be 9,000 ft³ (1,600 bbl) or more.

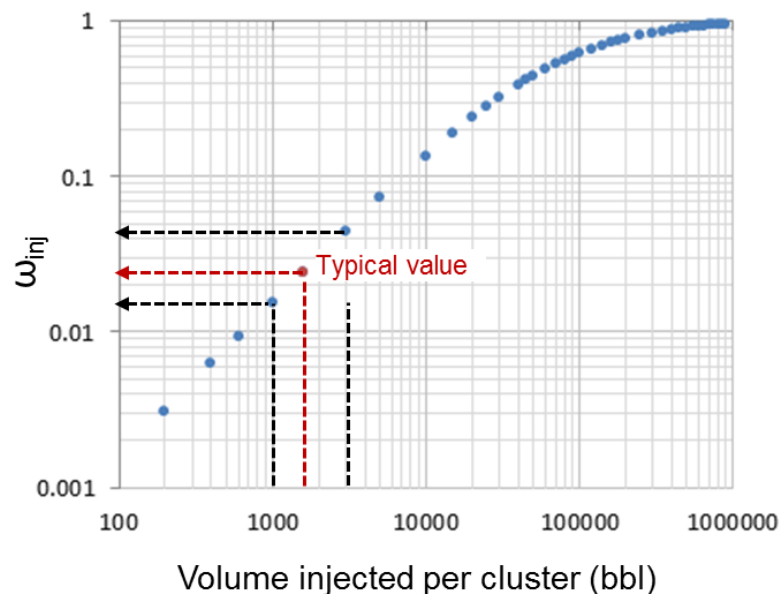


Figure 3.16: Typical ω value for the Barnett shale based on injection volume

The results indicate that the typical value for ω of the Barnett shale should be approximately 0.02 - 0.04 depends on the volume of injection fluid of 1000 to 3000 bbl per cluster. The ω that is larger than 0.1 is not expect for this Barnett shale because the injection volume per cluster generally does not exceed 6,000 bbl in this particular data set. Note that the volume per stage may exceed this value, but there are always more than one cluster per stage. Also note that the reopened fracture network is not expected to be propped due to its narrow width which is normally smaller than proppant diameter.

The higher value of ω might be possible with presence of the pre-existing active but unconnected natural fractures. However, these fractures could not contribute to the ω unless the reopened fracture network is present and connect those unconnected volumes together and provide flow paths to the wellbore. However, this is not likely to be present in the Barnett shale as the literature review had stated earlier, and even if they are the behavior of reopened fractures would dominate. Figure 3.16 could be used as a tool to crosscheck the value of ω when matching the field data.

Now, the sensitivity run on the range of ω value will be shown. Figure 3.17 is generated by varying ω from 0.001 to 1 based on the maximum permeability of 35 nd and λ of 0.01, for which it was shown earlier that only a 1/2 slope total system linear flow regime is expected to be seen clearly in long-term production data. In short-term buildup data, the results indicate that a 1/4 slope trend could be observed only when ω is less than 0.1 where the 1/4 slope lasts for one log cycle, but would be more obvious when it is less than 0.01 which allows the 1/4 slope to last for two log cycles.

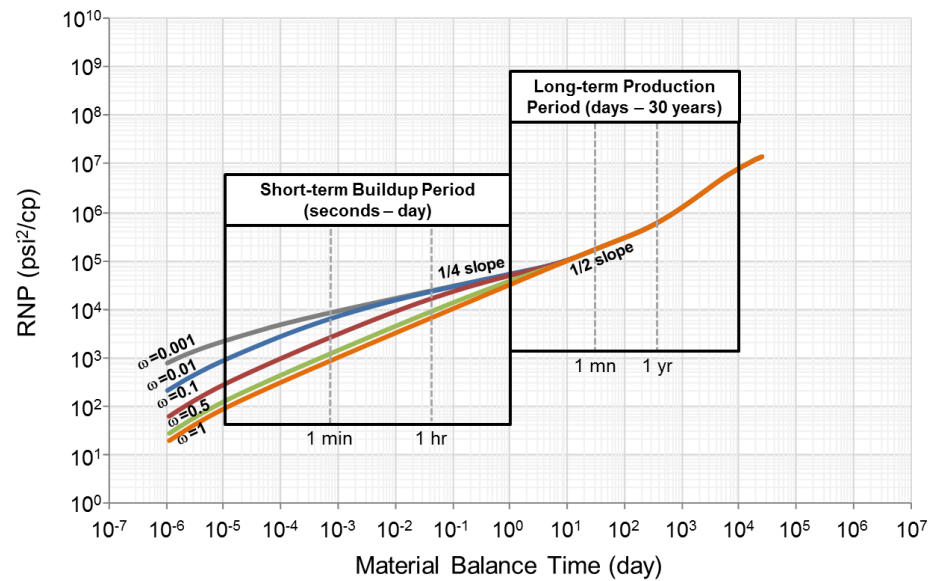


Figure 3.17: Barnett shale storativity ratio (ω) sensitivity results

The case of lower permeability, i.e., 3.5 nd, or ten-time lower than the previous case is also shown in Figure 3.18.

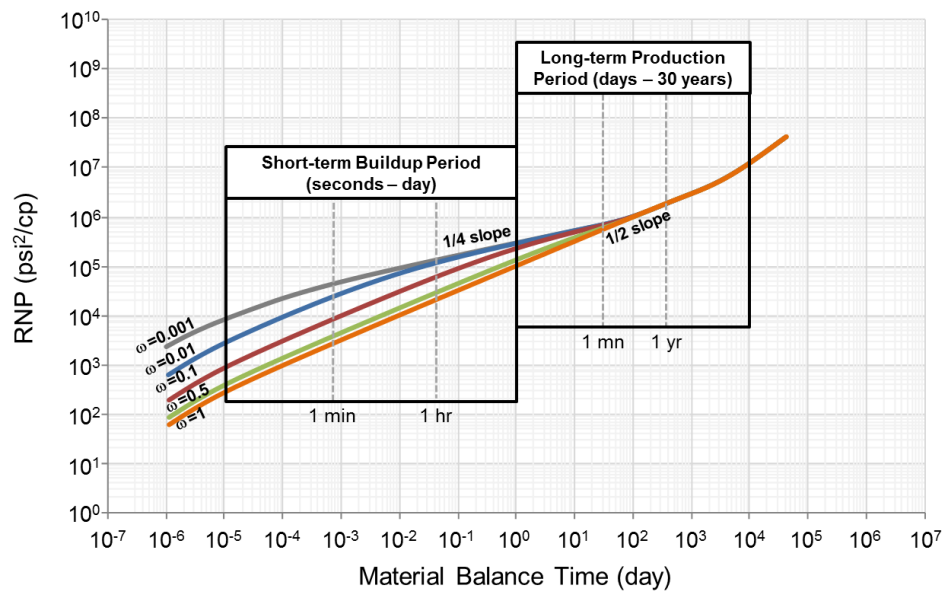


Figure 3.18: Barnett shale storativity ratio (ω) sensitivity results with lower fracture network permeability

It is found that when permeability is reduced by ten times, the end of a $1/4$ slope transition period will be delayed also by ten times or one log cycle. In this case, the ω value of 0.1 seems enough to allow a $1/4$ slope to be observed on the long-term production data. On the other hand, a $1/4$ slope may not be seen on the buildup data with $\omega=0.1$ but only the $1/2$ slope fracture dominated linear flow will be seen because the transition period occurs later than the buildup period window.

In the case that only a $1/2$ slope linear flow can be observed on the buildup data, the unified BU-RNP methods as proposed in Ehlig-Economides et al. (2009) should be used to investigate both the buildup data and production data together by overlaying the two linear flow regimes on the same log-log plot. If the linear flow being seen on buildup data and on production data can be overlain then it is confirmed that no fracture network should be expected and the conclusion might be made that the presence of fracture network, either active or reopened, is not likely and the shale matrix itself should be a major source of the well productivity. However, if the two linear flows cannot be overlain together, then the two linear flows do not belong to the same flow regime and the presence of a fracture network is confirmed.

Note that to allow the end of the bilinear transition period to occur at the same time as it would occur with higher permeability, the higher λ is required to offset the effect of permeability reduction. Anyway, the level of RNP will not be the same. Figure 3.19 illustrates the sensitivity runs with higher λ when permeability is reduced.

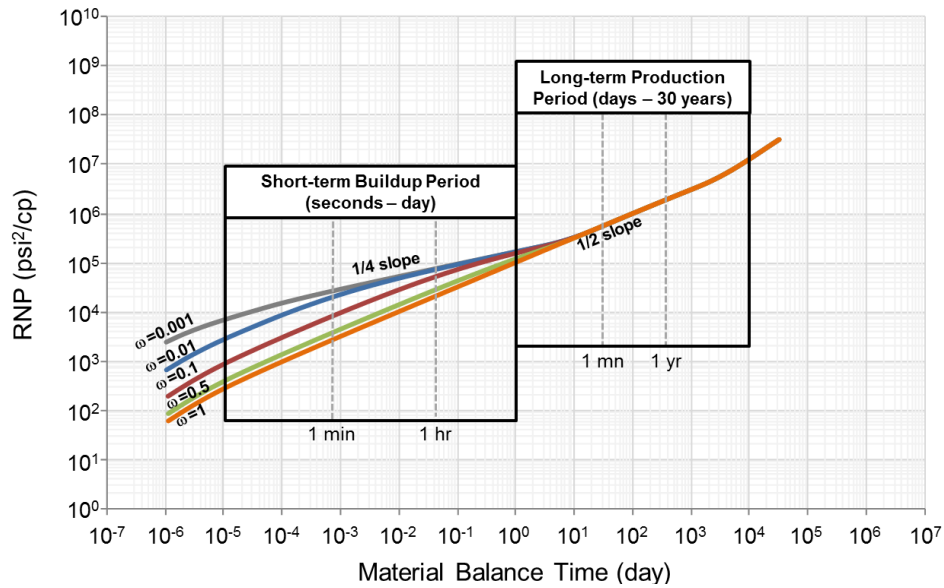


Figure 3.19: Barnett shale storativity ratio (ω) sensitivity results with lower fracture network permeability and higher λ

3.5 Model matches with Barnett well field data

In this section, the same well as was described in section 3.2.2 is matched with the single porosity homogeneous and dual porosity models. Various flow regime sequences that show the same behavior over the time window of the data will also be considered. A characterization will be given for each of the matches. Finally, we conclude which model and flow regime sequence should best represent the behavior of this well.

3.5.1 Data diagnosis

A MTFHW from the Barnett shale is selected as a representative for model matching in the following sections. We recall that most wells producing from the Barnett shale show evidence of liquid loading. However, this well shows minimal liquid loading

problem during a period of three years. The production and pressure history plots of the Barnett well are shown in Figure 3.20. Rate-normalized pressure (RNP) and pressure derivative (RNP') log-log diagnostic plots are shown in Figure 3.21.

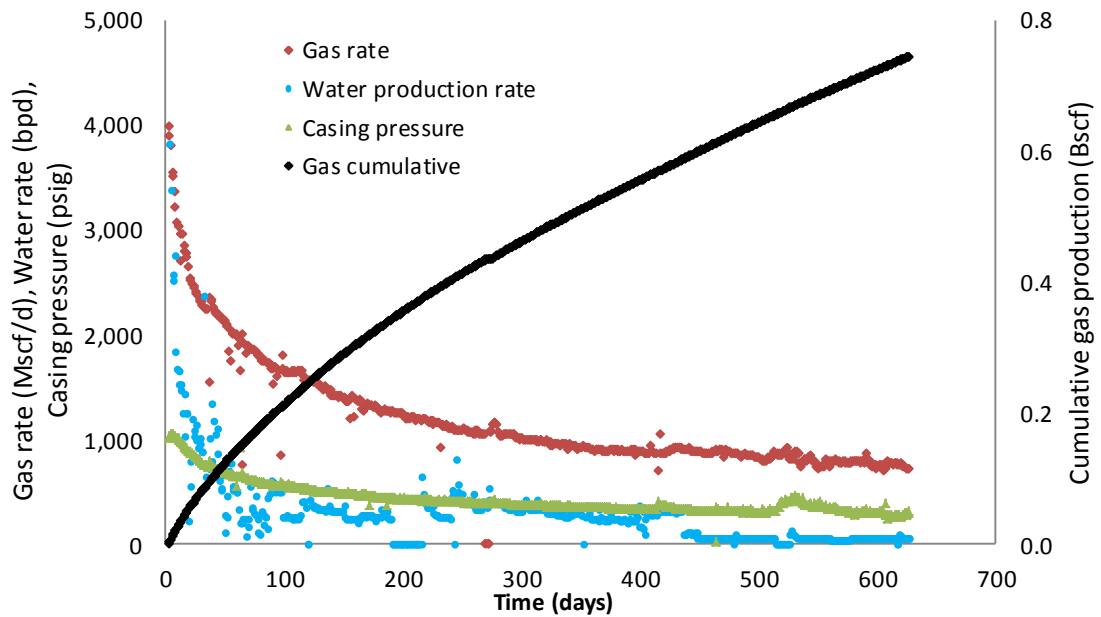


Figure 3.20: Pressure and production history plots of representative well for the Barnett shale

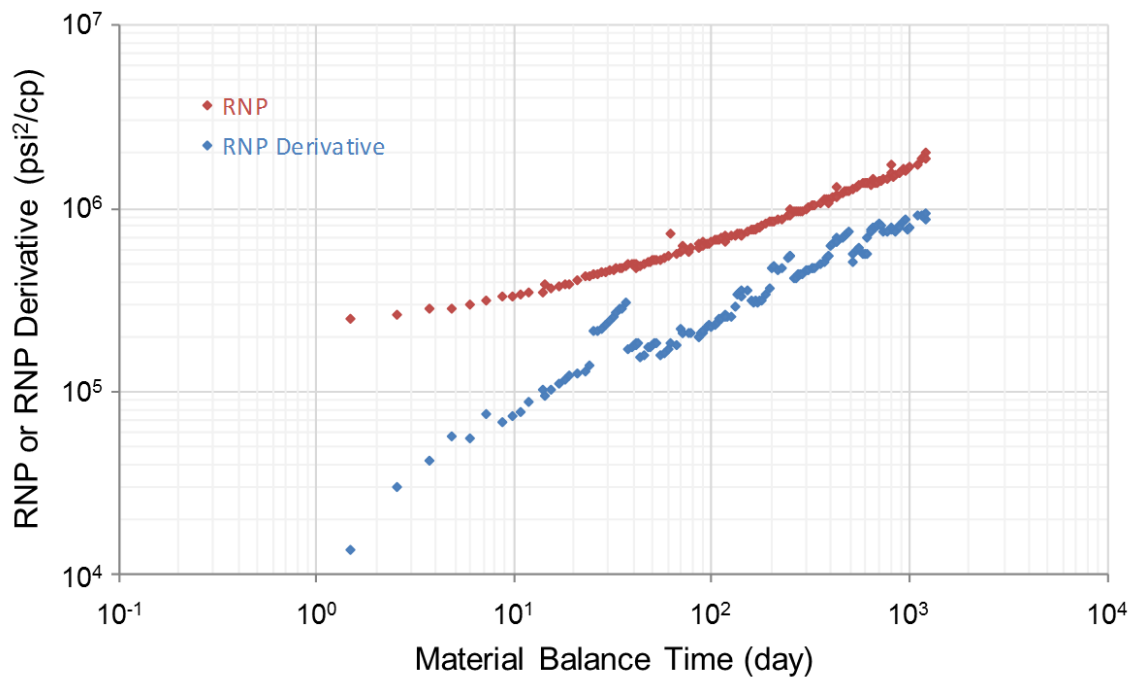


Figure 3.21: RNP and RNP' plots of the representative well for Barnett shale

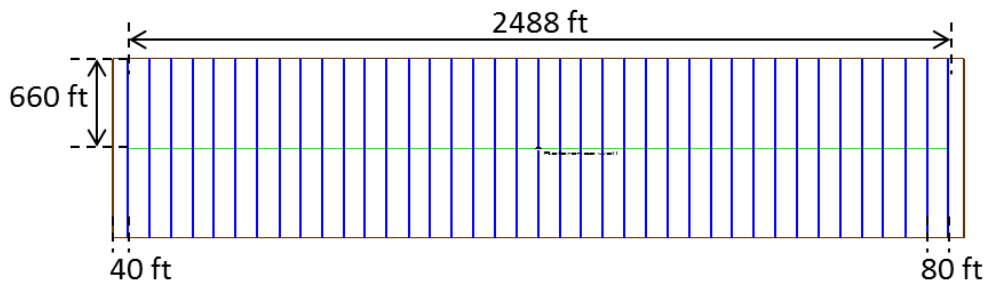
3.5.2 Model inputs

All input parameters used in this model study are summarized in **Table 3.2**. Note that these parameters are used for homogeneous and dual porosity model matching.

Table 3.2: Barnett shale model input parameters

Parameter	Symbol	Value	Unit
Well & Wellbore parameters			
Wellbore radius	r_w	0.35	ft
Horizontal well length	L_w	2488	ft
Vertical distance to lower boundary	z_w	150	ft
Number of hydraulic fractures	n_F	39	-
Hydraulic fractures half-length	x_F	660	ft
Hydraulic fracture spacing	x_s	80	ft
Fracture angle		90	°
Formation parameters			
Formation thickness	h	300	ft
Porosity	ϕ	0.03	fraction
Initial pressure at formation depth	p_i	3417	psia
Initial pressure converted to surface	$p_{i,s}$	2348	psia
Formation temperature	T	150	°F
Rocks and fluids properties			
Gas saturation	s_g	0.70	fraction
Water saturation	s_w	0.30	fraction
Gas specific gravity	γ_g	0.67	fraction
Initial gas compressibility	c_g	2.36E-04	1/psi
Initial water compressibility	c_w	3.17E-06	1/psi
Initial rock compressibility	c_f	4.00E-06	1/psi
Initial total compressibility	c_t	1.70E-04	1/psi
Gas viscosity	μ_g	0.02178	cp

Figure 3.22 shows the well geometry and boundary setting for the Barnett well model matching.

**Figure 3.22: Well geometry and boundary dimension for Barnett well**

3.5.3 Homogeneous model matching

Firstly, the observed data is matched with a single porosity model without the presence of reopened or pre-existing fracture network as illustrated in Chapter II and Appendix A. The log-log diagnostic plot indicates indicate only a half slope trend in the RNP derivative and a flat RNP trend in the early time period that may be the effect of fracture skin. With no evidence of late time upward departure from linear flow, the homogeneous model can only quantify the product of the fracture half-length and the square root of the formation permeability. Assuming that the hydraulic fracture half-length corresponds to 1/2 the horizontal well spacing gives formation permeability of 6.5 nd and a skin factor of 0.00013, providing an excellent global model match both on log-log and Cartesian axes, as seen in Figs. 3.23 and 3.24. Note that skin factor is very sensitive for RNP of MTFHW.

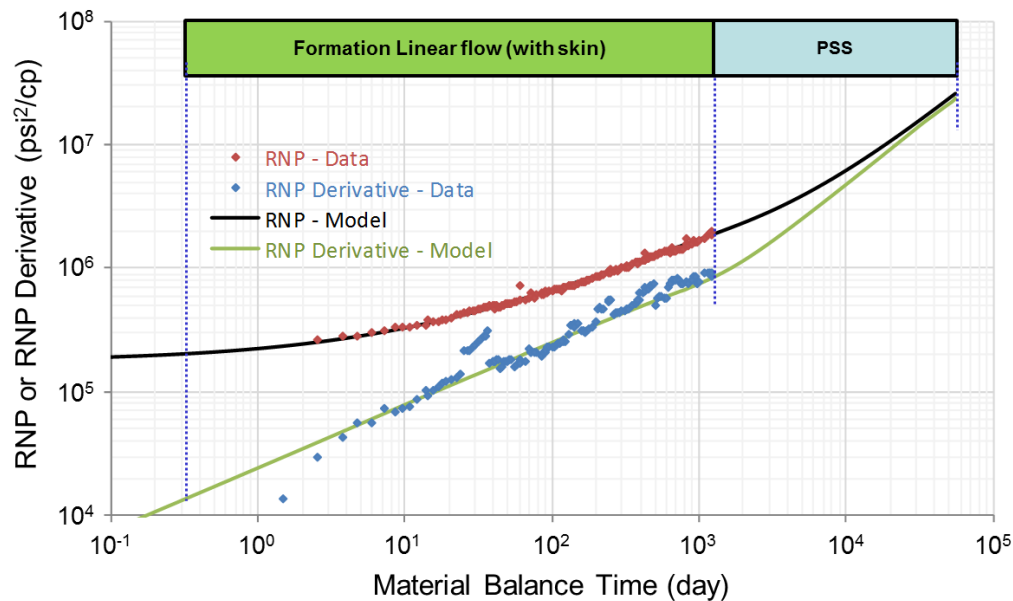


Figure 3.23: Log-log RNP and RNP' plots showing field data and homogeneous model matching comparison (k=6.5 nd, skin=0.00013)

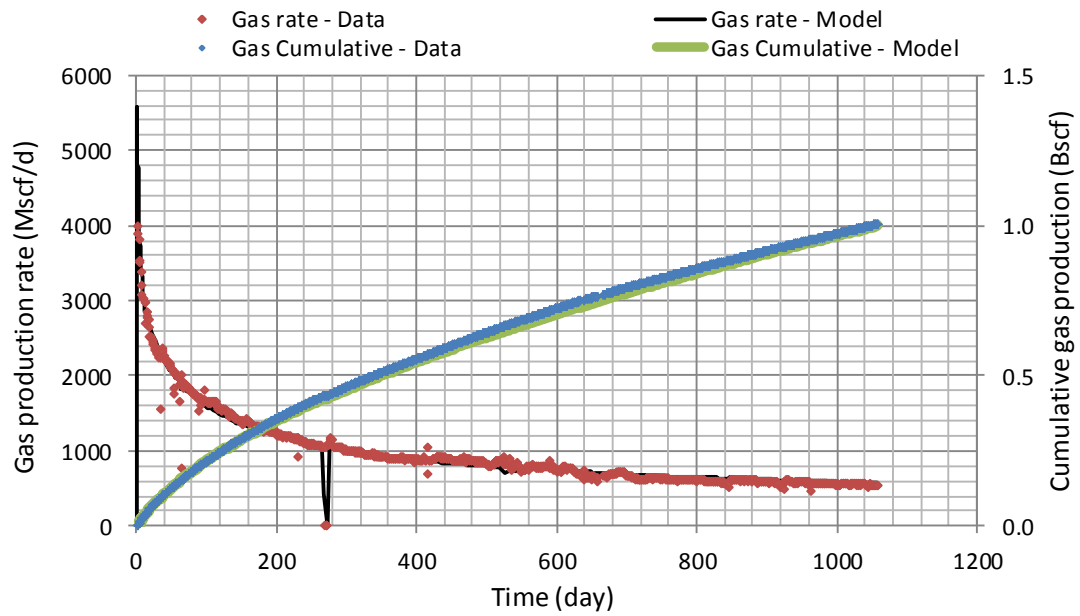


Figure 3.24: Production and cumulative production plots showing field data and homogeneous model matching comparison ($k=6.5$ nd, $skin=0.00013$)

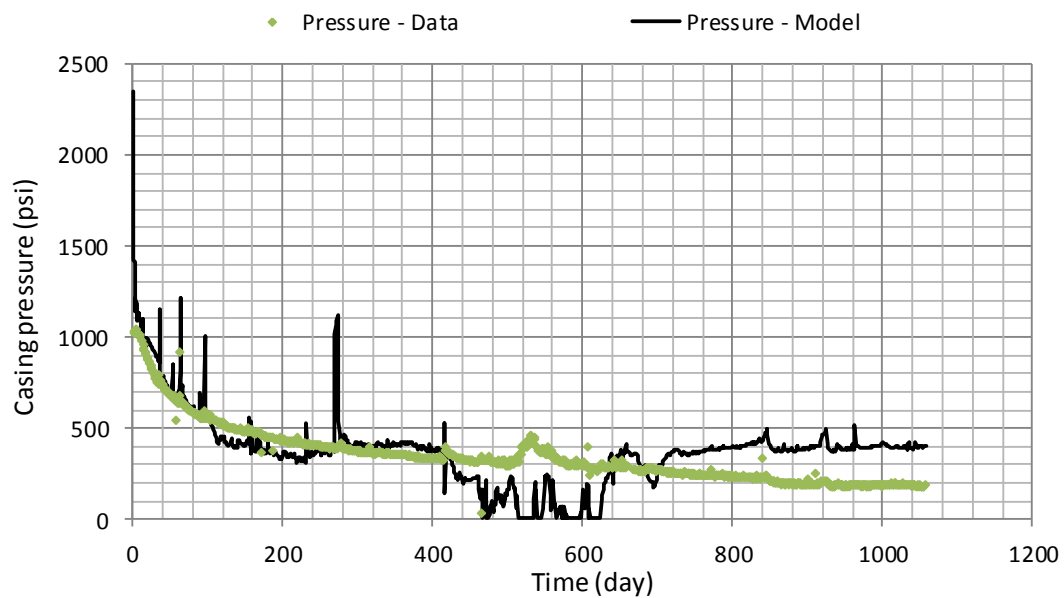


Figure 3.25: Casing pressure plots showing field data and homogeneous model matching comparison ($k=6.5$ nd, $skin=0.00013$)

The results indicate that homogeneous model can match the RNP, RNP', gas rate and cumulative production very well, but the casing pressure model trend in Figure 3.25 shows spikes that do not match the pressure data. This is partly because the model is actually computed in rate steps that only approximate the actual rate decline trend.

Another possible modeling approach is to treat the early flat response as a result of finite hydraulic fracture conductivity. The match results indicate the same permeability as the previous case of 6.5 nd, but now with F_c of 0.8 and skin of 0. The RNP and RNP' plots are shown in Figure 3.26 together with the Cartesian plots in Figure 3.27 and 3.28.

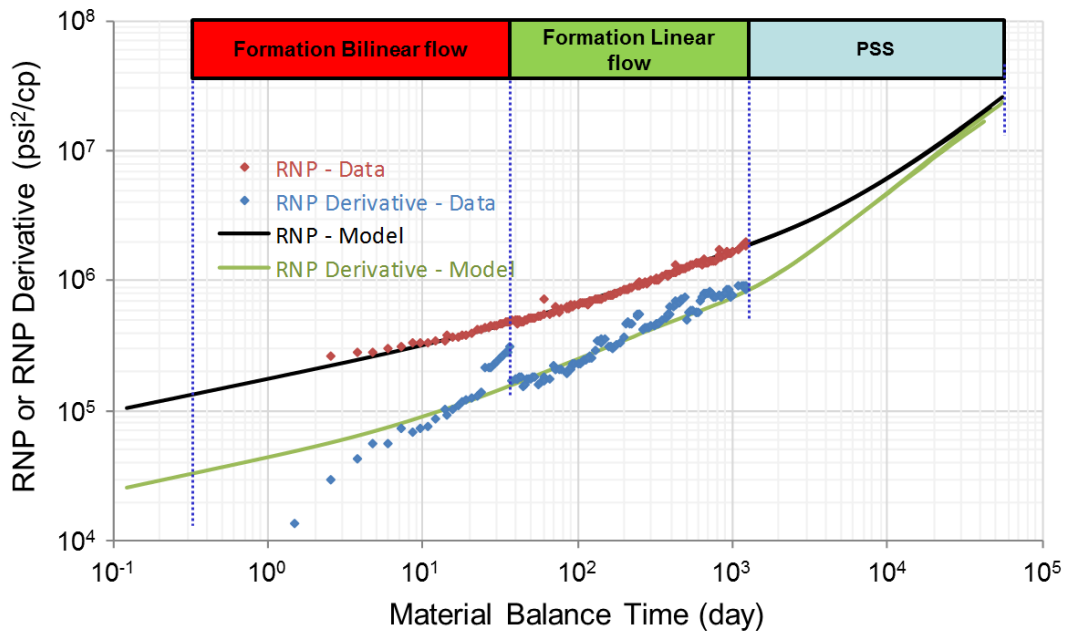


Figure 3.26: Log-log RNP and RNP' plots showing field data and homogeneous model matching comparison ($k=6.5$ nd, $F_c=0.8$ md-ft, skin=0)

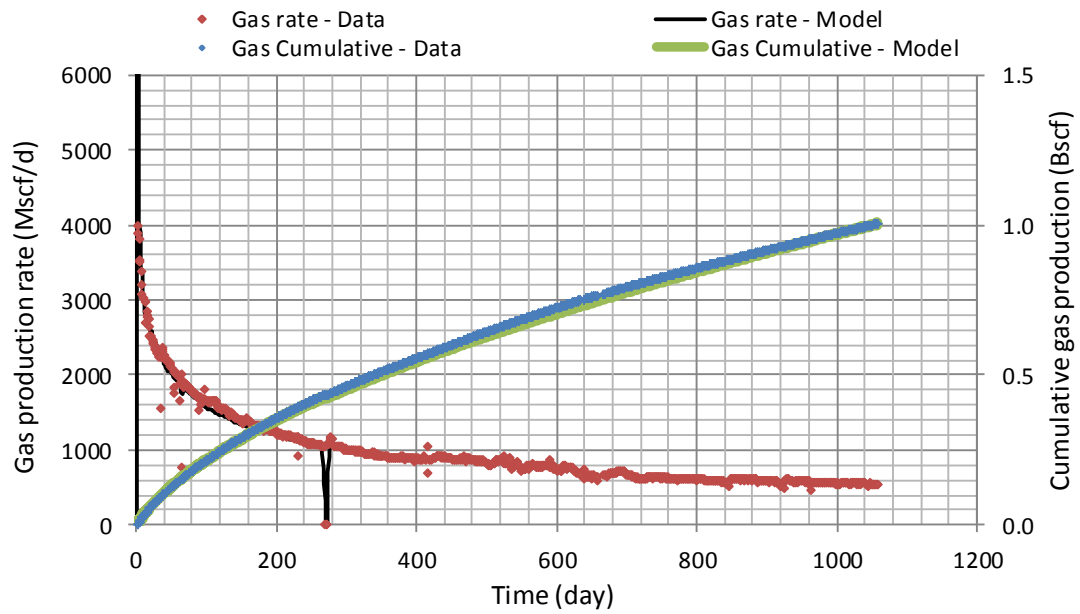


Figure 3.27: Production and cumulative production plots showing field data and homogeneous model matching comparison ($k=6.5$ nd, $F_C=0.8$ md-ft, skin=0)

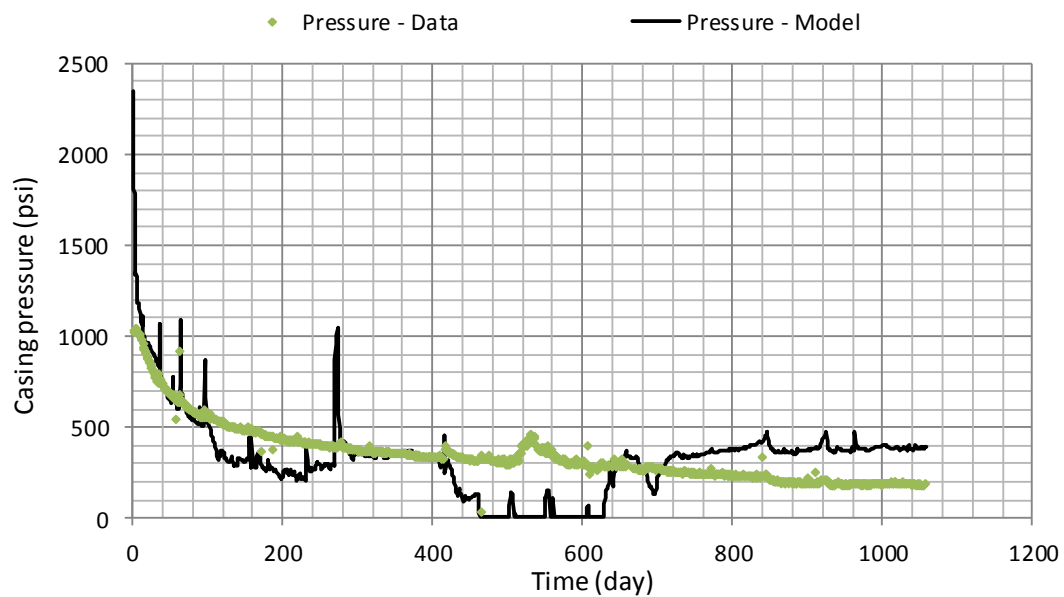


Figure 3.28: Casing pressure plots showing field data and homogeneous model matching comparison ($k=6.5$ nd, $F_C=0.8$ md-ft, skin=0)

Because the Cartesian match for this model is similar to the one shown previously, it may be that finite conductivity hydraulic fractures explain the apparent skin seen in the first match. Although the indicated fracture conductivity magnitude is low, the dimensionless fracture conductivity for this model match is nearly 300, which means the modeled fractures have effectively infinite conductivity.

In either case the permeability is the same. Also, a look at the late time model trends shown in Figs. 3.23 and 3.26 indicates that the hydraulic fractures cannot be much shorter than the assumed length without seeing the model derivative trend upward, thereby losing the late time log-log match. Therefore, even though this departure is missing in the data, the models imply that it should become apparent within another 3 years on production.

3.5.4 Dual porosity model matching

The dual porosity model is used to investigate the evidence of fracture networks discussed previously. In this section, both quarter and half slope trends will be considered. Therefore, three possible flow regime sequences that can occur as illustrated in Chapter II and Appendix B are:

- Fracture network to hydraulic fracture bilinear flow followed by fracture network linear flow (FN-HF \rightarrow FN)
- Total system to hydraulic fracture bilinear flow followed by total system linear flow (TS-HF \rightarrow TS), and

- Matrix to fracture network bilinear flow followed by total system linear flow
(M-FN \rightarrow TS)

3.5.4.1 Fracture network to hydraulic fracture bilinear flow followed by fracture network linear flow (FN-HF \rightarrow FN)

This flow regime sequence involves only the hydraulic fracture and the fracture network without effectively zero flow from shale matrix. The results indicate the bulk fracture permeability of 8.4 nd with hydraulic fracture conductivity of 0.80 md-ft. The storativity ratio (ω) and interporosity flow coefficient (λ) are found to be 0.80 and 1.00E-12, respectively. The match results are plotted in the pressure and pressure derivative plots as well as the Cartesian plots as shown in Figure 3.29 to 3.31.

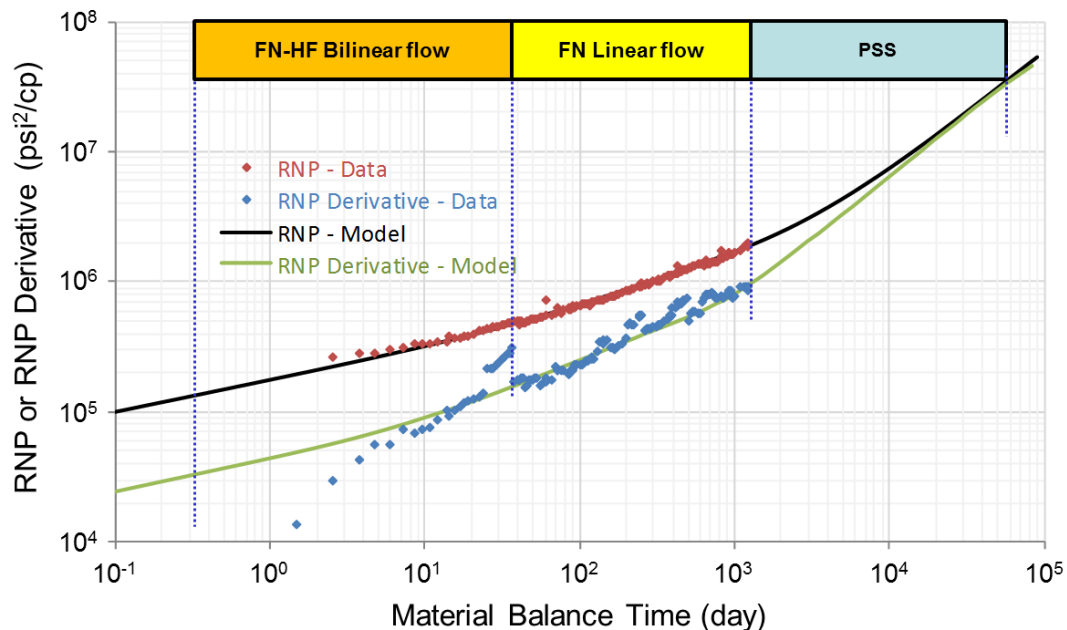


Figure 3.29: Log-log RNP and RNP' plots showing FN-HF and FN flow regime sequence matching ($k=8.6$ nd, $FC=0.80$ md-ft, $\omega=0.80$, $\lambda=1.0E-12$)

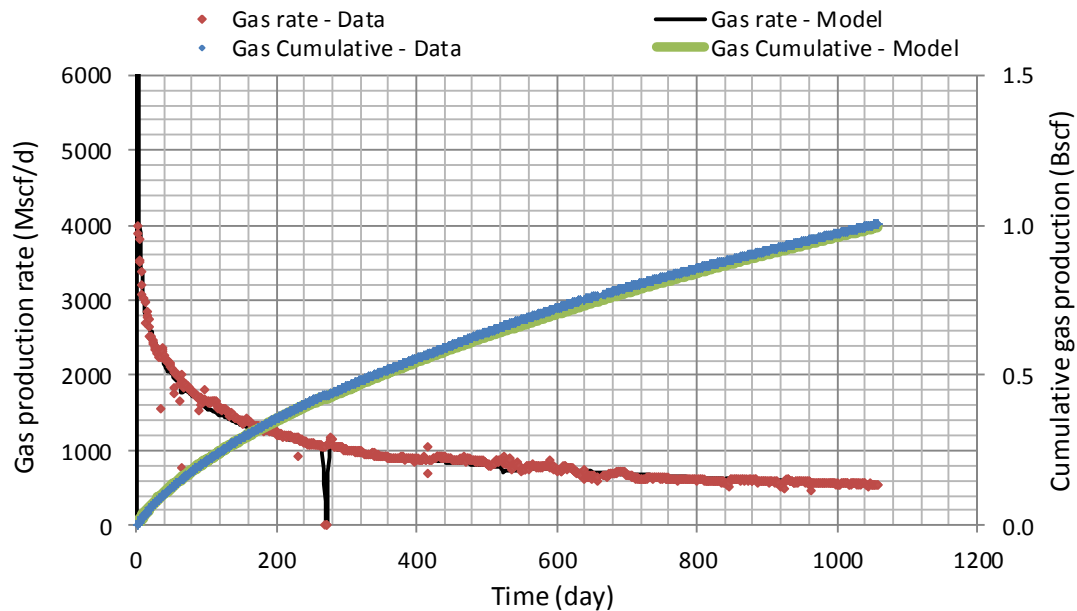


Figure 3.30: Gas rate and cumulative gas plots showing FN-HF and FN flow regime sequence matching ($k=8.6$ nd, $FC=0.80$ md-ft, $\omega=0.80$, $\lambda=1.0E-12$)

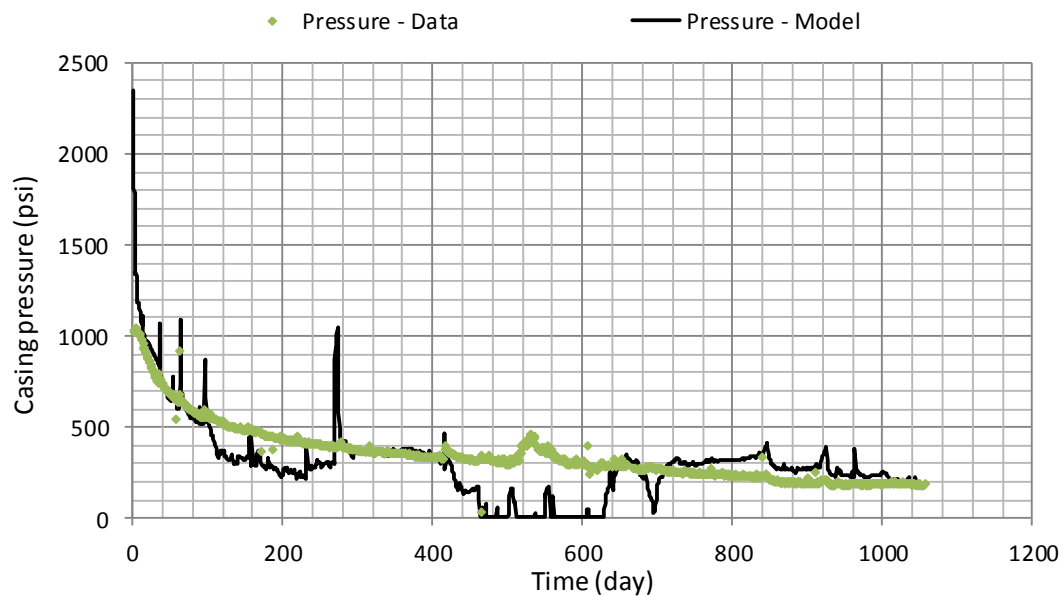


Figure 3.31: Casing pressure plots showing FN-HF and FN flow regime sequence matching ($k=8.6$ nd, $FC=0.80$ md-ft, $\omega=0.80$, $\lambda=1.0E-12$)

The low value of λ , which implies low matrix permeability compared to fracture network permeability, is required in order for the fracture network to dominate the system without disturbing the shale matrix, which thus has no contribution to the system. Even though we can get a good match, the ω value of 0.80 probably must be interpreted as microfractures and not fractures opened or reopened as a result of hydraulic fracturing. With this interpretation, the matrix permeability can be regarded as effectively zero.

3.5.4.2 Total system to hydraulic fracture bilinear flow followed by total system linear flow (TS-HF \rightarrow TS)

This flow regime sequence involves hydraulic fractures and the total dual porosity system. The total system includes shale matrix + fracture network storativity with essentially only fracture network permeability. The results indicate the bulk fracture permeability of 6.5 md with hydraulic fracture conductivity of 0.80 md-ft. The interporosity flow coefficient (λ) is found to be 1.0. Note that ω has no effect on the flow behavior because neither the fracture network linear flow nor the matrix to fracture network bilinear flow can be observed in this scenario. It appears that permeability and fracture conductivity in this case are exactly the same as were used to match with the homogeneous model. This indicates that the homogeneous model may be used to match the MTFHW in a dual porosity reservoir for which the matrix permeability is high but still less than that of the fracture network, but formation permeability in this case must

be fracture network permeability, not the matrix. From Eq. 2.6, for $\lambda = 1$, we have the following relationship:

$$h_{ma} = 60r_w \sqrt{\frac{k_{ma}}{k_f}} \quad \dots(3.2)$$

assuming spherical matrix porosity elements.

The match results are shown in Figure 3.32 to 3.34 to compare the observed data with the model matching. Note for Figure 3.32 that the model result also shows a 1/8 slope trend before 1 day. This is the trilinear flow regime resulted from transient linear flow in all three media, i.e., hydraulic fracture, fracture network, and shale matrix. (See Appendix B for more details.)

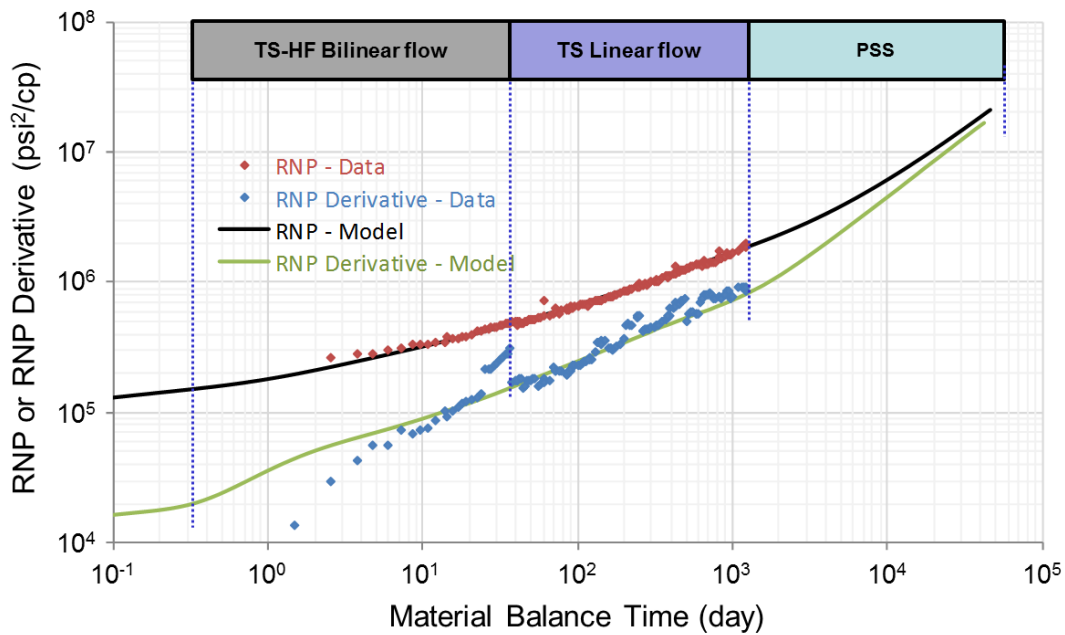


Figure 3.32: Log-log RNP and RNP' plots showing TS-HF and TS flow regime sequence matching ($k=6.5$ nd, $FC=0.80$ md-ft, $\omega=0.01$, $\lambda=1.0$)

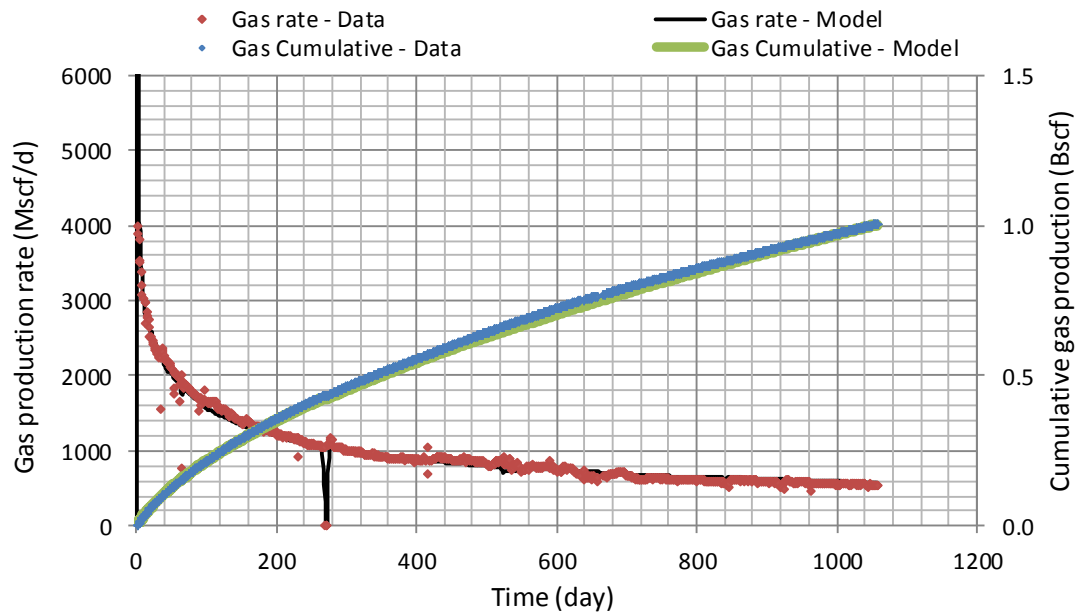


Figure 3.33: Gas rate and cumulative gas plots showing TS-HF and TS flow regime sequence matching ($k=6.5$ nd, $FC=0.80$ md-ft, $\omega=0.01$, $\lambda=1.0$)

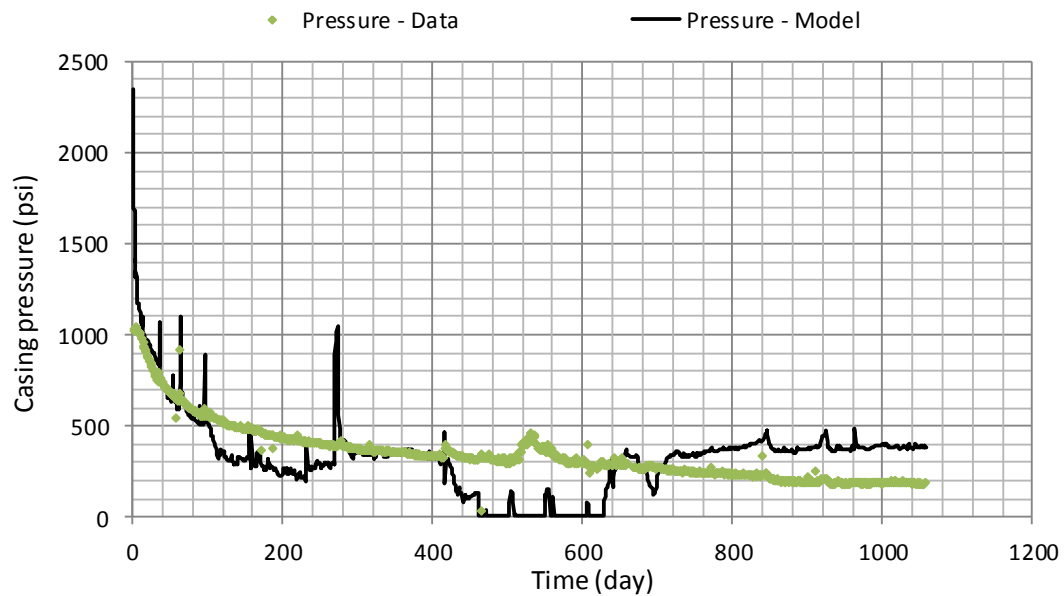


Figure 3.34: Casing pressure plots showing TS-HF and TS flow regime sequence matching ($k=6.5$ nd, $FC=0.80$ md-ft, $\omega=0.01$, $\lambda=1.0$)

3.5.4.3 Matrix to fracture network bilinear flow followed by total system linear flow (M-FN \rightarrow TS)

In this case the observed bilinear flow trend is due to flow from the matrix to the fracture network with evidence of flow to effectively infinite hydraulic fractures occurring earlier in time. This can be seen as an intermediate case between the two previously described cases. An explanation here could be that reopened and/or natural fractures provide a flow path with minimal storativity while the shale matrix has large storativity. The hydraulic fractures are considered as highly conductive and their behavior cannot be seen on the field data.

The results indicate that the bulk fracture permeability of 5.5 nd. The interporosity flow coefficient (λ) is found to be 0.008 with the storativity ω of 0.01. The match results are shown in Figure 3.35 to 3.37.

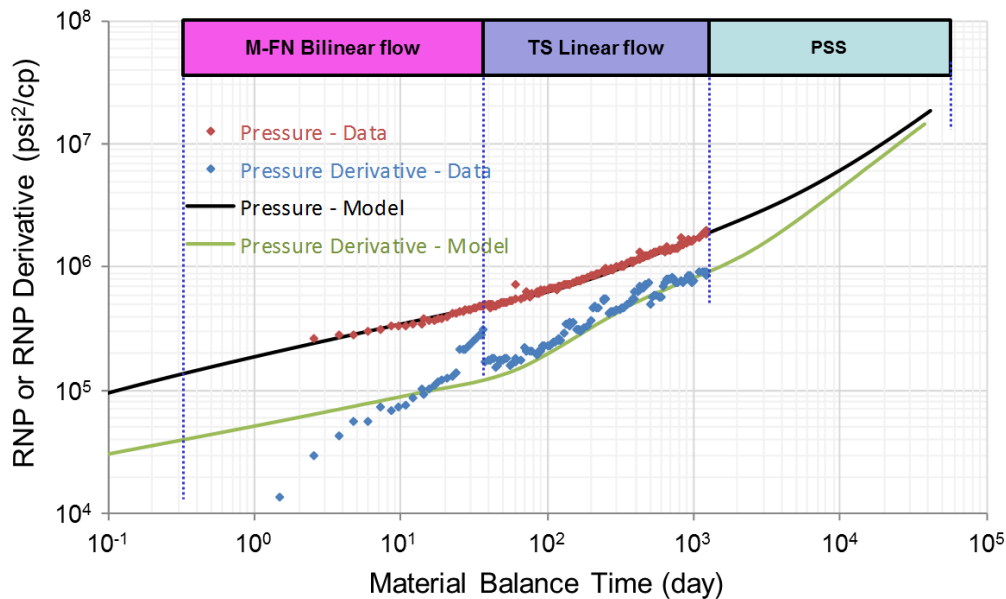


Figure 3.35: Log-log RNP and RNP' plots showing M-FN and TS flow regime sequence matching ($k=5.5$ nd, $F_C=IFC$, $\omega=0.01$, $\lambda=0.008$)

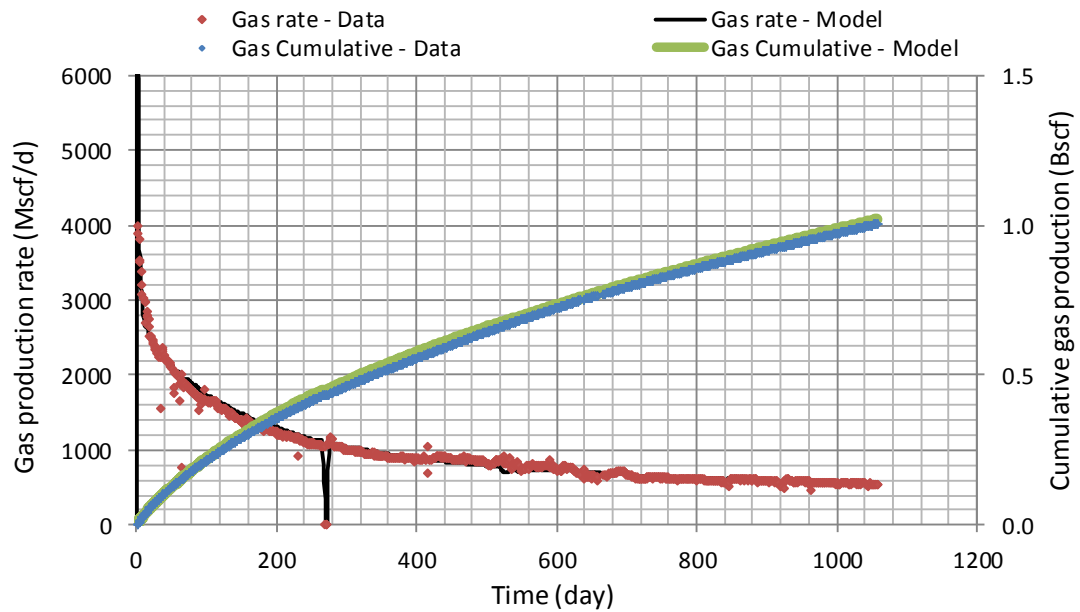


Figure 3.36: Gas rate and cumulative gas plots showing M-FN and TS flow regime sequence matching ($k=5.5$ nd, $F_C=IFC$, $\omega=0.01$, $\lambda=0.008$)

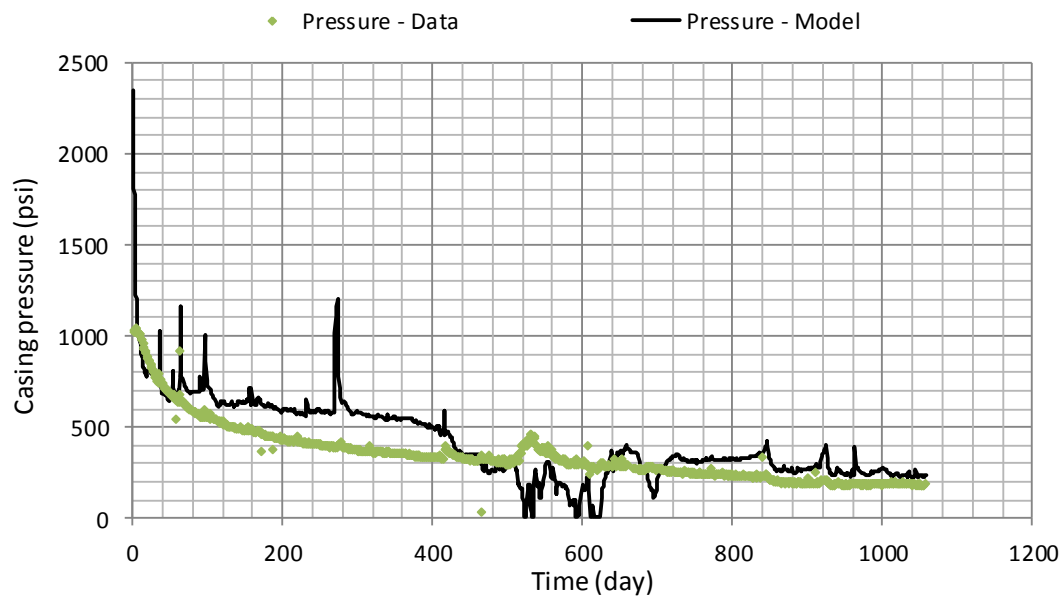


Figure 3.37: Casing pressure plots showing M-FN and TS flow regime sequence matching ($k=5.5$ nd, $F_C=IFC$, $\omega=0.01$, $\lambda=0.008$)

The value of ω corresponded to injection volume calculated by using the same type of chart as shown in Figure 3.9 but constructed with the input parameters of this well is found to be 0.012. When comparing with the matched result, it appears that the matched ω is almost the same as the injected volume derived ω_{inj} , i.e. 0.01 versus 0.012. Therefore, this model match may imply that the fractures in the model are opened or reopened during hydraulic fracturing. Note that when ω is represented by the reopened fracture network, the fracture volume which contributes to the value of ω will provide an additional pore volume. For example, the Barnett shale porosity is reported to be 3%. Therefore, the ω of 0.01 in this case indicates that reopened fracture network provides 1% additional pore volume to 3%, which means that the total porosity after stimulation would be 3.03%. However, this reopened fracture network does not store gas originally because they are healed prior to stimulation. Hence, this additional porosity does not contribute to the gas in place.

Considering again Eq. 2.6 for the value for λ of 0.008 and fracture permeability of 5.5 nd, for an assumed spacing between reopened fractures of 10 ft the resulting ratio between matrix and fracture permeability is 0.74, while if the spacing is assumed to be 0.1 ft, the ratio is 7.4E-5, assuming slab elements corresponding to roughly parallel opened or reopened fractures.

3.6 Discussion

All matches for the data suggest a working permeability less than 10 nd with effectively infinite conductivity hydraulic fractures, but different models give a different physical meaning. The matching results for of the Barnett well production data analysis for all models are summarized in Table 3.3. Figure 3.38 compares the results from all models matching on the log-log RNP and RNP derivative plots.

Table 3.3: Barnett shale dual porosity model matching results summary

No	Model	Flow regime	k_f (nd)	skin	F_c (md-ft)	C_D	ω	λ
1	Homogeneous	Linear + Skin	6.5	1.3E-4	IFC	IFC	-	-
2	Homogeneous	Bilinear \rightarrow Linear	6.5	0	0.80	186	-	-
3	FN-HF \rightarrow FN	Bilinear \rightarrow Linear	8.4	0	0.80	144	0.80	1E-12
4	TS-HF \rightarrow TS	Bilinear \rightarrow Linear	6.5	0	0.80	186	no influence	1.0
5	M-FN \rightarrow TS	Bilinear \rightarrow Linear	5.5	0	IFC	IFC	0.01	0.008

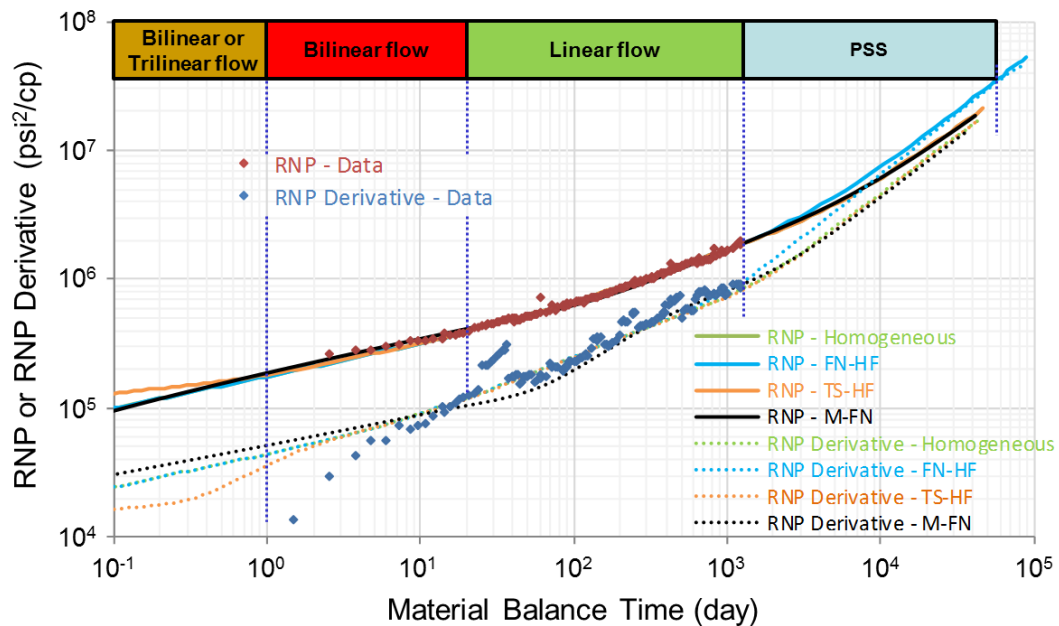


Figure 3.38: Log-log RNP and RNP' plots showing different flow regime matching comparison

Figure 3.38 shows that pressure buildup data acquired at sufficiently high data rate, perhaps 1 second, would distinguish between the models in Table 3.3, except for between the homogeneous models and Model 3. However, more time on production will indicate whether Model 3 is a fit for the data. Therefore, a key recommendation from this study is to encourage operators to acquire at least one buildup test designed to characterize the early time transient behavior.

Assuming a homogeneous model, the permeability value in the model corresponds to the formation permeability, and model matches are consistent with high conductivity hydraulic fractures.

Three possible matches for the data were found using dual porosity models. In one (FN-HF), the apparent fractures provide both storativity and transmissibility because the matrix permeability is very low and does not contribute to the flow behavior and production. Hence, lower potential gas recovery is expected. Note that slightly higher permeability is required to match the observed data because we need to compensate for the volume loss. Without this adjustment, the pressure depletes too fast. The bilinear flow in this case is a result of the fractures system (either opened microfractures or reopened fracture network) flowing to finite conductivity hydraulic fractures. The difference between this model and the homogeneous model is at the late time response. The FN-HF model will see RNP and RNP' bending earlier to PSS flow regime, thereby indicating the smaller productive volume as seen in Figure 3.38. The value of $\omega = 0.8$ is consistent with the leftward shift in the PSS behavior corresponding to $1/0.8$ of one log

cycle, or 80% of the volume seen for the other cases. The very small λ value indicates that the matrix contribution will be much too late in time to be of any practical value.

A second model (TS-HF), in contrast to the first one, has a shale matrix that with sufficiently high permeability that the matrix reaches its stabilization boundary so fast that the fracture linear flow regime cannot be observed on the long term production. The only linear flow seems viable is the total system linear. Therefore, the bilinear flow in this case results from the total dual porosity system flowing to finite conductivity hydraulic fractures. The ω in this scenario does not have an effect on the apparent flow regime behavior observed during the long term production period, namely, the 1/4 slope TS-HF bilinear flow and the late 1/2 slope total system linear flow. The matched permeability appears to be the same as homogeneous model. The difference between the two models is only at the early response. The TS-HF model shows trilinear flow preceding the bilinear flow while the homogeneous model shows continuous bilinear flow. (Figure 3.38) Note that the TS-HF model matching will give matrix permeability which is higher than fracture permeability if the fracture spacing is longer than 1 ft. This may indicate that the TS-HF model is not likely to represent the bilinear flow behavior of the Barnett well because the fracture spacing is expected to be around 10 to 20 ft based on literature.

The final model match (M-FN) involves a possible combination of existing microfractures, reopened fractures, and the shale matrix. The bilinear flow is a result of matrix flowing to a fracture network (opened or reopened). The main difference of this model when comparing with the other models is that the end of bilinear flow regime in

this scenario shows a sharp rise of RNP derivative response indicating the end of stabilization period while the other models in which the bilinear flow is related to the finite conductivity hydraulic fractures shows a smooth transition from bilinear to linear flow. For this model, the match with field data indicates an ω value that consistent with the calculated ω_{inj} for the Barnett well. This implies that pre-existing microfractures may not contribute to the fracture network flow behavior, and only the reopened fracture network is providing the modeled connectivity between shale matrix and the hydraulic fractures. In turn, depending on the assumed spacing between opened or reopened fractures, the matrix permeability could be comparable in magnitude to that of the fracture network. This observation could imply that the matrix permeability is actually that of existing microfractures or it could represent actual shale matrix permeability. Based on the matching result, the M-FN model is the most reasonable model among the three dual porosity models.

Note that the two reasonable matches for the Barnett well are the homogeneous and the M-FN model, but they consider bilinear flow as a result of different flow systems. The 1/4 slope bilinear flow of the homogeneous model results from the transient flow inside hydraulic fractures and the formation linear flow while the M-FN model exhibits a 1/4 slope as results of the transient flow from fracture network into hydraulic fractures and the transient flow from shale matrix to the fracture network.

Considering the set of model matches for the data, the conductivity of the hydraulic fractures governs the duration of bilinear flow regimes involving them directly, namely, FN-HF, TS-HF, and also M-HF or the homogeneous model with finite

conductivity hydraulic fractures. For these cases, the smaller the hydraulic fracture conductivity, the longer the bilinear flow will be. The fracture conductivity controls directly the *end* of bilinear flow, but does not indicate the *beginning* of the bilinear flow regime, which would likely be governed by wellbore storage and only visible in pressure buildup data. In contrast, for the M-FN case the storativity ratio (ω) governs the duration of the bilinear flow, and the smaller the ω value is, the shorter the bilinear flow. The value of ω does not directly control the *end* of bilinear flow, but rather indicates the *beginning* of the bilinear flow.

When the model value for ω exceeds the value for ω_{inj} calculated from an estimated leak-off volume during hydraulic fracturing, this is likely to be an indication that existing microfractures account for the fracture storativity, which may or may not involve fractures opened or reopened during hydraulic fracturing. The fracture pore volume contributing to the value of ω could be either from the pre-existing microfractures or the reopened fracture network, or both.

It is not possible to match the data with a model that assumes hydraulic fracture half-length smaller than 1/2 the well spacing. Therefore, presence of fractures opened or reopened during hydraulic fracturing (complexity) has not prevented stimulation of the volume to be drained by each horizontal well. However, the lack of distinction among the various models, whether homogeneous or dual porosity, indicates that complexity does not improve the drainage of the stimulated shale volume.

Fracture skin is found to have significant effect on the early time data, i.e., it will flatten the early RNP response, but not affect the RNP derivative. Note that the skin factor of only 0.0001 can change the response noticeably.

3.7 Chapter summary

This chapter reviewed descriptions for the Barnett shale and offered sensitivity studies for key parameters in the homogeneous and dual porosity models based on these descriptions. Then homogeneous and dual porosity model matches for the data were provided.

A discussion comparing the implications of the various model matches explains what the model parameters might indicate about flow in the Barnett shale. While the data do not conclusively reveal evidence of opened or reopened fractures that have been described as hydraulic fracturing induced complexity, dual porosity models supporting this possibility can match the data. However, even if fractures are opened or reopened during hydraulic fractures, they do not improve the drainage of the stimulated shale volume.

CHAPTER IV

MODEL SENSITIVITY STUDIES BASED ON THE HORN RIVER SHALE

This chapter will show sensitivity behavior of the three different models reviewed briefly in Chapter II using parameters typical for the Horn River shale. As in the previous chapter, we start with a description of the shale. Then the chapter will review sensitivities to parameters in an analogous way to the previous chapter, but emphasizing differences in the flow behavior of the 2 shale formations.

4.1 Horn River shale formation characterization

In this section, the background information of the Horn River shale will be reviewed including shale properties and typical well completion. Then the raw data will be shown to investigate the overall behavior of the wells producing from the Horn River shale.

4.1.1 Field background

*****Horn River Basin (HRB) is the biggest shale gas field in Canada located between British Columbia and the North Western Territories (**Figure 5.1**). The shale in HRB is of Devonian age and is comparable to the Barnett shale in aspects of depth, porosities, productivity, and shale qualities (Reynolds and Munn, 2010). However, it contains multiple potentially productive shale formations including the Carboniferous- Devonian Muskwa, Otter Park, Klua and Evie formations. A vertical well originally drilled in 1980

to evaluate the shale was re-entered in 2006 (McPhail et al, 2008). After the well was hydraulically fractured in two intervals, the well flowed at the rate of 460 mscf/d. The basin has been developed extensively since 2006 using multiple transverse fractured horizontal wells (MTFHWs).

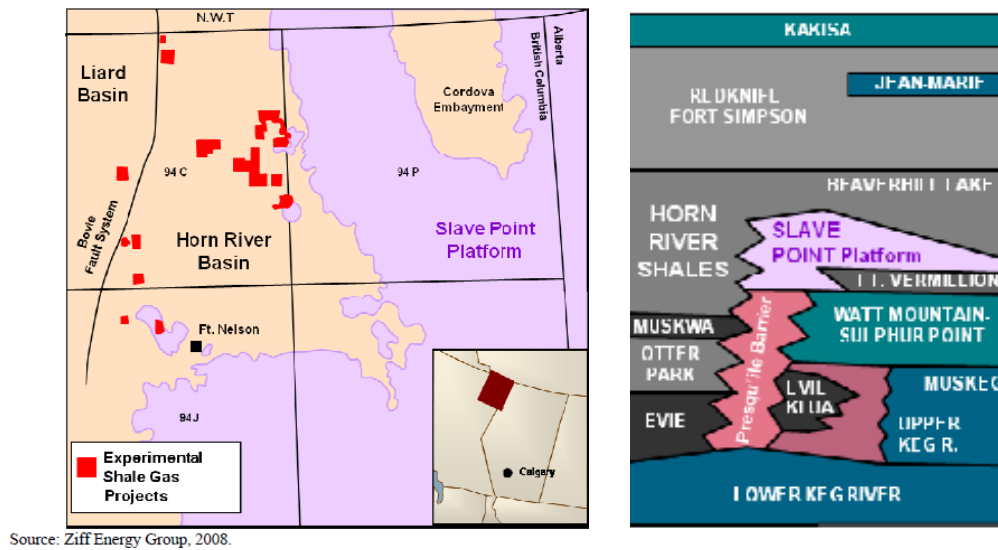


Figure 4.1: Horn River Basin stratigraphy and location (National Energy Board, 2009)

The Horn River Basin (HRB) shale is considered as high temperature and over-pressured with an average temperature of 350°F and an initial pressure ranging from 5500 to 7250 psi (Reynolds and Munn, 2010) for an equivalent formation pressure gradient of 0.6-0.8 psi/ft. The average porosity in the Muskwa/Otterpark formation is 0.052. The effective shale matrix permeability is reported to be in a range of nanodarcies (EOG website, 2008). Evidence of pre-existing natural fractures is observed from cores,

thin sections, and pressure leak-off behavior during fracture calibration test. A pre-stimulation test also showed gas producing to surface (Reynolds and Munn, 2010). Therefore, the existing natural fractures are assumed to improve productivity of the Horn River shale.

The well that is used in this study is one of sixteen wells drilled from the same pad with average well spacing between adjacent wells of 880 ft. The wells have approximate TD at around 15,500 ft.MD (9,000 ft.TVD) and have been completed with 5.5” casing. The sixteen wells drilled from the same pad were put on production within a 3-month time span. All the wells have at least one long shut-in period for 2-4 weeks started at the same time after around 5-6 months of production. On average, the wells were hydraulically fractured in 17 to 21 stages (18 on average) with a total of 25 to 45 perforation clusters (36 on averages) along the 5,700 ft average horizontal section length giving the average cluster spacing of about 160 ft. The wells are produced through a 2-7/8” production tubing.

Figure 4.2 summarizes the base case well dimension and SRV boundary setting. The fracture half-length of 440 ft is half of the average well spacing.

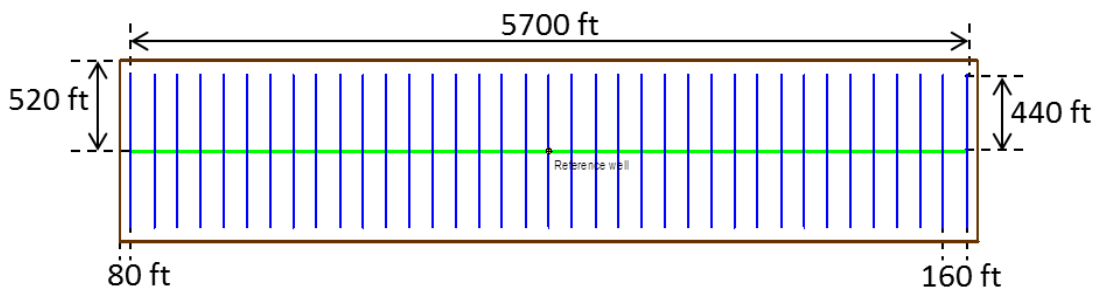


Figure 4.2: Base case MTFHW dimension and SRV boundary for Horn River shale

The general range of shale properties and well completion information from literatures and available raw data are summarized in Table 4.1. Note that the exact range will be investigated further in the following sections.

Table 4.1: Estimate range of sensitivity parameters for the Horn River shale study

Properties	Value	Unit
Shale matrix permeability (k)	0.000001-0.1 (1-100000)	md (nd)
Fracture network conductivity ($k_f b_f$) _D	0.4 - infinite conductivity	md-ft
Hydraulic fracture conductivity (C_{FD})	0.5 - infinite conductivity	-
Hydraulic fracture half-length (x_F)	55 - 440 - 880 (well spacing)	ft
Hydraulic fracture spacing (x_s)	80 - 160 - 640	ft

4.1.2 Data overview

Available data for the Horn River shale covers a period of almost two years. The gauge data include surface casing and tubing pressure, and surface production rate (gas and water). The pressure and production data are collected on an approximately daily basis. Casing pressure is used to represent flowing bottomhole pressure by adding gas column static pressure to the measured surface casing pressure. Production and pressure history plots of a representative Horn River well are shown in Figure 4.3.

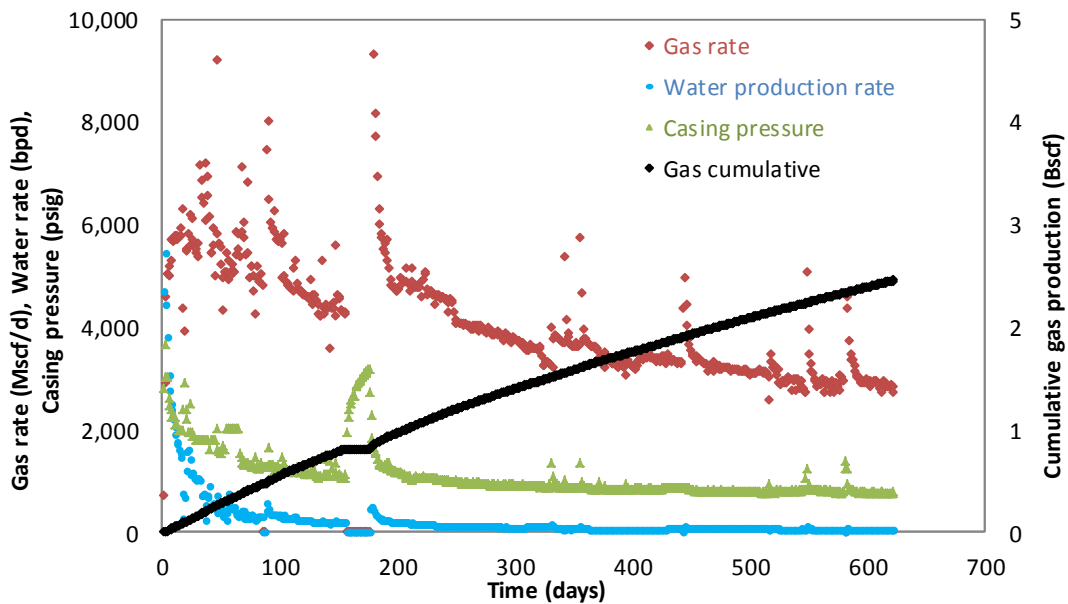


Figure 4.3: Pressure and production history of the well from Horn River shale

One long buildup period lasting from two to four weeks is seen after about 6 months. When more than one buildup is available, an analysis of both buildups can give evidence of fracture conductivity changes with time. Based on the data from 16 wells, it is found that most of them exhibit a $1/4$ slope trends during the buildup period. The example of buildup transient data for a Horn River shown in Figure 4.4 indicates only bilinear flow behavior.

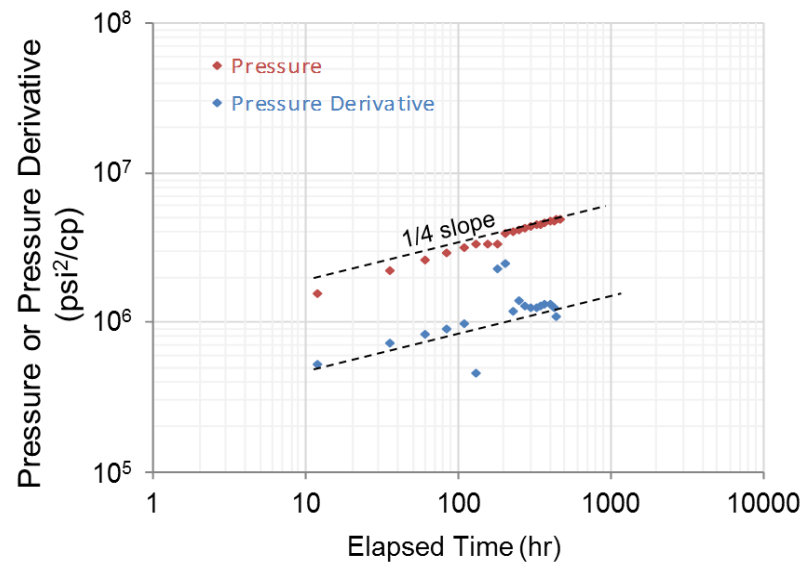


Figure 4.4: Log-log diagnostic plots example for a BU test of the Horn River well

Figure 4.5 shows a log-log RNP and RNP derivative (RNP') plot from the same well. The RNP trend seems smooth while considerable scatter in the RNP' makes it difficult to identify any obvious trend. The early-time RNP data are flat, suggesting a small fracture skin.

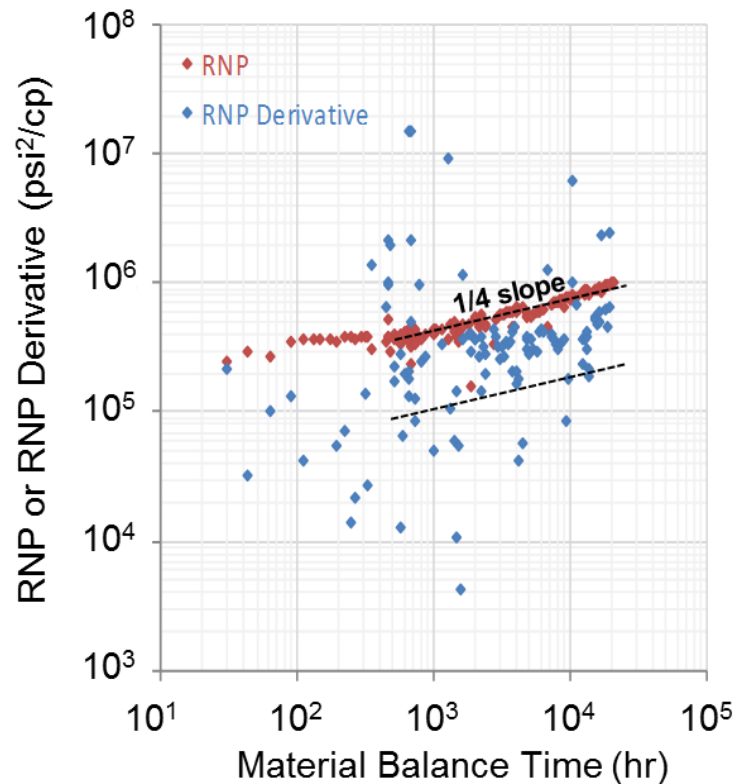


Figure 4.5: Log-log diagnostic plots example for the long term production data of the Horn River shale well

Figure 4.5 is dominated by a long 1/4 slope trend covering a period up to 10000 hrs. However, the RNP' data is too scattered to use the separation between RNP and RNP' to confirm the flow regime. An almost unit slope trend representing pseudo pseudosteady state (PPSS) boundary dominated flow regime is not obvious in Figure 4.5, but a slight bending up trend may be located after 10000 hrs. An obvious unit slope trend is observed in only one of the 16 wells, but analysis of liquid loading in that well implies the effect is misleading and should be discounted. As a result, it can be concluded that the PPSS boundary has not been observed before one year of production. This will be used as base case $t_{e,elf}$ for the Horn River shale when performing sensitivity

analysis. The set of specialized plots including linear plots, bilinear plots, log-log plots, Cartesian plots, WGR plots, and water production plots for some other wells can be found in Appendix F.

4.2 Sensitivity studies using the single porosity (homogeneous) model

The same procedure as being shown in Chapter III for the Barnett shale is applied in this section. The depth of investigation equation will be used to calculate the expected range of permeability for the Horn River shale. The sensitivity run will be performed to show the flow regimes we can expect to see in the practical time windows by varying hydraulic fracture spacing (x_s), hydraulic fracture half-length (x_F), and hydraulic fracture conductivity (C_{fD}) on the flow regime behavior. Note that the general effect of each of the parameter on the RNP and RNP' behavior will not be repeated in this section because it has been reviewed thoroughly in Chapter III. Only behavior that is distinct from trends seen in the Barnett well will be addressed.

4.2.1 Permeability

It has been shown earlier in the previous section that base case $t_{e,elf}$ is one year, with the possible longer $t_{e,elf}$ of two years or longer if the subtle upward departure in the RNP is not used. The depth of investigation equation is used to estimate the range of permeability. The results shown in Figure 4.6 indicate that the expected range of permeability for the Horn River shale is approximately between 80 nd and 200 nd based on average hydraulic fracture spacing of 160 ft. Hence, base case permeability of 100 nd

will be used for further sensitivity analysis of the Horn River shale. Figure 4.7 shows the log-log RNP and RNP' plots using base case parameters.

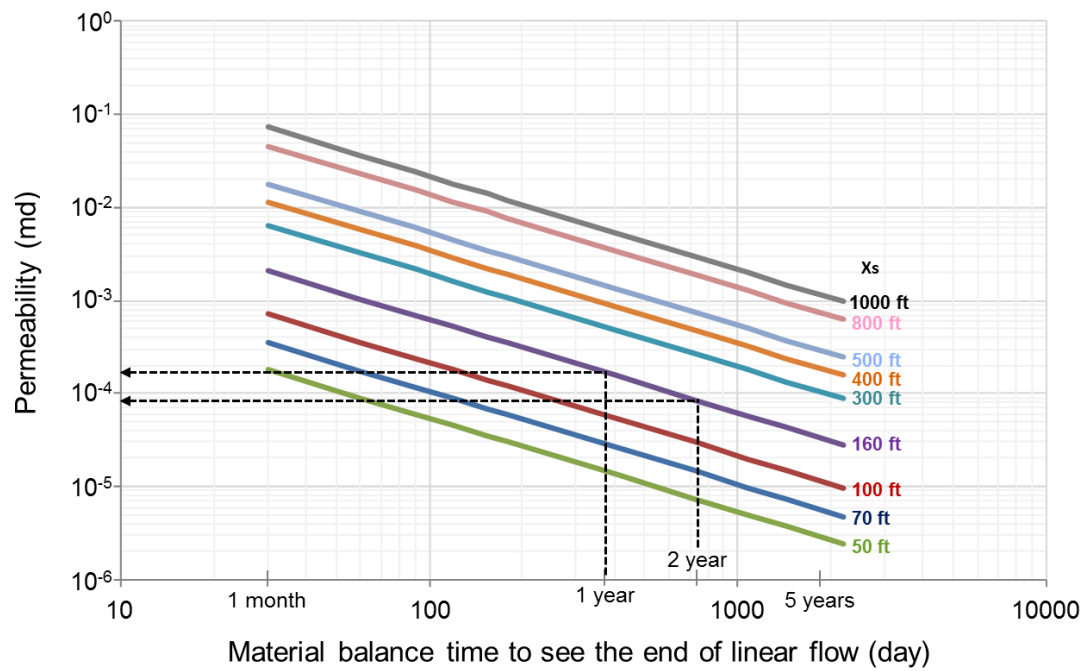


Figure 4.6: Permeability and fracture spacing versus material balance time for the Horn River shale

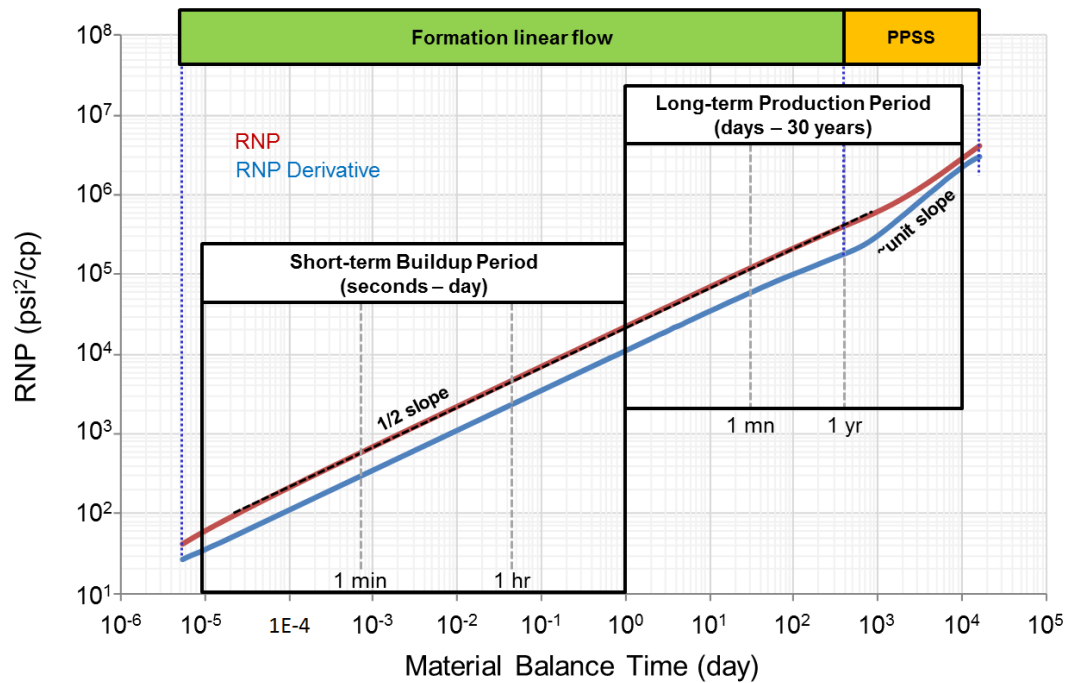


Figure 4.7: Log-log diagnostic plot based on base case parameters of Horn River

Base case parameters plots indicate that only 1/2 slope formation linear flow can be observed in buildup window, while long term production show a 1/2 slope trend followed by PPSS flow regime. However, it is obvious that a 1/4 slope trend is not seen. Therefore, finite conductivity of hydraulic fractures is expected, if the Horn River shale is not fractured reservoir that contains secondary porosity and causes a 1/4 slope to be seen. The expected value of C_{ID} will be investigated later in this section.

Once the base case formation permeability has been established, sensitivity runs on the permeability can be done. In this work, permeabilities were varied from 0.1 nd to 1000 nd to cover the entire expected range of permeability. Figure 4.8 shows the results of sensitivity runs on formation permeability.

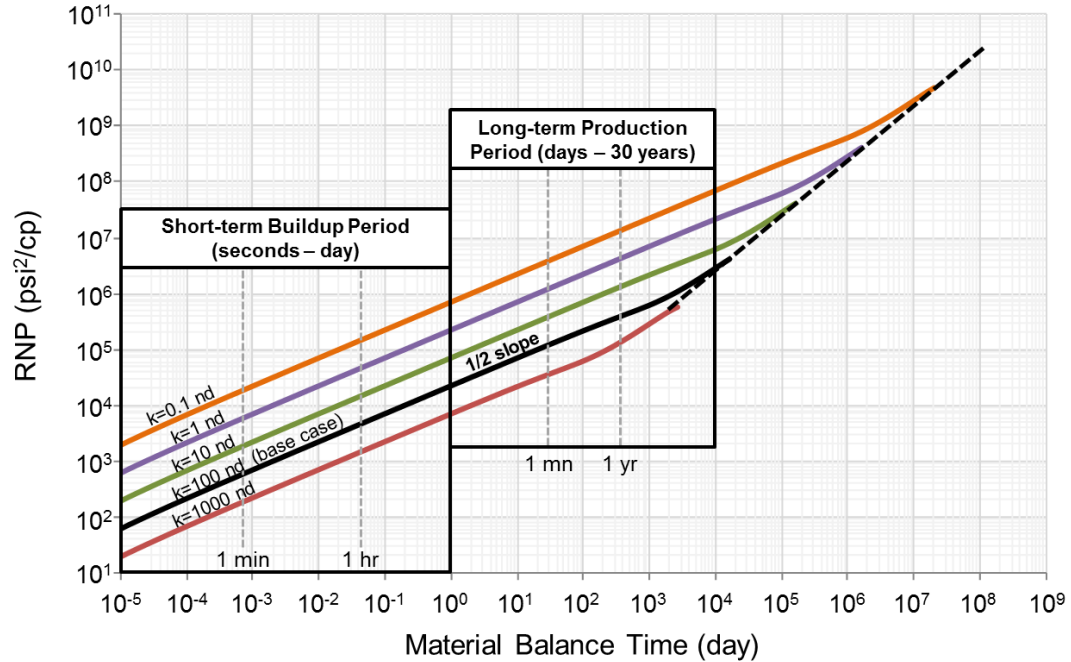


Figure 4.8: Horn River shale permeability sensitivity results

Sensitivity runs indicate that when permeability is as less as 1 nd, no PPSS boundary effect can be seen for the entire well life. Even when permeability is higher, i.e. 10 nd (10^{-5} md), it still take more than 10 years before well can see PPSS boundary effect. On the other hand, when permeability is 1000 nd (0.001 md), the PPSS boundary is expected to be observed at about 6 months.

The effect of formation permeability has been shown. However, the actual data is exhibiting a 1/4 slope. Therefore, the next parameter to be investigated is C_{fD} .

4.2.2 Dimensionless Hydraulic Fracture conductivity (C_{fD})

Hydraulic fracture conductivity is varied to find the expected value that allows a 1/4 slope to be seen in long term production data. The C_{fD} was varied from 0.5 to infinite fracture conductivity (IFC). The results are shown in Figure 4.9.

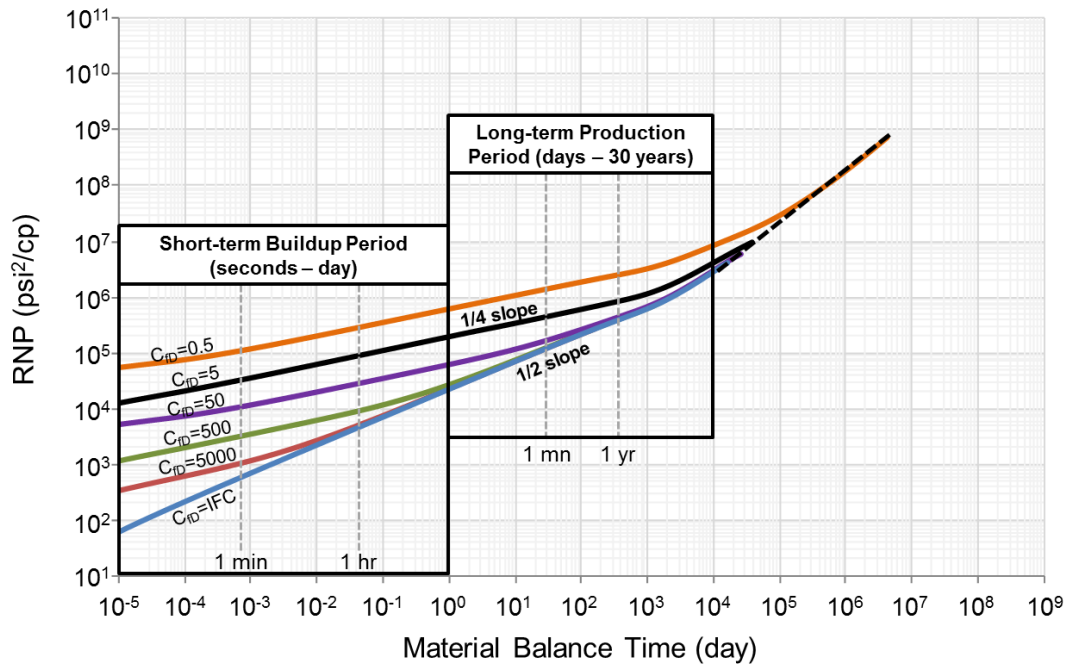


Figure 4.9: Horn River shale hydraulic fracture conductivity sensitivity results

The results indicate that only 1/4 slope will be observed during the buildup test period for all C_{fD} value, except when hydraulic fractures are having infinite conductivity. For the long term production data, C_{fD} must be smaller than 500 if order for the 1/4 slope to be observed in a production data practical window. Anyway, we have seen earlier that a 1/4 slope trend of the Horn River well could last up to 1 year. As a result, the expected value of C_{fD} for the groups of wells using in this study should be

approximately 5. Therefore, this C_{fD} will be used as base case for the MTFHW drilled and completed for the Horn River shale. Figure 4.10 shows the base case log-log diagnostic with finite hydraulic fracture conductivity. Note that the difference between Figure 4.9 and 4.10 is only C_{fD} which change the slope trend from a half slope formation linear into quarter slope formation to hydraulic fractures bilinear flow regime.

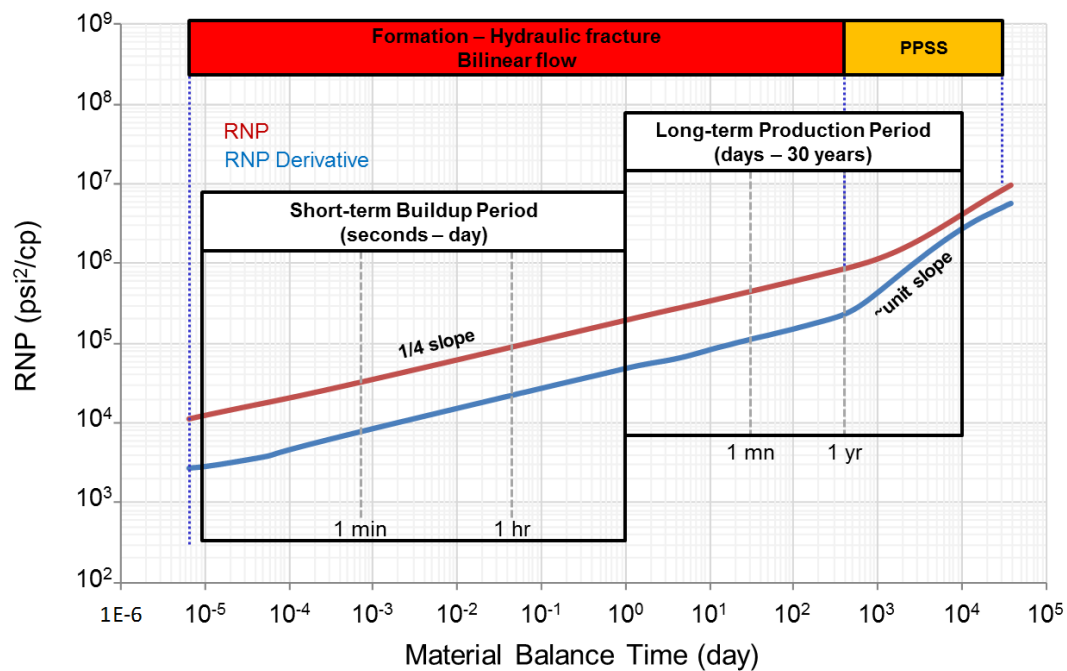


Figure 4.10: Log-log diagnostic plot based on base case parameters of Horn River shale with finite C_{fD}

4.2.3 Hydraulic fracture half-length (x_F)

Figure 4.11 shows the results of sensitivity runs on various hydraulic fracture half-lengths (x_F) ranging from 55 ft to 880 ft (average well spacing). It can be seen that x_F does not have any effect on the shape or slope of the RNP plots. It only affects the

level of RNP. Therefore, the same flow regimes as illustrated earlier on the base case will also be observed for all value of x_F .

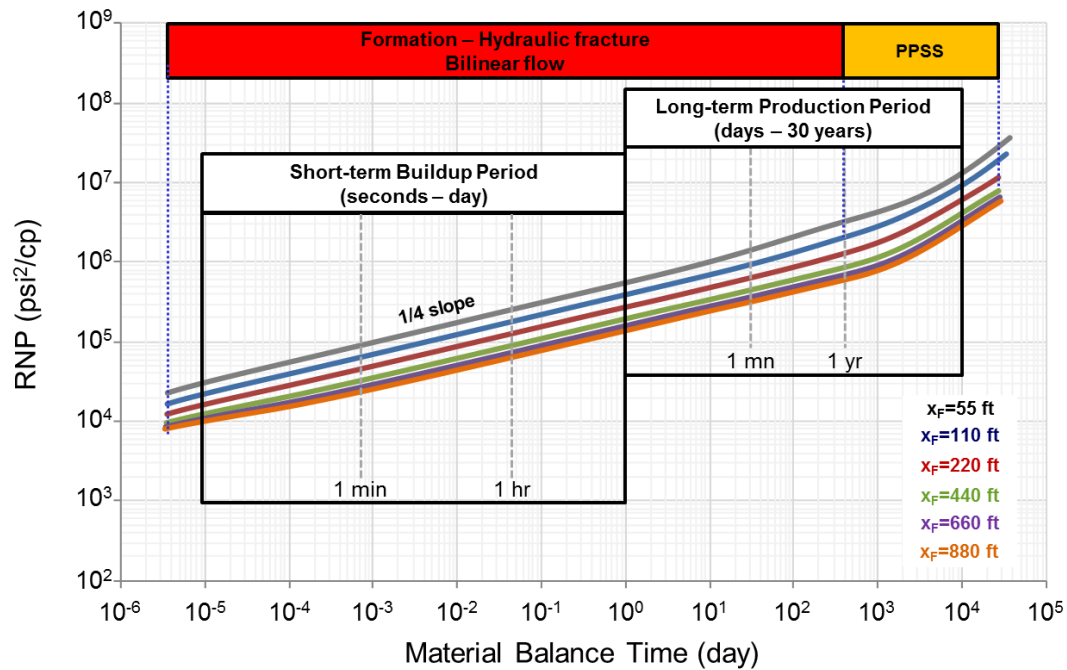


Figure 4.11: Horn River shale hydraulic fracture half-length sensitivity results

4.2.4 Hydraulic fracture spacing (x_s)

Figure 4.12 shows the results of hydraulic fracture spacing (or number of hydraulic fractures, n_F).

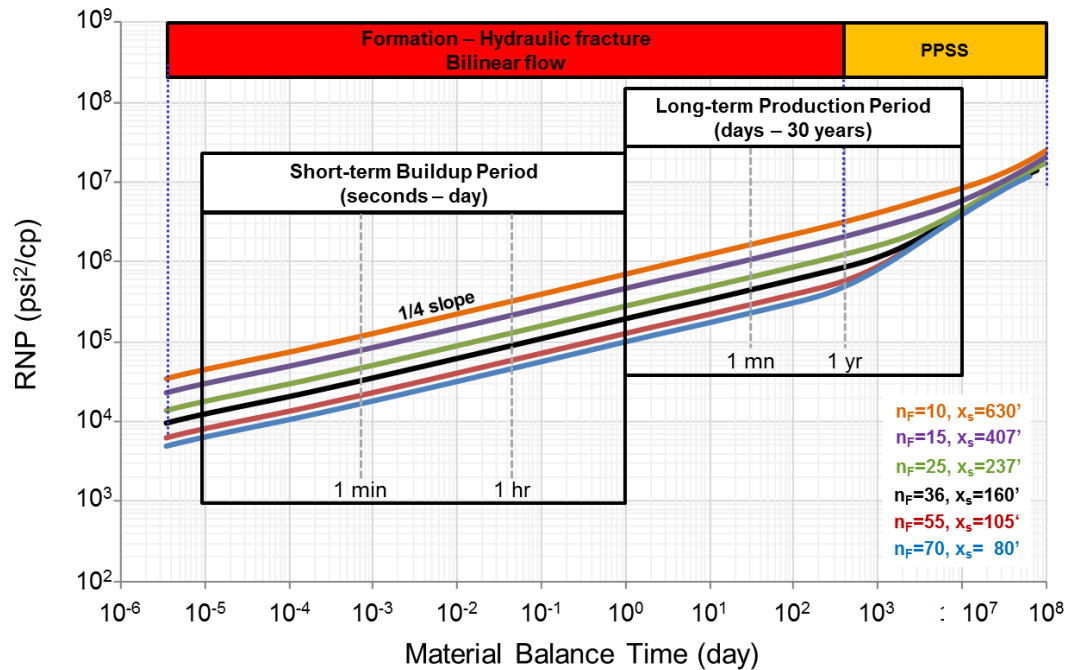


Figure 4.12: Horn River shale hydraulic fracture spacing sensitivity results

As illustrated in Chapter III, x_s and n_F do not have effect on the shape or slope of the RNP and RNP' plots. Therefore, the same characteristic as the permeability sensitivity is also seen here, i.e., only 1/2 slope fracture linear flow will be seen in the BU timeframe, while both 1/2 slope and almost unit slope PPSS flow regime will be seen during long term production period. Anyway, n_F is important because it indicates whether the SRV will be produced within practical timeframe or not. Figure 4.12 indicates that when fracture spacing is larger than 407 ft, PPSS boundary could not be observed for the entire well life of 30 years. Therefore, it also implies that the minimum number of fracture should be 15, unless the SRV will not be produced completely and there will be gas left unproduced, or be produced at impractical long time. The results also indicate that the current n_F of 36 is quite optimum. Anyway, production can still be

accelerated by increasing n_F , which will reduce x_s , but incremental gain by doing this should be assessed first to see whether the additional volume gain can justify economic of adding more hydraulic fractures or not.

In the next section, the dual porosity model will be used to investigate if the $1/4$ slope seen on the field data can be modeled with the presence of natural fractures or reopened fracture network or not.

4.3 Sensitivity studies using the dual porosity model

In the previous section, a $1/4$ slope trend has been characterized as a result of low hydraulic fracture conductivity. In this section we show that it is also possible that the $1/4$ slope is actually a result of either pre-existing natural fractures or fracture network complexity, or both. This section will investigate this possibility by running sensitivity analysis on the inter-porosity flow coefficient (λ) and the storativity ratio (ω).

As mentioned earlier, there are two options available in transient dual porosity model, i.e. slab or sphere. In the case of Horn River shale, the system is more suitable to the dual porosity transient sphere model based on reports of pre-existing natural fractures by Reynolds and Munn, 2010. In any case, Figure 4.13 shows that the slab and sphere transient dual porosity models give almost identical RNP and RNP derivative results. However, the dual porosity transient sphere model will be used to investigate the Horn River shale in order to follow the model description.

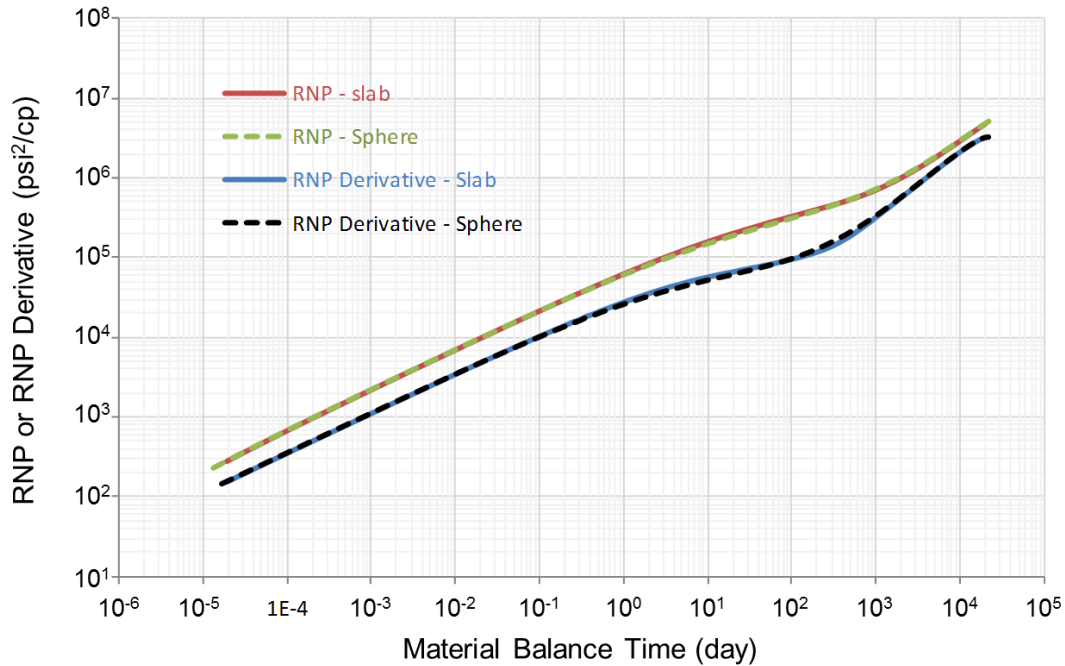


Figure 4.13: Dual porosity transient slab versus sphere model comparison

4.3.1 Interporosity flow coefficient (λ)

Figure 4.14 shows the sensitivity analysis results on the value of λ using base case parameters defined earlier, assuming an arbitrary ω value of 0.1. The results indicate that λ of 10^{-4} should be expected to be base case value because it can give a 1/4 slope to last until approximately 1 year which is the same as what we have seen in the Horn River field data. Note that a 1/4 slope trend shown in Figure 4.14 does not begin from the first day of long term production practical time window as shown in the field data. Therefore, it also indicates that ω for the Horn River shale should be smaller than 0.1 used in this figure because ω controls the duration of the 1/4 slope transition in the dual porosity model while λ defines the end of transition period.

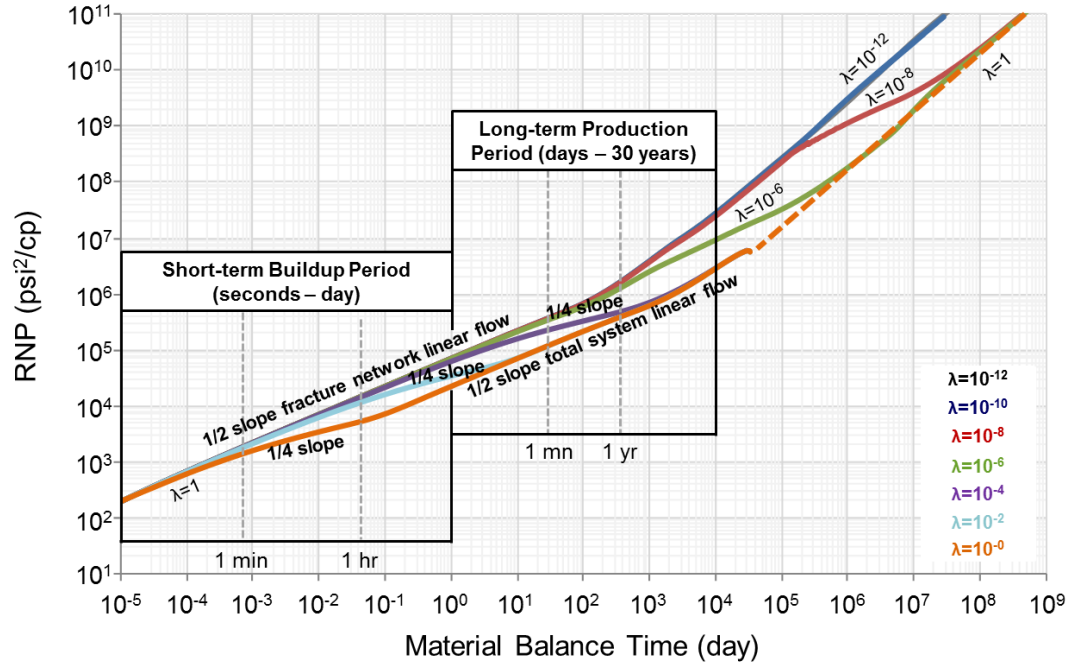


Figure 4.14: Horn River shale interporosity flow coefficient (λ) sensitivity results

4.3.2 Storativity ratio (ω)

First, recall again the definition of ω which is defined as the ratio between fracture storativity to the total system storativity and can be shown as:

$$\omega = \frac{(\phi V c_t)_f}{(\phi V c_t)_f + (\phi V c_t)_{ma}} = \frac{(\phi V c_t)_f}{(\phi V c_t)_t} \quad \dots(3.1)$$

Based on the claims in the literature of the Horn River shale as mentioned earlier, the opening-mode natural fractures are expected to presence. Therefore, the fractures flow behaviors which are observed in the field data is probably represented by these microfractures. In this case, the fracture volume that contributes to the value of storativity ratio will be mainly from the natural fractures, and the ω would not relate directly to the volume of injection fluid injected during fracturing treatment. Hence, the

ω expected to see in the Horn River shale data matching should be higher than the ω derived from injected volume (ω_{inj}). Note that if the matched ω is higher than the ω calculated from injection volume, it could suggest the presence of microfractures which provides additional fracture volume and thus give higher ω . However, it will be inconclusive if the matched ω is seen smaller than the ω_{inj} .

The typical ω_{inj} estimated from the average injection volume for the Horn River shale well is shown in Figure 4.15.

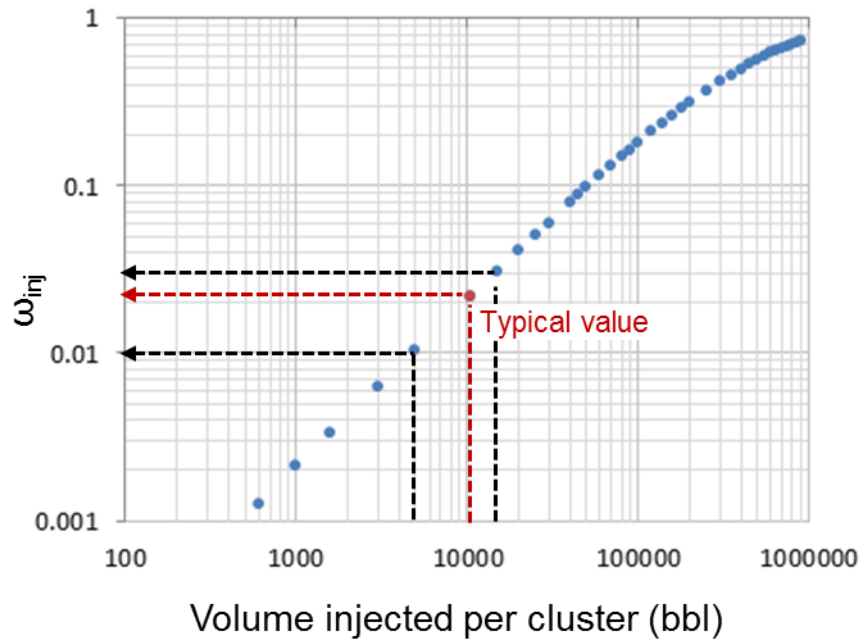


Figure 4.15: Typical ω value for Horn River shale based on injection volume

Note that the injection volume from 16 wells used in this study range from 6,000 to 15,000 bbl/cluster, with 10,200 bbl/cluster on averages. Therefore, the expected range of ω_{inj} for the Horn River shale is from 0.01 to 0.03. Note that this result also agrees with

the observation we have made previously when performing sensitivity on the λ that ω should be smaller than 0.1. This range of the ω_{inj} will be used to cross-check with the matched value obtained in the subsequent section of this chapter.

Figure 4.16 illustrates the results of sensitivity run on the value of ω ranging from 0.001 to 1.0 (homogeneous).

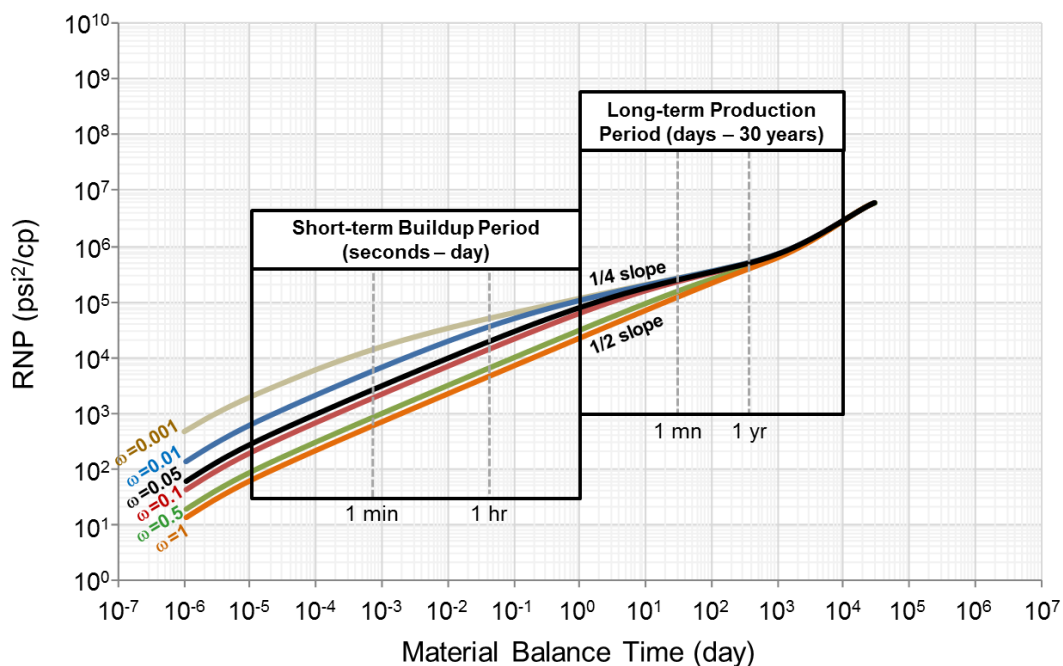


Figure 4.16: Horn River shale storativity ratio (ω) sensitivity results

The results indicate the maximum expected value of ω to be about 0.05 which will give the 1/4 slope to begin at about 5 days as seen on the field data. Note that there is no earlier data available to help confirming the value of ω because there is no short term buildup test with high data sampling frequency available in our dataset. Anyway,

this sensitivity run can help to narrow down the possible range of ω which can facilitate the final effort to match the observed data with a global model.

4.4 Model matches with Horn River well field data

In this section, one well is selected to represent behavior of MTFHW producing from the Horn River shale. First, the raw data will be reviewed to see overall quality of the data. Then a base case model input will be summarized before performing model matching using the homogeneous model and the dual porosity model with various flow regimes. An apparent meaning for each of the matches will be provided. Finally, the conclusion will be made to which model and flow regime should best represent the behavior of the Horn River shale.

4.4.1 Data diagnosis

One well from 16 wells from the Horn River shale dataset is selected. Available data covers a period of almost two years. The well was shut-in two times, once for about 4 weeks and the other time for only 2 weeks. Production and pressure history plots for the selected Horn River well are shown in Figure 4.17.

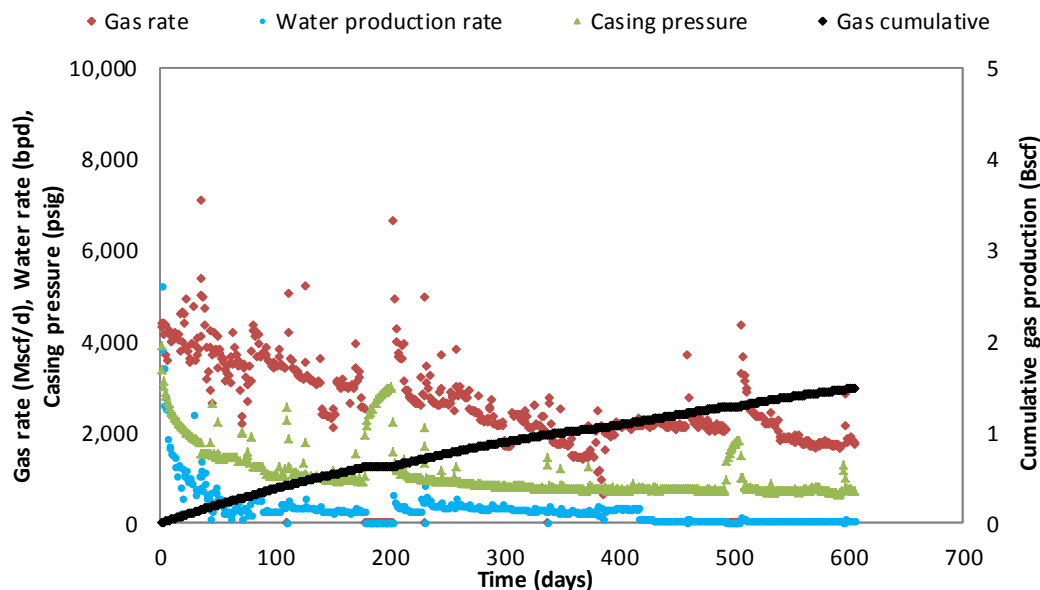


Figure 4.17: Pressure and production history of the Horn River well

From Figure 4.17, it should be noted that several changes in the trend of gas rate can be observed. One occurs at around 75 days where gas rate suddenly increased. Another one is the very high production rate right after the first build-up at about 200 days, to a nearly constant-rate trend starting at approximately 380 days. Although this increase in apparent well productivity may be related to a decrease in water production which can be observed around that time, the casing pressure does not agree with this as it always shows a relatively constant-pressure trend. Finally, very high rate is again seen after the second shut in at about 500 days. Lack of information explaining this behavior causes difficulty in modeling since these behaviors may not be captured properly with a single phase flow model.

Rate-normalized pressure (RNP) and pressure derivative (RNP') log-log diagnostic plots are shown in Figure 4.18.

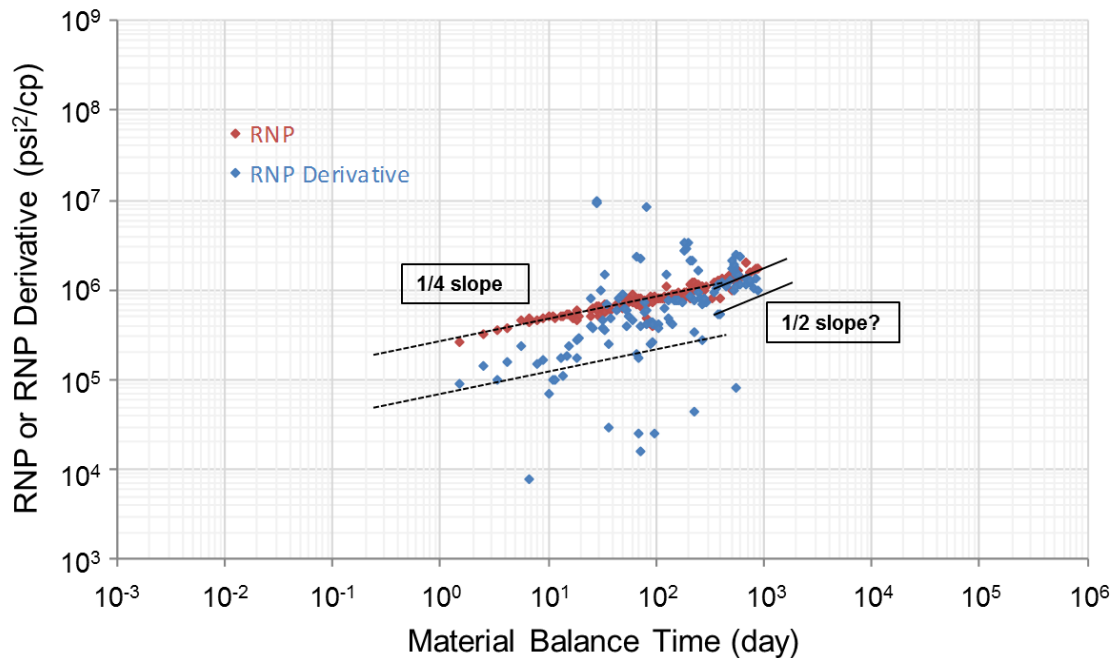


Figure 4.18: Long term production RNP and RNP derivative log-log plots for a Horn River shale well

The RNP data is quite smooth with potential quarter and half slope trends while the RNP' plot seems scattered and does not reveal any obvious trend. As a result, the RNP will be used as first priority for the matching, while the RNP' will only be used as supportive evidence.

Two pressure build-up periods are plotted in Figure 4.19. The obvious quarter slope trend can be seen only on the first build-up while the second build-up data shows a slightly higher than 1/4 slope trend that might indicate a transition from bilinear flow to linear flow. Moreover, it is interesting that the overall pressure trend is shifted to a lower level which may indicate increasing conductivity with time. This will be investigated further in this chapter.

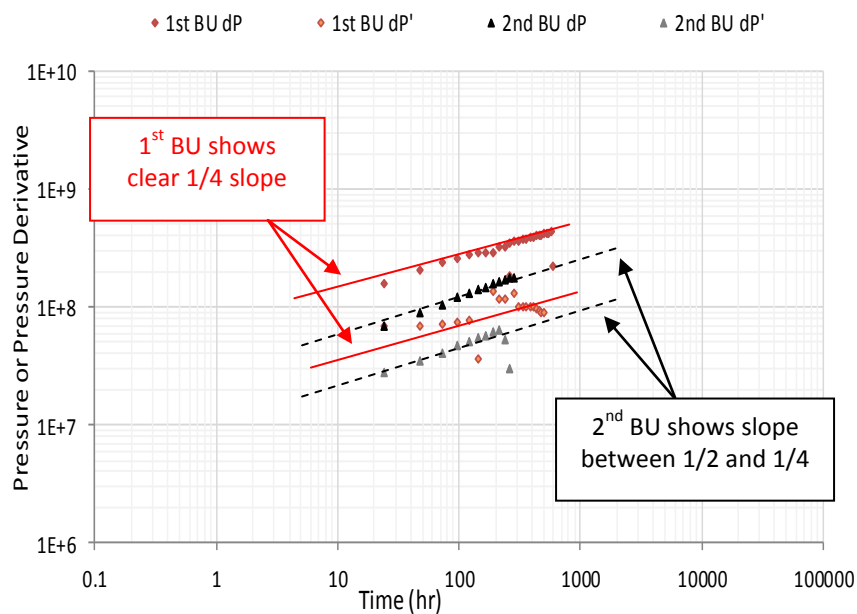


Figure 4.19: Pressure and pressure derivative for the two build-up periods for Horn River well

4.4.2 Model inputs

All input parameters used in this model study are summarized in **Table 4.2**. Note that these parameters are used for homogeneous and dual porosity model matching.

Table 4.2: Horn River model input parameters

Parameter	Symbol	Value	Unit
Well & Wellbore parameters			
Wellbore radius	r_w	0.354	ft
Horizontal well length	L_w	6515	ft
Vertical distance to lower boundary	z_w	180	ft
Number of hydraulic fractures	n_F	39	-
Hydraulic fractures half-length	x_F	440	ft
Hydraulic fracture spacing	x_s	171	ft
Fracture angle		90	°
Formation parameters			
Formation thickness	h	360	ft
Porosity	ϕ	0.052	fraction
Initial pressure at formation depth	p_i	5455	psia
Initial pressure converted to surface	$p_{i,s}$	4452	psia
Formation temperature	T	141	°F
Rocks and fluids properties			
Gas saturation	s_g	0.75	fraction
Water saturation	s_w	0.25	fraction
Gas specific gravity	γ_g	0.69	fraction
Initial gas compressibility	c_g	1.84E-04	1/psi
Initial water compressibility	c_w	5.34E-06	1/psi
Initial rock compressibility	c_f	5.00E-06	1/psi
Initial total compressibility	c_t	1.44E-04	1/psi
Gas viscosity	μ_g	0.02335	cp

Figure 4.20 illustrates the well geometry and boundary dimensions for all matching in the following sections. While the sensitivity analysis indicated the possibility to match the data using fracture half-length as short as 170 ft, we assume effectively fully penetrating hydraulic fractures in this section in order to focus mainly on comparisons between homogeneous and dual porosity model implications.

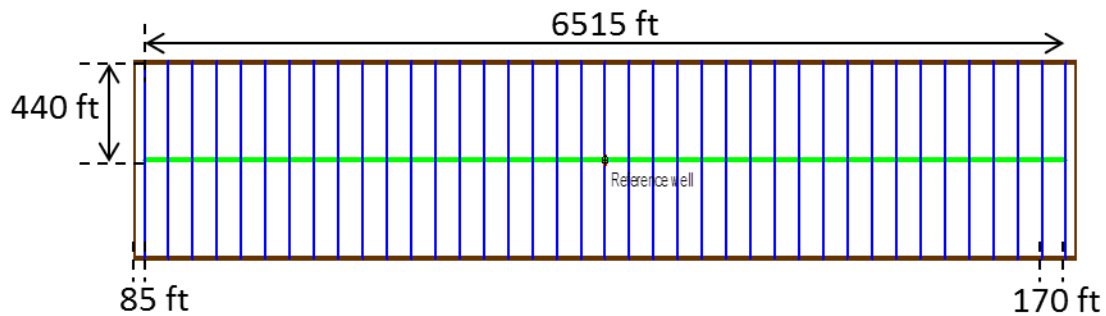


Figure 4.20: Well geometry and boundary dimension for Horn River well

4.4.3 Homogeneous model matching

First, the observed data are matched using the single porosity or homogeneous model without the presence of reopened fracture network as illustrated in Chapter II and Appendix A. Since a quarter-slope trend is observed in the RNP and in pressure buildup transients, the finite conductivity hydraulic fracture model is used. The match with a homogeneous model gives matrix permeability of 19 md with hydraulic fracture conductivity of 0.30 md-ft, which results in dimensionless fracture conductivity of 36. The model matches on RNP and derivative plots as well as on Cartesian plots are shown in Figure 4.21 to 4.23. The moderate fracture conductivity results in a flow transition between the bilinear and pseudosteady state flow that nearly reaches the $1/2$ slope trend characteristic of linear flow for material balance time between 100 and 1000 days. The behavior of the second pressure buildup transient also reflects this transition.

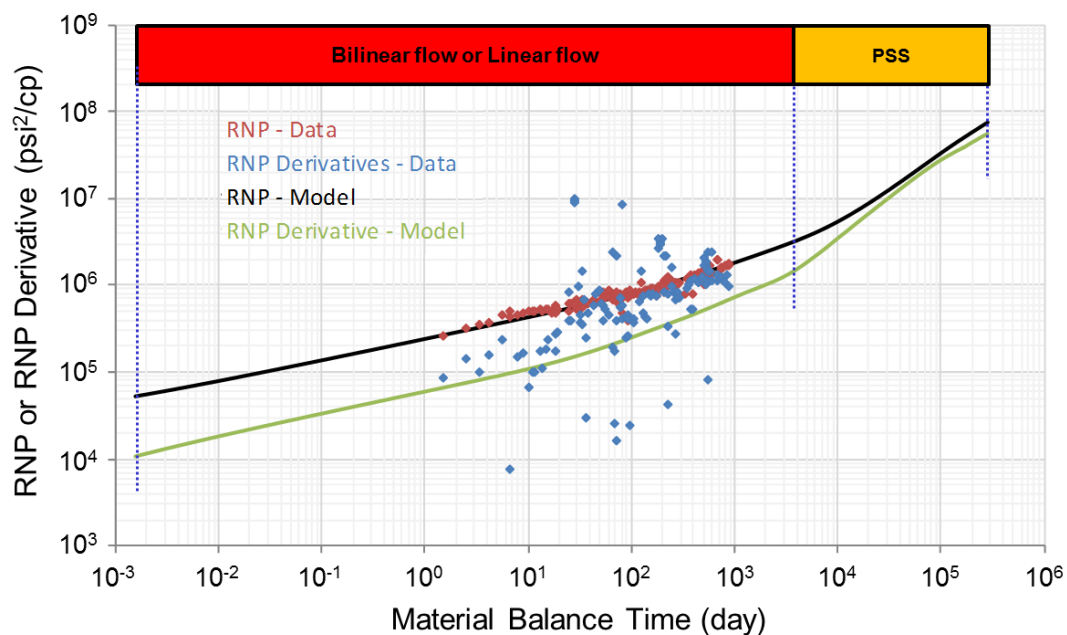


Figure 4.21: Log-log RNP and RNP' plots showing field data and homogeneous model matching comparison ($k = 19$ nd, $F_C = 0.30$ md-ft)

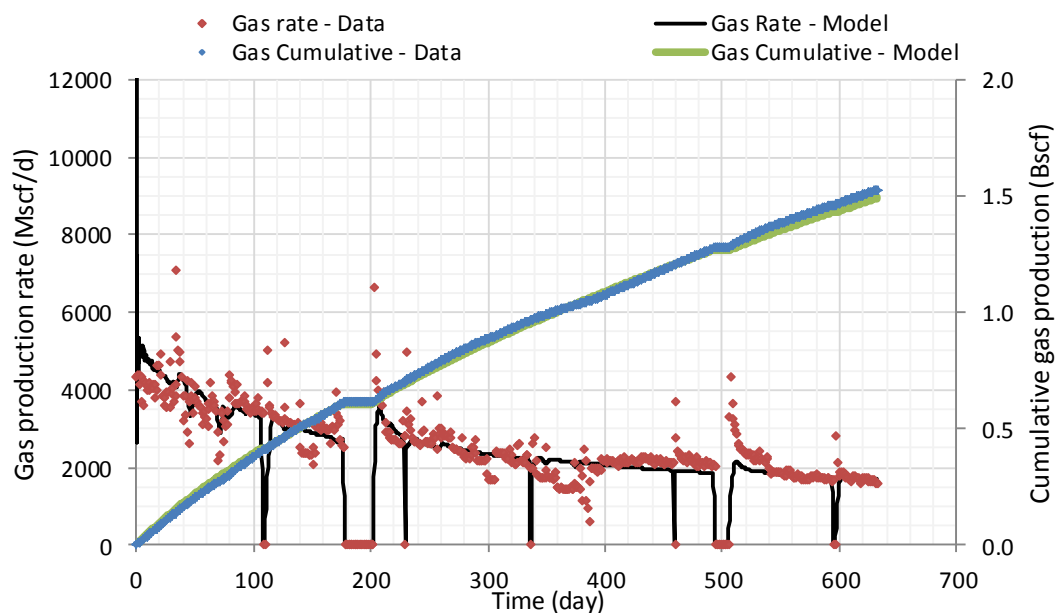


Figure 4.22: Production and cumulative production plots showing field data and homogeneous model matching comparison ($k=19$ nd, $F_C=0.30$ md-ft)

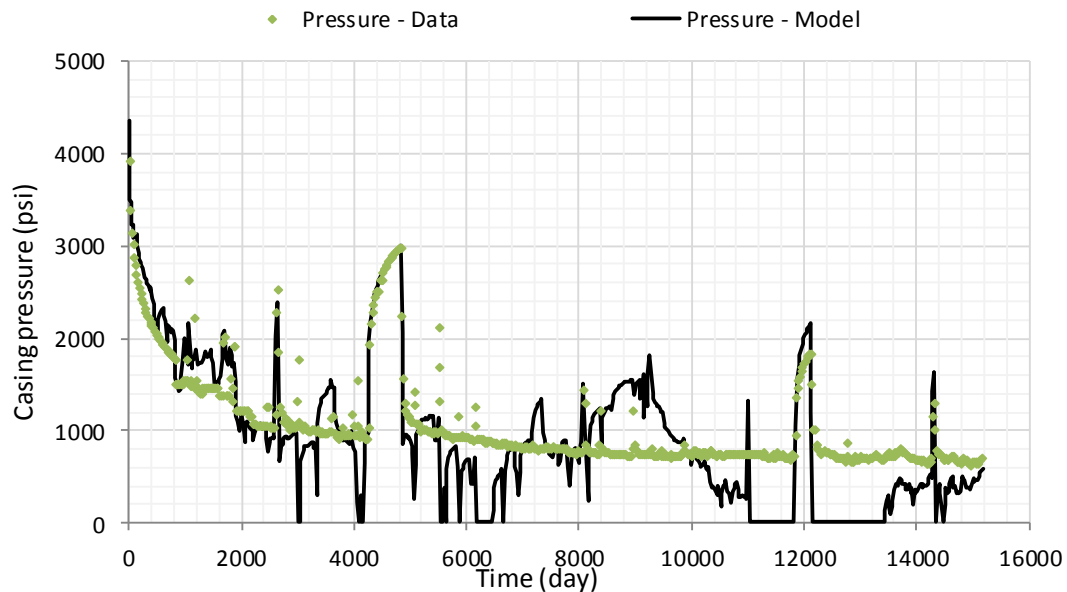


Figure 4.23: Casing pressure plots showing field data and homogeneous model matching comparison ($k = 19$ nd, $F_C = 0.30$ md-ft)

The results indicate that homogeneous model can match the observed rate data very well. However, casing pressure can be matched quite well only during the period before and slightly after the first build-up period. Apart from that, the matching accuracy is deteriorated because of the changing productivity trend revealed by the second BU.

Two pressure build-up periods are also analyzed to confirm the matches. Figure 4.24 and 4.25 show the results for the first and second build-up, respectively. As expected earlier during data diagnostic process, it is found that a higher hydraulic fracture conductivity of 1.30 md-ft must be used instead of 0.30 md-ft in order to match the second build-up, but matrix permeability was also decreased slightly from 19 nd to 16 nd. It should be noted that in this particular field case example, changing only hydraulic fracture conductivity while using the same permeability value cannot match

the two buildups. A good match can be achieved only when both the permeability and hydraulic fracture conductivity are changed together.

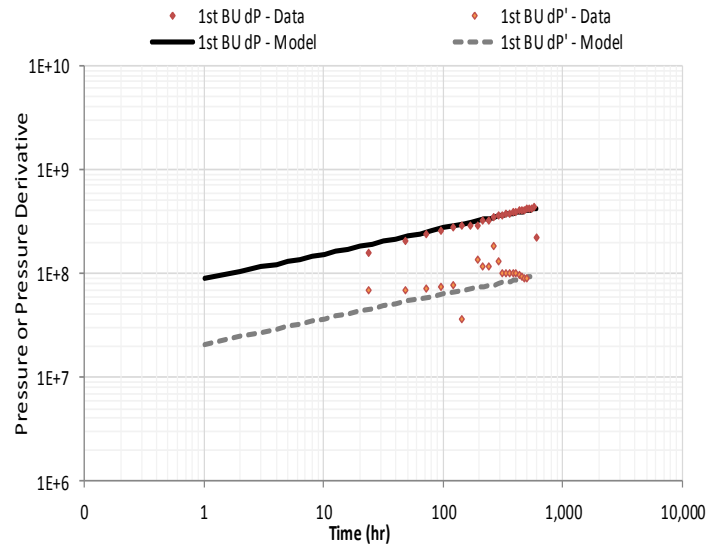


Figure 4.24: Pressure and pressure derivative showing field data and homogeneous model matching comparison for the 1st buildup ($k = 19$ nd, $F_C = 0.30$ md-ft)

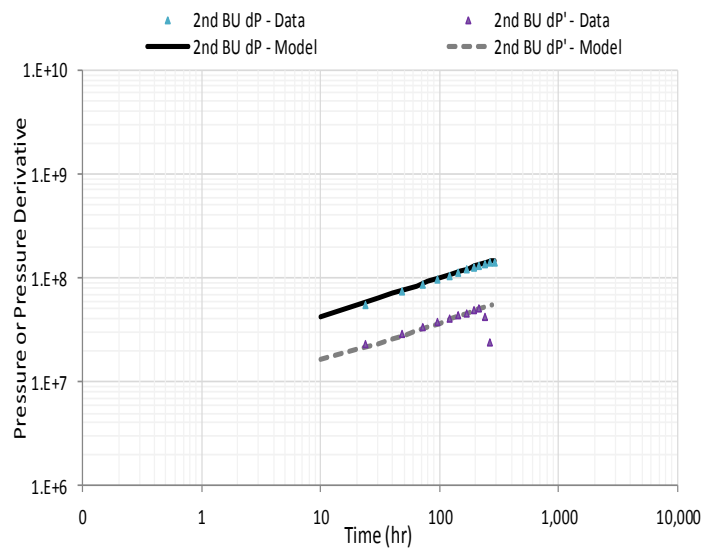


Figure 4.25: Pressure and pressure derivative showing field data and homogeneous model matching comparison for the 2nd buildup ($k = 16$ nd, $F_C = 1.30$ md-ft)

Though the changes of hydraulic fracture conductivity may give a good match for the two build-up periods, this cannot seem to explain the abrupt changes of production rate observed at around 380 days. This is because the changing of conductivity should show a gradual change which is not agreed with the observed behavior.

4.4.4 Dual porosity model matching

To investigate the evidence of natural fractures, the dual porosity model is used to match the observed data. Since a 1/4 slope behavior is observed on log-log plots, there are three possibilities resulting from different sequences of flow regimes illustrated in Appendices A and B: fracture network to hydraulic fracture bilinear flow, total system to hydraulic fractures bilinear flow, and matrix to fracture network bilinear flow.

4.4.4.1 Fracture Network to Hydraulic Fracture Bilinear Flow (FN-HF)

This flow regime is a combination of the hydraulic fracture linear flow and fracture network linear flow into the hydraulic fracture. The model match indicates bulk fracture permeability of 36 md with hydraulic fracture conductivity of 0.30 md-ft. The storativity ratio (ω) and interporosity flow coefficient (λ) are found to be 0.50 and $1.00\text{E-}8$, respectively. The match results are plotted in the pressure and pressure derivative plots as well as the Cartesian plots as shown in Figure 4.26 to 4.28 to compare the observed data with the model matching.

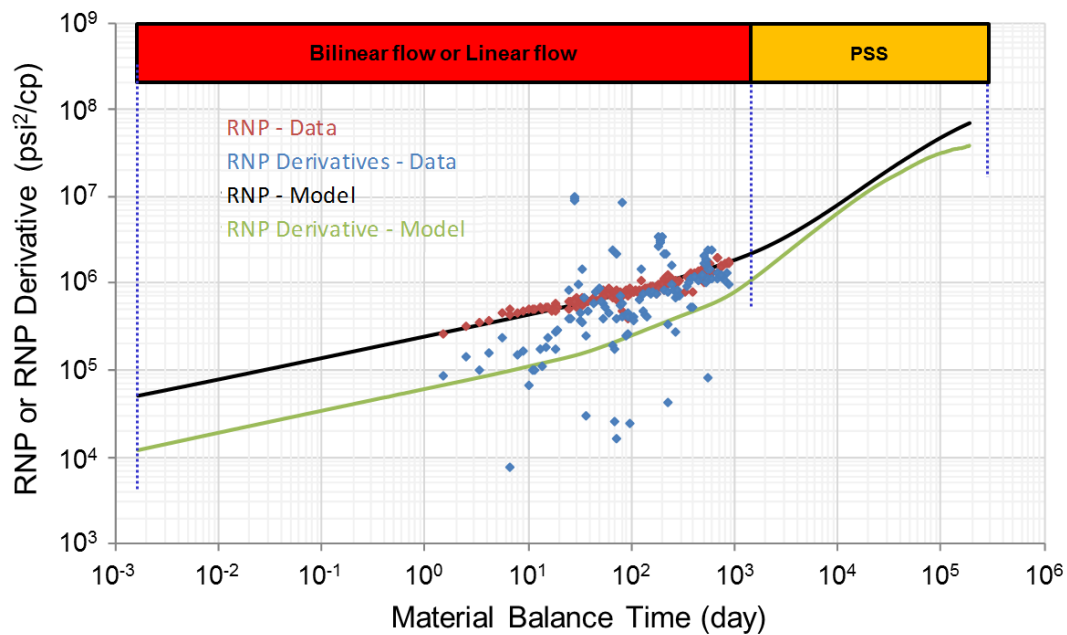


Figure 4.26: Log-log RNP and RNP' plots showing FN-HF flow regime matching ($k = 36$ nd, $F_C = 0.30$ md-ft, $\omega = 0.50$, $\lambda = 1.0\text{E-}8$)

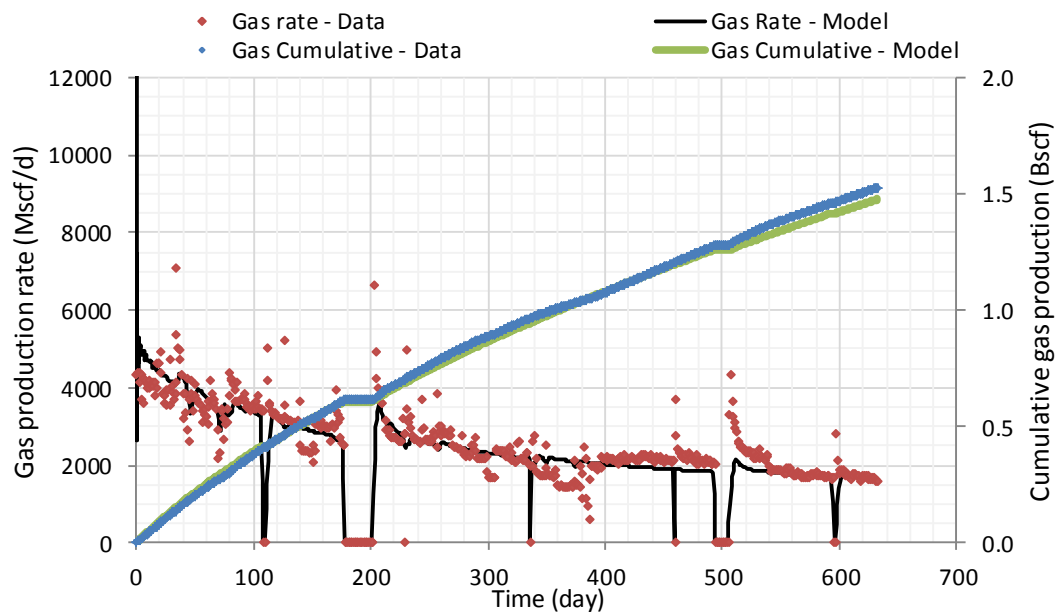


Figure 4.27: Gas rate and cumulative gas plots showing FN-HF flow regime matching ($k=36$ nd, $F_C=0.30$ md-ft, $\omega=0.50$, $\lambda=1.0\text{E-}8$)

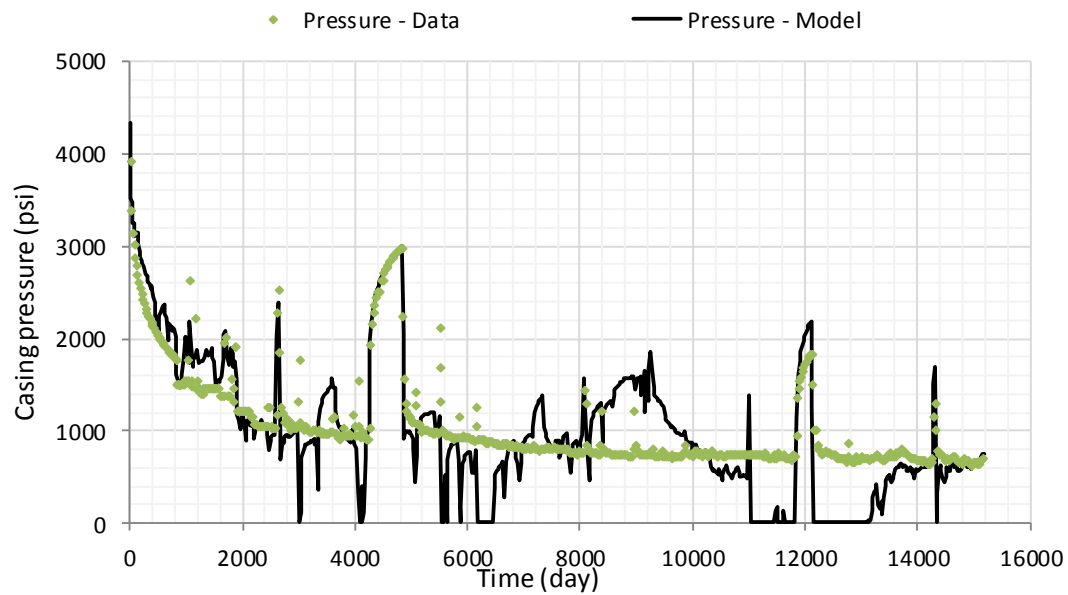


Figure 4.28: Casing pressure plots showing FN-HF flow regime matching ($k=36$ nd, $F_C = 0.30$ md-ft, $\omega = 0.50$, $\lambda = 1.0E-8$)

The low λ value indicates that permeability of the shale matrix is very low compared with the fracture network which is agreed with the definition of this flow regime where the flow inside the formation is dominated solely by the fracture network without influence from the matrix. However, the ω of 0.50 required to achieve the match seems too high to be explained by a reopened fracture network carrying half of the total gas-filled pore space.

A more reasonable explanation for these values of λ and ω would be that the fracture network represents microfractures that represent about 1/2 of the reported shale porosity. The value of λ defines a relationship between the ratio of matrix and fracture permeability values and the average dimension of a matrix volume element. For

example, Eq. 2.6 implies that a ratio of matrix to fracture permeability of 10^{-13} is consistent with a matrix volume element length of 0.01 ft for this λ value.

It is also possible that both active natural fractures and reopened fractures are present together with the indicated fracture system permeability. In this case, the active natural fractures present in the formation carry storativity and contribute to the high ω value while the reopened fractures provide additional connections among the natural fractures and transmit the fluids into the wellbore without major contribution to the ω . Nonetheless, whichever the case is happening, it implies the presence of natural fractures with large storativity, with or without the reopened fracture networks depending on how connected the active natural fractures originally are.

The two buildup periods are also analyzed as shown in Figure 4.29 and 4.30. By using the same ω and λ , the results indicate that higher hydraulic fracture conductivity of 0.52 md-ft must be used instead of 0.30 md-ft to match the second build-up, and the shale matrix permeability needs to be decreased from 36 nd to 30 nd, similar to the results obtained from homogeneous model matching.

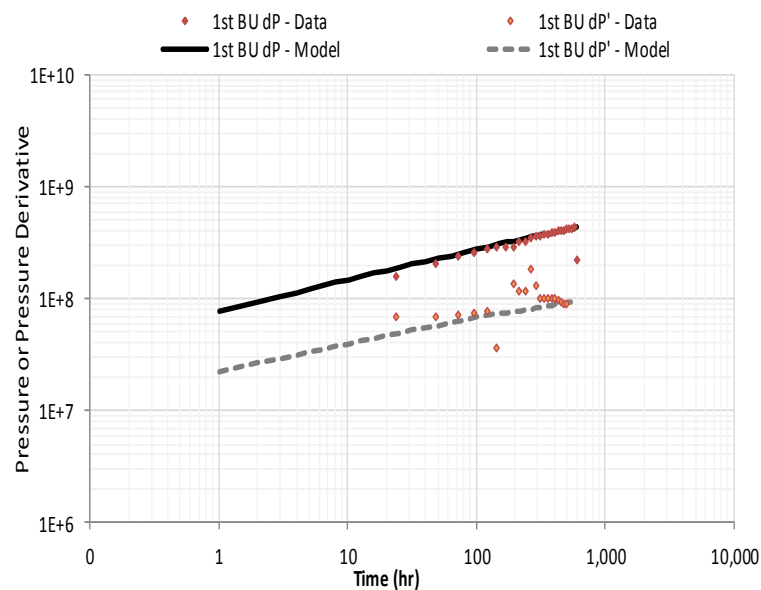


Figure 4.29: Pressure and pressure derivative FN-HF flow regime matching for the 1st buildup ($k=36$ nd, $F_C=0.30$ md-ft, $\omega=0.50$, $\lambda=1.0E-8$)

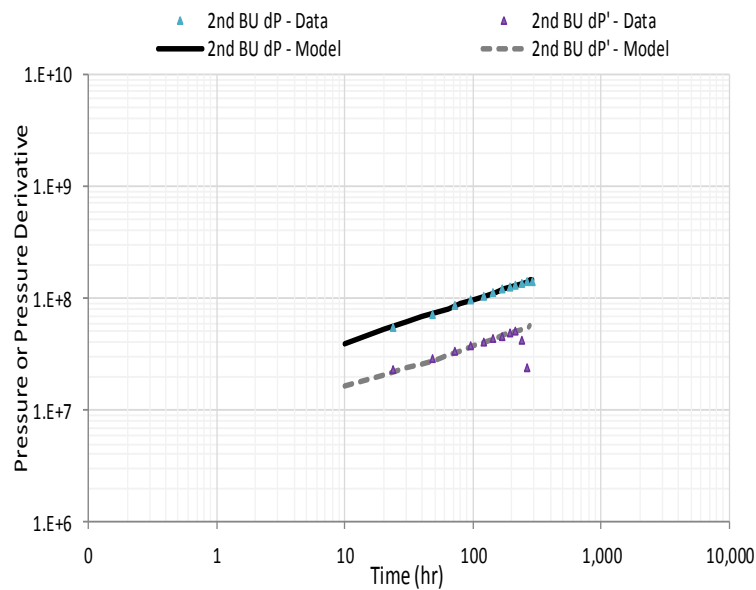


Figure 4.30: Pressure and pressure derivative FN-HF flow regime matching for the 2nd buildup ($k=30$ nd, $F_C=0.52$ md-ft, $\omega=0.50$, $\lambda=1.0E-8$)

4.4.4.2 Total System to Hydraulic Fractures Bilinear Flow (TS-HF)

This flow regime is a combination of the hydraulic fracture linear flow and the total system dominated linear flow in the formation while the fracture network linear flow had already reached its boundary stabilization. The results indicate bulk fracture permeability of 19 nd with hydraulic fracture conductivity of 0.30 md-ft which is exactly the same as the permeability and fracture conductivity used to match the homogeneous model. The interporosity flow coefficient (λ) is found to be 10 while the storativity ω has no effect on this type of flow regime. The match results are plotted in the pressure and pressure derivative plots as well as the Cartesian plots as shown in Figure 4.31 to 4.33 to compare the observed data with the model matching.

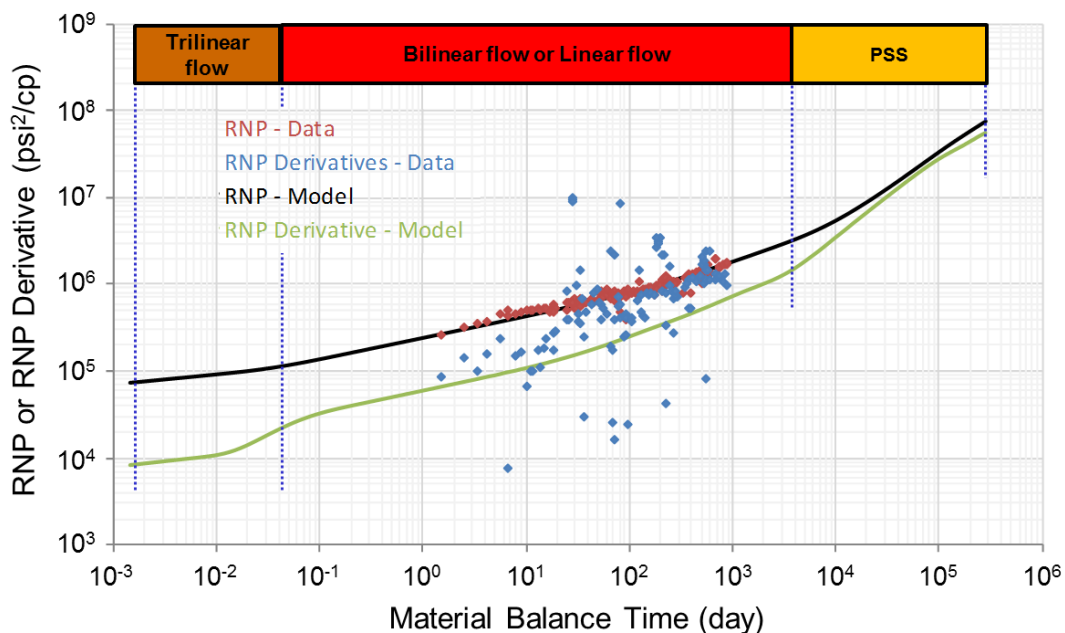


Figure 4.31: Log-log RNP and RNP' plots showing TS-HF flow regime matching ($k = 19$ nd, $F_C = 0.30$ md-ft, $\omega = 0.001$, $\lambda = 10$)

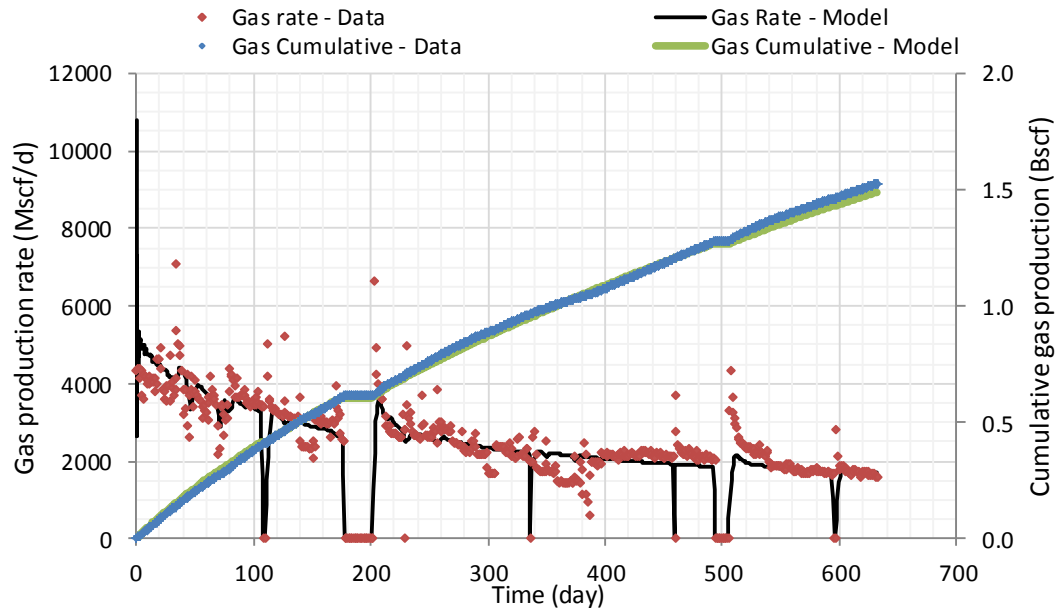


Figure 4.32: Gas rate and cumulative gas plots showing TS-HF flow regime matching ($k = 19$ nd, $F_C = 0.30$ md-ft, $\omega = 0.001$, $\lambda = 10$)

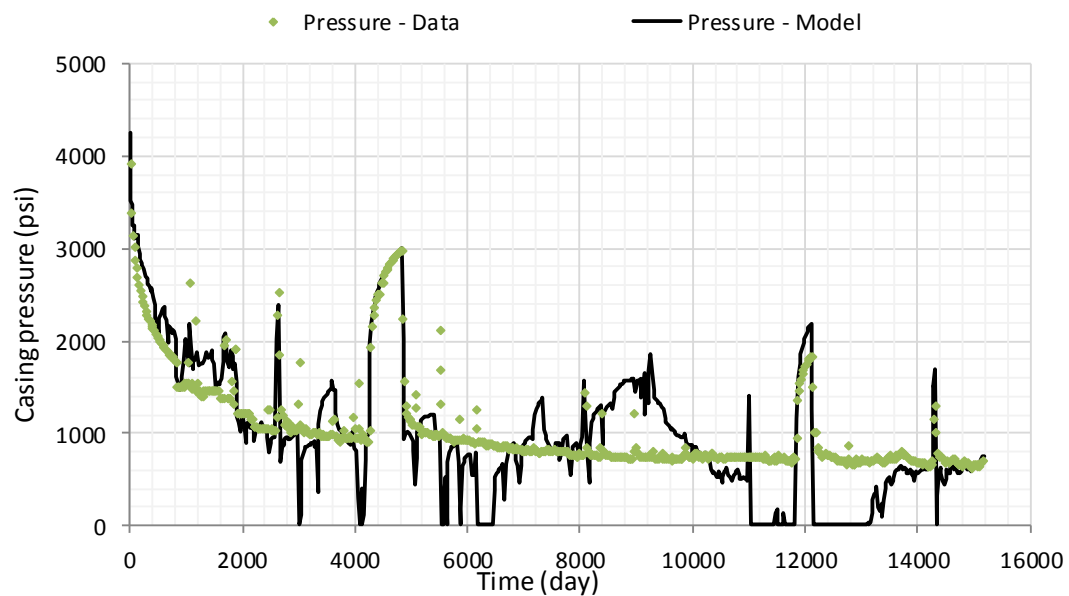


Figure 4.33: Casing pressure plots showing TS-HF flow regime matching comparison ($k = 19$ nd, $F_C = 0.30$ md-ft, $\omega = 0.001$, $\lambda = 10$)

The high λ value found for this scenario implies that flow from the shale matrix enters the fracture system so early that observed bilinear flow represents flow from the total system into the hydraulic fractures. Only earlier time transient trends like what might be revealed in a pressure buildup test with sufficiently high data rate can establish a value for ω . For the ω value of 0.001 used for the models shown in Figs. 4-31 to 4.33 trilinear flow would be seen between 0.001 and 0.01 days (~1-10 min) of material balance time. Note that the trilinear flow results from the transient bilinear flow of matrix to fracture network together with the transient flow of finite conductivity hydraulic fractures. Hence the duration of this flow regime depends on the value of ω and might disappear for much larger ω values.

Again, considering Eq. 2.6, for $\lambda = 10$, and for unit ratio of matrix to fracture permeability, the implied length for the matrix element in the dual porosity system becomes about 0.73 ft or about 9 in. Still larger spacing would imply matrix permeability that is higher than that of the fracture system, which is not the intent of the dual porosity model. Therefore, this model must be used with caution, and it may be better to consider it as effectively homogeneous.

The two buildup periods are also analyzed as shown in Figure 4.34 and 4.35.

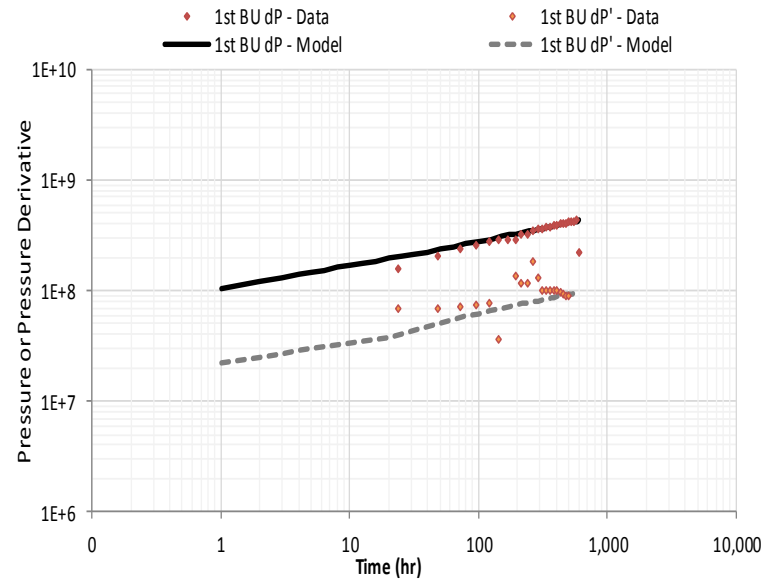


Figure 4.34: Pressure and pressure derivative showing TS-HF flow regime matching for the 1st buildup ($k=19$ nd, $F_C=0.30$ md-ft, $\omega=0.001$, $\lambda=10$)

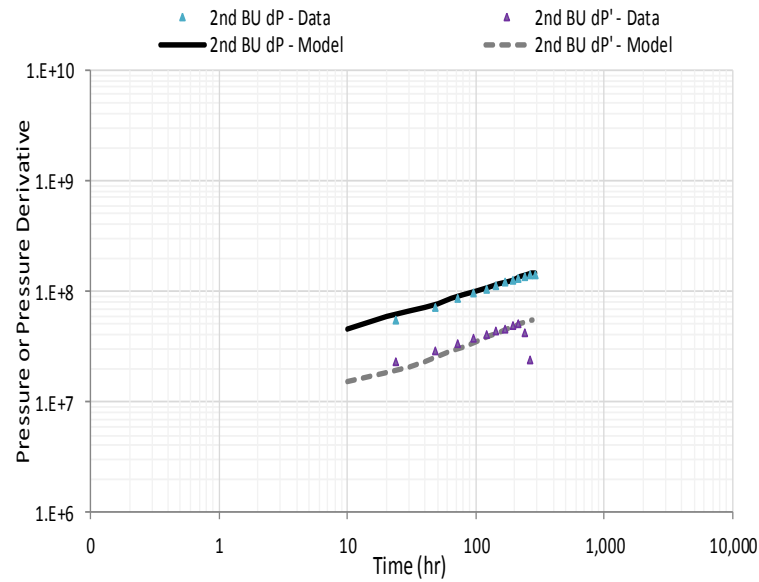


Figure 4.35: Pressure and pressure derivative showing TS-HF flow regime matching for the 2nd buildup ($k=15.8$ nd, $F_C=0.57$ md-ft, $\omega=0.001$, $\lambda=10$)

By using the same ω and λ while matching the two buildups, the results indicate that higher hydraulic fracture conductivity of 0.57 md-ft must be used instead of 0.30 md-ft to match the second build-up, and the total system permeability needs to be decreased from 19 nd to 15.8 nd which are the same behavior as observed in the fracture network to hydraulic fracture bilinear flow matching.

Note that the hydraulic fracture conductivity and the permeability are having the same effect during production or drawdown period, i.e., reducing pressure drop with increasing conductivity or permeability. However, it is found that the pressure is much more sensitive to permeability than to hydraulic fracture conductivity during the buildup period. This finding could help to narrow down the possible matching scenarios, and, hence, it is recommended that buildup period are acquired and analyzed whenever possible.

4.4.4.3 Matrix to Fracture network bilinear flow (M-FN)

This flow regime represents a combination of the fracture network linear flow and the shale matrix linear flow while the hydraulic fractures have infinite conductivity. The results indicate that bulk fracture permeability of 16 nd with infinite conductive hydraulic fractures. The interporosity flow coefficient (λ) is found to be 6E-4 with storativity ω of 0.05. Note that a potential 1/2 slope trend at early time not indicated by other models shown previously can be seen with this model. Figures 4.36 to 4.38 show the match results plotted in the RNP and derivative plots as well as the Cartesian plots of flow rate and pressure.

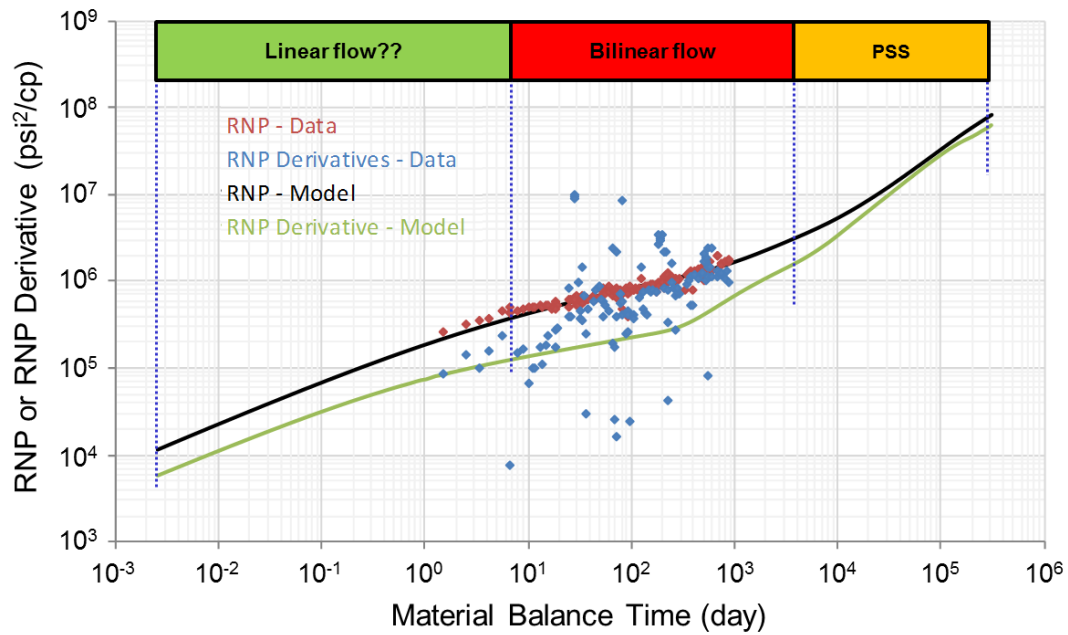


Figure 4.36: Log-log RNP and RNP' plots showing M-FN flow regime matching ($k=16$ nd, $F_C=IFC$, $\omega=0.05$, $\lambda=6E-4$)

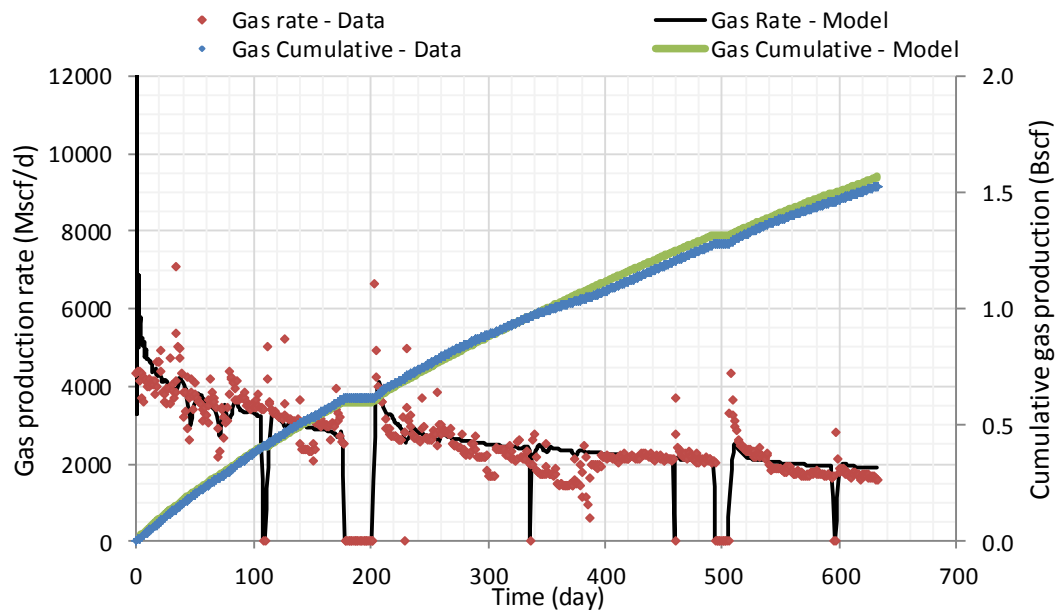


Figure 4.37: Gas rate and cumulative gas plots M-FN flow regime matching ($k=16$ nd, $F_C=IFC$, $\omega=0.05$, $\lambda=6E-4$)

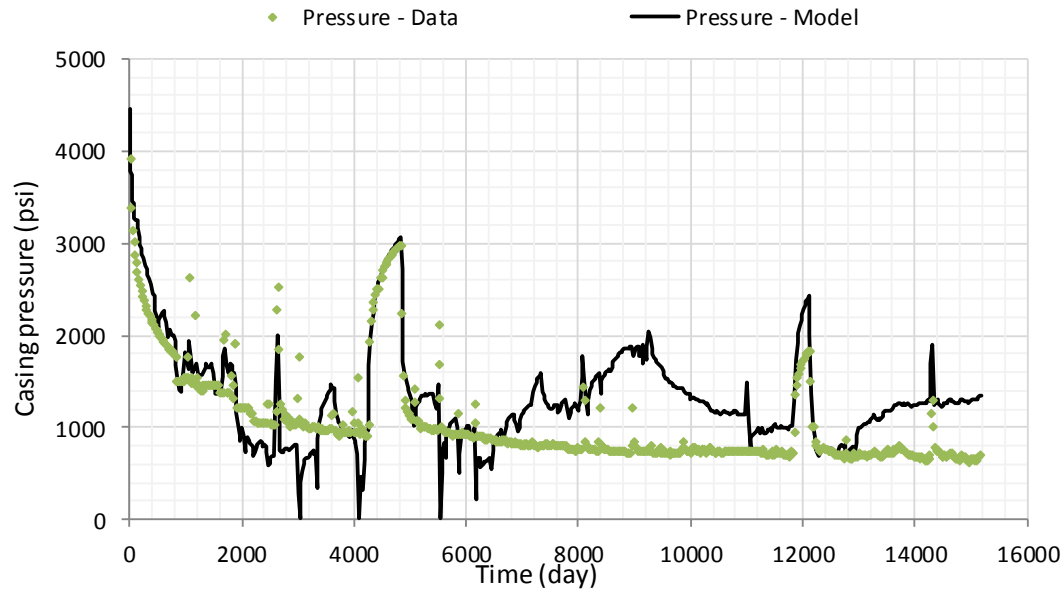


Figure 4.38: Casing pressure plots showing M-FN flow regime matching ($k=16$ nd, $F_C=IFC$, $\omega=0.05$, $\lambda=6E-4$)

The matrix-fracture network bilinear flow regime is the case where the reopened and/or natural fracture network provides the flow path to the system with minimal storativity while the shale matrix carries large storativity but having very low permeability that it may not flow without permeability enhancement from the reopened networks. The hydraulic fractures are considered as highly conductive and their behavior cannot be seen on the field data.

The value of ω corresponded to injection volume calculated by using the same type of chart as shown in Figure 3.9 but constructed with the input parameters of this well is found to be 0.019. When comparing with the matched result, it appears that the

matched ω is about 2-3 times larger than the ω_{inj} , i.e. 0.05 versus 0.019. Therefore, it implies that a pre-existing fracture network may also contribute to the value of ω .

Note that when ω is represented by both the pre-existing microfractures and the reopened fracture network, the porosity that contributes to gas in place will come from only the pre-existing microfractures which are not completely sealed and can provide storativity for gas. For example, with the ω_{inj} of 0.019 and matched ω of 0.05, this indicates that microfractures carry ~3% of total fractures volume. However, this 3% microfractures porosity should already be included in the reported shale porosity. Note that when comparing with the Barnett shale case, the microfracture contribution seems to be negligible suggesting that in that case no gas is stored in microfracture porosity.

Considering again Eq. 2.6 for the value for λ of 6E-4 and fracture permeability of 16 nd with the estimated fracture spacing of 10 ft, matrix permeability can be calculated to range from 0.2 to 0.9 nd for spherical or slab elements, respectively. This implies that matrix permeability is approximately 20 to 80 times, or less than two orders of magnitude, smaller than fracture permeability.

Analyses for the two buildup periods are shown in Figure 4.39 and 4.40.

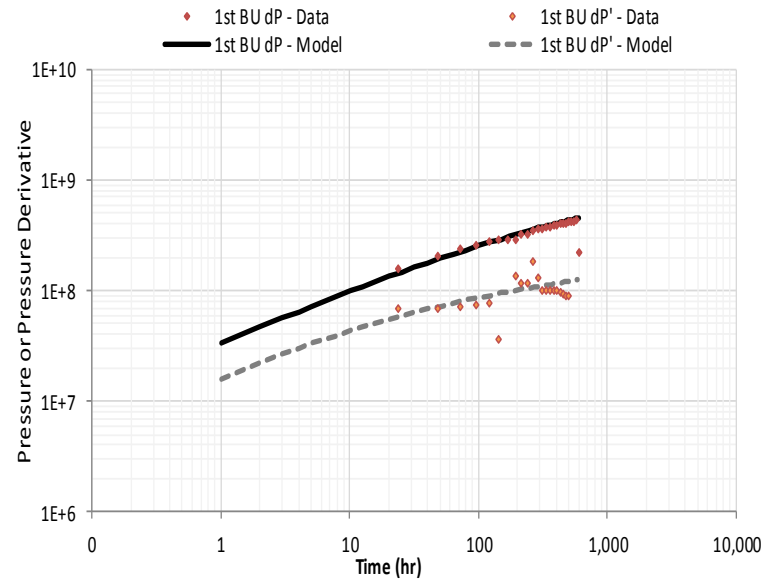


Figure 4.39: Pressure and pressure derivative showing M-FN flow regime matching for the 1st buildup ($k=16$ nd, $F_C=IFC$, $\omega=0.05$, $\lambda=6E-4$)

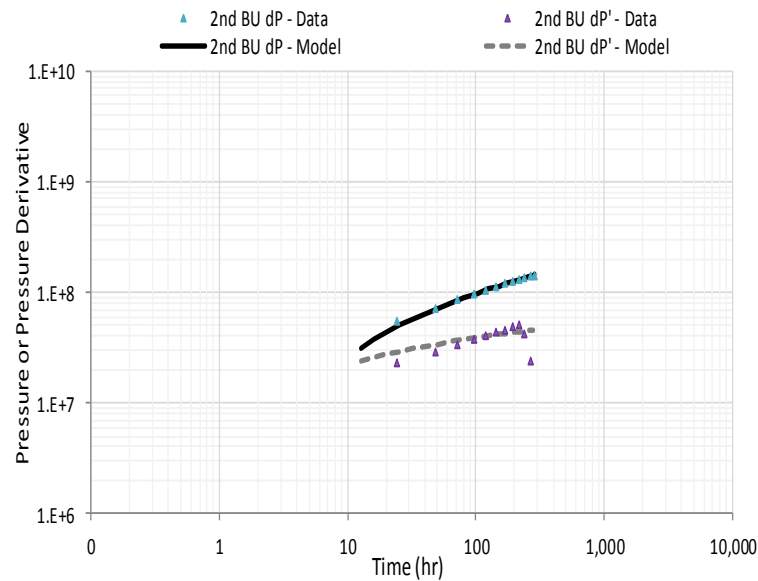


Figure 4.40: Pressure and pressure derivative showing M-FN flow regime matching for the 2nd buildup ($k=13.8$ nd, $F_C=IFC$, $\omega=0.1$, $\lambda=0.01$)

In this case, it appears that the first buildup can be matched using the same parameters as those been used in drawdown matching. However, the same λ and ω cannot be used to match the two buildups. The results indicate that higher ω of 0.1 and higher λ of 0.01 are needed to match the second build-up. The permeability also needs to be decreased from 16 nd to 13.8 nd which is the same behavior as observed in the other flow regimes matching.

4.5 Discussion

All matches for the Horn River data suggest a working permeability in a range of 10 to 40 nd, but again different models give a different meaning for this value. The detailed description and the meaning of each flow regime and parameter are discussed thoroughly in section 3.6. Therefore, this section will only discuss the behavior of the Horn River shale which is unique from those of the Barnett shale. The matching results for of the Horn River well production data analysis are summarized in Table 4.3.

Table 4.3: Horn River shale dual porosity model matching results summary

No.	Model	Flow regime	k_f (nd)	F_C (md-ft)	C_D	ω	λ
1	Homogeneous	Bilinear	19	0.30	36	-	-
2	Fracture Network to Hydraulic Fracture	Bilinear	36	0.30	19	0.5	1E-08
3	Total System to Hydraulic Fracture	Bilinear	19	0.30	36	no influence	10
4	Matrix to Fracture Network	Bilinear	16	IFC	IFC	0.05	6E-04

Figure 4.41 compares the results from all models matching on the log-log RNP and RNP derivative plots.

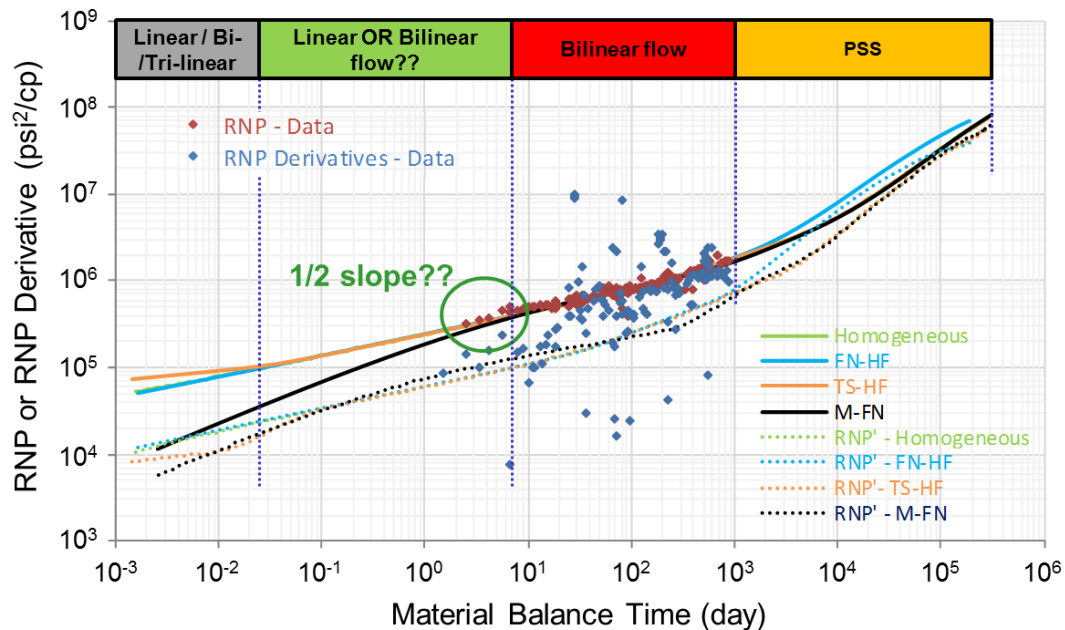


Figure 4.41: Log-log RNP and RNP' plots showing different flow regime matching comparison

All models can match the RNP response very well, but the scatter of RNP derivative reduces the confidence of matching. Only the M-FN case considers the bilinear flow as a result of shale matrix and the fractures system. Also, the early response seen as a 1/2 slope can only be captured by the dual porosity M-FN case as a result of the transient flow from reopened fracture network and/or preexisting microfractures to effectively infinite conductivity hydraulic fractures. However, this 1/2 slope trend is not very strong because it exists only less than 1 log cycle.

Because the ω value for this match is larger than ω_{inj} calculated from the average fluid injected per Horn River fracture, this may imply that pre-existing microfractures are very likely to contribute to the flow behavior in this case. The presence of the reopened fracture network, however, is inconclusive because the fracture volume making up the matched ω value could be represented by either only pre-existing microfractures or both microfractures and reopened fracture network.

For all the other models bilinear flow is related to finite conductivity hydraulic fractures and cannot be preceded by an early linear flow regime because the only possible early linear flow regime is hydraulic fracture linear flow which normally ends very early in time and would be masked by wellbore storage in an early buildup transient and would be long gone by the start of what can be seen in long term production data.

Since there is no PPSS or PSS boundary response can be observed from the Horn River well data, no confirmation of the hydraulic fractures half-length can be estimated. It is found that all model matching can match the observed data with shorter x_f , except for the FN-HF models where the volume is constraint by the value of ω .

4.6 Chapter summary

In this chapter, the flow behavior of the Horn River shale has been investigated using both homogeneous and dual porosity models. The quarter slope bilinear flow dominates the RNP trend for production data from the Horn River wells. The sensitivity runs on the time to see the end of linear flow with the average hydraulic fracture spacing show that the maximum formation permeability should be in a range of hundreds

nanodarcies because no upwards departure from the bilinear RNP trend is observed on the field data. Models matching the production data indicate permeability in the range of 20 to 40 nanodarcies when hydraulic fracture half-length is assumed to be the maximum possible value of 1/2 the horizontal well spacing.

A dual porosity model can generate a bilinear flow regime which is related only to flow from the matrix to the fracture network. For this case the matched λ value of 6E-4 agrees with the sensitivity runs.

While the Horn River shale data do not conclusively reveal evidence of opened or reopened fractures network induced by hydraulic fracturing, the dual porosity models matching the data support the presence of pre-existing microfractures and imply that a reopened fracture network is not likely to be the only source of Horn River shale productivity.

CHAPTER V

CONCLUSIONS AND RECOMMENDATIONS

The objective of this study was to confirm whether fracture complexity is evident in long term pressure and rate production data acquired from MTFHWs in Barnett and Horn River shale formations. Because homogeneous, dual porosity, and triple porosity models can match long term production data, only comparisons of the various possible models providing matches for the data can provide insight about the importance of fracture complexity to the apparent well performance.

This study used rate-normalized pressure (RNP) and its derivative to diagnose possible explanations for observed dominant flow behavior. The RNP and its derivative show a sequence of flow regimes in long term production that must be honored by any model selected to match the data. In addition, for the Horn River well, the existence of pressure buildup transients recorded when the well is shut in provided flow regimes in earlier time that what could be seen in production data. Mathematical justification for use of the RNP and its derivative as effectively equivalent to long term drawdown pressure change and derivative under constant rate production was provided.

Expected flow regime sequences in BU and RNP responses were cataloged for homogeneous, dual porosity, and triple porosity models. In all cases, flow regime sequences that have not previously been identified in the literature were added.

This study shows that the behaviors of the Barnett shale and Horn River shale are not the same. Production data from a MTFHW in the Barnett shale shows mainly only

1/2 slope behavior with possible 1/4 slope behavior in early time. In contrast, production data from Horn River shale shows mainly only 1/4 slope behavior with possible 1/2 slope behavior in early time.

Even though both homogeneous and dual porosity models can match long term production data very well, the physical meaning and descriptions of each model match are different. Comparisons among possible models can provide insight about the importance of fracture complexity to the apparent well performance.

The quarter-slope trend observed on log-log plots of the Barnett shale is likely to result from only the reopened fracture network because the matching results indicate the storativity ratio which is comparable to the injection volume derived storativity ratio (ω_{inj}).

On the other hand, because the matched ω is larger than the ω_{inj} the quarter-slope trend observed on the Horn River field data could be a result of fracture systems which could be either a combination of reopened fractures and pre-existing microfractures, or only the latter.

Models for which hydraulic fractures are the source of the quarter slope behavior seen for the Horn River shale require a moderate value for C_{fD} . However, the C_{fD} in models that match the Barnett shale data is effectively infinite, and the quarter slope behavior is seen only in very early time.

While the Barnett shale production data can be matched with a homogeneous model with effectively infinite conductivity hydraulic fractures, it is also possible to match the data with a dual porosity model that can account for fractures opened or

reopened during hydraulic fracturing like what some in the literature have called complexity. However, the evidence for this is not particularly strong, and parameters from other dual porosity models that provide a better match for the flow regimes seen in processed data are not so consistent with the complexity assumption.

For the Horn River shale, the dual porosity model with moderate shale matrix permeability and fracture volume might be more favorable because it can model the potential early $1/2$ slope which cannot be modeled by the other models. However, the evidence of this $1/2$ slope is not very obvious because it only covers a period that is shorter than 1 log cycle. Also, the scatter in RNP derivative is problematic, better RNP processing could differentiate the models.

A buildup test with high data sampling rate would be valuable for both shales because transient behavior that distinguishes some of the models occurs in earlier time than data acquired once per day can provide. For example, the value of ω for the Barnett shale and the early $1/2$ slope trend for the Horn River shale could be confirmed with a buildup test showing the response minutes or even hours after the well is shut in

The transient slab model is more suitable for the reopened fracture network while the transient sphere model is more suitable for the pre-existing microfractures. However, the two models do not give much difference on the matching results.

The importance of considering flow regime sequence rather than just individual flow regime is emphasized in Appendices A to C. It shows that when more than one flow regimes are seen, it is possible to reduce number of possible flow regime and allows more consistent model matching.

The observations about the material balance time function when it is used during linear and bilinear flow regime provided in Appendix D indicates that the conventional equation for distance of investigation might need modifications when using material balance time instead of the actual time.

REFERENCES

- Agarwal, R.G., Gardner, D.C., Kleinsteinber, S.W. et al. 1998. Analyzing Well Production Data Using Combined Type Curve and Decline Curve Analysis Concepts. Paper SPE 49222 presented at the SPE Annual Technical Conference and Exhibition, New Orleans, Louisiana, 27-30 September. doi: 10.2118/49222-ms
- Ahmadi, H.a.A., Almarzooq, A.M., and Wattenbarger, R.A. 2010. Application of Linear Flow Analysis to Shale Gas Wells - Field Cases. Paper SPE 130370 presented at the SPE Unconventional Gas Conference, Pittsburgh, Pennsylvania, USA, 23-25 February. doi: 10.2118/130370-ms
- Anderson, D.M. and Mattar, L. 2003. Material-Balance-Time During Linear and Radial Flow. Paper PETSOC 2003-201 presented at the Canadian International Petroleum Conference, Calgary, Alberta, 10-12 June. doi: 10.2118 /2003-201
- Bello, R.O. and Wattenbarger, R.A. 2009. Modelling and Analysis of Shale Gas Production with a Skin Effect. Paper PETSOC 2009-082 presented at the Canadian International Petroleum Conference, Calgary, Alberta, 16 – 18 June. doi: 10.2118/2009-082
- Blasingame, T.A., Mccray, T.L., and Lee, W.J. 1991. Decline Curve Analysis for Variable Pressure Drop/Variable Flowrate Systems. Paper SPE 21513 presented at the SPE Gas Technology Symposium, Houston, Texas, 22-24 January. doi: 10.2118/21513-ms

- Bowker, K.A. 2007. Barnett Shale Gas Production, Fort Worth Basin: Issue and Discussion. *AAPG Bulletin* **91** (4): 523-533. doi: 10.1306/06190606018
- Cinco-Ley, H. and Meng, H.-Z. 1988. Pressure Transient Analysis of Wells with Finite Conductivity Vertical Fractures in Double Porosity Reservoirs. Paper SPE 18172 presented at the SPE Annual Technical Conference and Exhibition, Houston, Texas, 2-5 October. doi: 10.2118/18172-ms
- Cinco-Ley, H. and Samaniego-V., F. 1981. Transient Pressure Analysis for Fractured Wells. *SPE Journal of Petroleum Technology* **33** (9): 1749-1766. doi: 10.2118/7490-pa
- Cinco L., H., Samaniego V., F., and Dominguez A., N. 1978. Transient Pressure Behavior for a Well with a Finite-Conductivity Vertical Fracture. *Society of Petroleum Engineers Journal* **18** (4): 253-264. doi: 10.2118/6014-pa
- Cipolla, C.L., Lolon, E.P., Erdle, J.C. et al. 2010. Reservoir Modeling in Shale-Gas Reservoirs. *SPE Reservoir Evaluation & Engineering* **13** (4): pp. 638-653. doi: 10.2118/125530-pa
- Cipolla, C.L., Warpinski, N.R., Mayerhofer, M.J. et al. 2008. The Relationship between Fracture Complexity, Reservoir Properties, and Fracture Treatment Design. Paper SPE 115769 presented at the SPE Annual Technical Conference and Exhibition, Denver, Colorado, USA, 21-24 September. doi: 10.2118/115769-ms
- Ehlig-Economides, C.A., Martinez, H., and Okunola, D.S. 2009. Unified Pta and Pda Approach Enhances Well and Reservoir Characterization. Paper SPE 123042-MS presented at the Latin American and Caribbean Petroleum Engineering

Conference, Cartagena de Indias, Colombia, 31 May-3 June. doi: 10.2118/123042-ms

Fisher, M.K., Heinze, J.R., Harris, C.D. et al. 2004. Optimizing Horizontal Completion Techniques in the Barnett Shale Using Microseismic Fracture Mapping. Paper SPE 90051 presented at the SPE Annual Technical Conference and Exhibition, Houston, Texas, 26-29 September. doi: 10.2118/90051-ms

Gale, J.F.W., Reed, R.M., and Holder, J. 2007, Natural Fractures in the Barnett Shale and Their Importance for Hydraulic Fracture Treatments: *AAPG Bulletin* **91** (4): 603-622. doi: 10.1306/11010606061

Gaskari, R. and Mohaghegh, S.D. 2006. Estimating Major and Minor Natural Fracture Pattern in Gas Shales Using Production Data. Paper SPE 104554-MS presented at the SPE Eastern Regional Meeting, Canton, Ohio, USA, 11-13 October. doi: 10.2118/104554-ms

Guppy, K.H., Cinco, H., and Ramey Jr., H.J. 1981. Transient Flow Behavior of a Vertically Fractured Well Producing at Constant Pressure. Paper SPE 9963. available from SPE, Richardson, Texas

Kale, S.V., Rai, C.S., and Sondergeld, C.H. 2010. Petrophysical Characterization of Barnett Shale. Paper SPE 131770 presented at the SPE Unconventional Gas Conference, Pittsburgh, Pennsylvania, USA, 23-25 February. doi: 10.2118/131770-ms

- Kazemi, H. 1969. Pressure Transient Analysis of Naturally Fractured Reservoirs with Uniform Fracture Distribution. *Society of Petroleum Engineers Journal* **9** (4): 451-462. doi: 10.2118/2156-a
- Kucuk, F. and Sawyer, W.K. 1980. Transient Flow in Naturally Fractured Reservoirs and Its Application to Devonian Gas Shales. Paper AIME 9397 presented at the SPE Annual Technical Conference and Exhibition, Dallas, Texas, 21-24 September. doi: 10.2118/9397-ms
- Mayerhofer, M.J., Lolon, E.P., Youngblood, J.E. et al. 2006. Integration of Microseismic Fracture Mapping Results with Numerical Fracture Network Production Modeling in the Barnett Shale. Paper SPE 102103 presented at the SPE Annual Technical Conference and Exhibition, San Antonio, Texas, USA, 24-27 September. doi: 10.2118/102103-ms
- Meyer, B.R., Bazan, L.W., Jacot, R.H. et al. 2010. Optimization of Multiple Transverse Hydraulic Fractures in Horizontal Wellbores. Paper SPE 131732 presented at the SPE Unconventional Gas Conference, Pittsburgh, Pennsylvania, USA, 23-25 February. doi: 10.2118/131732-ms
- Montgomery, S. L., Jarvie, D.M., Bowker, K. A., and Pollastro, R. M. 2005. Mississippian Barnett Shale, Fort Worth Basin, North Central Texas: Gas-Shale Play with Multi-Trillion Cubic Foot Potential: *AAPG Bulletin* **89** (2): 155–175. doi: 10.1306/09170404042

- NEB. 2009. A Primer for Understanding Canadian Shale Gas - Energy Briefing Note.
National Energy Board, ISSN 1917-506X, Calgary, Alberta, Canada (November 2009)
- Nieto, J., Bercha, R., and Chan, J. 2009. Shale Gas Petrophysics - Montney and Muskwa, Are They Barnett Look-Alikes? Paper SPWLA 2009-84918 presented at the SPWLA 50th Annual Logging Symposium, The Woodlands, Texas, 21 – 24 June.
- Palacio, J.C. and Blasingame, T.A. 1993. Decline-Curve Analysis with Type Curves - Analysis of Gas Well Production Data. Paper SPE 25909 presented at the SPE Rocky Mountain Regional/Low Permeability Reservoirs Symposium, Denver, Colorado, USA, 12-14 April. doi: 10.2118/25909-ms
- Reynolds, M.M. and Munn, D.L. 2010. Development Update for an Emerging Shale Gas Giant Field - Horn River Basin, British Columbia, Canada. Paper SPE 130103 presented at the SPE Unconventional Gas Conference, Pittsburgh, Pennsylvania, USA, 23-25 February. doi: 10.2118/130103-ms
- Samandarli, O., Ahmadi, H.a.A., and Wattenbarger, R.A. 2011. A New Method for History Matching and Forecasting Shale Gas Reservoir Production Performance with a Dual Porosity Model. Paper SPE 144335 presented at the North American Unconventional Gas Conference and Exhibition, The Woodlands, Texas, USA, 14-16 June. doi: 10.2118/144335-ms
- Serra, K., Reynolds, A.C., and Raghavan, R., 1983. New Pressure Transient Analysis Methods for Naturally Fractured Reservoirs (includes associated papers 12940

- and 13014). *SPE Journal of Petroleum Technology* **35** (12): 2271-2283. doi: 10.2118/10780-PA
- Song, B., Economides, M.J., and Ehlig-Economides, C.A. 2011. Design of Multiple Transverse Fracture Horizontal Wells in Shale Gas Reservoirs. Paper SPE 140555 presented at the SPE Hydraulic Fracturing Technology Conference, The Woodlands, Texas, USA, 24-26 January. doi: 10.2118/140555-ms
- Song, B. and Ehlig-Economides, C.A. 2011. Rate-Normalized Pressure Analysis for Determination of Shale Gas Well Performance. Paper SPE 144031 presented at the North American Unconventional Gas Conference and Exhibition, The Woodlands, Texas, USA, 14-16 June. doi: 10.2118/144031-ms
- Turner, R.G., Hubbard, M.G., and Dukler, A.E. 1969. Analysis and Prediction of Minimum Flow Rate for the Continuous Removal of Liquids from Gas Wells. *SPE Journal of Petroleum Technology* **21** (11): 1475-1482. doi: 10.2118/2198-pa
- Warpinski, N., Kramm, R.C., Heinze, J.R. et al. 2005. Comparison of Single- and Dual-Array Microseismic Mapping Techniques in the Barnett Shale. Paper SPE 95568 presented at the SPE Annual Technical Conference and Exhibition, Dallas, Texas, 9-12 October. doi: 10.2118/95568-ms
- Warpinski, N.R. and Teufel, L.W. 1987. Influence of Geologic Discontinuities on Hydraulic Fracture Propagation (Includes Associated Papers 17011 and 17074). *SPE Journal of Petroleum Technology* **39** (2): 209-220. doi: 10.2118/13224-pa
- Warren, J.E. and Root, P.J. 1963. The Behavior of Naturally Fractured Reservoirs. *Society of Petroleum Engineers Journal* **3** (3): 245-255. doi: 10.2118/426-pa

Wattenbarger, R.A., El-Banbi, A.H., Villegas, M.E. et al. 1998. Production Analysis of Linear Flow into Fractured Tight Gas Wells. Paper SPE 39931 presented at the SPE Rocky Mountain Regional/Low-Permeability Reservoirs Symposium, Denver, Colorado, 5-8 April. doi: 10.2118/39931-ms

APPENDIX A

SINGLE POROSITY (HOMOGENEOUS) MODEL BEHAVIOR

The complete flow regimes for the single porosity model are shown in Song et al. (2011). However, only pseudolinear flow and pseudo pseudosteady state flow regime are likely to be seen in the shale gas field data since the shale matrix generally has very low permeability and the time required to reach compound linear flow regime or beyond is longer than the expected well life. Also, Song et al. (2011) generated the flow regimes using effectively infinite hydraulic fracture dimensionless conductivity (C_{fD}). In our work, however, the case with finite hydraulic fracture conductivity will also be considered to capture the bilinear flow regime which can also be observed in field data. Cinco-Ley et al., 1978, indicated that the fracture conductivity is effectively finite when C_{fD} is less than 300. This section will begin with the formation pseudolinear flow regime and later the formation to hydraulic fracture (F-HF) bilinear flow regime will be shown.

A.1. Formation Pseudolinear flow

The formation pseudolinear flow represents the flow from formation into hydraulic fracture plane before the boundary effect is sensed. During this period, each hydraulic fracture cluster is producing independently. The formation linear flow regime equation for shale gas flow from MTFHW is given by Eq. A.1 and A.2 in terms of RNP and RNP', respectively.

$$RNP = \frac{40.93T}{n_F h x_F \sqrt{k} \sqrt{(\phi \mu c_t)_i}} \sqrt{t} \quad \dots(a.1)$$

$$RNP' = \frac{1}{2} \left[\frac{40.93T}{n_F h x_F \sqrt{k} \sqrt{(\phi \mu c_t)_i}} \sqrt{t} \right] \quad \dots(a.2)$$

Eq. a.1 and a.2 indicate that the formation pseudolinear flow regime will exhibit a 1/2 slope straight line for both RNP and RNP' on log-log plots versus material balance time. Also, it emphasizes that the RNP and RNP' always separate by factor of two (2).

Figure a.1 shows the simulated example of the formation pseudolinear flow regime.

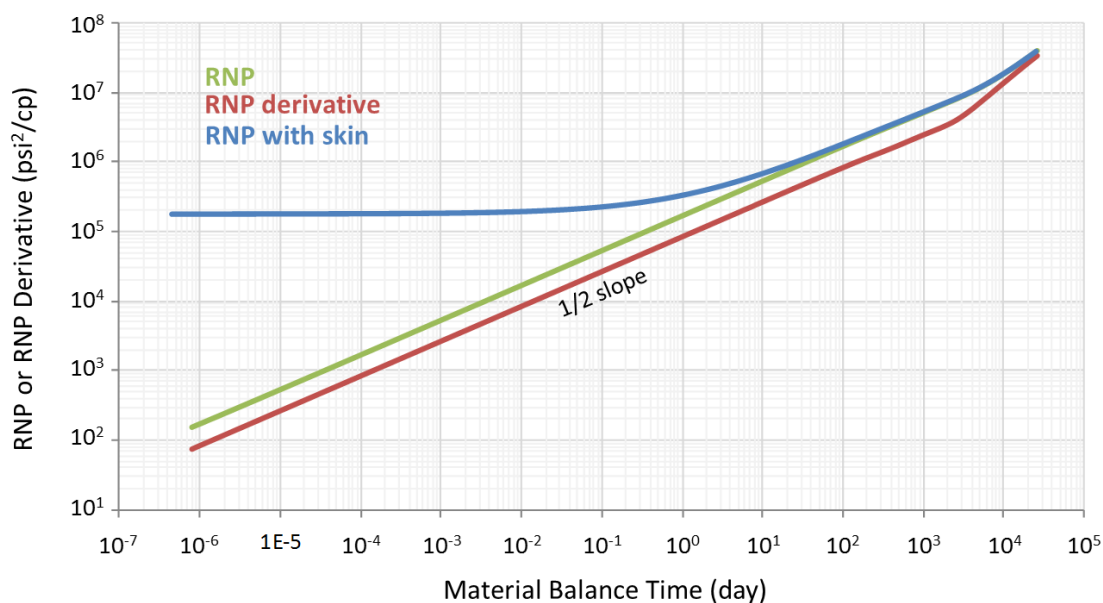


Figure A.1: Potential flow regimes during MTFHW production

The products of formation permeability and fracture half-length can be found from the log-log plots using Eq. a.1 or a.2. However, in general RNP' is more reliable because the RNP behavior may be affected by a fracture skin factor that alters the value of RNP. Figure A.2 shows that the RNP' is independent of skin effect. Note that independent values for formation permeability and fracture half-length cannot be found because the linear flow relationship provides only one equation for these 2 unknowns.

A.2 Hydraulic Fractures - Matrix Bilinear flow

When hydraulic fractures have finite conductivity, the pressure drop along the fracture length cannot be neglected. In this case, bilinear flow will be observed in production and pressure data as a result of simultaneous linear flow in two perpendicular directions, i.e. flow inside hydraulic fracture and flow from the formation to the fracture plane. Cinco-Ley et al. (1978) demonstrated that infinite conductivity assumption is valid only when dimensionless fracture conductivity, $(k_f b_f)_D = \frac{k_f b_f}{k x_F}$, is less than 300. Otherwise the finite conductivity fracture model must be used.

Constant rate dimensionless solution for bilinear flow as presented by Cinco-Ley and Samaniego (1981) is shown in Eq. (a.3) while constant pressure dimensionless solutions as provided by Guppy et al. (1981) is shown in Eq. (a.4).

Constant rate

$$p_{wD} = \frac{\pi}{I\left(\frac{5}{4}\right)\sqrt{2(k_F b_F)_D}} t_{Dx_F}^{1/4} \quad \dots(a.3)$$

Constant pressure

$$\frac{1}{q_D} = \frac{\pi I\left(\frac{3}{4}\right)}{\sqrt{2(k_F b_F)_D}} t_{Dx_F}^{1/4} \quad \dots(a.4)$$

Where dimensionless variables for gas are defined by

$$p_{wD} = \frac{kh[m(p_i) - m(p_{wf})]}{1424qT} \quad \dots(a.5)$$

$$t_{Dx_F} = \frac{0.0002637kt}{(\phi\mu c_t)_i x_F^2} \quad \dots(a.6)$$

$$(k_F b_F)_D = \frac{k_F b_F}{k x_F} \quad \dots(a.7)$$

By comparing Eq. (a.3) with (a.4), it can be observed that the solutions for constant rate and constant pressure differ by factor of $\left[\Gamma\left(\frac{3}{4}\right) / \frac{1}{\Gamma\left(\frac{5}{4}\right)} \right]$ or 1.11 which indicates that the well producing at constant rate condition will encounter 1.1 times more pressure drop than when producing at constant pressure *during bilinear flow*. In section A.1 we saw that for linear flow the two solutions are separated by factor of $\frac{\pi}{2}$ or 1.57 times.

Substituting Eq. (a. 3) and (a.4) with definition of dimensionless variables defined by Eq. (a.5) thru (a.7), with modification by adding number of hydraulic fractures (n_F) into the equation as to apply for multi-traverse fractured horizontal well, gives the dimensional equations for both constant rate and constant pressure condition as follows.

Constant rate

$$\Delta m(p) = \frac{444.75qT}{n_F h \sqrt{k_F b_F} (\phi \mu c_t)^{1/4} k^{1/4}} \sqrt[4]{t} \quad \dots(a.8)$$

Constant pressure

$$\frac{1}{q} = \frac{494 \Delta m(p) T}{n_F h \sqrt{k_F b_F} (\phi \mu c_t)^{1/4} k^{1/4}} \sqrt[4]{t} \quad \dots(a.9)$$

Next, differentiating Eq. (3.28) and (3.29) with respect to natural log of time to obtain pressure derivative solutions as follows:

Constant rate

$$\frac{d\Delta m(p)}{d \ln(t)} = \frac{1}{4} \left[\frac{444.75qT}{n_F h \sqrt{k_F b_F} (\phi \mu c_t)^{1/4} k^{1/4}} \sqrt[4]{t} \right] \quad \dots(a.9)$$

Constant pressure

$$\frac{d^{\frac{1}{4}}_q}{d\ln(t)} = \frac{1}{4} \left[\frac{494\Delta m(p)T}{n_F h \sqrt{k_F b_F} (\phi \mu c_t)^{1/4} k^{1/4}} \sqrt[4]{t} \right] \quad \dots(a.10)$$

Comparing Eq. (a.8) and (a.9) with (a.10) and (a.11) respectively indicates that pressure different and pressure derivative always separate by factor of four (4) during the *bilinear flow* period. Again, note that constant rate and constant pressure solutions for bilinear flow case s are separated by factor of 1.11.

Now, taking logarithmic both sides of Eq. (a.8) thru (a.11) gives bilinear flow solutions in log-log coordinate as follows:

Constant rate

$$\log[\Delta m(p)] = \frac{1}{4} \log(t) + \log \left[\frac{444.75qT}{n_F h \sqrt{k_F b_F} (\phi \mu c_t)^{1/4} k^{1/4}} \right] \quad \dots(a.12)$$

and

$$\log \left[\frac{d\Delta m(p)}{d\ln(t)} \right] = \frac{1}{4} \log(t) + \frac{1}{4} \log \left[\frac{444.75qT}{n_F h \sqrt{k_F b_F} (\phi \mu c_t)^{1/4} k^{1/4}} \right] \quad \dots(a.13)$$

Constant pressure

$$\log \left[\frac{1}{q} \right] = \frac{1}{4} \log(t) + \log \left[\frac{494\Delta m(p)T}{n_F h \sqrt{k_F b_F} (\phi \mu c_t)^{1/4} k^{1/4}} \right] \quad \dots(a.14)$$

and

$$\log \left[\frac{d^{\frac{1}{4}}_q}{d\ln(t)} \right] = \frac{1}{4} \log(t) + \frac{1}{4} \log \left[\frac{494\Delta m(p)T}{n_F h \sqrt{k_F b_F} (\phi \mu c_t)^{1/4} k^{1/4}} \right] \quad \dots(a.15)$$

Again, these log-log form solutions emphasize that both pressure difference and pressure derivative will exhibit a quarter slope straight line on log-log pressure difference or pressure derivative versus time plot. Moreover, this confirms that the value of the pressure difference will always be higher than of pressure derivative by 4 times

during bilinear flow regardless of at which condition the well is producing, provided there is no fracture skin. As for linear flow, when there is fracture skin, the derivative response will show $1/4$ slope even if the pressure difference does not.

Though the condition is not likely, the single porosity model may be used to represent a dual porosity formation characterized with primary porosity of the shale matrix and secondary porosity as a fracture network if the difference in conductivity between the media is small. In this case, the flow from the matrix may not only flow into the reopened fracture network, but will also enter directly into the hydraulic fractures. This condition could be considered as simultaneous flows from multiple layers with different permeabilities into the well, and the single porosity model might work fine but the “average” or “effective” permeability must be used instead of the absolute matrix permeability to represent the average properties of the formations and fracture network.

Also, the single porosity model may be adjusted to represent the flow from the shale matrix into the fracture network by considering that parameters previously related to hydraulic fracture as applying instead to the fracture network. This will be equivalent to the triple porosity model when the hydraulic fracture conductivity is very high.

APPENDIX B

DUAL POROSITY MODEL BEHAVIOR

Cinco-Ley and Meng (1988) has presented a semi-analytical model that characterizes behavior of a vertical well with a single vertical finite conductivity fracture in a double porosity reservoir (Figure B.1). The dual porosity reservoir is defined so that at any point in the formation, the pore space consists of two media, the primary porosity with high storativity but low permeability, and the secondary porosity with high permeability but low storativity.

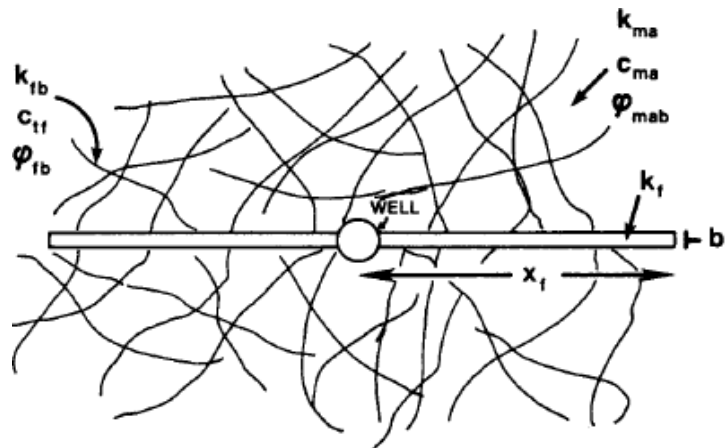


Figure B.1: Map view showing vertically fractured well in double porosity reservoir (Cinco-Ley and Meng, 1988)

The model by Cinco-Ley and Meng also can be applied for flow to multiple hydraulic fractures from a horizontal well. For shale gas produced from a MTFHW, the primary porosity could be the shale matrix porosity, and the secondary porosity could be a natural fracture consisting of existing microfractures in the shale formation or

unpropped fractures opened or reopened in the formation during the hydraulic fracturing process.

Cinco-Ley and Meng (1988) presented models for both pseudo-steady state and transient flow between matrix blocks and fractures. However, only the transient flow model is investigated in our work because the ultra-low permeability of the shale formation is more likely to induce transient flow conditions. . This study used the model provided by Kappa Engineering that adapted the Cinco-Ley and Meng model to the MTFHW completion configuration.

To summarize, the MTFHW in a homogeneous reservoir may exhibit the flow following flow behaviors:

- *Linear flow in the hydraulic fractures:* during this period, there is only a flow inside hydraulic fracture which can be treated as linear flow since they are elongated with their width much smaller than their length. Nonetheless, this flow regime usually exists at very early time and is unlikely to be seen in practical field data.
- *Bilinear flow from the formation to finite conductivity Hydraulic fractures:* linear flow occurs in two directions at the same time, i.e. the flow inside hydraulic fractures and the flow from formation into hydraulic fracture perpendicular to fracture plane. This flow regime can occur when hydraulic fracture conductivity is not effectively infinite, i.e. $(k_f b_f)_D$ is less than 300 (Cinco-Ley et al., 1978).

- *Formation linear flow*: during this period, pressure variation is dominated by the flow from the formation into hydraulic fractures; either because they have effectively infinite conductivity, or because the pressure gradient inside the fractures is much smaller than the pressure gradient in the formation. In effect, the flow in each hydraulic fracture reaches a sort of pseudosteady state, in the sense that the pressure profile in the fracture remains unchanged even as the pressure magnitude in the well may change. We will call this hydraulic fracture boundary flow. On the other hand, an un-fractured well in a double porosity reservoir will exhibit the following three flow regimes:
- *Fracture network dominated flow*: during this period, the flow is dominated by expansion of fracture network storativity while matrix contribution can be neglected.
- *Transition flow*: during this period, as the flow from the matrix into fracture network increases, its pressure gradient becomes increasingly important. During this time, an analog to the previously described bilinear flow from the formation to hydraulic fractures, but this time between the matrix and fractures in the fracture network. *Total system (matrix + fracture network) dominated flow*: this flow regime occurs after transition flow when the flow contribution from the matrix has stabilized.

The combination of dual porosity flow in the formation with linear and bilinear flow to the fracture leads to a set of flow regime combinations that include linear, bi-linear, and even tri-linear flow. Trilinear flow occurs when pressure gradients in the

hydraulic fractures, in network fractures, and in the matrix become comparable. These flow regimes are the results of combination of all flow behaviors mentioned above. The combinations which are of interest for the purpose of our study are listed in Table B.1. Among the six flow behaviors shown in Table B.1, the behaviors which are seen the most are linear and bilinear flow. As explained in Chapter II, evidence of linear or bilinear flow is identified as a straight trend in the RNP derivative with slope 1/2 or 1/4, respectively. In many shale gas wells production and pressure data processed as RNP and derivative show evidence of only these two straight line trends.

Table B.1: Fractured well in Double porosity formation flow regime combinations

Name	Abbrev.	Visible Slope	Flow Behavior		
			Fractured well in Homogeneous reservoir	Vertical well in Double porosity reservoir	System Flow Character
Fracture Network to Hydraulic Fracture Bilinear	FN-HF	1/4	Hydraulic fracture linear flow	Fracture dominated linear flow	bilinear flow
Matrix to Fracture Network and Hydraulic Fractures Trilinear	M-FN-HF	1/8	Hydraulic fracture linear flow	bilinear flow	trilinear flow
Total System to Hydraulic Fractures Bilinear	TS-HF	1/4	Hydraulic fracture linear flow	Total system dominated linear flow	bilinear flow
Fracture Network Linear	FN	1/2	Hydraulic fracture boundary flow	Fracture dominated linear flow	linear flow
Matrix to Fracture Network Bilinear	M-FN	1/4	Hydraulic fracture boundary flow	bilinear flow	bilinear flow
Total System Linear	TS	1/2	Hydraulic fracture boundary flow	Total system dominated linear flow	linear flow

**flow period as shown in Table 2 in Cinco-Ley & Meng (1988)*

The model derivation and flow regime equations are illustrated thoroughly in Cinco-Ley & Meng (1988) and will not be addressed in detail here. However, Cinco-Ley

& Meng (1988) modeled a single vertically fractured vertical well which is not typical for current shale gas well completions. Moreover, fracture network “slab” model has been defined as horizontal fracture planes interbedded with matrix layers or layer-cake model (Figure B.2) which is not likely for shale formation unless shale gas exists at very shallow depth. Therefore, the following sections offer clarification for the equations associated with the flow regimes in Table B.1

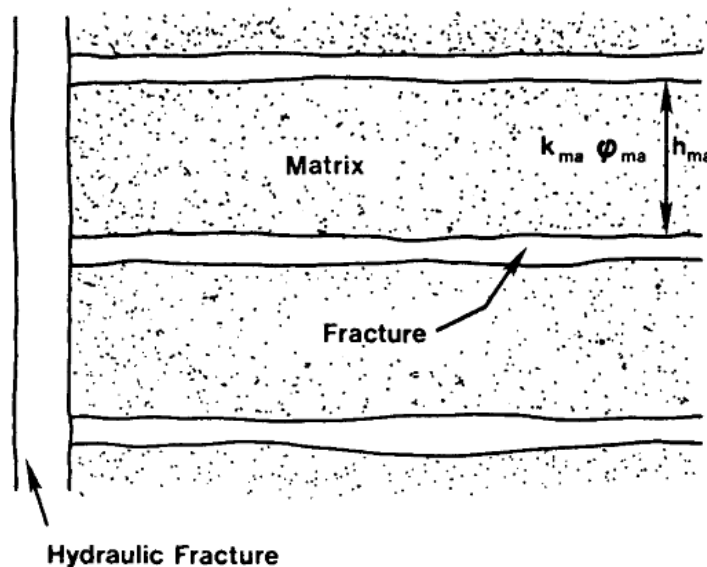


Figure B.2: Cross-sectional view of slab matrix blocks (Cinco-Ley & Meng, 1988)

B.1 Fracture Network to Hydraulic Fracture Bilinear Flow (FN-HF)

In general, the bilinear flow regime occurs when two linear pressure gradients occur simultaneously in perpendicular directions. For a particular case of the *fracture network to hydraulic fracture bilinear flow*, the first flow must be the linear flow inside hydraulic fractures and the second flow must be the flow from the double porosity

fracture network into hydraulic fracture plane. Moreover, the second linear flow must be dominated by low fracture network diffusivity, and the flow contribution from the matrix must be minimal, a condition that may occur when much of the total system porosity is in the fracture network and when the fracture network permeability is considerably greater than that of the matrix. These conditions can occur when low hydraulic fracture conductivity and/or extended fracture half-length increases the duration of hydraulic fracture linear flow while low fracture network diffusivity increases the duration of fracture network dominated linear flow. Therefore, if this flow regime is attributed to bilinear flow observed in field data, it indicates that the effectively only the fracture network is being produced.

The fracture network to hydraulic fracture bilinear flow behavior is seen as a quarter slope straight line on log-log plots of production rate or pressure and pressure derivative versus time which can be characterized by the following equations:

Constant rate

$$p_{wD} = \frac{\pi}{I\left(\frac{5}{4}\right)\sqrt{2(k_F b_F)_D}} \left(\frac{t_{Dx_F}}{\omega}\right)^{\frac{1}{4}} \quad \dots(b.1)$$

where dimensionless variables for gas are defined by

$$p_{wD} = \frac{k_{fb} h [m(P_i) - m(P_{wf})]}{1424 q T} \quad \dots(b.2)$$

$$t_{Dx_F} = \frac{0.0002637 k_{fb} t}{(\phi \mu c_t)_i x_F^2} \quad \dots(b.3)$$

$$(k_F b_F)_D = \frac{k_F b_F}{k_{fb} x_F} \quad \dots(b.4)$$

Dimensionless variables are in the same form as those shown in Eq. (a.5) thru (a.7), but the indicated permeability, k_{fb} represents the fracture network permeability

instead of permeability k that is used in homogeneous model. For this interpretation, k_{fb} is so much larger than matrix permeability, k_{ma} , that the total system permeability is k_{fb} .

The dimensionless storativity, ω , is defined as the ratio between fracture storativity to total system storativity.

$$\omega = \frac{(\phi c_t)_f}{(\phi c_t)_f + (\phi c_t)_{ma}} = \frac{(\phi c_t)_f}{(\phi c_t)_t} \quad \dots(b.5)$$

Substituting Eq. (b.1) with all dimensional variables defined above finally yields dimensional form of the equation for bilinear flow of gas from the fracture network to hydraulic fracture bilinear characteristic as follows:

Constant rate

$$\Delta m(p) = \frac{444.75qT}{n_F h \sqrt{k_F b_F} (\phi \mu c_t)^{1/4} k_{fb}^{1/4}} \sqrt[4]{\frac{t}{\omega}} \quad \dots(b.6)$$

By comparing Eq. (b.6) to the single porosity bilinear flow Eq. (a.8) we can see that the difference between the two flow regimes is the presence of storativity ratio (ω). The smaller the ω is, the larger is the difference between fracture storativity and matrix storativity, and the bigger is the difference between the double porosity and single porosity models. Therefore, considering the value of pressure difference $[\Delta m(p)]$ at the same time (t), it can be seen that the fracture network to hydraulic fracture bilinear flow double porosity model will give higher pressure difference than the bilinear homogeneous model by the factor of $\left[\sqrt[4]{1/\omega} \right]$. For example, if ω is 0.1, then the difference between the two models will be $\left[\sqrt[4]{1/0.1} \right]$ or 100 times which means that the

two models will separate by two orders of magnitude, in other words, they will separate by 2 log cycles on horizontal scale of the log-log plots.

B.2 Matrix to Fracture Network to Hydraulic Fractures Trilinear Flow (M-FN-HF)

When transient flow occurs simultaneously in both the matrix and the fracture network, this is a form of bilinear flow because each fracture in the network is a plane containing linear flow, and flow in the matrix to the fracture plane is also linear. As such, bilinear flow can occur in the transient dual porosity system even without any hydraulic fracture. In a double porosity reservoir the bilinear flow regime may appear after the fracture network dominated flow period and before the total system flow is established. The establishment of total system flow in a dual porosity reservoir means that matrix elements surrounded by natural fractures reach stabilized drainage limited flow. The timing of dual porosity bilinear flow depends on the value of the interporosity flow parameter, λ .

When the fracture network to hydraulic fracture flow is also bilinear, there are three simultaneous transient linear flow regimes, resulting in the trilinear flow regime identified by Cinco-Ley and Meng (1988) with a $1/8$ slope. As such, for the case of MTFHW with low hydraulic fracture conductivity, the presence of a fracture network combined with flow contribution from the shale matrix will be $\frac{1}{8}$ slope on log-log plots of production or pressure versus time. Note that, even though this flow regime can be shown theoretically that it can exist, it is not often been seen in actual pressure and

production data. The matrix to fracture network and hydraulic fractures trilinear flow regime can be modeled using the following equations.

Constant rate

$$p_{wD} = \frac{\pi}{\Gamma\left(\frac{9}{8}\right)\sqrt{2(k_F b_F)_D} A_{fD}^{1/4} \eta_{maD}^{1/8}} t_{Dx_F}^{1/8} \quad \dots(b.7)$$

All dimensionless variables are defined the same as shown in Eq. (b.2) thru (b.4) while η_{maD} and A_{fD} are the dimensionless matrix hydraulic diffusivity and dimensionless fracture network area, respectively. Note that η_{maD} in Eq. (b.7) is equivalent to λ that is used in a conventional double porosity model as presented in Warren and Root (1963). η_{maD} is used, however, for transient flow condition while λ is used for the pseudosteady state flow condition.

$$\eta_{maD} = \frac{k_{ma}/(\phi c_t)_{ma} x_F^2}{k_{fb}/(\phi c_t)_t L_f^2} = \frac{\lambda}{12(\omega-1)} \quad \dots(b.8)$$

$$A_{fD} = \frac{A_{fb} L_f V_b}{V_{ma}} = A_{fma} L_f \quad \dots(b.9)$$

Where A_{fb} = fracture network area per bulk volume

A_{fma} = fracture network area per matrix volume

L_f = reopened fracture network spacing

Substituting Eq. (b.7) with all dimensional variables definitions finally yields a dimensional form of the solution for constant rate gas flow with matrix to fracture network and hydraulic fractures trilinear characteristic as follows.

Constant rate

$$\Delta m(p) = \frac{1199.1 q T}{n_F h \sqrt{k_F b_F} k_{fb}^{1/4} (\phi \mu c_t)^{1/8} A_{fb}^{1/4} k_{ma}^{1/8}} \sqrt[8]{t} \quad \dots(b.10)$$

B.3 Total System to Hydraulic Fractures Bilinear Flow (TS-HF)

The total system dominated flow regime occurs after the end of the bilinear flow regime in the double porosity model, when flow in the matrix becomes stabilized. During this period, the pressure and production behavior is dominated by flow contributions from both the matrix and the fracture network.

In case that hydraulic fracture linear flow lasts sufficiently long that the double porosity flow reaches total system flow conditions, it is possible that the hydraulic fracture linear flow and total system dominated linear flow may occur simultaneously. In this circumstance, the *total system to hydraulic fractures bilinear flow* regime can be observed as quarter slope on log-log pressure or rate versus time plots and can be represented by the following equation.

Constant rate

$$p_{wD} = \frac{\pi}{I\left(\frac{5}{4}\right)\sqrt{2(k_F b_F)_D}} t_{Dx_F}^{1/4} \quad \dots(b.11)$$

It can be seen that Eq. (b.11) has the same formation as Eq. (a.3) shown earlier as the bilinear flow regime in the single porosity or homogeneous model. The final dimensional form of Eq. (b.11) is also found to be in the same form as Eq. (a.3) except that k is replaced by fracture bulk permeability, k_{fb} , in the double porosity model as shown in the following equation.

Constant rate

$$\Delta m(p) = \frac{444.75qT}{n_F h \sqrt{k_F b_F} (\phi \mu c_t)^{1/4} k_{fb}^{1/4}} \sqrt[4]{t} \quad \dots(b.12)$$

Thus, it is implied that the two models may exhibit exactly the same flow behavior during this flow regime even though the flow systems are totally different, i.e. the homogeneous reservoir model without fracture network versus the double porosity model with fracture network.

B.4 Fracture Network Linear Flow (FN)

Fracture network linear flow occurs when the only dominant flow behavior is a linear flow in a fracture network with low diffusivity. This flow regime is comparable to the *Fracture network to hydraulic fracture bilinear flow regime* defined earlier, but in this case hydraulic fracture has either effectively infinite conductivity or has sufficient short half-length that the flow inside hydraulic fracture stabilized very early.

The fracture network linear flow regime appears as a 1/2 slope straight derivative trend on log-log plots. The constant rate flow equation for dimensionless pressure drop with no skin is given as:

Constant rate

$$p_{wD} = \sqrt{\frac{\pi t_D x_F}{\omega}} + \frac{\pi}{3(k_F b_F)_D} \quad \dots(b.13)$$

Substituting all dimensionless variables defined in Eq. (b.2) to (b.5) to obtain flow solution in dimensional form for shale gas wells as follows.

Constant rate

$$\Delta m(p) = \frac{40.99qT}{n_F h x_F \sqrt{k_{fb}} \sqrt{\phi \mu c_t}} \sqrt{\frac{t}{\omega}} + \frac{1491.2qT}{n_F h} \frac{x_F}{k_F b_F} \quad \dots(b.14)$$

Eq. (b.14) explains an important characteristic of the flow during fracture network linear flow period, i.e. that the flow depends only on the fracture network permeability, k_{fb} , and the flow area perpendicular to the formation flow direction, $n_F * h * x_F$, which represents the area of the hydraulic fracture plane.

Also, comparing double porosity flow solution Eq. (b.14) to the single porosity linear flow solution Eq. (a.1), shows that the difference between the two flow models is the presence of storativity ratio (ω). The smaller the ω is the larger the difference between fracture storativity and matrix storativity is, and the bigger is the difference between the double porosity and single porosity models.

Therefore, considering the value of pressure difference ($\Delta m(p)$) at the same time (t), it can be seen that the fracture network dominated linear flow regime in a double porosity reservoir will give higher pressure difference than the bilinear flow regime in a homogeneous reservoir by the factor of $\left[\sqrt{1/\omega} \right]$. For example, if ω is 0.1, then the differences between the two models will be $\left[\sqrt{1/0.1} \right]$ or 10 times which indicates that the two models will separate by one order of magnitudes or 1 log cycles on log-log plots.

B.5 Matrix to fracture Network Bilinear Flow (M-FN)

This flow regime was already explained in Section B.2, but equations were not provided. As implied by its name, double porosity transition bilinear flow can be observed as a straight line of quarter slope on log-log plots. The flow equation is given by the following:

Constant rate

$$p_{wD} = \frac{\pi}{\Gamma(\frac{5}{4})2A_{fD}^{1/2}\eta_{maD}^{1/4}} t_{Dx_F}^{1/4} + \frac{\pi}{3(k_F b_F)_D} \quad \dots(b.15)$$

Applying dimensionless variables given by Eq. (b.2) through (b.4) and (b.8) to (b.9) gives the solution in dimensional form for shale gas wells as the following:

Constant rate

$$\Delta m(p) = \frac{314.47qT}{n_F h x_F \sqrt{A_{fb} k_{fb}} k_{ma}^{1/4} (\phi \mu c_t)^{1/4}} \sqrt[4]{t} + \frac{1491.2qT}{n_F h} \frac{x_F}{k_F b_F} \quad \dots(b.16)$$

Considering Eq. (b.16), matrix permeability, k_{ma} , has less importance on the pressure drop than bulk fracture permeability, k_{fb} , since k_{ma} is under the fourth root while k_{fb} is under a square root. Hence, during this period both matrix and fracture network are contributing to the system, but the fracture network flow dominates.

B.6 Total System Linear Flow (TS)

Total system linear flow occurs after flow in the fracture network has stabilized. During this period, the flow can be considered as linear flow in a homogeneous reservoir with dual porosity total system properties. This flow regime can be compared with total system to hydraulic fractures bilinear flow regime shown in section B.3, but in this case the effect of hydraulic fracture is not seen and the dominant flow is from shale matrix.

Total system linear flow regime can be seen as a half-slope straight line on log-log pressure or production versus time plot. The dimensionless flow solution is given by:

Constant rate

$$p_{wD} = \sqrt{\pi t_{Dx_F}} + \frac{\pi}{3(k_F b_F)_D} \quad \dots(b.17)$$

Substituting dimensionless variables from Eq. (b.2) to (b.4) gives the dimensional form of total system linear flow as:

Constant rate

$$\Delta m(p) = \frac{40.99qT}{n_F h x_F \sqrt{k_{fb}} (\phi \mu c_t)^{1/2}} \sqrt{t} + \frac{1491.2qT}{n_F h} \frac{x_F}{k_F b_F} \quad \dots(b.18)$$

Note that Eq. (b.18) can be identical to Eq. (a.1) when the hydraulic fracture has infinite conductivity so that the second part of the equation becomes negligible. This indicates that if only one linear flow is seen in the production and pressure data, it cannot be concluded without additional external information whether the reservoir is homogeneous or contains a fracture network.

Table B.2 concludes all flow solutions for dual porosity models mentioned earlier.

Table B.2: Flow solutions for dual porosity models

Regime	Dimensionless Solutions	Dimensional Solutions
FN-HF	$p_{wD} = \frac{\pi}{\Gamma\left(\frac{5}{4}\right)\sqrt{2(k_F b_F)_D}} \left(\frac{t_{DXF}}{\omega}\right)^{\frac{1}{4}}$	$\Delta m(p) = \frac{444.75qT}{n_F h \sqrt{k_F b_F} (\phi \mu c_t)^{1/4} k_{fb}^{1/4}} \sqrt[4]{\frac{t}{\omega}}$
M-FN-HF	$p_{wD} = \frac{\pi}{\Gamma\left(\frac{9}{8}\right)\sqrt{2(k_F b_F)_D} A_{fD}^{1/4} \eta_{maD}^{1/8}} t_{DXF}^{1/8}$	$\Delta m(p) = \frac{1199.1qT}{n_F h \sqrt{k_F b_F} k_{fb}^{1/4} (\phi \mu c_t)^{1/8} A_{fb}^{1/4} k_{ma}^{1/8}} \sqrt[8]{t}$
TS-HF	$p_{wD} = \frac{\pi}{\Gamma\left(\frac{5}{4}\right)\sqrt{2(k_F b_F)_D}} t_{DXF}^{1/4}$	$\Delta m(p) = \frac{444.75qT}{n_F h \sqrt{k_F b_F} (\phi \mu c_t)^{1/4} k_{fb}^{1/4}} \sqrt[4]{t}$
FN	$p_{wD} = \sqrt{\frac{\pi t_{DXF}}{\omega}} + \frac{\pi}{3(k_F b_F)_D}$	$\Delta m(p) = \frac{40.93qT}{n_F h x_F \sqrt{k_{fb}} \sqrt{\phi \mu c_t}} \sqrt{\frac{t}{\omega}} + \frac{1491.2qT}{n_F h} \frac{x_F}{k_F b_F}$
M-FN	$p_{wD} = \frac{\pi}{\Gamma\left(\frac{5}{4}\right) 2A_{fD}^{1/2} \eta_{maD}^{1/4}} t_{DXF}^{1/4} + \frac{\pi}{3(k_F b_F)_D}$	$\Delta m(p) = \frac{314.47qT}{n_F h x_F \sqrt{A_{fb} k_{fb}} k_{ma}^{1/4} (\phi \mu c_t)^{1/4}} \sqrt[4]{t} + \frac{1491.2qT}{n_F h} \frac{x_F}{k_F b_F}$
TS	$p_{wD} = \sqrt{\pi t_{DXF}} + \frac{\pi}{3(k_F b_F)_D}$	$\Delta m(p) = \frac{40.93qT}{n_F h x_F \sqrt{k_{fb}} (\phi \mu c_t)^{1/2}} \sqrt{t} + \frac{1491.2qT}{n_F h} \frac{x_F}{k_F b_F}$

APPENDIX C

TRIPLE POROSITY MODEL BEHAVIOR

Al-Ahmadi (2010) introduced a triple porosity solution for flow in hydraulically fractured wells in fractured reservoir. The three porosities in this model refer to three different media, i.e. hydraulic (propped) fractures, natural (unpropped) fractures, and matrix. The matrix has ultra-low permeability but represents most of the bulk formation storativity while the other two fracture media have high permeability but with small storativity. The flow occurs in sequence, i.e. fluids flow from the matrix to the unpropped fractures in which fluids flow to the propped fractures. Moreover, it is assumed that there is no direct communication between the matrix and propped fractures, none between the matrix and the wellbore, and none between unpropped fractures and the wellbore. As such, the fluids only enter wellbore through propped fractures. This assumption is valid when the permeability difference between the shale matrix and unpropped fractures is large, which is very likely for shale gas formations with fractures that were originally in the shale or which were opened or reopened during hydraulic fracturing.

Figure C.1 presents the triple porosity model setting. The figure uses Al-Ahmadi's terminology, calling the propped fractures macrofractures and the unpropped fractures microfractures. Letter L in Figure 3.6 represents fracture spacing while F and f represent spacing between macrofractures and microfractures, respectively. The x_e is used for the total length of stimulated shale volume.

There are four sub-models had been presented in Al-Ahmadi (2010) based on the interporosity flow condition between the two media, i.e. transient or pseudosteady state flow. However, behaviors of shale gas are more likely to flow in a transient condition due to its ultra-low permeability and thus only the fully transient model will be considered in this work.

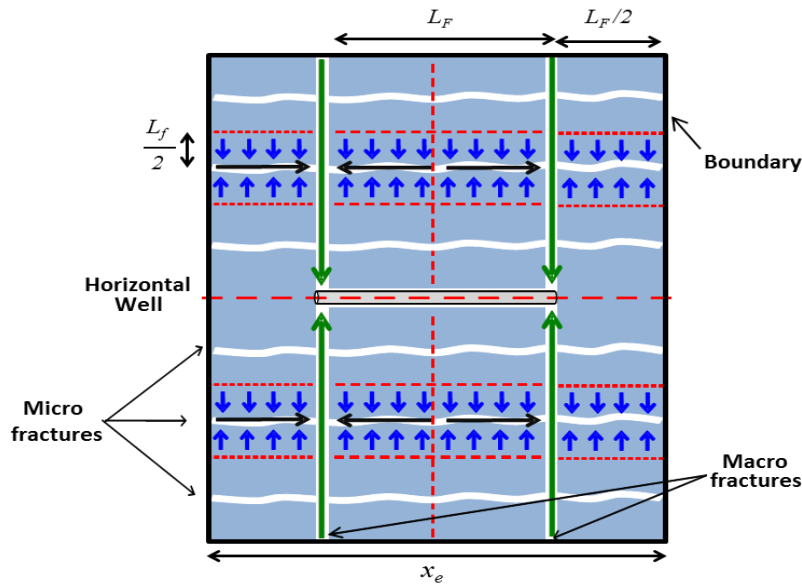


Figure C.1: Top view representing multi-traverse fractured horizontal well in triple porosity system (Modified from Al-Ahmadi, 2010)

C.1 Main flow regimes

The six main flow regimes listed below are included in the triple porosity model:

- *Propped fracture linear flow*: during this period, there is only flow inside hydraulic fractures. Again, this period usually occurs at very early time and is not likely to be observed in field data.

- *Propped fracture - Unpropped fracture bilinear flow*: during this period, there are flows in both hydraulic fractures and in unpropped fractures. This flow regime is equivalent to the *fracture network to hydraulic fracture bilinear flow* in the dual porosity model described in Appendix B.
- *Unpropped fracture linear flow*: The pressure drop is mainly inside unpropped fractures during this period while the pressure drop in hydraulic fracture has reached its boundary, and flow there has stabilized. This flow regime is equivalent to the *fracture dominated linear flow* in the dual porosity model.
- *Unpropped fractures - matrix bilinear flow*: during this period, there are pressure gradients with similar magnitude both in the unpropped fractures and in the shale matrix. This is equivalent to the *matrix to fracture network bilinear flow* in dual porosity model.
- *Matrix linear flow*: this is equivalent to the *total system dominated flow* in dual porosity model.
- *Boundary dominated flow*: this regime occurs last and reflects the boundary of the stimulated volume. Note that no flow beyond the hydraulic (propped) fracture tips is allowed in this model.

Based on the list provided above, there are three linear, two bilinear, and one boundary dominated flows can be seen. However, it is important to note that these complete flow regimes can only be seen when each flow regime occurs in a completely

sequential condition. Therefore, the situations where all these six flow regimes can be seen together in field data are not likely.

C.2 Flow regime combinations

A more realistic flow condition can be considered by combining these six main flow regimes in the same way as what we have illustrated earlier in the dual porosity model to investigate more flow regime combinations which may occur. For example, when hydraulic fracture linear flow lasts very long, or matrix flow reaches its boundary stabilization before this occurs in the unproped fractures and/or hydraulic fractures. These flow regime combinations are summarized in the C.1.

Table C.1 shows that at least twenty-seven flow regime combinations may occur when considering the flows in three media, i.e. hydraulic fractures, reopened natural network, and shale matrix. These twenty-seven flow regime combinations can be categorized further into two groups based on characteristic of hydraulic fractures.

The first group occurs when hydraulic fractures have finite conductivity and/or have very long half-length, or when reopened fractures are very conductive so that there exists a time where hydraulic fracture linear flow and reopened fracture network linear flow occur simultaneously. This group is represented by flow regime number 1 to 22 in Table C.1 and will be seen as a series of a half slope straight line followed by a quarter slope straight line on the log-log plots of pressure or production rate versus time.

The second group occurs when hydraulic fractures are highly conductive or the fracture half-length is very short, or when the reopened fractures have very low

conductivity so that hydraulic fractures had reached their boundary before the reopened fractures started to flow into hydraulic fractures. As a result, there is no quarter slope can be seen between hydraulic fractures and reopened fractures flows. The characteristic is represented by flow regime number 23 to 27 in Table C.1 and will be seen as a half slope straight line of hydraulic fracture linear flow followed by boundary dominated flow then another half slope straight line representing reopened fracture network linear flow.

It is also found that some flow regimes have exactly the same flow characteristic. For example, flow regime number 17 to 22 are all showing a linear flow behavior on log-log plots of pressure or production rate with the same sequence of slope, i.e. $1/2 \rightarrow 1/4 \rightarrow 1/8 \rightarrow 1/4 \rightarrow 1/2$, sequentially. However, the position of these linear flows on the log-log plots will be different. Flow regime number 17 and 19 are showing a hydraulic fracture linear flow while flow regime number 18 and 21 are showing a fracture network linear flow, and flow regime number 20 and 22 are showing matrix linear flow. Therefore, they also require different set of properties, i.e. hydraulic fractures, fracture network, or shale matrix accordingly. Hence, it is obvious that different equations are necessary to characterize these flow regimes although they all show exactly the same flow characteristic. Figure C.2 summarize all 27 possible flow regimes in a decision tree format for better understanding.

Table C.1: Triple porosity flow regime combinations

No.	Slope *	Flow condition in each medium at the time of regime's occurrence			Flow regime occurrence sequence	Slope occurrence sequence*,***
		Hydraulic Fractures	Fracture Network	Matrix		
1	1/2	transient	-	-	1	1/2
2	1/4	transient	transient	-	1 - 2	1/2 - 1/4
3	1/2	boundary	transient	-	1 - 2 - 3	1/2 - 1/4 - 1/2
4	1/4	boundary	transient	transient	1 - 2 - 3 - 4	1/2 - 1/4 - 1/2 - 1/4
5	1/2	boundary	boundary	transient	1 - 2 - 3 - 4 - 5	1/2 - 1/4 - 1/2 - 1/4 - 1/2 - B
6	1/2	boundary	transient	boundary	1 - 2 - 3 - 4 - 6	1/2 - 1/4 - 1/2 - 1/4 - 1/2 - B
7	1/2	boundary	boundary	transient	1 - 2 - 3 - 7	1/2 - 1/4 - 1/2 - B - 1/2 - B
8	1/2	transient	boundary	boundary	1 - 2 - 8	1/2 - 1/4 - 1/2
9	1/4	transient	boundary	transient	1 - 2 - 8 - 9	1/2 - 1/4 - 1/2 - 1/4
10	1/2	boundary	boundary	transient	1 - 2 - 8 - 9 - 10	1/2 - 1/4 - 1/2 - 1/4 - 1/2 - B
11	1/2	transient	boundary	boundary	1 - 2 - 8 - 9 - 11	1/2 - 1/4 - 1/2 - 1/4 - 1/2 - B
12	1/2	boundary	boundary	transient	1 - 2 - 8 - 12	1/2 - 1/4 - 1/2 - B - 1/2 - B
13	1/8	transient	transient	transient	1 - 2 - 13	1/2 - 1/4 - 1/8
14	1/4	transient	transient	boundary	1 - 2 - 13 - 14	1/2 - 1/4 - 1/8 - 1/4
15	1/4	transient	boundary	transient	1 - 2 - 13 - 15	1/2 - 1/4 - 1/8 - 1/4
16	1/4	boundary	transient	transient	1 - 2 - 13 - 16	1/2 - 1/4 - 1/8 - 1/4
17	1/2	transient	boundary	boundary	1 - 2 - 13 - 14 - 17	1/2 - 1/4 - 1/8 - 1/4 - 1/2 - B
18	1/2	boundary	transient	boundary	1 - 2 - 13 - 14 - 18	1/2 - 1/4 - 1/8 - 1/4 - 1/2 - B
19	1/2	transient	boundary	boundary	1 - 2 - 13 - 15 - 19	1/2 - 1/4 - 1/8 - 1/4 - 1/2 - B
20	1/2	boundary	boundary	transient	1 - 2 - 13 - 15 - 20	1/2 - 1/4 - 1/8 - 1/4 - 1/2 - B
21	1/2	boundary	transient	boundary	1 - 2 - 13 - 16 - 21	1/2 - 1/4 - 1/8 - 1/4 - 1/2 - B
22	1/2	boundary	boundary	transient	1 - 2 - 13 - 16 - 22	1/2 - 1/4 - 1/8 - 1/4 - 1/2 - B
23	1/2	boundary**	transient	-	1 - 23	1/2 - B - 1/2
24	1/4	boundary**	transient	transient	1 - 23 - 24	1/2 - B - 1/2 - 1/4
25	1/2	boundary**	transient	boundary	1 - 23 - 24 - 25	1/2 - B - 1/2 - 1/4 - 1/2 - B
26	1/2	boundary**	boundary	transient	1 - 23 - 24 - 26	1/2 - B - 1/2 - 1/4 - 1/2 - B
27	1/2	boundary**	boundary	transient	1 - 23 - 27	1/2 - B - 1/2 - B - 1/2

* Slope on log-log production rate or pressure function versus time

** Hydraulic fracture boundary occur prior to the beginning of fracture network transient

*** B means boundary dominated flow corresponding to the preceding medium

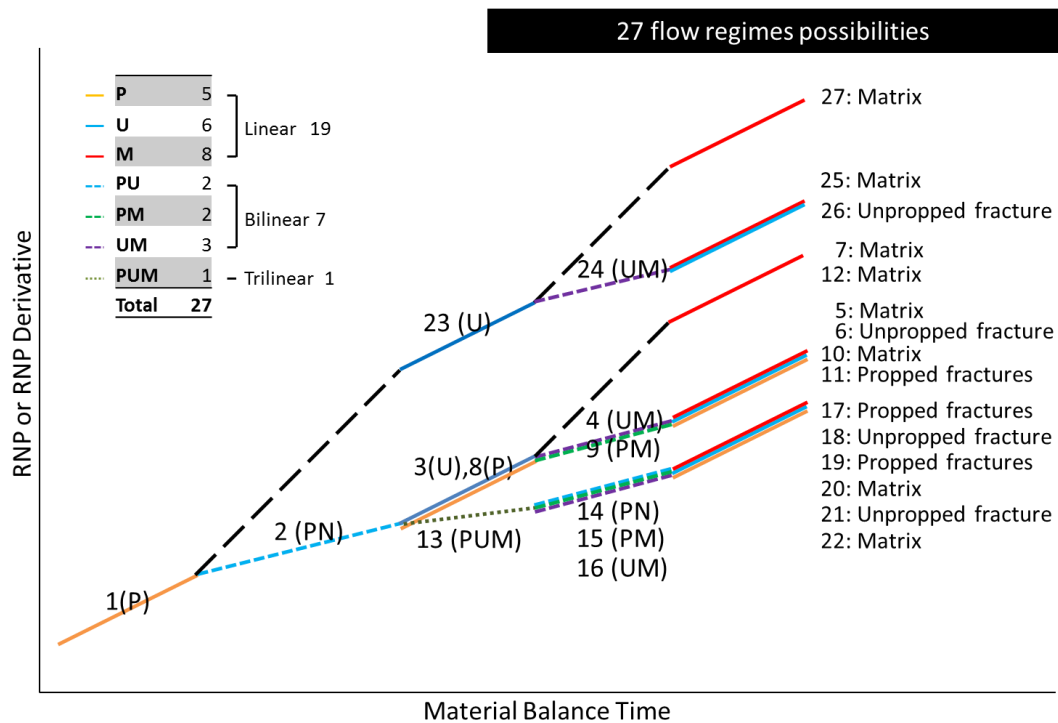


Figure C.2: Flow regime combinations scenario for triple porosity model

By considering Figure C.2, it can be concluded that, of the 27 flow regime combinations, there are total of 19 linear, 7 bilinear, and 1 trilinear flow regimes which may be seen. Of those 19 linear flow regimes, 5 of them belong to hydraulic fractures, another 6 belong to unpropped fractures, and the last eight belong to shale matrix. For bilinear flow regimes, 2 regimes belong to the combination between hydraulic fracture and unpropped fractures, another 3 regimes belong to the combination between unpropped fractures and shale matrix, and the other 2 belongs to the combination of hydraulic fracture and shale matrix. The only trilinear flow regime can occur when all three media are flowing in the transient condition simultaneously.

The complexity of these flow regime combinations for the triple porosity model emphasizes the ambiguity of flow regime characterization when analyzing the field data. Obviously when only one $1/2$ slope is visible, there are 19 possibilities, even if before that $1/2$ slope there exists a $1/4$ slope, still 14 possible flow regimes remain which also needs more than one flow regime equations and thus give several or more different solutions to the parameters.

Table C.1 can be illustrated further based on flow characteristic, i.e. linear flow, bilinear flow, or trilinear flow. Figure C.3 to Figure C.6 summarizes the sequence of flow in each media and its flow condition at the time that the flow regime is occurring. The number or letters in the top row of each flow regime indicate the slope on log-log plots of pressure or flow rate versus time; the $1/2$ slope represents linear flow, $1/4$ slope represents bilinear flow, $1/8$ slope represents trilinear flow, and the letters BDF means boundary dominated flow. The color in each column, when present, indicates that there is a transient flow occurring in that medium, except when BDF is labeled in that column. For example, the transient bilinear flow occurs when there are two colors present in one column, and the trilinear flow occurs when all three medium are colored in the same column. Note that the rightmost colored column is the one that is representing that specific flow regime while the preceding colored columns represent the earlier sequence of flow regime.

Figure C.2 indicates that of the 27 flow regime sequences shown in the tables, only 15 of them represent the total productive life of the well. Of the 15 flow regime sequences, those in Figure C.2 that have the same endpoint are lookalikes. That is, the

same sequence of flow regimes can fit more than one flow scenario. In reality, Figure C. 2 suggests that there are only 5 distinct flow regime sequences describing the complete life of a well, some of which can represent as many as 6 distinct flow characterizations. Furthermore, the number of logarithmic time cycles required to reveal any complete flow regime sequence is 22.

Since the number of logarithmic time cycles from 1 second to 100 years is 9, no entire flow regime sequence will ever be seen. Instead, as shown in Chapter III, pressure buildup tests see up to a maximum of 6 cycles (for a month long buildup with data acquired every second), production data acquired on a daily basis represents 3 cycles (for 2 years of production), and the two combined can produce at most 7 cycles and usually only 4-5 cycles are interpretable.

1 - Hydraulic fracture : Linear flow					
Media / Slope sequence	1/2				
Hydraulic fracture					
Fracture network					
Matrix					
8 - Hydraulic fracture : Linear flow					
Media / Slope sequence	1/2	1/4	1/2		
Hydraulic fracture					
Fracture network					
Matrix					
11 - Hydraulic fracture : Linear flow					
Media / Slope sequence	1/2	1/4	1/2	1/4	1/2
Hydraulic fracture					
Fracture network					
Matrix					
17 - Hydraulic fracture : Linear flow					
	1/2	1/4	1/8	1/4	1/2
Hydraulic fracture					
Fracture network					
Matrix					
19 - Hydraulic fracture : Linear flow					
	1/2	1/4	1/8	1/4	1/2
Hydraulic fracture					
Fracture network					
Matrix					

Figure C.3: Summary of hydraulic fractures linear flow regimes for the triple porosity model

3 - Fracture network : Linear flow					
Media / Slope sequence	1/2	1/4	1/2		
Hydraulic fracture					
Fracture network					
Matrix					
6 - Fracture network : Linear flow					
Media / Slope sequence	1/2	1/4	1/2	1/4	1/2
Hydraulic fracture					
Fracture network					
Matrix					
18 - Fracture network : Linear flow					
Media / Slope sequence	1/2	1/4	1/8	1/4	1/2
Hydraulic fracture					
Fracture network					
Matrix					
21 - Fracture network : Linear flow					
Media / Slope sequence	1/2	1/4	1/8	1/4	1/2
Hydraulic fracture					
Fracture network					
Matrix					
23 - Fracture network : Linear flow					
Media / Slope sequence	1/2	BDF	1/2		
Hydraulic fracture					
Fracture network					
Matrix					
25 - Fracture network : Linear flow					
Media / Slope sequence	1/2	BDF	1/2	1/4	1/2
Hydraulic fracture					
Fracture network					
Matrix					

Figure C.4: Summary of fracture network linear flow regimes for the triple porosity model

5 - Matrix : Linear flow					
Media / Slope sequence	1/2	1/4	1/2	1/4	1/2
Hydraulic fracture					
Fracture network					
Matrix					
7 - Matrix : Linear flow					
Media / Slope sequence	1/2	1/4	1/2	BDF	1/2
Hydraulic fracture					
Fracture network					
Matrix					
10 - Matrix : Linear flow					
Media / Slope sequence	1/2	1/4	1/2	1/4	1/2
Hydraulic fracture					
Fracture network					
Matrix					
12 - Matrix : Linear flow					
Media / Slope sequence	1/2	1/4	1/2	BDF	1/2
Hydraulic fracture					
Fracture network					
Matrix					
20 - Matrix : Linear flow					
Media / Slope sequence	1/2	1/4	1/8	1/4	1/2
Hydraulic fracture					
Fracture network					
Matrix					
22 - Matrix : Linear flow					
Media / Slope sequence	1/2	1/4	1/8	1/4	1/2
Hydraulic fracture					
Fracture network					
Matrix					
26 - Matrix : Linear flow					
Media / Slope sequence	1/2	BDF	1/2	1/4	1/2
Hydraulic fracture					
Fracture network					
Matrix					
27 - Matrix : Linear flow					
Media / Slope sequence	1/2	BDF	1/2	BDF	1/2
Hydraulic fracture					
Fracture network					
Matrix					

Figure C.5: Summary of matrix linear flow regimes for the triple porosity model

2 - Hydraulic fracture + Fracture network : Bilinear flow					
Media / Slope sequence	1/2	1/4			
Hydraulic fracture					
Fracture network					
Matrix					
14 - Hydraulic fracture + Fracture network : Bilinear flow					
	1/2	1/4	1/8	1/4	
Hydraulic fracture					
Fracture network					
Matrix					
9 - Hydraulic fracture + Matrix : Bilinear flow					
Media / Slope sequence	1/2	1/4	1/2	1/4	
Hydraulic fracture					
Fracture network					
Matrix					
15 - Hydraulic fracture + Matrix : Bilinear flow					
	1/2	1/4	1/8	1/4	
Hydraulic fracture					
Fracture network					
Matrix					
4 - Fracture network + Matrix : Bilinear flow					
Media / Slope sequence	1/2	1/4	1/2	1/4	
Hydraulic fracture					
Fracture network					
Matrix					
16 - Fracture network + Matrix : Bilinear flow					
	1/2	1/4	1/8	1/4	
Hydraulic fracture					
Fracture network					
Matrix					
24 - Fracture network + Matrix : Bilinear flow					
	1/2	BDF	1/2	1/4	
Hydraulic fracture					
Fracture network					
Matrix					
13 - Hydraulic fracture + Fracture network + Matrix : Trilinear flow					
	1/2	1/4	1/8		
Hydraulic fracture					
Fracture network					
Matrix					

Figure C.6: Summary of bilinear and trilinear flow regimes for the triple porosity model

APPENDIX D

DIAGNOSIS USING RNP AND ITS DERIVATIVE

As the actual production data are never limited to just constant rate, or constant pressure behavior, it is useful to be able to use only one model to characterize both behaviors. The concept of using superposition time function instead of the actual time has been introduced. The material balance time (t_e) is one of superposition time functions which is defined as cumulative production divided by instantaneous rate, or

$$t_e = \frac{Q}{q} \quad \dots(d.11)$$

Blasingame et al. (1991) and Agarwal et al. (1998) have shown that when the material balance time can be used instead of actual time rate-normalized pressure (RNP) behaves like the drawdown pressure resulting from constant rate production. They showed that the concept accurately represents the boundary dominated flow regime. However, for this study we need to evaluate whether the RNP processing of rate decline during constant pressure production produces the same behavior as would occur by modeling drawdown under constant rate production for the linear and bilinear flow regimes.

D.1 Bilinear flow

First, the constant rate and constant pressure equations are shown in equations (d.1) and (d.2), respectively.

$$p_{wD} = \frac{\pi}{\Gamma\left(\frac{5}{4}\right)\sqrt{2(k_F b_F)_D}} t_{Dx_F,r}^{1/4} \quad \dots(d.2)$$

$$\frac{1}{q_D} = \frac{\pi \Gamma\left(\frac{3}{4}\right)}{\sqrt{2(k_F b_F)_D}} t_{Dx_F,p}^{1/4} \quad \dots(d.3)$$

Where $t_{Dx_F,r}$ and $t_{Dx_F,p}$ are the dimensionless time function for constant rate and constant pressure conditions, respectively.

First, equating Eq. (d.2) and (d.3) to find the relation between two time functions when $P_{wD} = 1/q_D$:

$$\frac{\pi}{\Gamma\left(\frac{5}{4}\right)\sqrt{2(k_F b_F)_D}} t_{Dx_F,r}^{1/4} = \frac{\pi \Gamma\left(\frac{3}{4}\right)}{\sqrt{2(k_F b_F)_D}} t_{Dx_F,p}^{1/4} \quad \dots(d.4)$$

Cancelling terms in Eq. (d.4) to have:

$$\frac{1}{\Gamma\left(\frac{5}{4}\right)} t_{Dx_F,r}^{1/4} = \Gamma\left(\frac{3}{4}\right) t_{Dx_F,p}^{1/4} \quad \dots(d.5)$$

Adjusting the form and solve for $t_{Dx_F,r}$ in terms of $t_{Dx_F,p}$:

$$t_{Dx_F,r} = \left[\Gamma\left(\frac{5}{4}\right) \cdot \Gamma\left(\frac{3}{4}\right) \right]^4 t_{Dx_F,p} \quad \dots(d.6)$$

Since $\Gamma\left(\frac{5}{4}\right)=0.9064$ and $\Gamma\left(\frac{3}{4}\right) = 1.2254$. Therefore, Eq. (d.6) can be rewritten as:

$$t_{Dx_F,r} = 1.52 t_{Dx_F,p} \quad \dots(d.7)$$

Equation (d.7) indicates that constant rate time function will be larger than constant pressure function by 1.52 times during bilinear flow regime.

Now, let's find material balance time function for bilinear flow regime that converts constant pressure to virtual constant rate:

Rearranging Eq. (d.3) for flow rate, we have

$$q_D = \frac{\sqrt{2(k_F b_F)_D}}{\pi \Gamma\left(\frac{3}{4}\right) t_{Dx_F,p}^{1/4}} \quad \dots(d.8)$$

Integrating Eq. (d.8) respect to time to get cumulative production equation:

$$Q_D = \int q_D dt_{Dx_F,p} = \frac{4}{3} \frac{\sqrt{2(k_F b_F)_D}}{\pi I\left(\frac{3}{4}\right)} t_{Dx_F,p}^{3/4} \quad \dots(d.9)$$

Dividing Eq. (d.9) with Eq. (d.8) to get a material balance time function, $t_{eD,p}$, in terms of $t_{Dx_F,p}$:

$$t_{eD,p} = \frac{Q_D}{q_D} = \frac{4}{3} t_{Dx_F,p} \quad \dots(d.10)$$

Equation (d.10) indicates that the RNP and RNP' diagnostic plots using material balance time function will shift the plots the right (later) by factor of (4/3) or 1.33 times during bilinear flow regime.

Rearranging Eq. (d.10), we know that

$$t_{Dx_F,p} = \frac{3}{4} t_{eD,p} \quad \dots(d.11)$$

Substituting Eq. (d.11) into (d.7) to get

$$t_{Dx_F,r} = 1.522 \left[\frac{3}{4} t_{eD,p} \right] \quad \dots(d.12)$$

Finalize Eq. (d.12), we have

$$t_{Dx_F,r} = 1.14 t_{eD,p} \quad \dots(d.13)$$

Therefore, the constant rate time function will be larger than the material balance time function by a factor of 1.14 during bilinear flow regime.

Comparing Eq. (d.13) with (d.7), it appears that material balance time function will shift constant pressure plots to be closer to constant rate plots, but still not identical. This implies that when plotting RNP and RNP derivative by using material balance time function, a multiplier correction factor of 1.14 is required to convert completely the constant pressure plots to the constant rate plots.

D.2 Linear flow

The observations for linear flow have been presented by Anderson and Mattar (2003). The same methodology as shown for the bilinear flow is used. The results are recapped here for completeness.

First, the constant rate and constant pressure equations for linear flow regime are shown in Eq. (d.14) and (d.15), respectively.

$$p_{wD} = \sqrt{\pi t_{D,r}} \quad \dots(d.14)$$

$$\frac{1}{q_D} = \frac{\pi}{2} \sqrt{\pi t_{D,p}} \quad \dots(d.15)$$

Where $t_{D,r}$ and $t_{D,p}$ are the dimensionless time function for constant rate and constant pressure conditions, respectively.

Now, equating Eq. (d.14) and (d.15) to find the relation between two time functions when $P_{wD} = 1/q_D$, we have:

$$\sqrt{\pi t_{D,r}} = \frac{\pi}{2} \sqrt{\pi t_{D,p}} \quad \dots(d.16)$$

Cancelling terms in Eq. (d.16) to have:

$$\sqrt{t_{D,r}} = \frac{\pi}{2} \sqrt{t_{D,p}} \quad \dots(d.17)$$

Adjusting the form and solve for $t_{D,r}$ in terms of $t_{D,p}$:

$$t_{D,r} = \frac{\pi^2}{4} t_{D,p} = 2.46 t_{D,p} \quad \dots(d.18)$$

Equation (d.18) indicates that constant rate time function will be larger than constant pressure function by 2.46 times during linear flow regime.

Now, let's find material balance time function for linear flow regime that converts constant pressure to virtual constant rate.

Rearranging Eq. (d.15) for flow rate, we have

$$q_D = \frac{2}{\pi\sqrt{\pi t_{D,p}}} \quad \dots(d.19)$$

Integrating Eq. (D.19) respect to time to get cumulative production equation:

$$Q_D = \int q_D dt_{Dx_F,p} = 2 \left[\frac{2}{\pi\sqrt{\pi}} \right] t_{D,p}^{1/2} \quad \dots(d.20)$$

Dividing Eq. (d.20) with Eq. (d.19) to get a material balance time function,

$t_{eD,p}$, in terms of $t_{D,p}$:

$$t_{eD,p} = 2t_{D,p} \quad \dots(d.21)$$

Equation (d.21) indicates that the RNP and RNP' diagnostic plots using material balance time function will shift the plots the right (later) by factor of 2 during linear flow regime.

Rearranging Eq. (d.21), we know that

$$t_{D,p} = \frac{1}{2} t_{eD,p} \quad \dots(d.22)$$

Substituting Eq. (d.22) into (d.18) to get

$$t_{D,r} = 2.46 \left[\frac{1}{2} t_{eD,p} \right] = 1.23 t_{eD,p} \quad \dots(d.23)$$

Therefore, the constant rate time function will be larger than the material balance time function by a factor of 1.23 during linear flow regime.

Comparing Eq. (d.23) with (d.18), it indicates that material balance time function will shift constant pressure response to be closer to constant rate response, but still do not overlay completely. This implies that when plotting RNP and RNP derivative by using material balance time function, a multiplier correction factor of 1.23 is required to convert completely the constant pressure plots to the constant rate plots.

To summarize, during linear flow period, using material balance time will shift constant pressure time function to the right by a factor of 2. However, it will not convert the constant pressure to constant rate perfectly because the constant rate time function is larger than constant pressure time function by a factor of 2.46. This indicates that the constant rate time function will still larger than the material balance time function by a factor of $2.46 / 2 = 1.23$. Figure D.1 summarize these concepts.

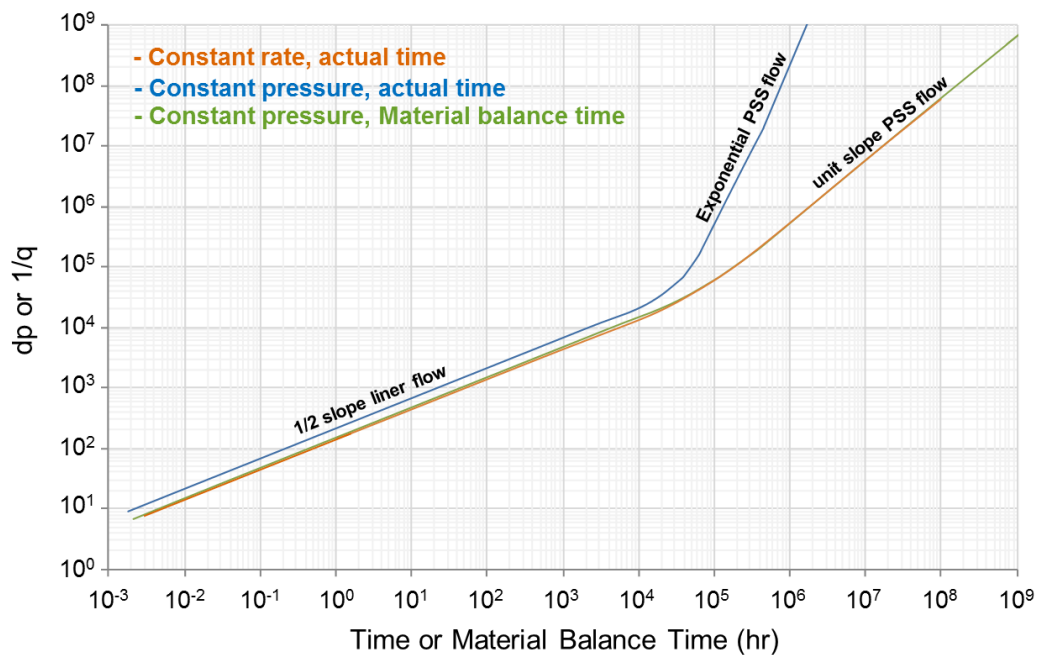


Figure D.1: Flow behavior comparison among different flow conditions and time function

Note that material balance time works perfectly during PSS flow regime as shown in Figure D.1 that both constant rate and constant pressure using material balance time plots are overlain perfectly.

D.3 Distance of investigation

Now, let's consider a distance of investigation equation for linear flow in constant pressure condition shown in Eq. (d.24).

$$x = 0.159 \sqrt{\frac{kt_{elf}}{(\phi\mu c_t)_i}} \quad \dots(d.24)$$

Where t_{elf} is the actual time in days at the end of linear flow seen as a deviation from a 1/2 slope trend on log-log plots.

Note that the relations among the dimensionless time functions derived earlier are also applicable with dimensional time function. Eq. (d.25) shows dimensional form of Eq. (d.22).

Linear flow

$$t = \frac{1}{2} t_e \quad \dots(d.25)$$

Where t is a constant rate time function, and t_e is a material balance time function used to convert constant pressure response to virtual constant rate response.

Substituting t and t_e in Eq. (d.25) with t_{elf} and t_e with $t_{e,elf}$ respectively to have

$$t_{elf} = \frac{1}{2} t_{e,elf} \quad \dots(d.26)$$

Where $t_{e,elf}$ is material balance time in days at the end of 1/2 slope linear flow as seen on log-log RNP and RNP' versus material balance time plots.

Substituting Eq. (d.26) into Eq. (d.24) we have

$$x = 0.159 \sqrt{\frac{k(t_{e,elf})/2}{(\phi\mu c_t)_i}} \quad \dots(d.27)$$

Finalize Eq. (d.27) to get

$$x = 0.1125 \sqrt{\frac{kt_{e,elf}}{(\phi\mu c_t)_i}} \quad \dots(d.28)$$

Eq. (d.28) must be used to calculate distance of investigation instead of Eq. (d.24) when material balance time directly read from the log-log RNP plots is used instead of the actual time.

D.4 Observations

First, let's recap the dimensionless time function used to derive the distance of investigation equation shown below (Wattenbarger et al., 1998).

$$t_{Dye} = \frac{0.00633kt}{(\phi\mu c_t)_i x^2} \quad \dots(d.29)$$

where x is the distance from fracture.

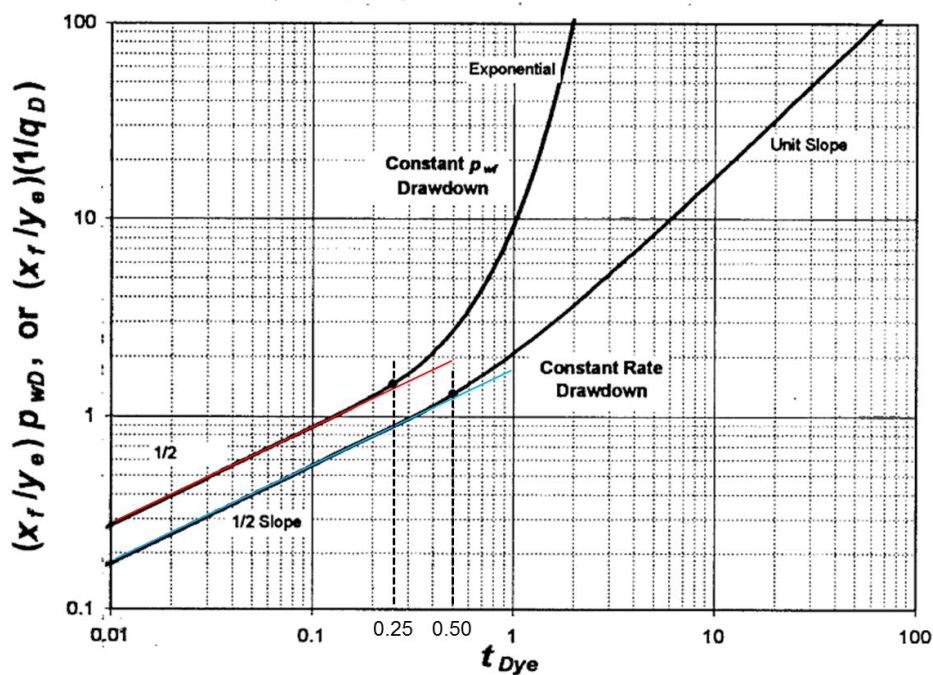


Figure D.2: t_{Dye} assumption for distance to boundary equation derivation

From Figure D.2, the time corresponding to the distance to boundary are assumed at $t_{Dye} = 0.50$ for constant rate, and $t_{Dye} = 0.25$ for constant pressure. Note that these values are defined as the departure time that can *visually* see on log-log plots, and not the first points that deviated from the 1/2 slope straight line.

The distance to boundary equations are then derived by substituting these values into Eq. (d.29) and solve for y_e . Eq.(d.30) and (d.31) show the equations for constant rate and constant pressure cases, respectively.

$$x = 0.113 \sqrt{\frac{kt_{ehs}}{(\phi\mu c_t)_i}} \quad \dots(d.30)$$

$$x = 0.159 \sqrt{\frac{kt_{ehs}}{(\phi\mu c_t)_i}} \quad \dots(d.31)$$

Here, it should be noted that the assumed t_{Dye} for constant pressure and constant rate cases are separated by a factor of 2. However, we've shown earlier that the constant rate and constant pressure time function are separated by the factor of 2.46, not 2 as assumed. Therefore, these equations may need to be revised for more consistency.

APPENDIX E

BARNETT WELL SPECIALIZED PLOTS

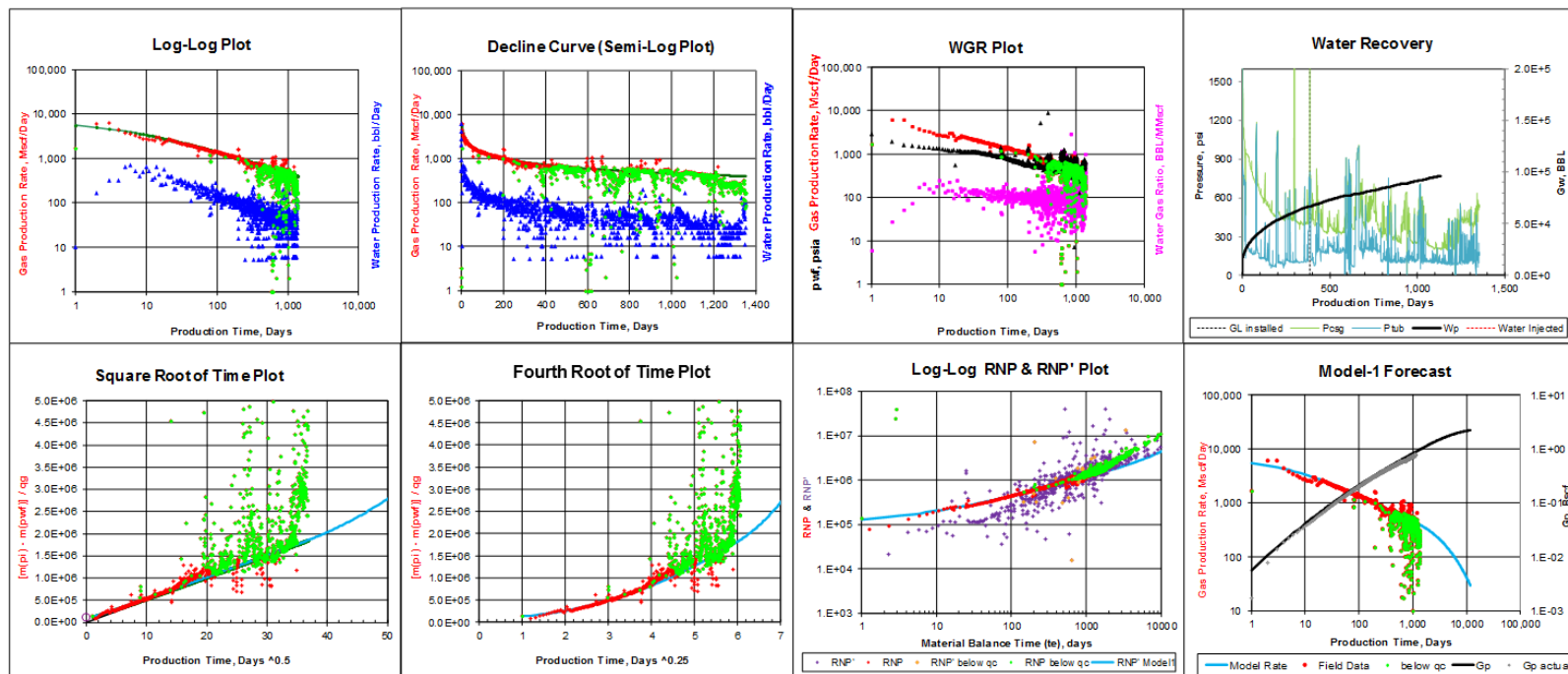
While the *RNP* and its derivative have been featured in this study, many other specialized plots are commonly used in the industry. To illustrate how RNP trends appear on these plots, samples are shown for several Barnett shale wells in this appendix. The use of specialized plots should be based on what is seen in the RNP and derivative representation.

Run Analysis

Show / Hide $q_g < \text{critical}$

Run Model 1 Forecast

well: **ADIT1H**

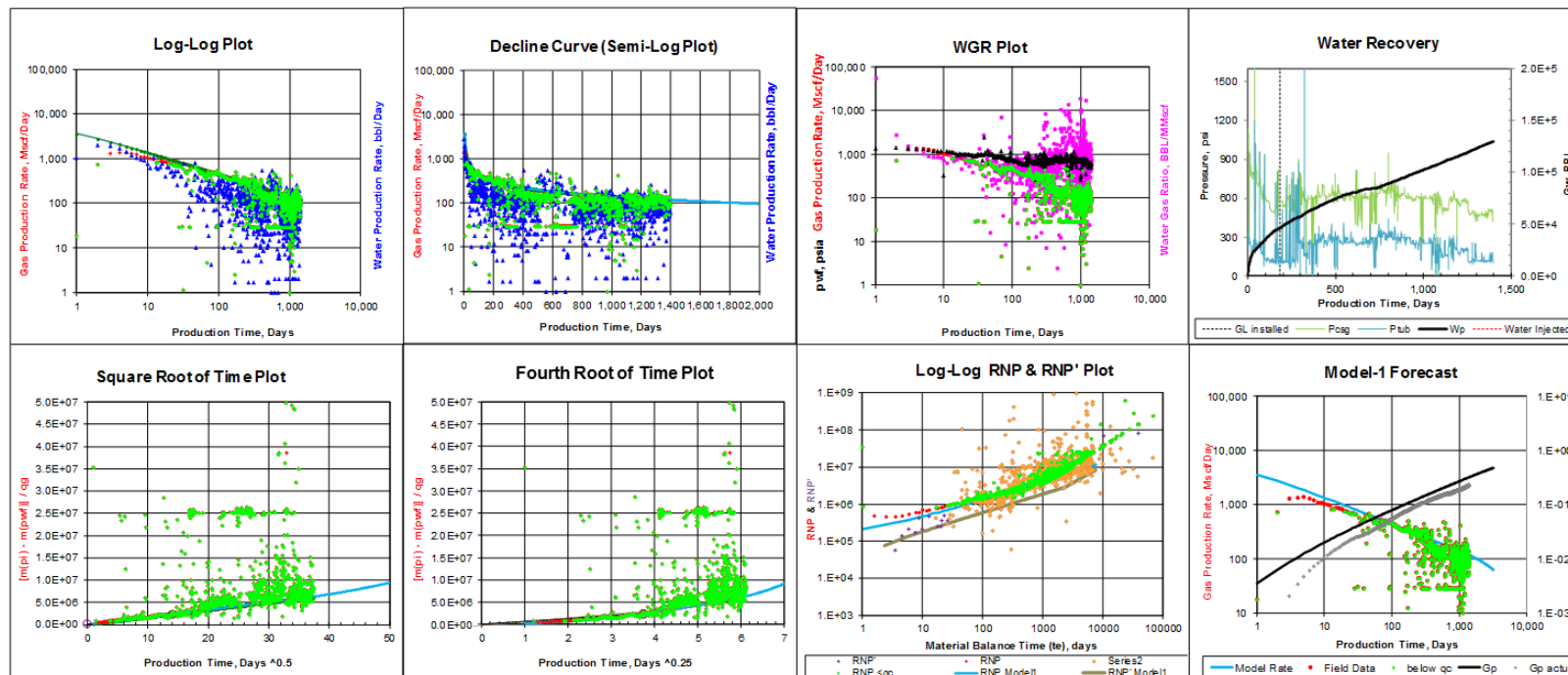


Run Analysis

Show / Hide $qg < \text{critical}$

Run Model 1 Forecast

well: **AFUN1H**

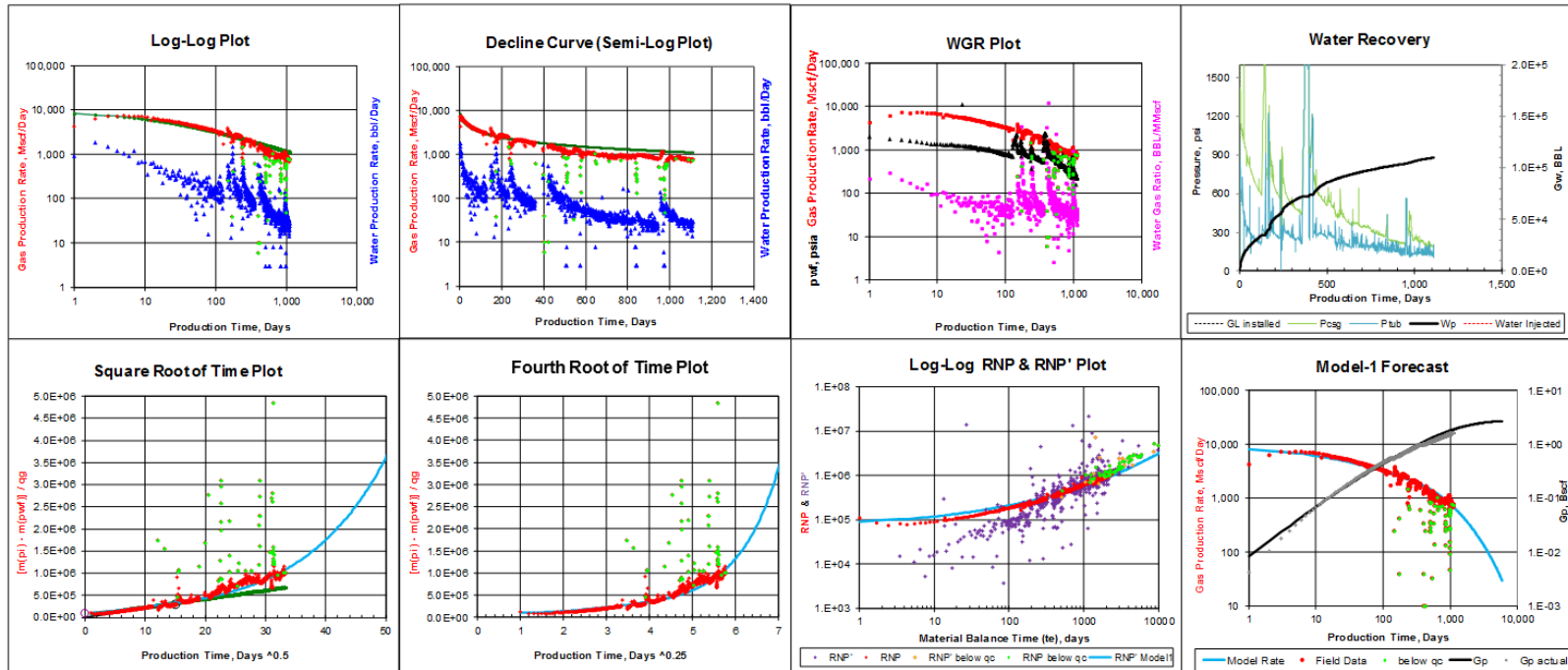


Run Analysis

Show / Hide qg<critical

Run Model 1 Forecast

well: **BANI1H**

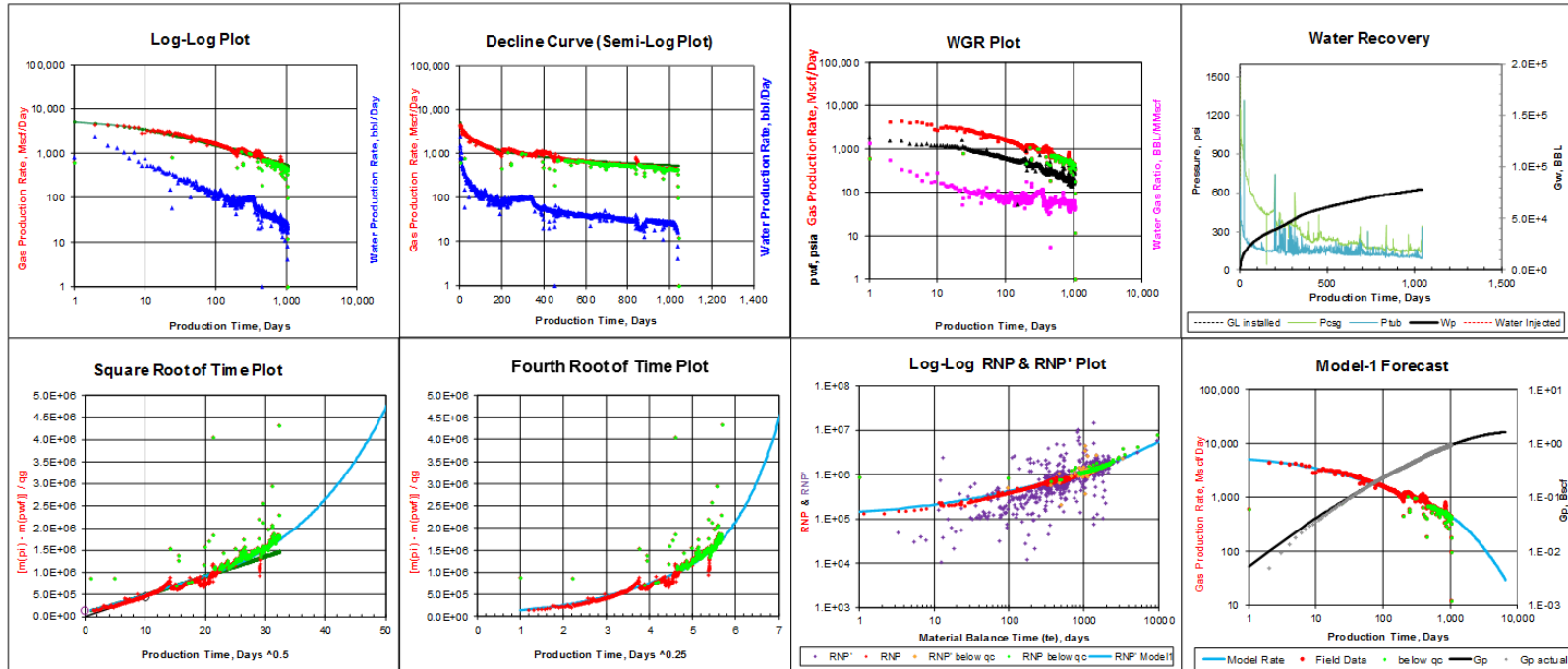


Run Analysis

Show / Hide $q_g < \text{critical}$

Run Model 1 Forecast

well: CANS5H

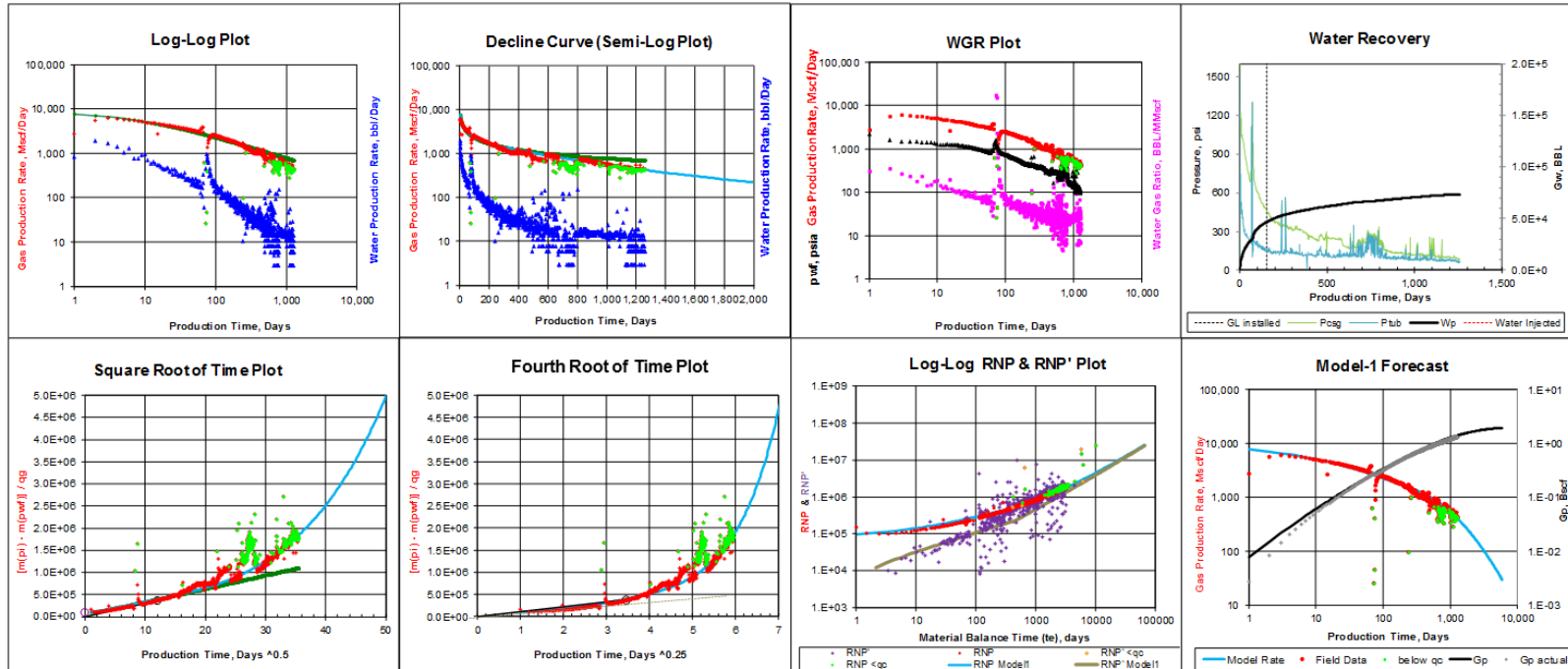


Run Analysis

Show / Hide $q_g < \text{critical}$

Run Model 1 Forecast

well: CA U4H

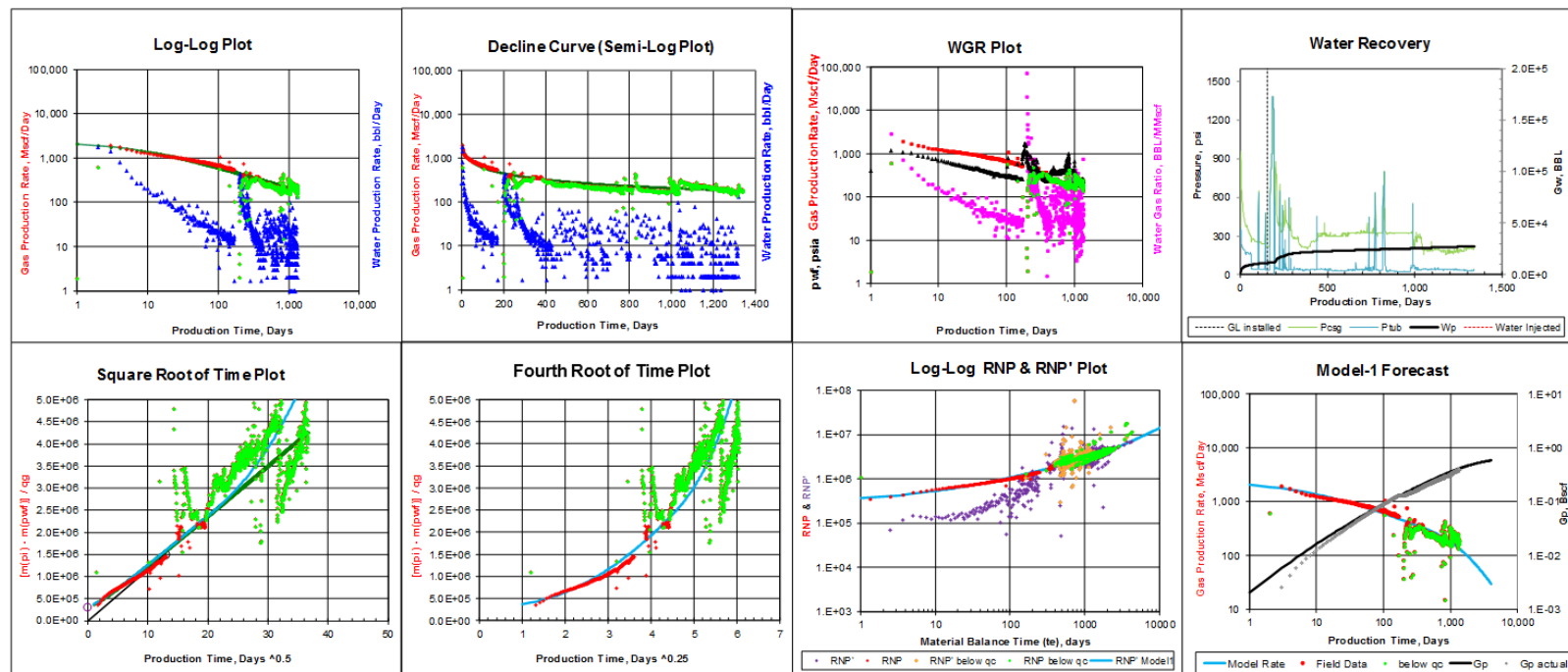


Run Analysis

Show / Hide $q_g < \text{critical}$

Run Model 1 Forecast

well: **DIUN**

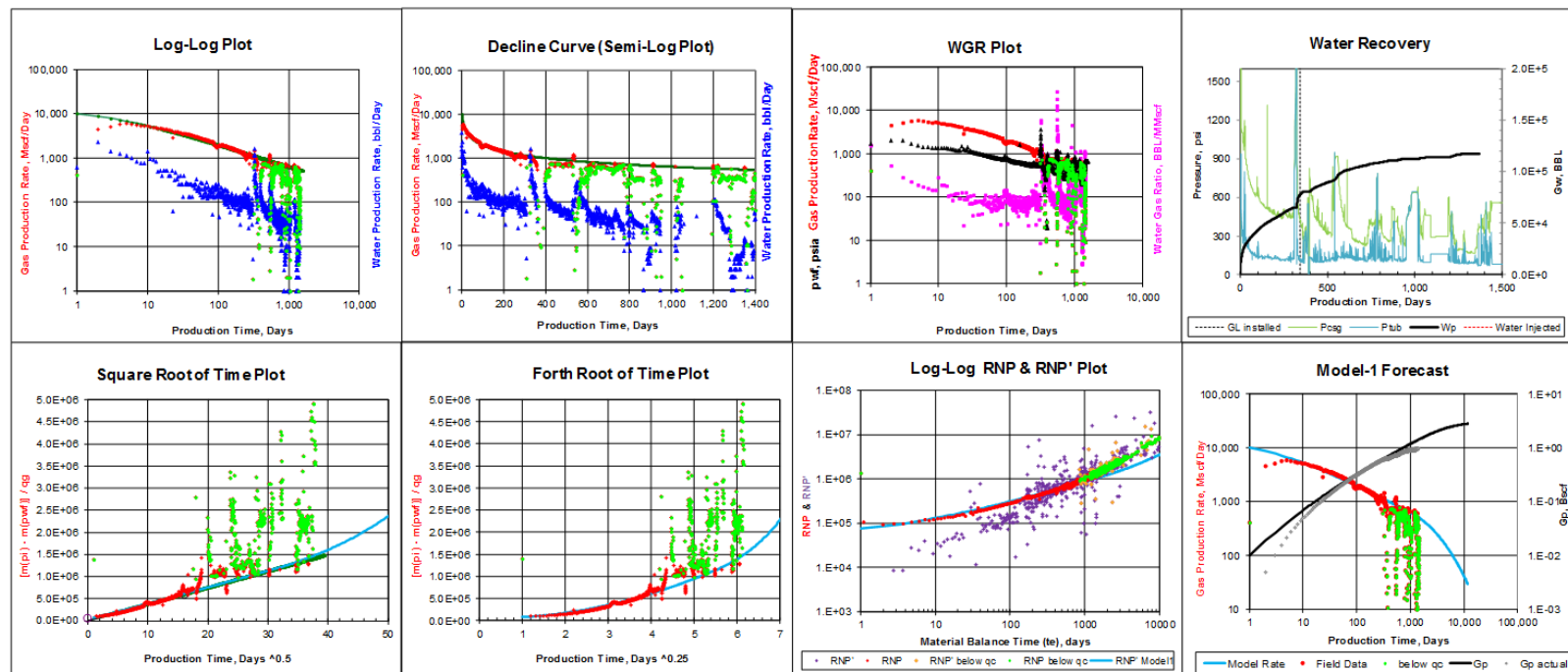


Run Analysis

Show / Hide $q_g < \text{critical}$

Run Model 1 Forecast

well: EARD1H

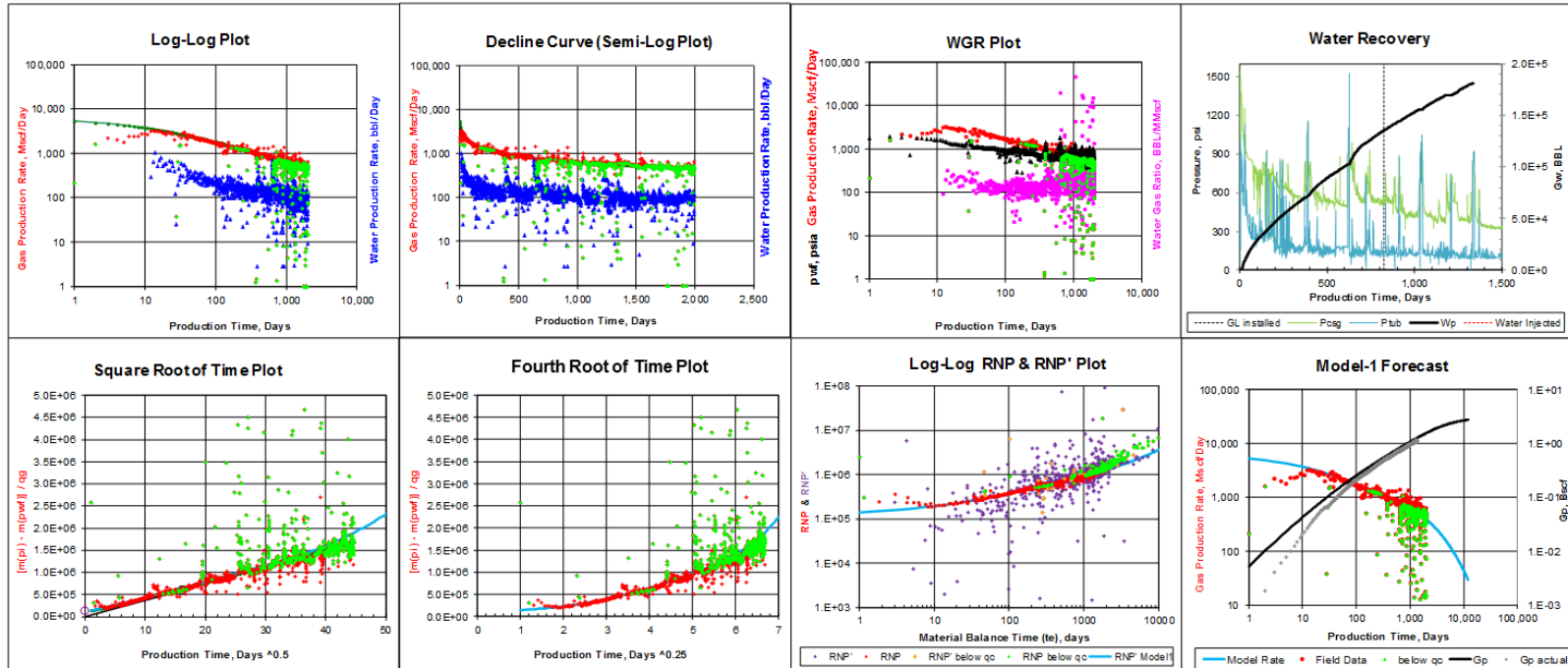


Run Analysis

Show / Hide $q_g < \text{critical}$

Run Model 1 Forecast

well: **FAA'1H**

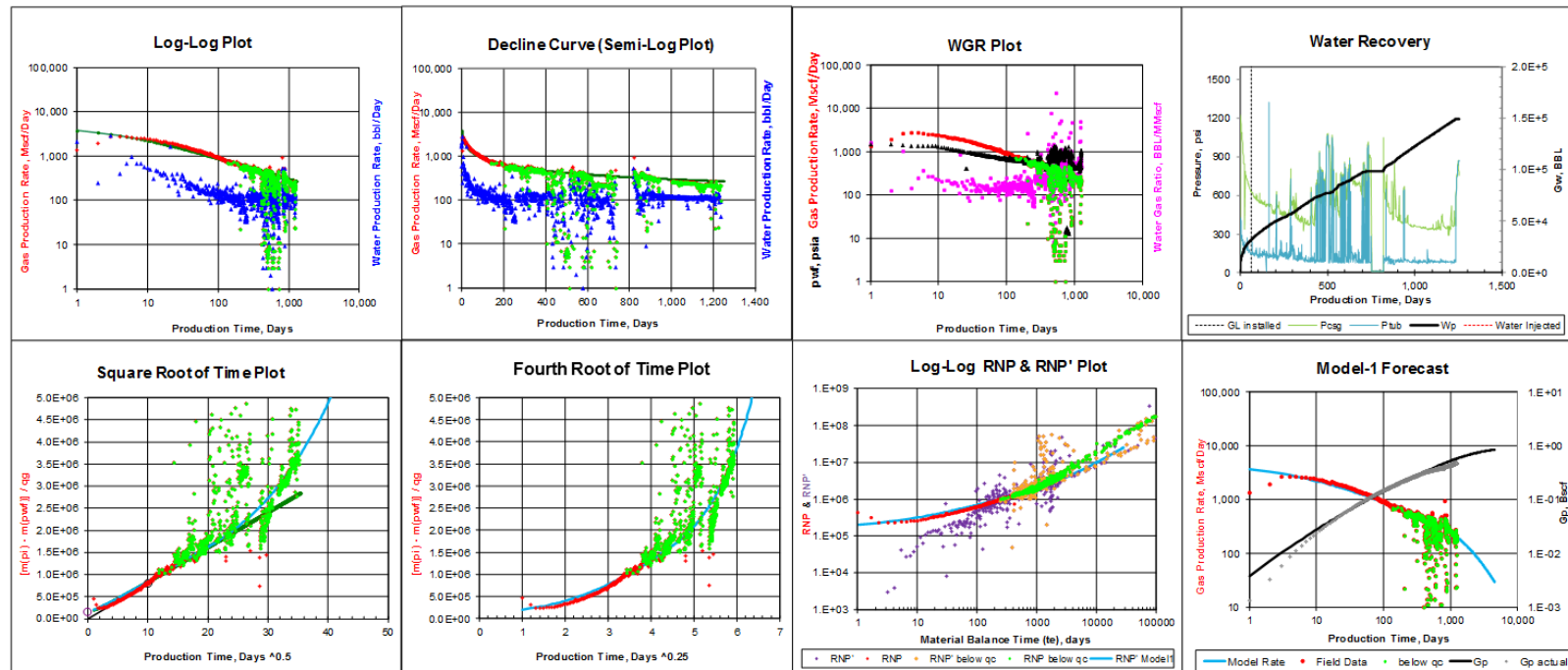


Run Analysis

Show / Hide $q_g < \text{critical}$

Run Model 1 Forecast

well: **GEH0H**

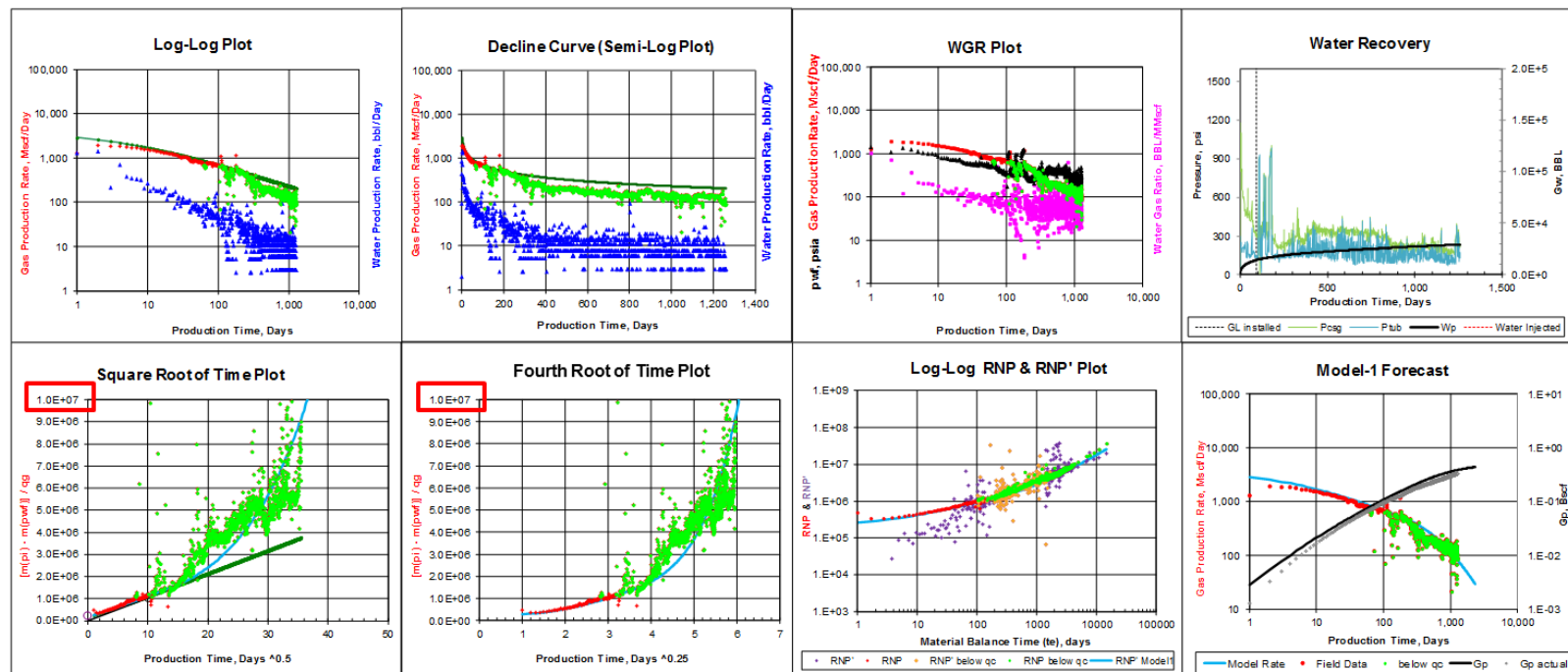


Run Analysis

Show / Hide $q_g < \text{critical}$

Run Model 1 Forecast

well: HA1H

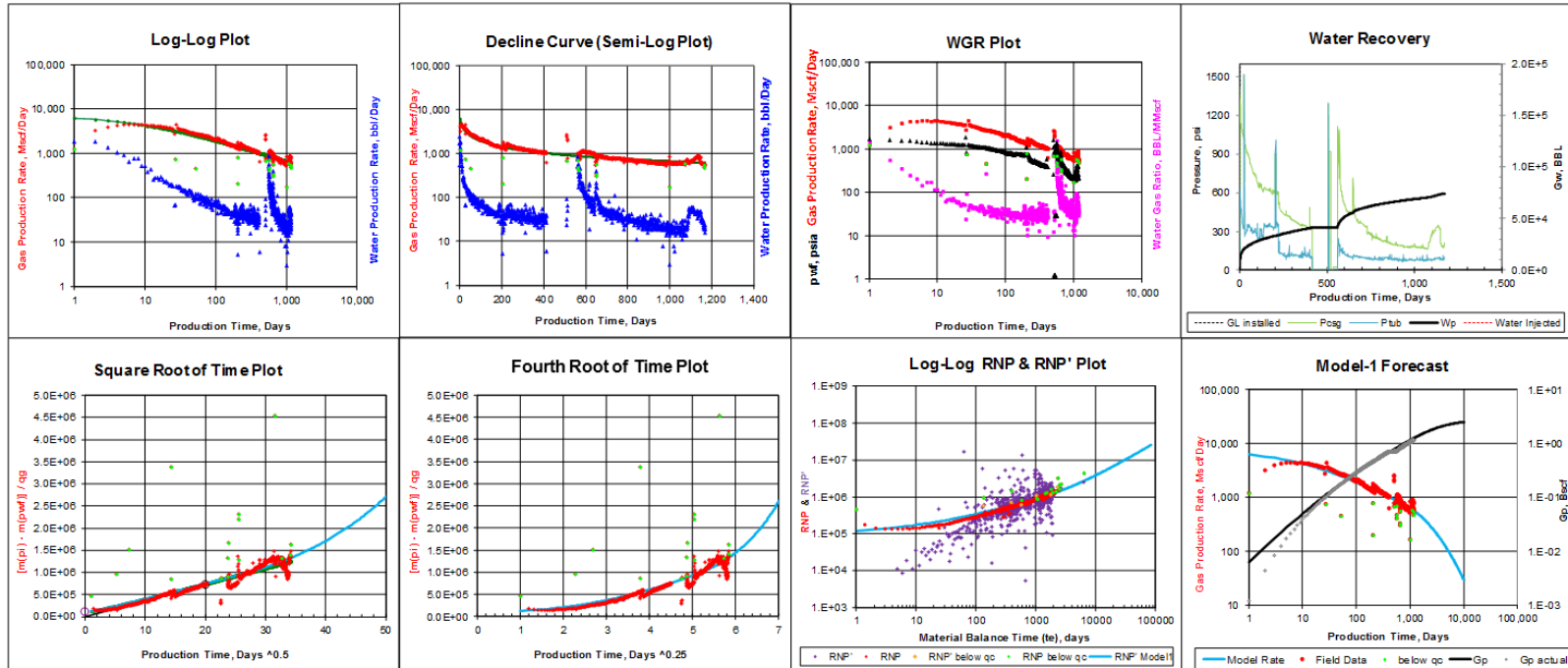


Run Analysis

Show / Hide $q_g < \text{critical}$

Run Model 1 Forecast

well: JCES1H

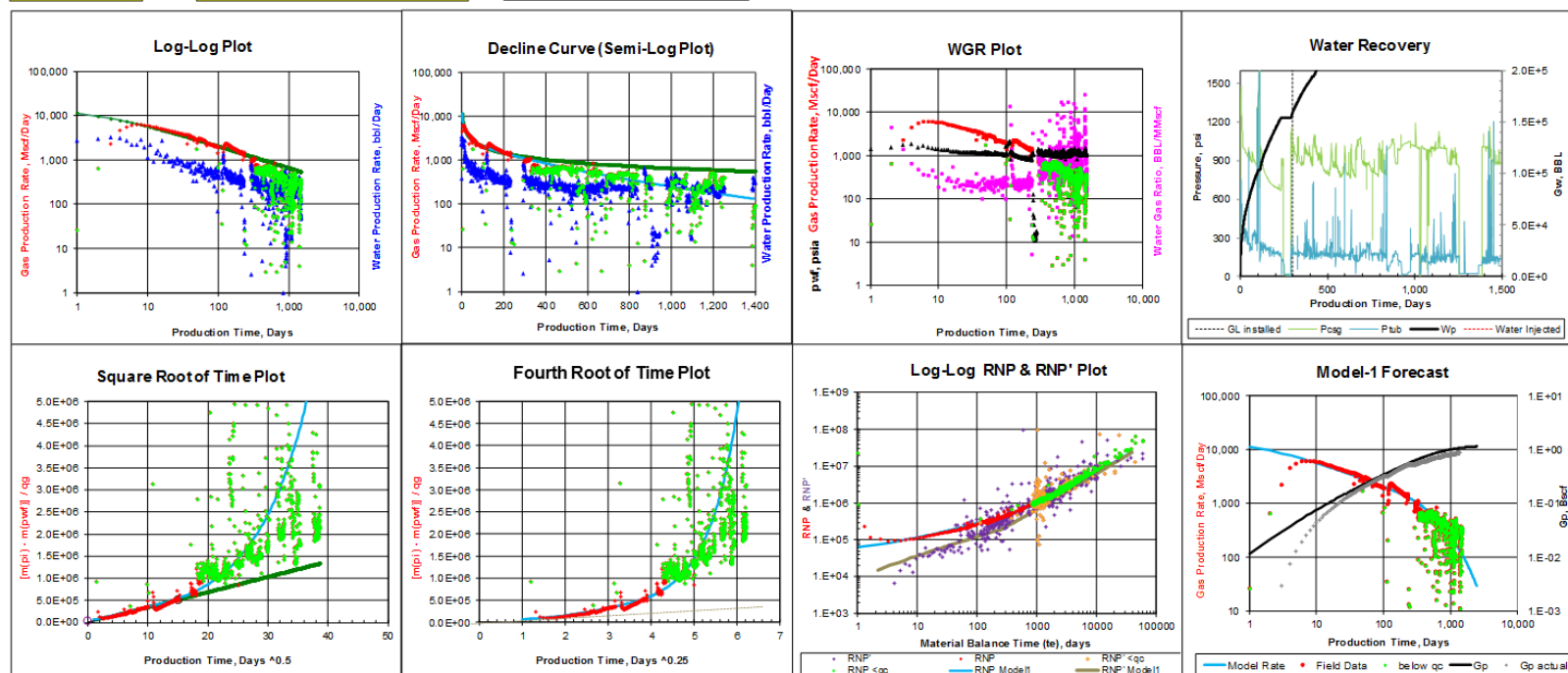


Run Analysis

Show / Hide $q_g < \text{critical}$

Run Model 1 Forecast

well: **K12H**

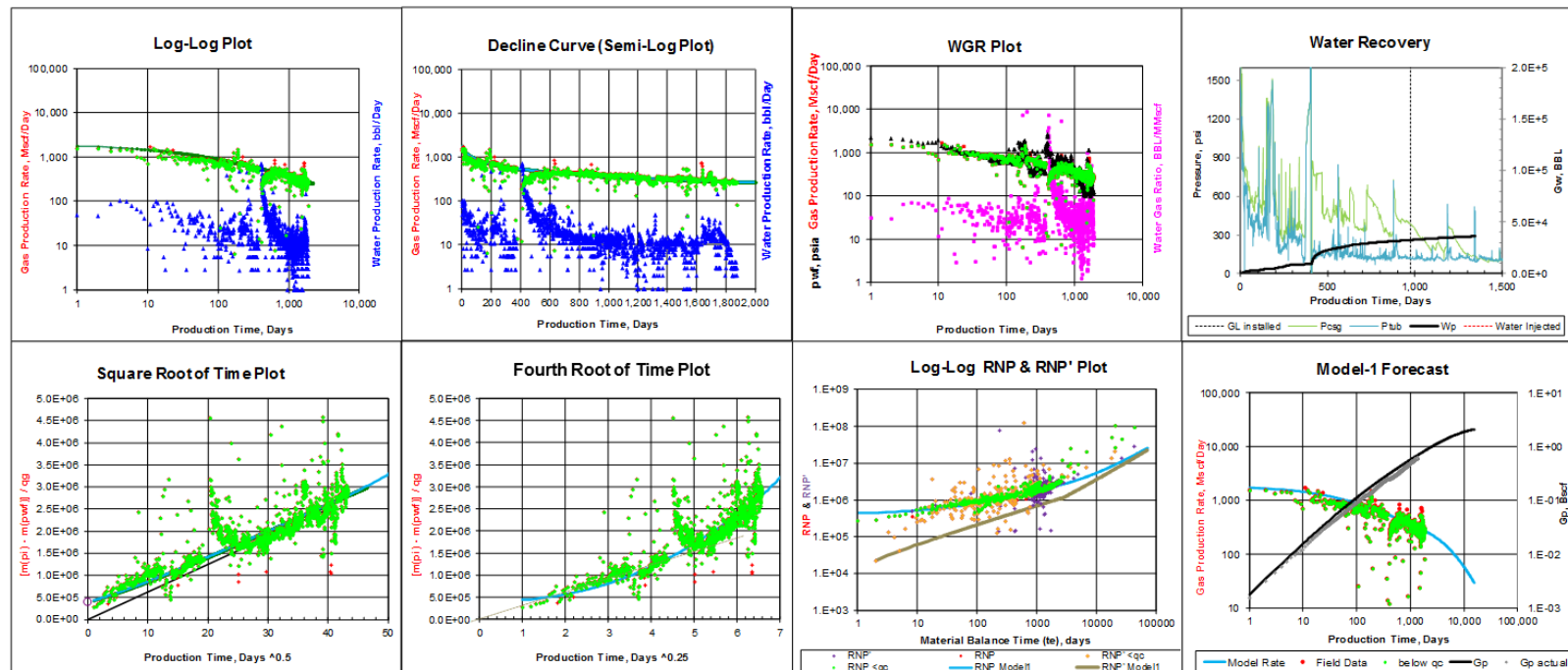


Run Analysis

Show / Hide $q_g < \text{critical}$

Run Model 1 Forecast

well: LAR 1H

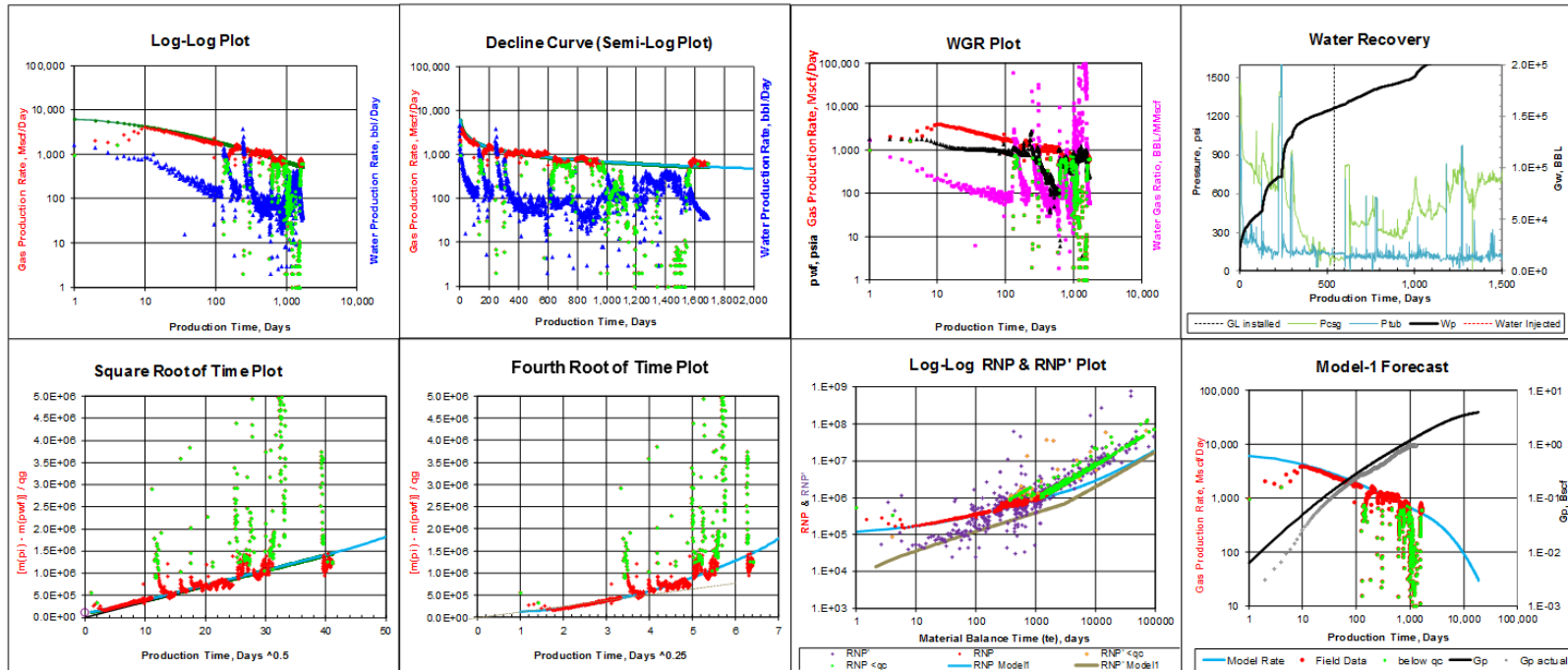


Run Analysis

Show / Hide $q_g < \text{critical}$

Run Model 1 Forecast

well: **MANI1H**

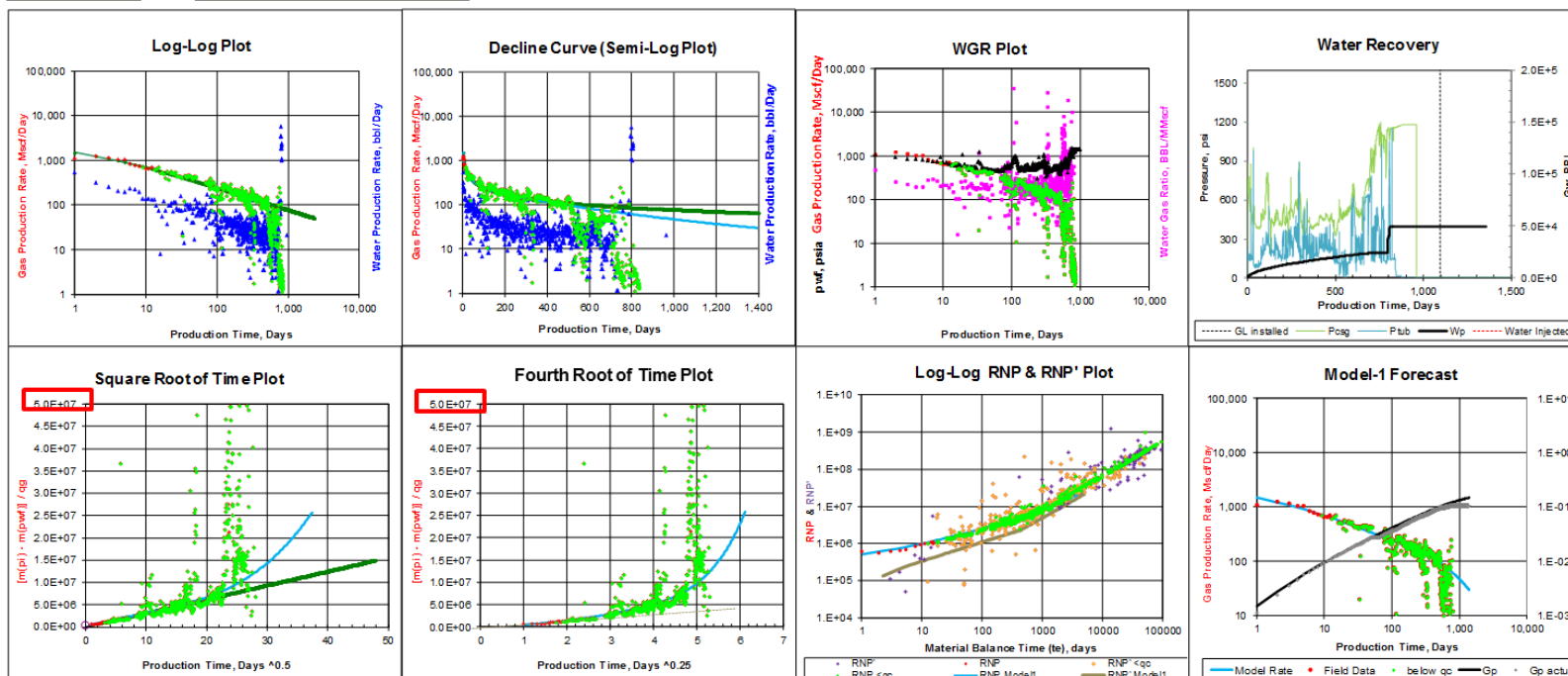


Run Analysis

Show / Hide $q_g < q_c$

Run Model 1 Forecast

well: O'H1H

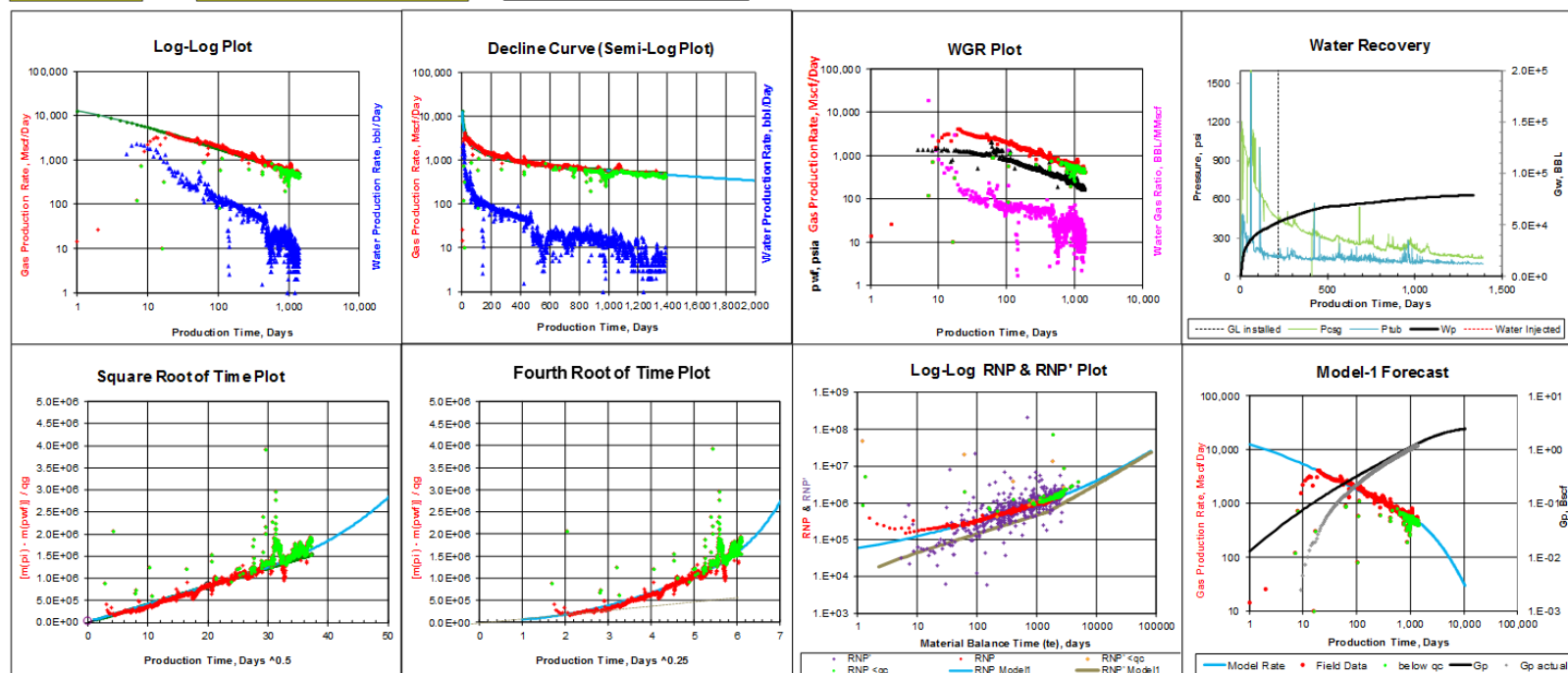


Run Analysis

Show / Hide $q_g < \text{critical}$

Run Model 1 Forecast

well: PAH1H

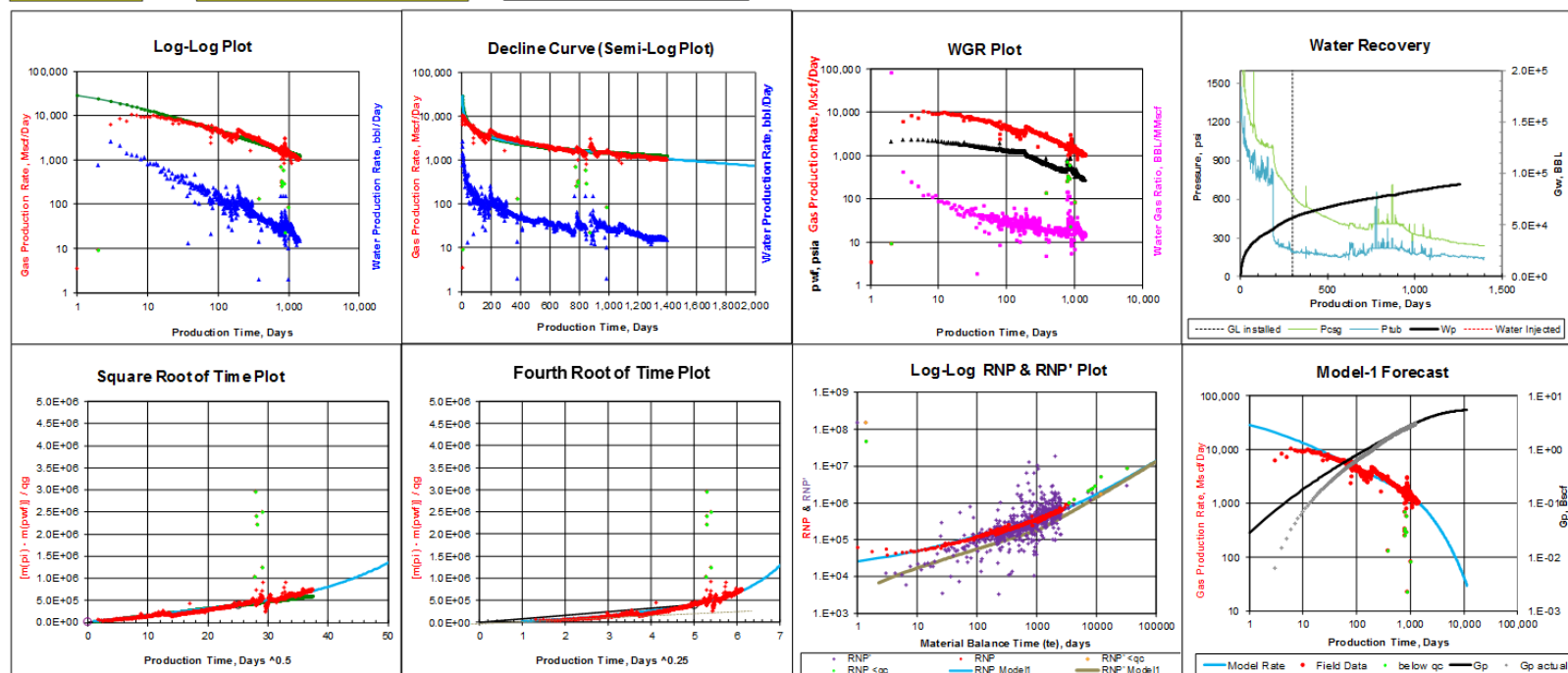


Run Analysis

Show / Hide $q_g < q_c$

Run Model 1 Forecast

well: **RAIT3H**

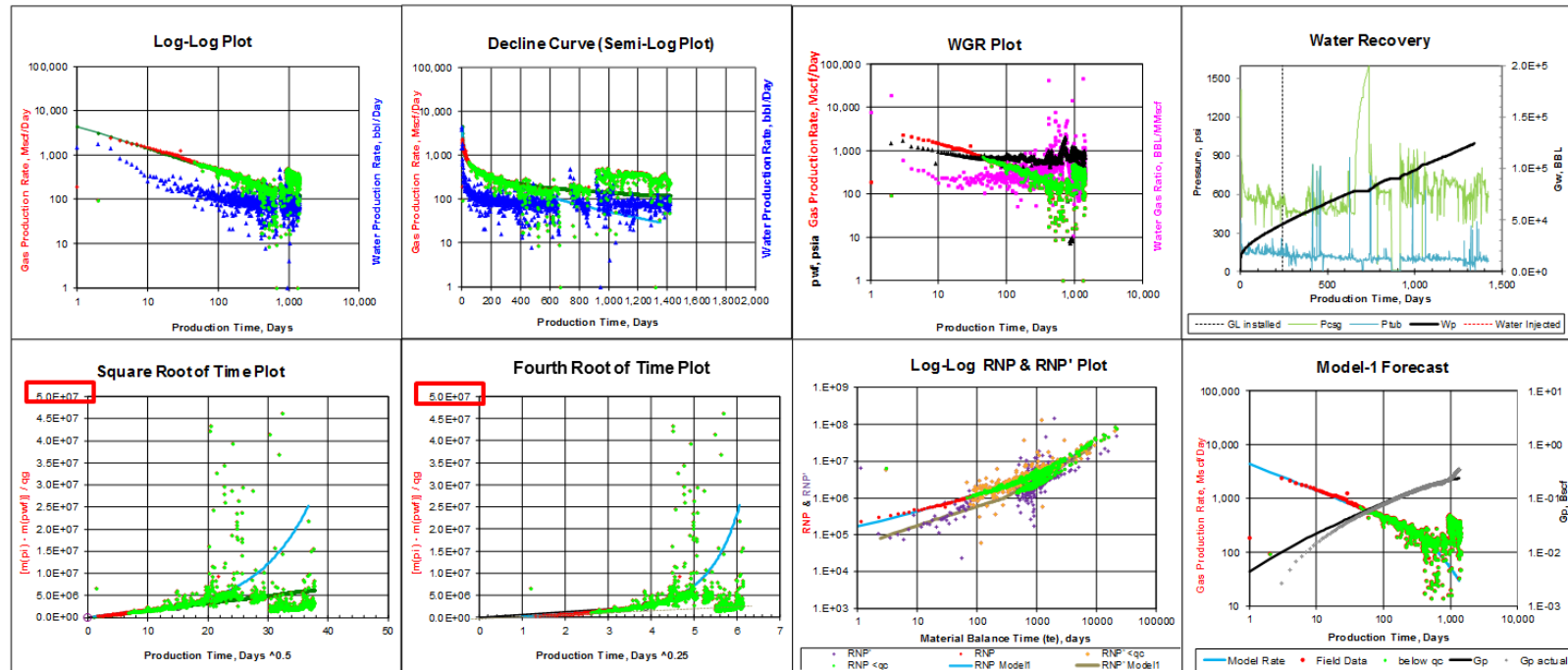


Run Analysis

Show / Hide $q_g < q_c$

Run Model 1 Forecast

well: SANI1H

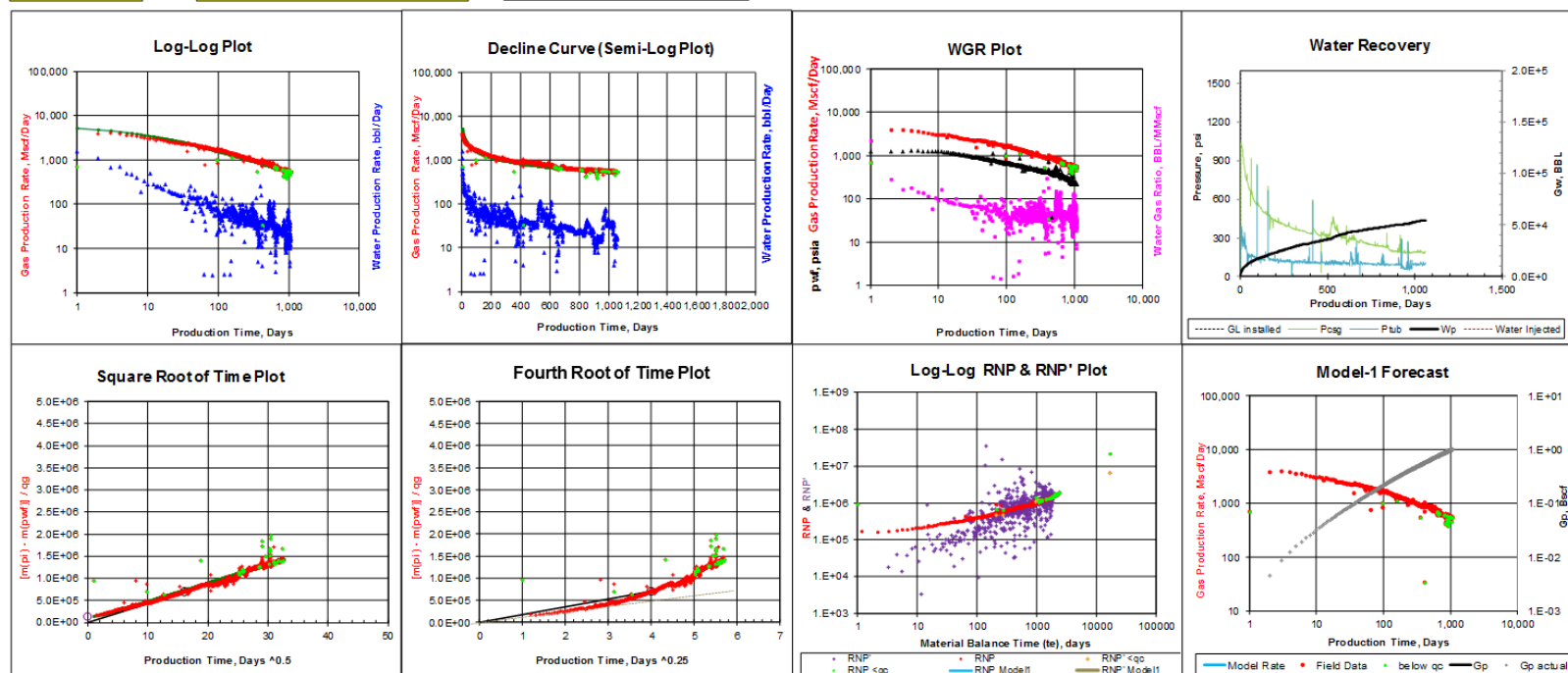


Run Analysis

Show / Hide $q_g < q_c$

Run Model 1 Forecast

well: SCA 3H

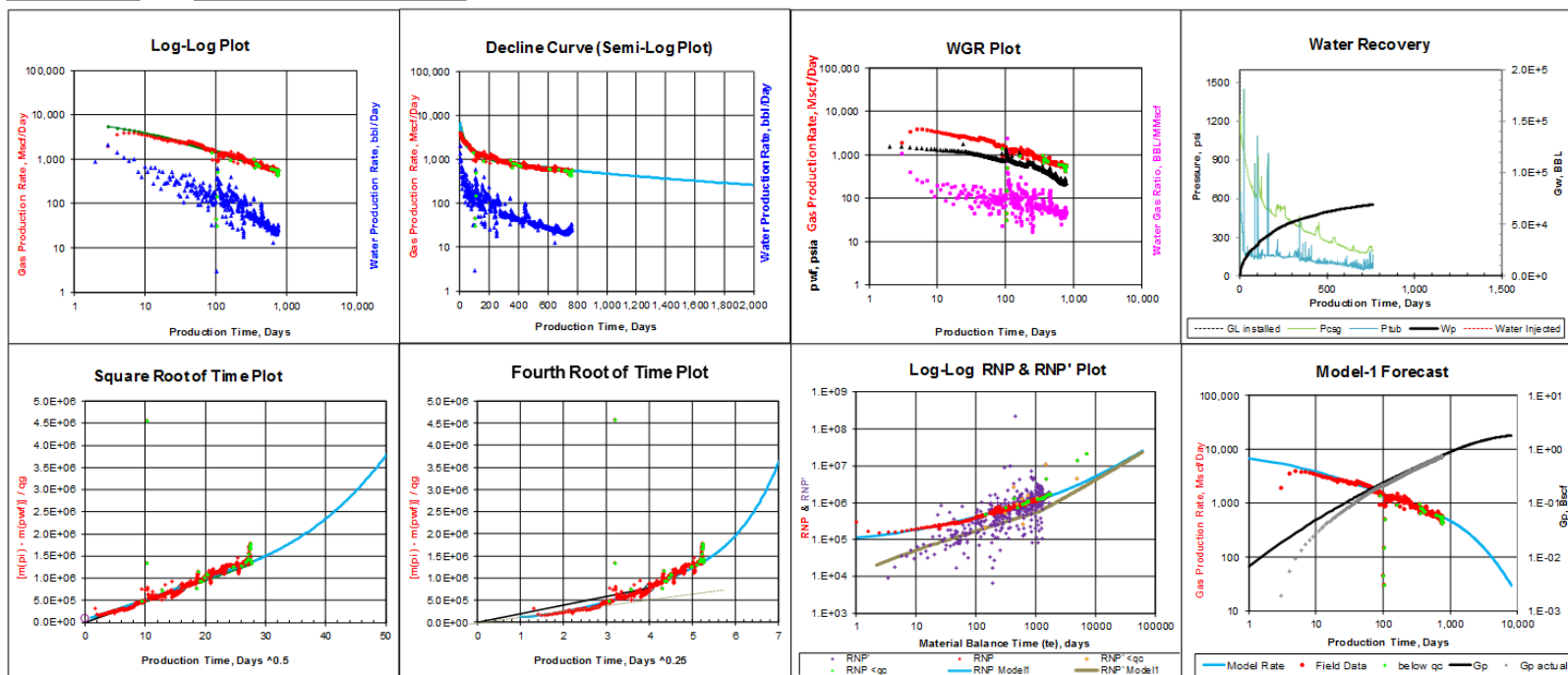


Run Analysis

Show / Hide $q_g < q_c$

Run Model 1 Forecast

well: STUN5H

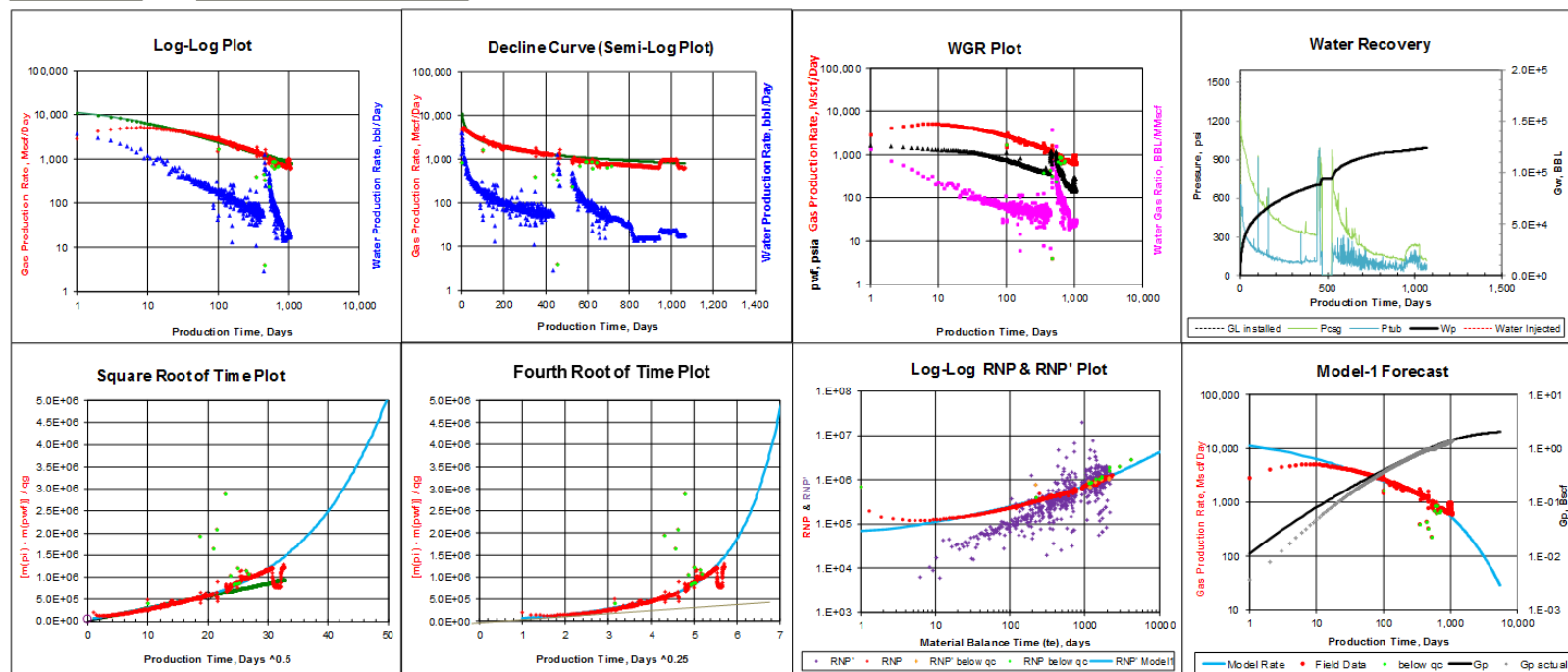


Run Analysis

Show / Hide qq<critical

Run Model 1 Forecast

well: TRUN4H

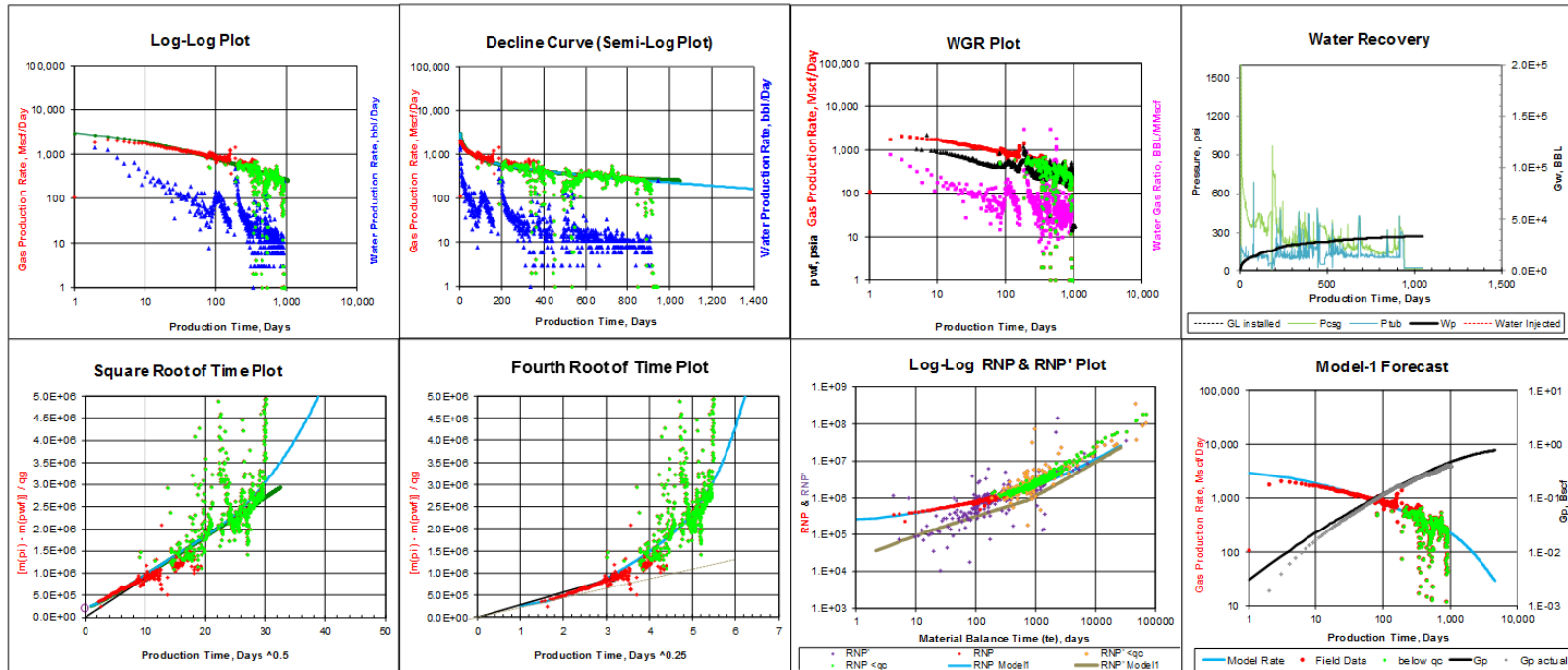


Run Analysis

Show / Hide $q_g < \text{critical}$

Run Model 1 Forecast

well: **US144H**

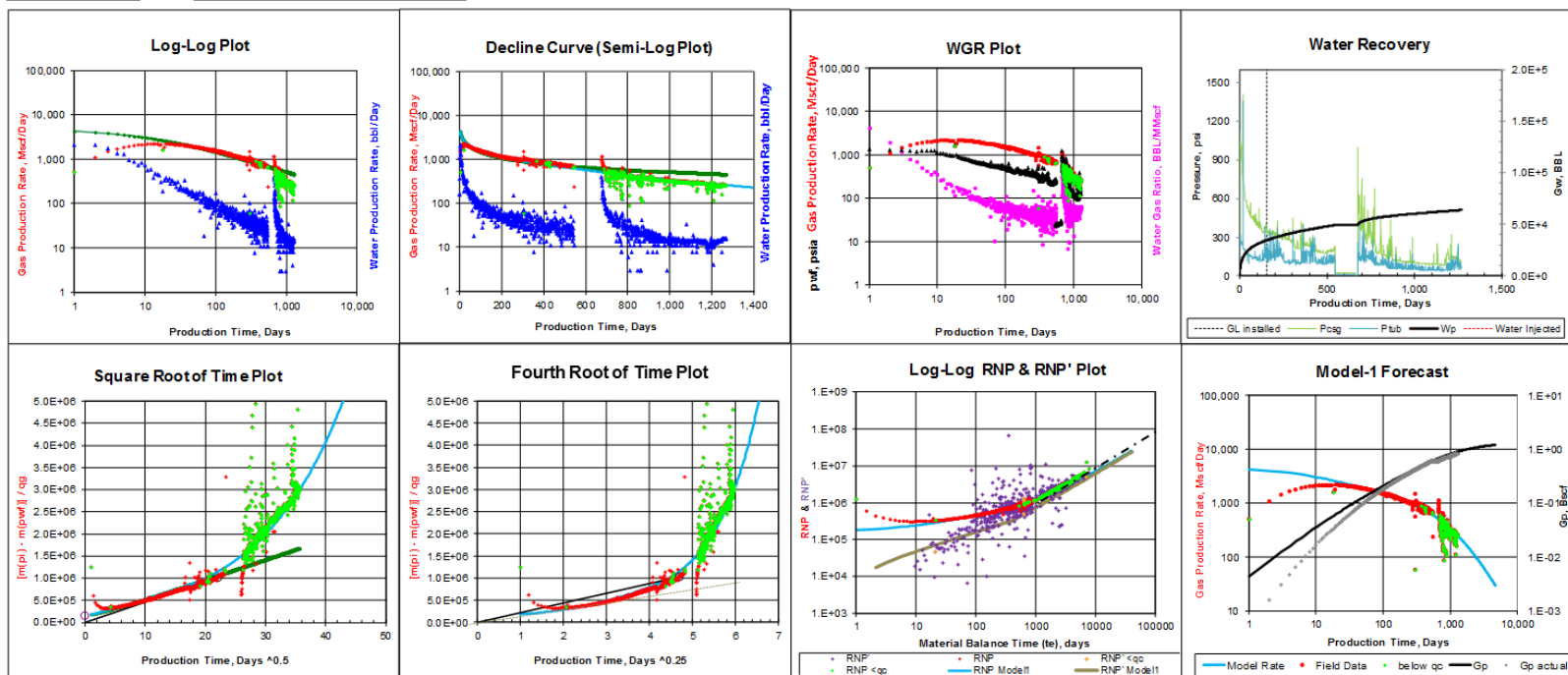


Run Analysis

Show / Hide $q_g < \text{critical}$

Run Model 1 Forecast

well: **WA1H1H**



APPENDIX F

HORN RIVER SHALE SPECIALIZED PLOTS

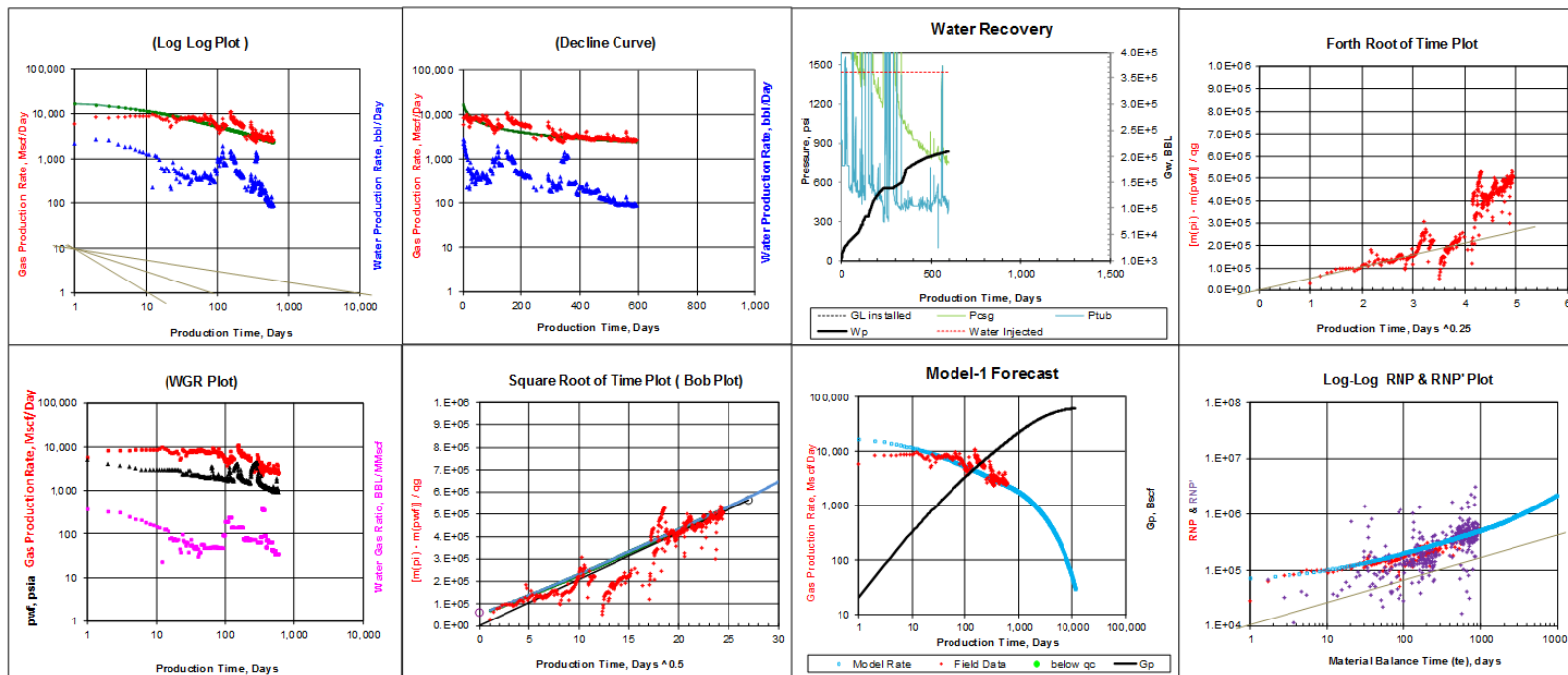
While the RNP and its derivative have been featured in this study, many other specialized plots are commonly used in the industry. To illustrate how RNP trends appear on these plots, samples are shown for several Horn River shale wells in this appendix. The use of specialized plots should be based on what is seen in the RNP and derivative representation.

Run Analysis

Show / Hide $q_g < \text{critical}$

Run Model 1 Forecast

Well : dA

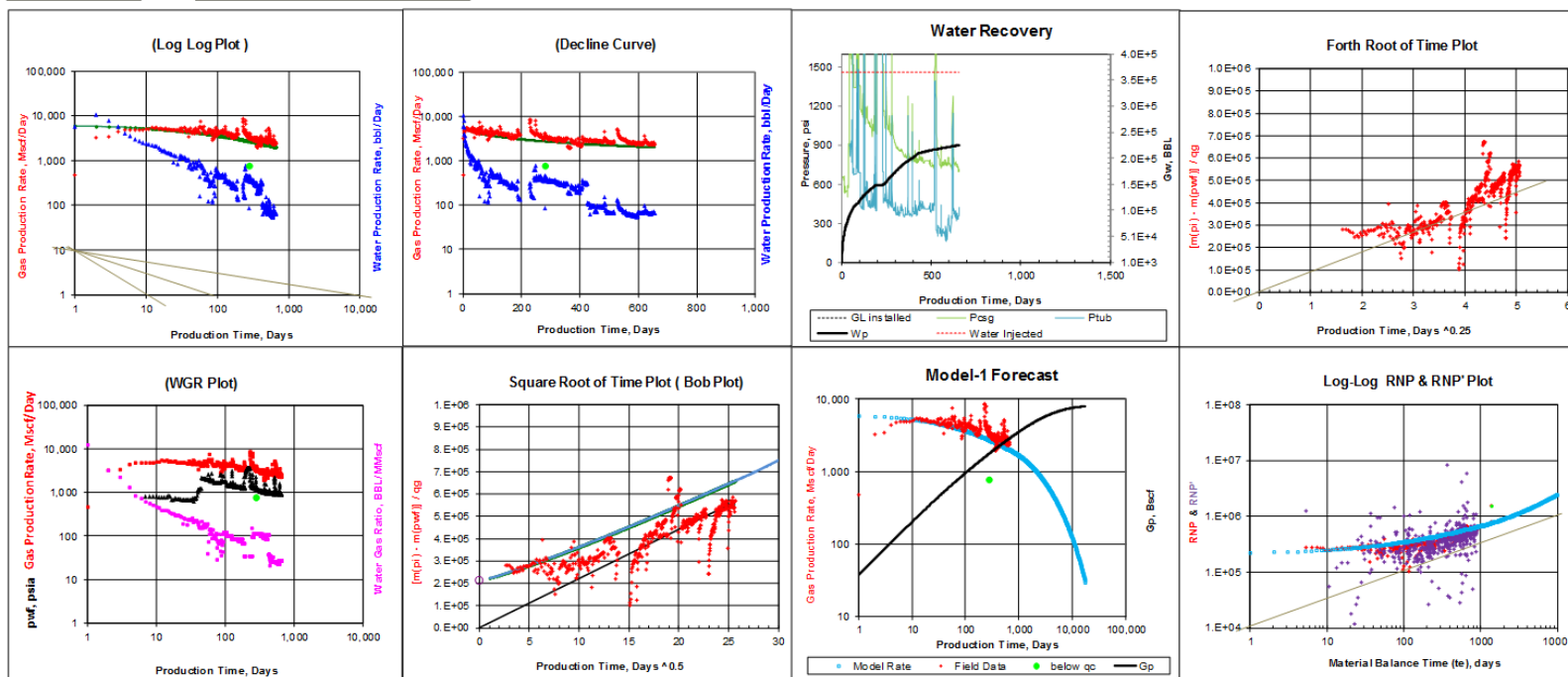


Run Analysis

Show / Hide $q_g < \text{critical}$

Run Model 1 Forecast

Well : **dB**

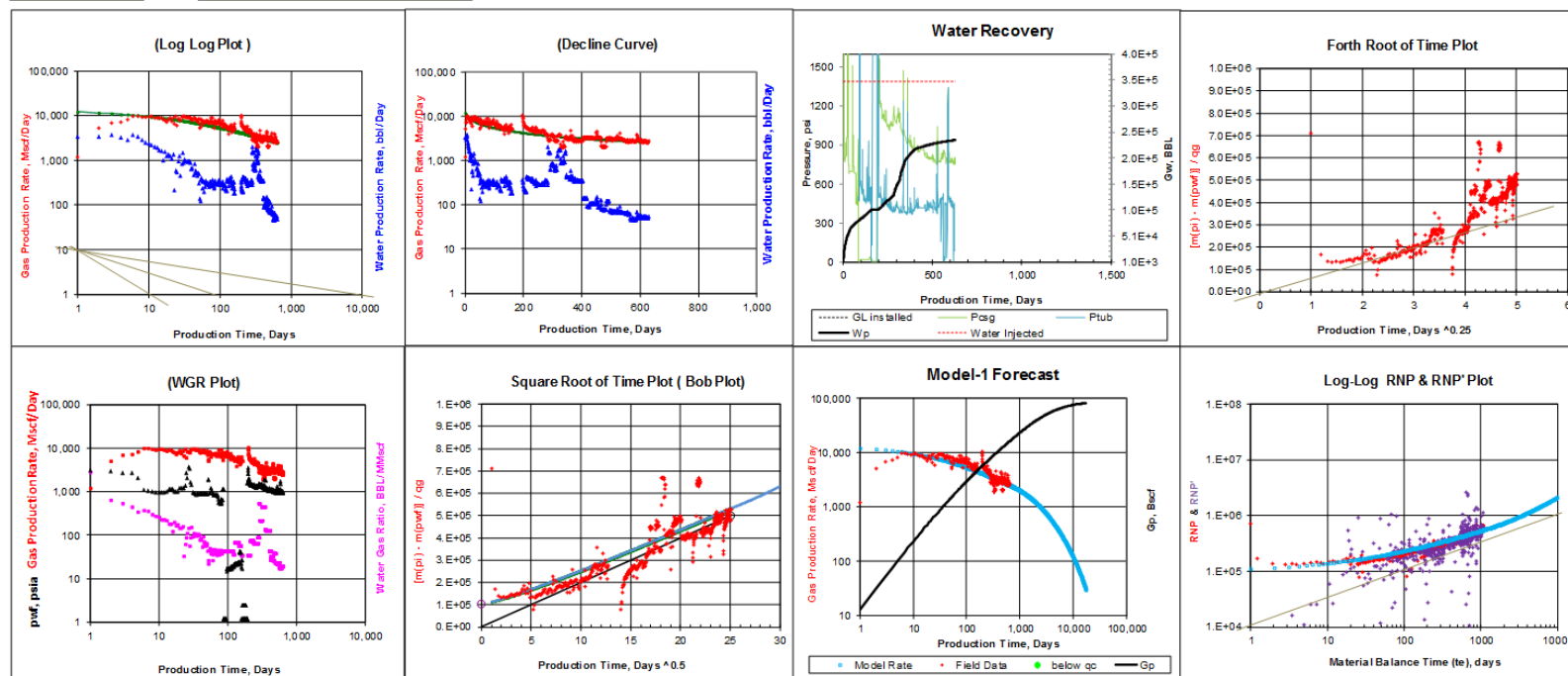


Run Analysis

Show / Hide $q_g < \text{critical}$

Run Model 1 Forecast

Well : dC

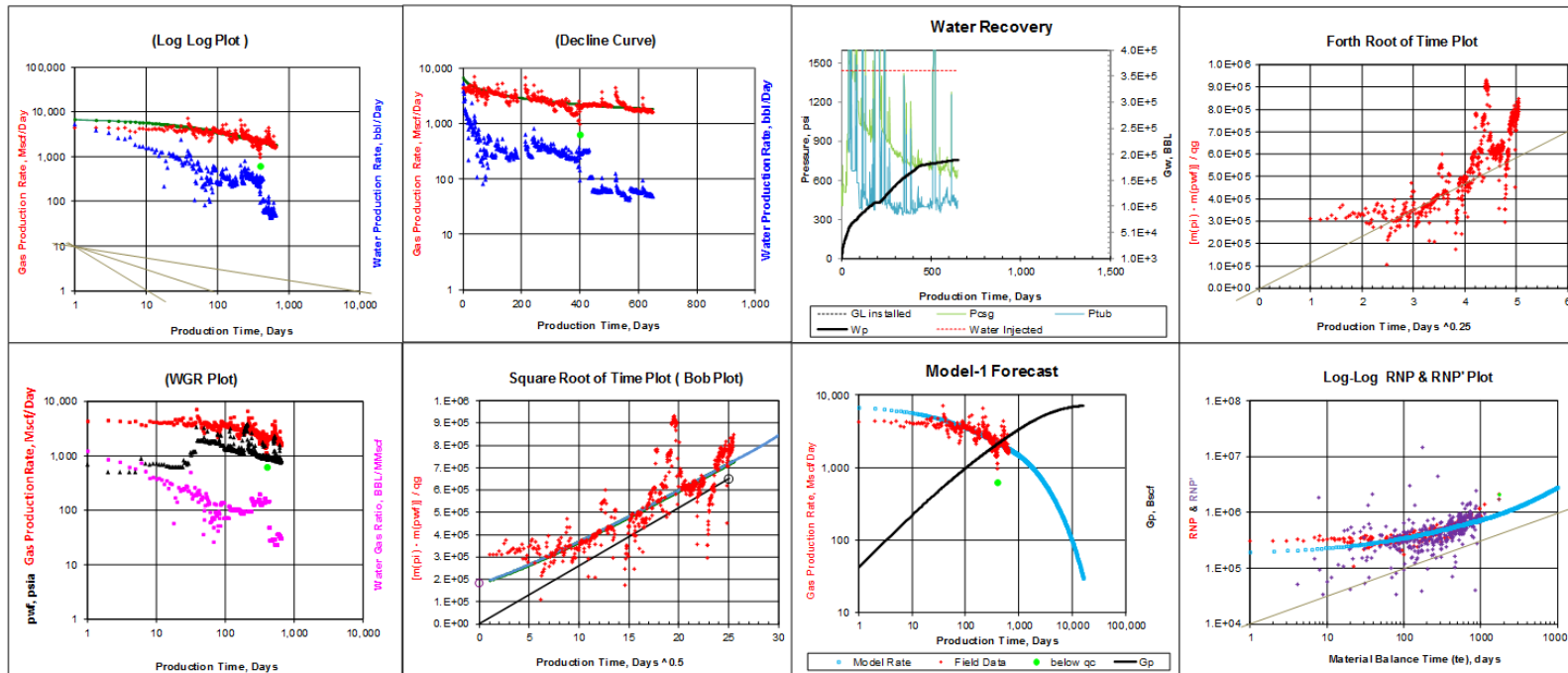


Run Analysis

Show / Hide $q_g < \text{critical}$

Run Model 1 Forecast

Well : dD

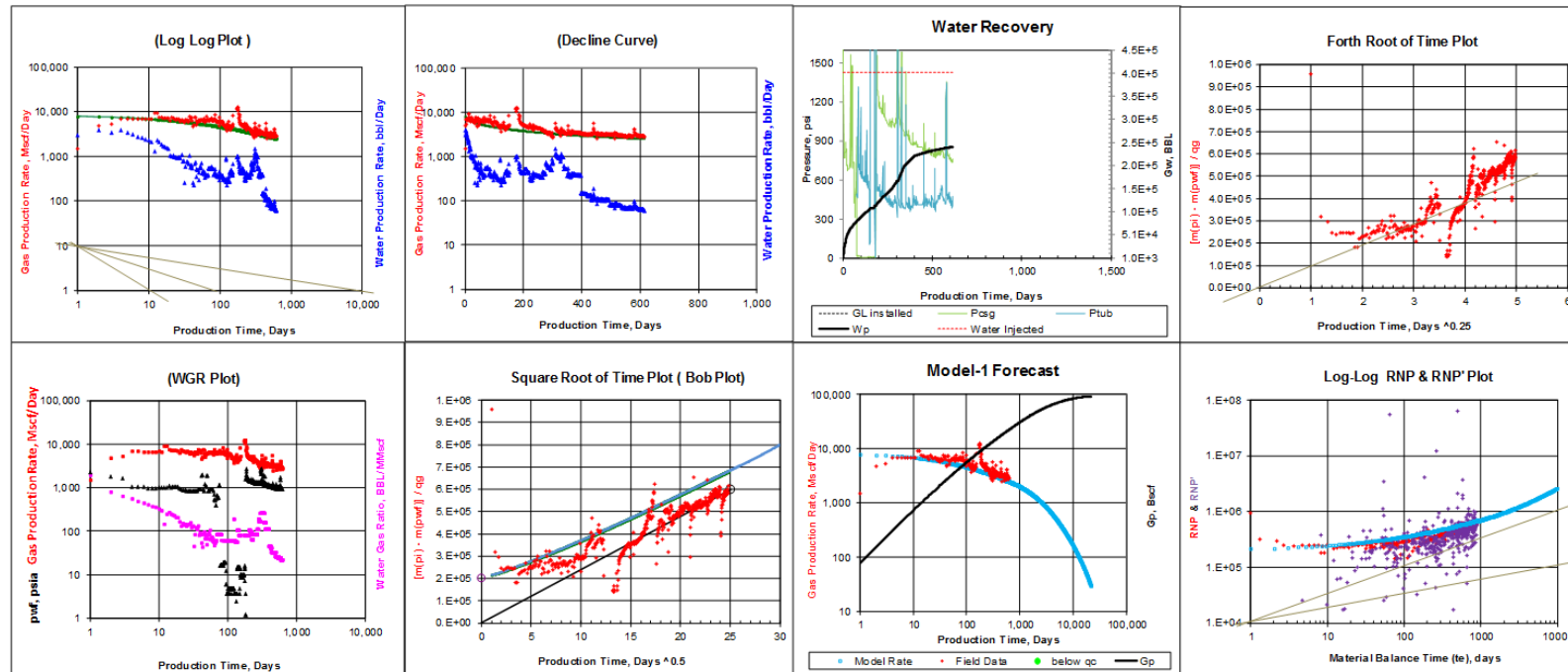


Run Analysis

Show / Hide $q_{g < critical}$

Run Model 1 Forecast

Well : dE

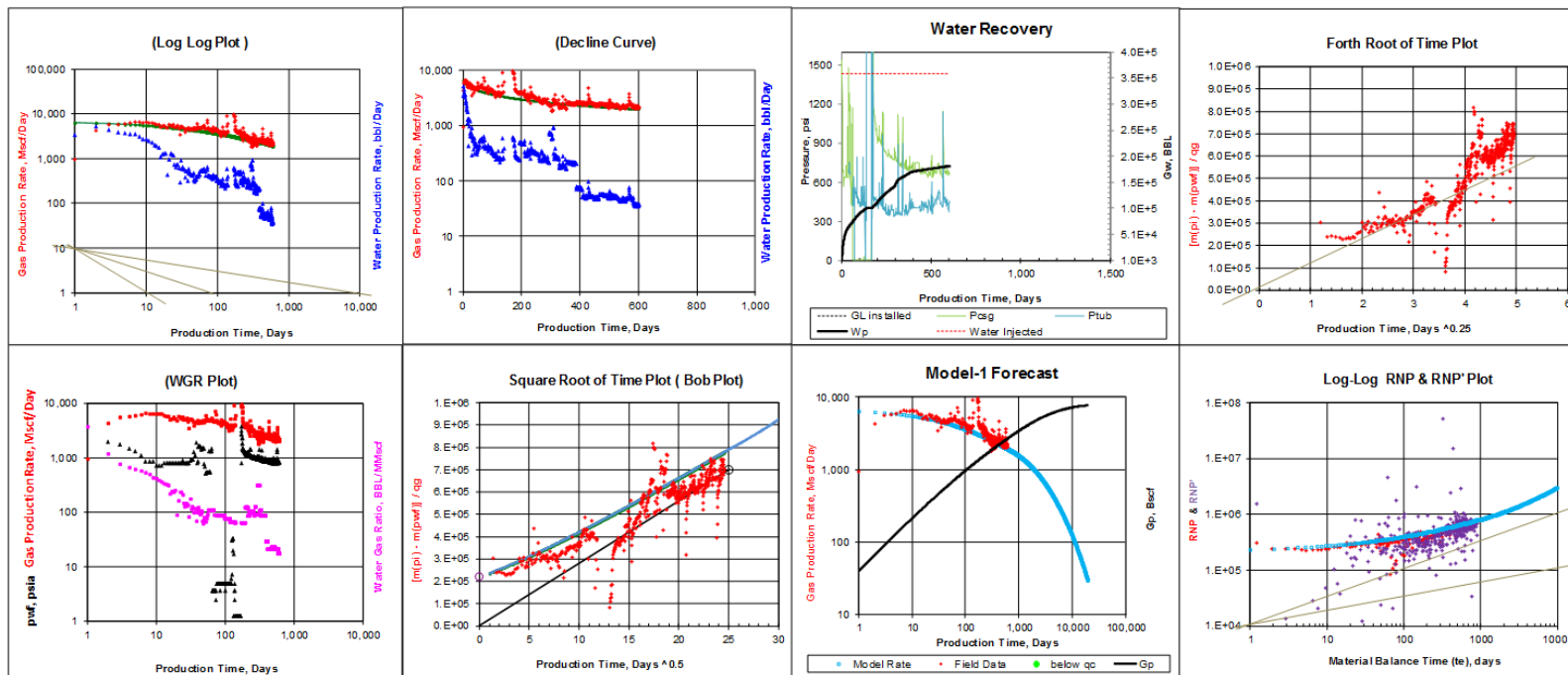


Run Analysis

Show / Hide $q_g < \text{critical}$

Run Model 1 Forecast

Well : dG

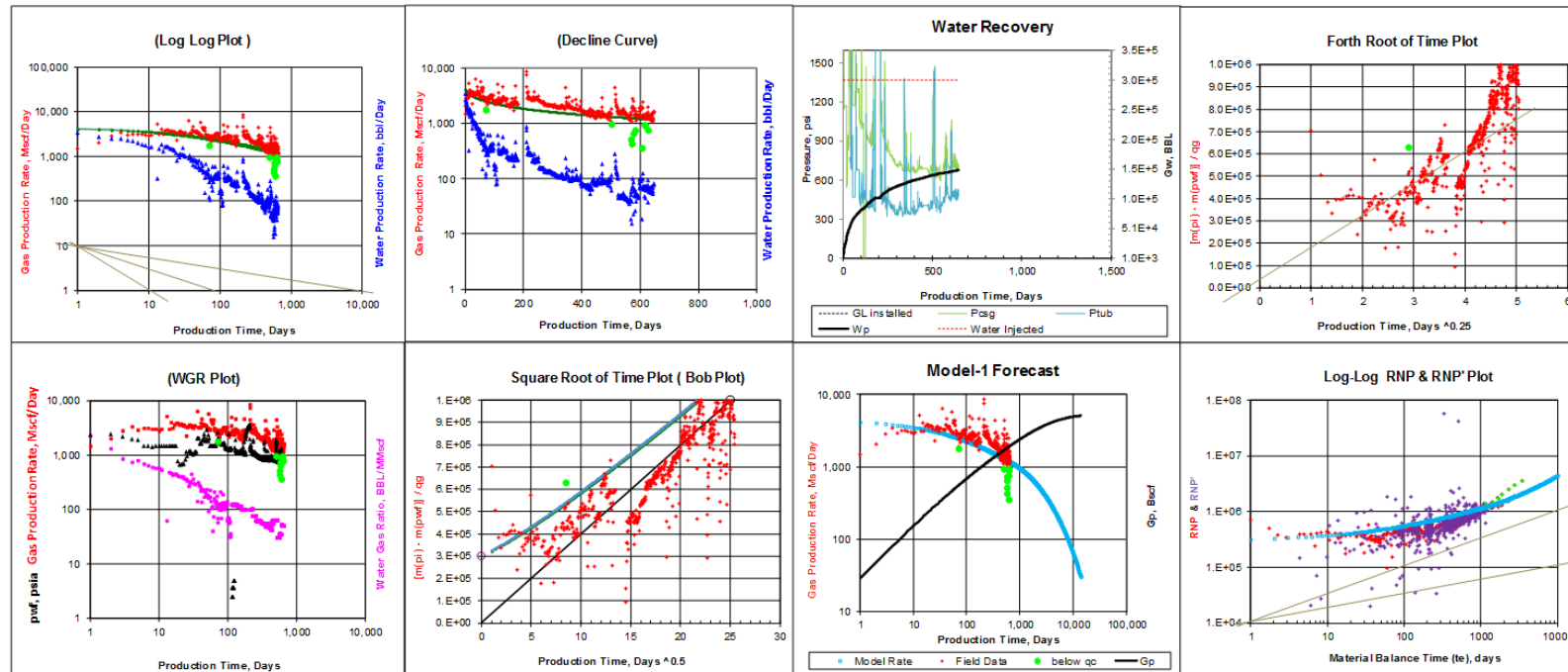


Run Analysis

Show / Hide $q_g < \text{critical}$

Run Model 1 Forecast

Well : dH

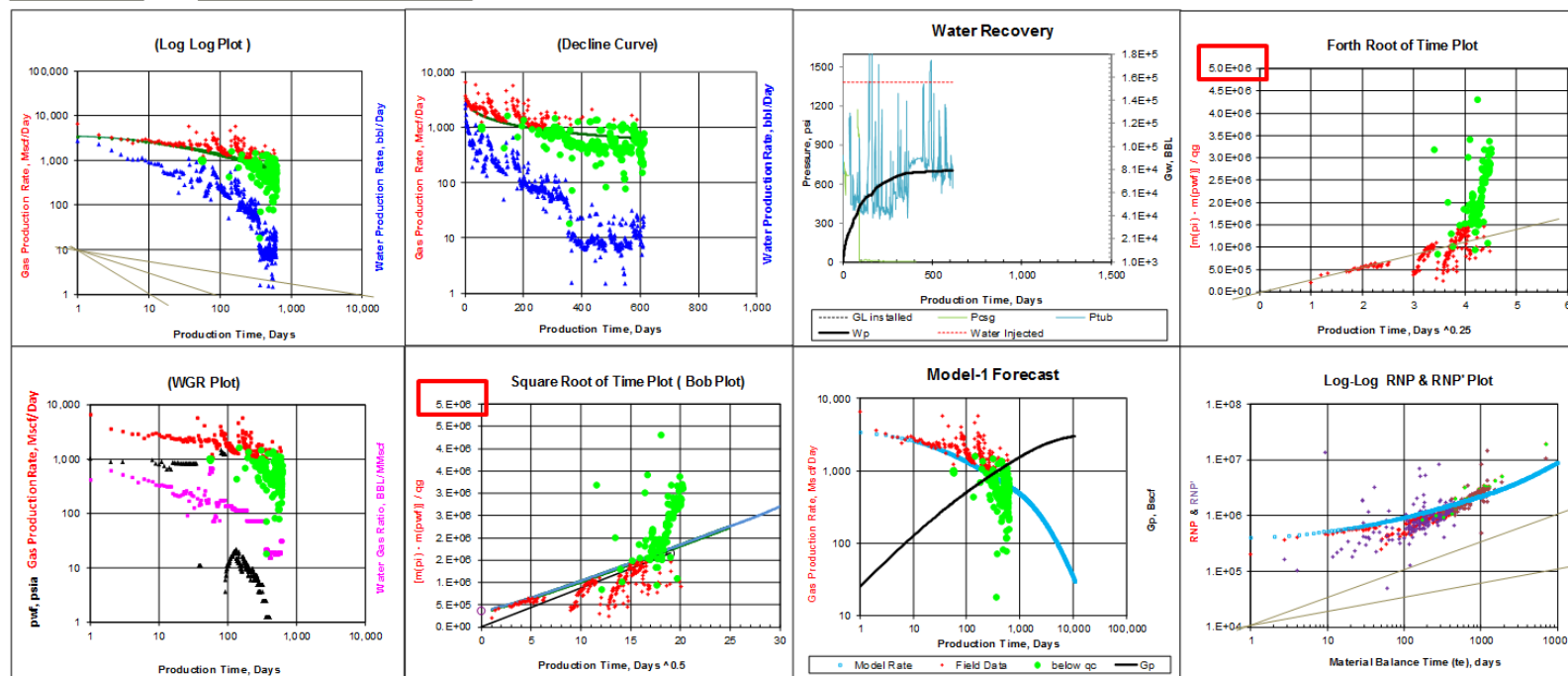


Run Analysis

Show / Hide $q_g < \text{critical}$

Run Model 1 Forecast

Well : dl

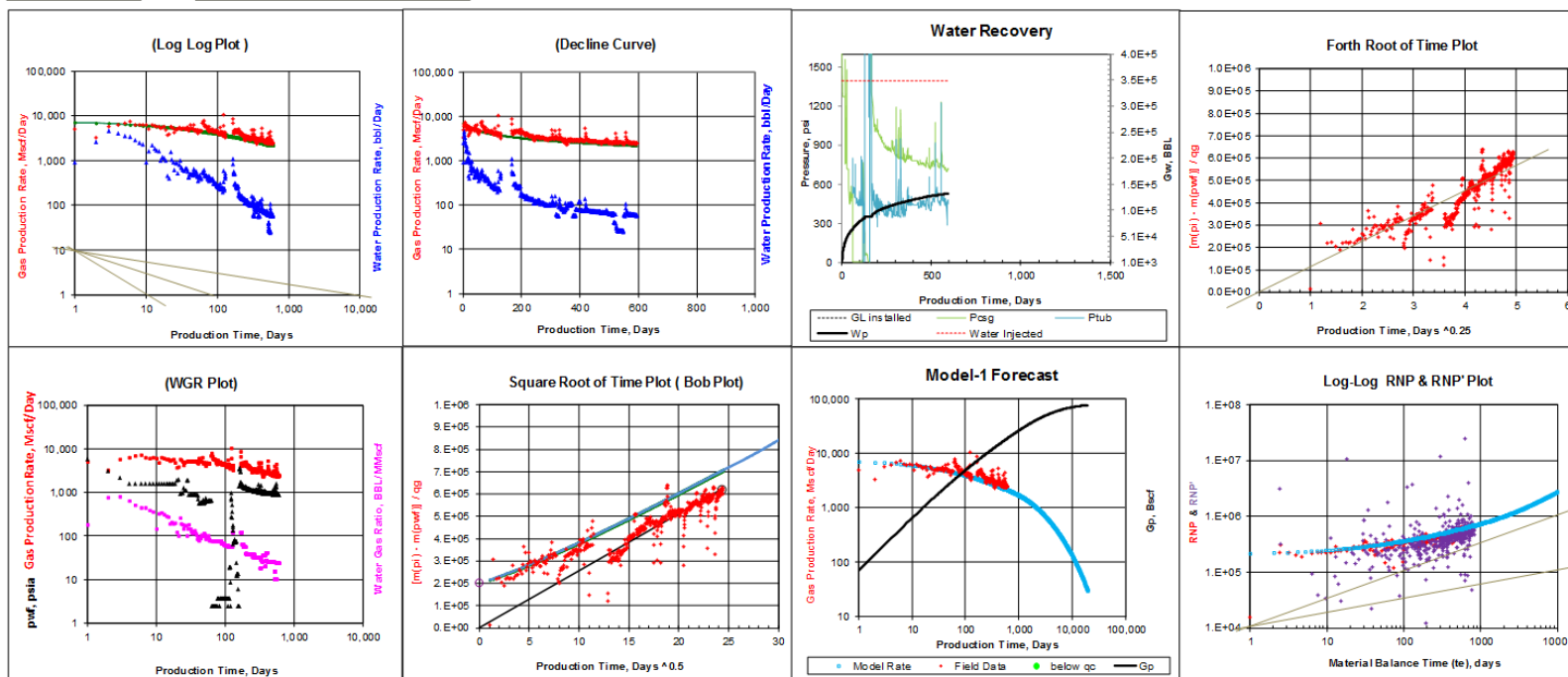


Run Analysis

Show / Hide $qg < \text{critical}$

Run Model 1 Forecast

Well : dJ

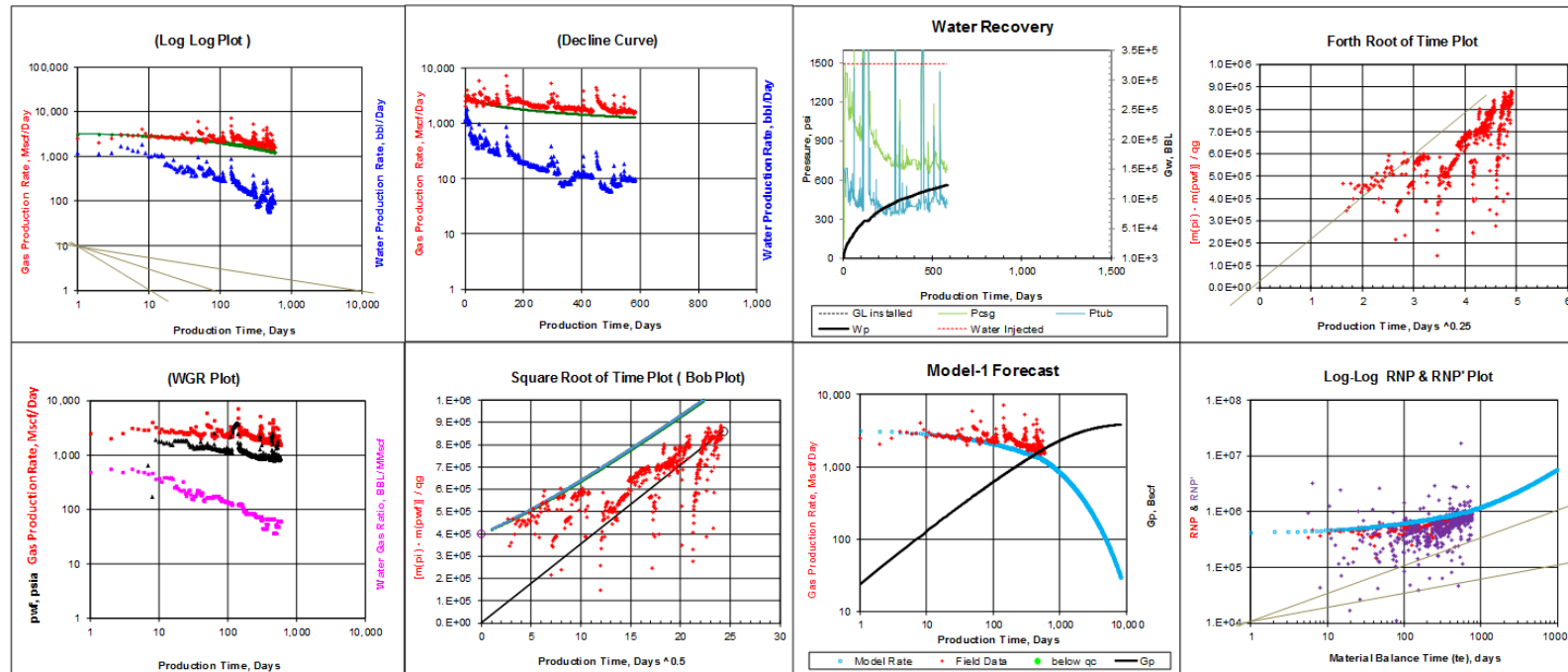


Run Analysis

Show / Hide $q_g < \text{critical}$

Run Model 1 Forecast

Well : dK

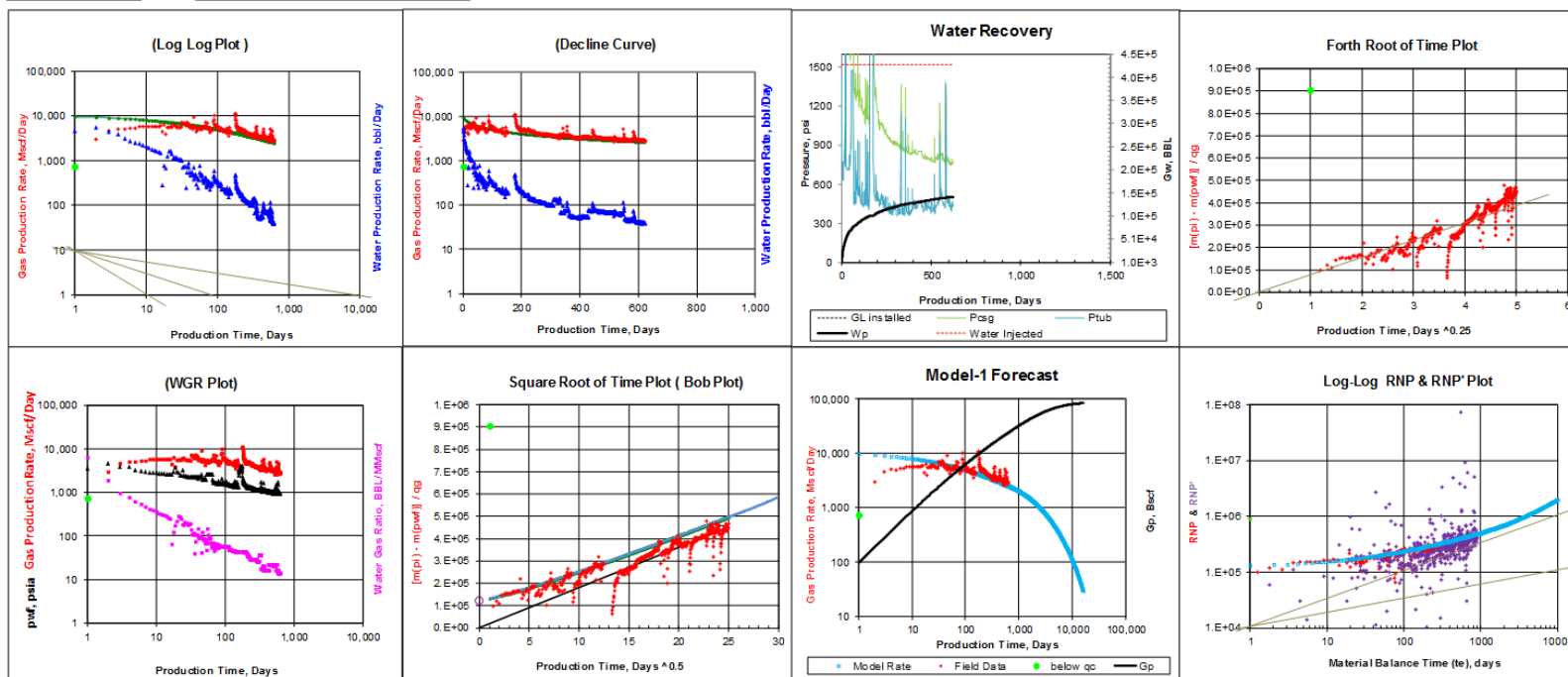


Run Analysis

Show / Hide $q_g < \text{critical}$

Run Model 1 Forecast

Well : dL

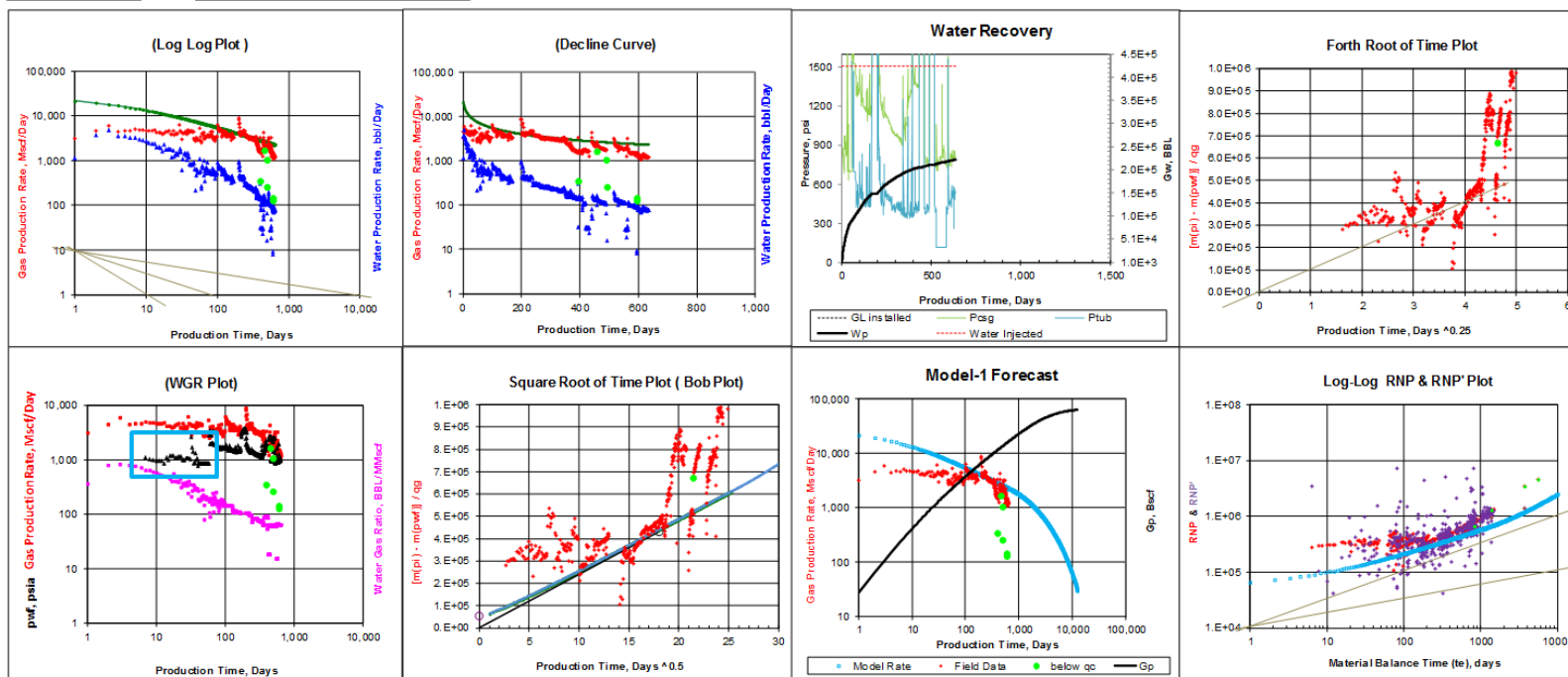


Run Analysis

Show / Hide $q_g < \text{critical}$

Run Model 1 Forecast

Well : dM

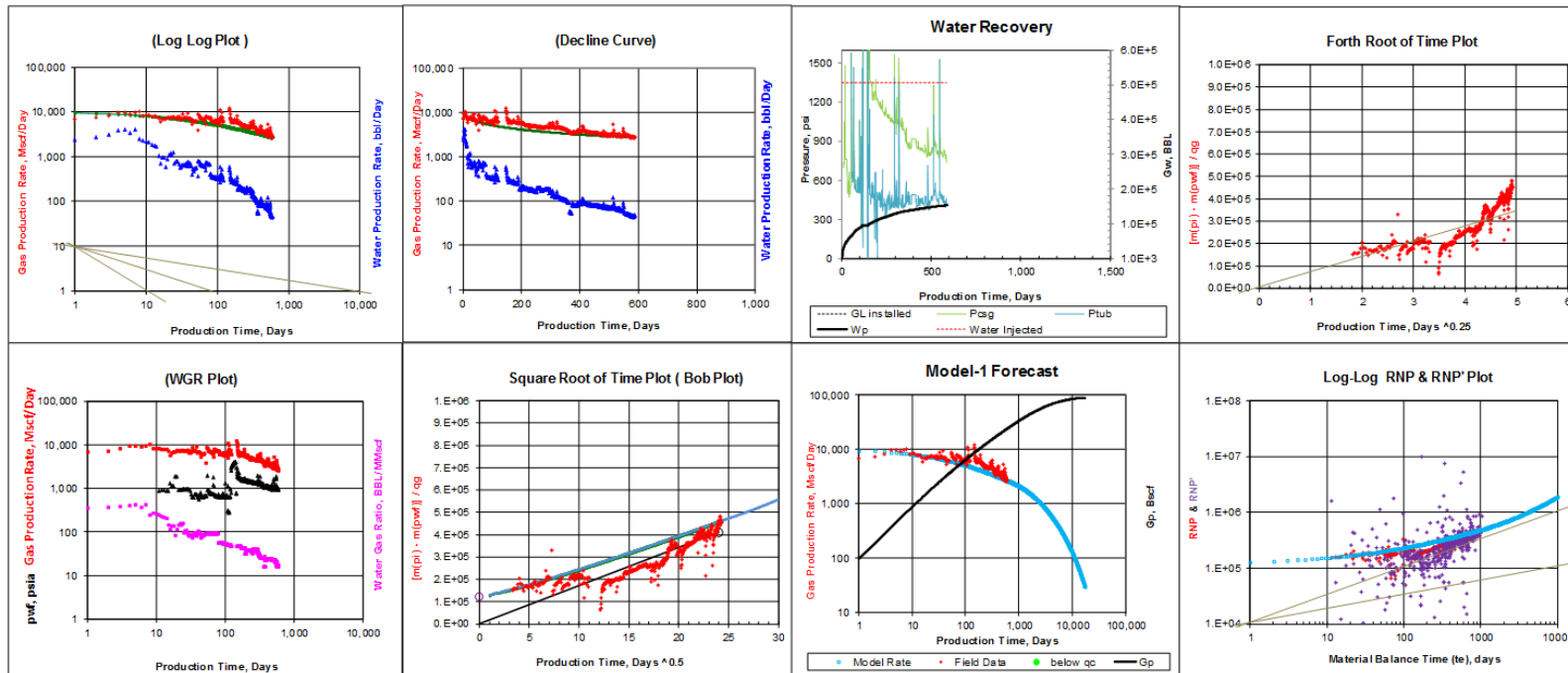


Run Analysis

Show / Hide $q_g < \text{critical}$

Run Model 1 Forecast

Well : dN

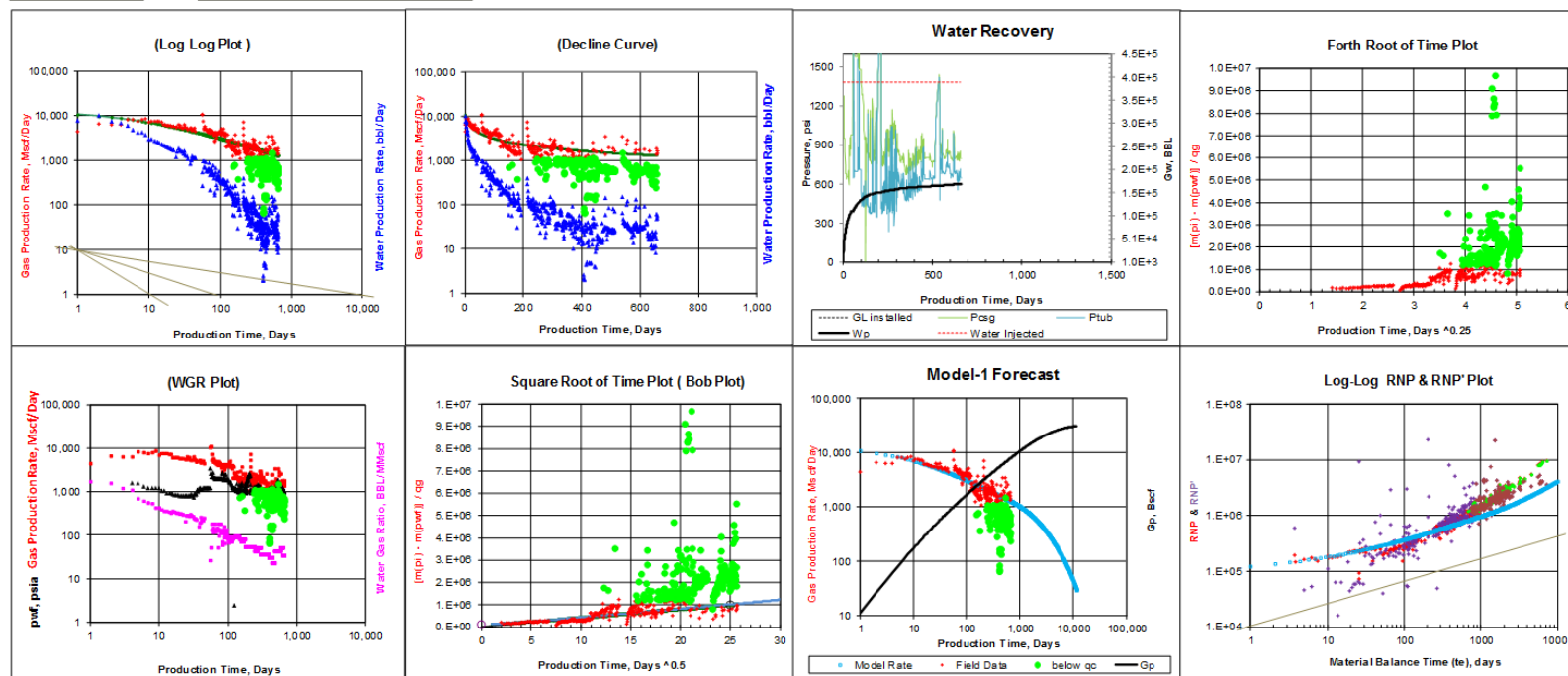


Run Analysis

Show / Hide $q_g < \text{critical}$

Run Model 1 Forecast

Well : dO



VITA

Name: Sippakorn Apiwathanasorn

Address: 3116 Texas A&M University
719 Richardson Building
College Station, TX 77843-3116

Email Address: SippakornA@gmail.com

Education: B.Eng., Petroleum Engineering, Chulalongkorn University,
Bangkok, THAILAND, 2006

M.S., Reservoir Geoscience and Engineering, IFP School,
Rueil- Malmaison, FRANCE, 2012

M.S., Petroleum Engineering, Texas A&M University,
College Station, Texas, USA, 2012